From three dimensional crystals to single molecular magnets: Electronic and magnetic properties of low dimensional advanced materials

Habilitationsschrift

vorgelegt dem

Fachbereich Physik

der Universität Osnabrück

von

Dr. rer. nat. Karsten Küpper

Osnabrück, im Juni 2019

Table of Contents

Introduction

Transition and rare earth metals as well as their oxides represent a large class of materials and exhibit an enormous variety of chemical, structural, magnetic, electronic and transport properties, giving rise to rich physics and a vast number of potential applications. Emergent phenomena, such as superconductivity, magnetism or multiferroicity, are the hallmark of many-body systems, and yet to unravel their nature remains one of the challenges in state-of-the-art condensed-matter physics.

These drastic effects are accompanied by phase transitions, for instance from one magnetic state to another one (antiferromagnetic / ferromagnetic / paramagnetic) or metal-to-insulator transitions. Collective ordering phenomena occur, mediated by a complex interplay of the structural order parameters and the electron's orbital, charge, and spin degrees of freedom, which frequently obscures the underlying physics. These phase transitions lead to significant changes in the underlying electronic structure of the compound in question. Thus, a careful study of the electronic properties is of utmost importance for understanding the above mentioned complex ordering phenomena.

Furthermore, in low dimensional systems, where at least one of the three dimensions is intermediate between those characteristic of atoms/molecules and those of the bulk material, generally in the range 100 nm or below, the dimensional constraint gives rise to size effects, which can significantly change the electronic structure and hence the overall properties of the material in question. A careful characterization of the magnetic and electronic structure is of interest also with respect to potential future applications in various fields such as spintronics, novel magneto resistive devices, e.g. magnetic tunnel junctions, advanced materials for anodes in batteries, or improved nanoparticles for applications in biological labeling and imaging.

This habilitation thesis is dedicated to the comprehensive electronic and magnetic

structure characterization of a number of transition-metal and rare-earth- based materials showing collective ordering or coupling phenomena on different length scales and dimensions and is based on selected publications which can be attributed to three different subject areas.

In the first chapter, publications [**H1-H4**] deal with the electronic and partly magnetic structure of different rare earth ($4f$) and transition metal ($3d$) oxides. Firstly, the electronic structure of the ternary oxide scandates $REScO_3$ (RE = Pr, Nd, Sm, Eu, Gd, Tb, and Dy) [**H1,H2**], which are interesting due to their high dielectric constant k and their suitability to serve as substrates for highly strained ferroelectric thin films, for instance. Furthermore, the interplay of spin and orbital moments with the lattice parameters across structural phase transitions in the colossal magneto resistance manganites $La_{1-x}Sr_xMnO_3$ [**H3**] is investigated. Finally, we study the magnetic ground state of the charge frustrated, two dimensional layered, and magneto electric compound $LuFe_2O_4$ [**H4**].

The second chapter is devoted to (two-dimensional) magnetite thin films and Fe_3O_4/NiO - bilayers with thicknesses less than 100 nm. Such thin films and bilayers are of significant interest for future applications in the field of spintronics or as building block of novel magnetic tunnel junctions. However, for the optimization of such potential all oxidic devices as mentioned above, detailed characterization and understanding of the underlying structural, chemical, electronic, and magnetic properties of the thin films and the interfaces, e.g., between magnetite and the substrate or the antiferromagnetic NiO are indispensable. Therefore, we studied the underlying structural, chemical, electronic, and magnetic properties of a number of Fe_3O_4/NiO bilayers grown in MgO (001) and Nb-doped $SrTiO_3$ (001) [**H5**], as well as thermally induced interdiffusion of Ni^{2+} ions out of NiO into Fe_3O_4 ultrathin films resulting in off-stoichiometric nickel ferrite-like thin layers [**H6**].

The third and final chapter is dedicated to zero-dimensional nanomaterials, i.e. all three dimensions are measured within the nanoscale (below 100 nm). $NaREF_4$ (RE: rare earth) nanoparticles, which have attracted increasing interest in recent years for applications in biological labeling and imaging, photodynamic therapy and drug delivery, photovoltaics, photonics and security labeling, are the topic of the first part of this chapter. In the framework of this chapter core-shell systems composed of a β-

$NaEuF_4$ core and a β-$NaGdF_4$ shell, with respect to their structural, chemical, optical and magnetic properties were studied [**H7**]. The second section is about magnetic molecules, which contain a finite number of interacting spin centers (e.g. paramagnetic ions), thus providing ideal opportunities to study basic concepts of magnetism. In such magnetic molecules, spin coupling between paramagnetic transition-metal ions is mediated via bridging ligand atoms, leading to a variety of interesting fundamental properties such as intramolecular exchange interactions or magnetic anisotropy. Iron-based magnetic polyoxometalates with $\{Mo_{72}Fe_{30}\}$- and $\{W_{72}Fe_{30}\}$-core [**H8**], as well as a number of star-shaped molecules with intriguing magnetic properties, have been characterized in the framework of this habilitation thesis by means of X-ray Magnetic Circular Dichroism (XMCD) in conjunction with SQUID-measurements and suitable theoretical approaches [**H9-H12**].

Electronic and magnetic properties of selected three dimensional 3d and 4f single crystals

1.1 The ternary oxides $RE ScO_3$ (RE = Pr, Nd, Sm, Eu, Gd, Tb, and Dy)

Dielectric and ferroelectric "d^0-perovskites" like $BaTiO_3$, $LaTiO_3$ or $SrTiO_3$ are subject to intense research activities due to their remarkable dielectric properties and the possibility to control the electrical polarization, which is a required pre-requisite for constructing a ferroelectric memory (FeRAM) [1, 2]. Studying these materials significantly changed our fundamental understanding of electron correlation effects within the last three decades. Basically, transition-metal oxides can be classified into two type of insulators: Mott-Hubbard insulators (whose band gap is ruled by the repulsive interaction potential U_{dd} between the $3d$ electrons), and charge transfer insulators, in which the energy between the filled ligand p bands and the unoccupied upper $3d$ states (Δ_{pd}) dominates the band gap [3]. In this relation, two issues of interest may be outlined: *i*) by analyzing detailed trends in the band gap variation, try to learn more about the nature of correlation in the material(s) in question; *ii*) use the detected trends for tailoring the optical band-gap in wide-gap oxidic insulators to desired values for possible applications – e.g., as a high-k gate dielectric, or a transparent conducting oxide [4]. Among a number of other wide gap oxides, the scandates of type $RE ScO_3$ (RE = Pr, Nd, Sm, Eu, Gd, Tb, and Dy) are particularly promising candidates for replacing SiO_2 as the gate dielectric (due to potentially reduced gate leakage currents) [5–8]; moreover they can be used as a model system for applications in the terahertz regime [9]. Furthermore, in particular $DyScO_3$ and $GdScO_3$ belong to the best avail-

able thin film substrates concerning the growth of highly strained thin ferroelectric films [10, 11]. A reduction of the band-gap between DyScO3 and $SrTiO_3$ has been predicted [12], and GdScO3 supports have been used to control the magnetic anisotropy via a strain mediated tailoring of the oxygen coordination environment in a $SrRuO_3$ layer [13] and to create a periodic array of flux closures in ferroelectric $PbTiO_3$ films, mediated by tensile strain of the used $GdScO_3$ substrate [14]. In order to understand the complex properties and the interaction of the scandates at the interface with other materials, a comprehensive study of the electronic structure is indispensable. However, only quite a few information is available, in particular Delugas *et al.* [8] carried out *ab initio* investigations on $DyScO_3$; Luckovsky *et al.* [6] published some oxygen X-ray absorption spectra. Therefore, we performed a detailed and systematic electronic structure invesitgation of $REScO_3$ (RE = Pr, Nd, Sm, Eu, Gd, Tb, and Dy) with emphasis on complementary x-ray spectroscopic approaches in combination with *ab initio* electronic structure calculations [**H1,H2**].

The ternary $4f$-$3d$ oxides $REScO_3$ crystallize in space group Pbnm (no. 62) corresponding to an orthorhombic perovskite structure with $a \approx b \approx \sqrt{2a_p}$, and $c \approx 2a_p$ (where a_p is the cubic perovskite cell parameter), and four formula units per units per cell [15] (c.f. Table 1.1).

	$PrScO_3$	$NdScO_3$	$SmScO_3$	$EuScO_3$	$GdScO_3$	$TbScO_3$	$DyScO_3$
a (Å)	5.6118(1)	5.5809(1)	5.5343(1)	5.5109(1)	5.4862(1)	5.4654(1)	5.4494(1)
b (Å)	5.7802(1)	5.7765(1)	5.7622(1)	5.7565(1)	5.7499(1)	5.7292(1)	5.7263(1)
c (Å)	8.0276(1)	8.0072(1)	7.9674(1)	7.9515(1)	7.9345(1)	7.9170(1)	7.9132(1)

Table 1.1: Lattice parameters of $RScO_3$ determined by Liferovich *et al.* [15]

Fig. 1.1 presents a schematic plot of the orthorhombic perovskite structure. Due to their congruent melting behavior, the high quality $REScO_3$ (RE = Pr, Nd, Sm, Eu, Gd, Tb and Dy) bulk single crystals investigated here have been grown from the melt by the conventional Czochralski technique by R. Uecker, Institute for Crystal Growth, Berlin [10, 16].

X-ray spectrocopic techniques based upon the interaction of light with matter belong

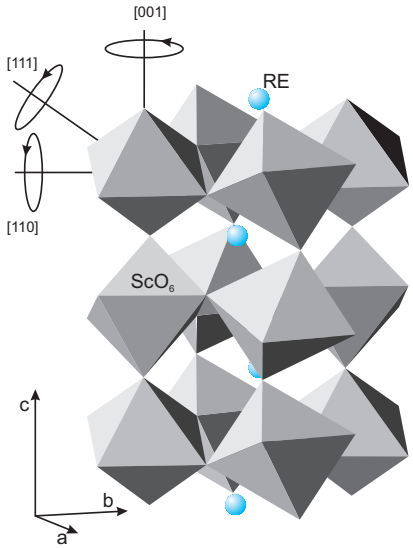

Figure 1.1: Representation of the orthorhombic $RE ScO_3$ crystal structure; also indicating the $GdFeO_3$-like distortion of the perovskite structure [17].

to the most powerful tools to probe the electronic structure of atoms, molecules and solids of all kinds. Here, we probed the electronic structure of $RE ScO_3$ by a set of complimentary x-ray spectroscopic techniques in the soft x-ray regime (mainly x-ray absorption near edge spectroscopy (XANES) across the O K, Sc $L_{2,3}$ and rare earth $M_{4,5}$ edges and corresponding (normal) x-ray emission spectroscopy ((N)XES)). These two complementary approaches are now explained in brief.

Fig. 1.2 displays schematic illustrations of the x-ray absorption and the x-ray emission process, respectively. In x-ray absorption spectroscopy (c.f. Fig. 1.2 left), the absorptivity of a material as function of incident x-ray energy $h\nu$ is probed [20], i.e. the energy of the exciting photons is tuned across the desired absorption edge [21]. During x-ray absorption, an electron is excited into the unoccupied states (see arrow marked with 1 in Fig. 1.2 left), leaving a core hole. Recombination of the excited electron or an electron out of the valence band (2) occurs at an ultrafast femto- or attosecond time scale, which is followed by secondary excitation processes, either by Auger electrons or fluorescence (photons). According to the dipole selection rule for photon-excited transitions the angular quantum number is changed by 1 ($\Delta l = \pm 1$) while the spin is

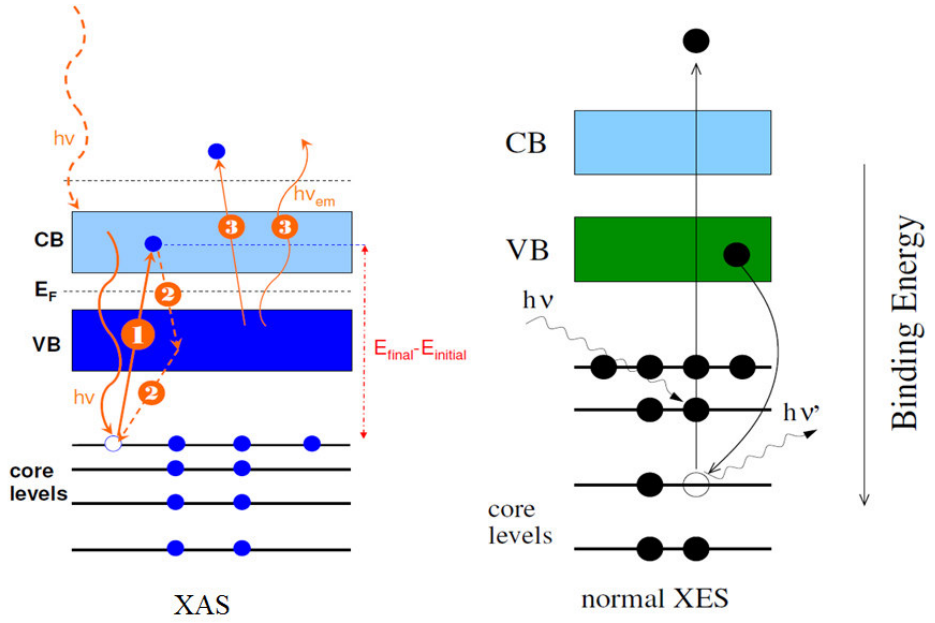

Figure 1.2: Schematic representation of x-ray absorption spectroscopy (XAS) (left) [18] and (normal) x-ray emission spectroscopy (XES) [19].

conserved ($\Delta s = 0$). In case of transition metal compounds, XAS is often performed across the ligand K and transition metal L edges. In case of the ligand, e.g. O K edges (O $1s$ ($L = 0$) $\rightarrow$ O $2p$ ($L = 1$) transition) the resulting XA-spectra reflect a part of the unoccupied density of states, or the conduction band. Contrary, the transition metal $L_{2,3}$ XA-spectra are often dominated by atomic and short range multiplet effects. Hence, XAS across the transition metal $L_{2,3}$ edges leads to information about the local chemical structure of the transition metal ion in question as well as about its local coordination and crystal field, including potential charge transfer effects between transition metal ion and the ligand.

X-ray absorption spectra can be measured by different detection techniques. Ultrathin samples, often grown on membranes, can be probed in transmission, for bulk samples often the drain current caused by the emission of Auger electrons is taken, which is known as total electron yield (TEY). If one measures only electrons in a certain energy range, e.g. by means of a channeltron, one measures the partial electron yield (PEY). These detection methods are rather surface sensitive, whereas detecting the emitted photons by a photodiode leads to bulk sensitive XA-spectra in total fluores-

cence yield (TFY). If the photons are discriminated by energy dispersive gratings and then collected by x-ray emission or CCD detectors, one gets spectra in partial fluorescence yield (PFY). Whereas the FY modes can be used to measure also (highly) insulating samples, in particular transition metal L and rare earth M edge spectra recorded in FY detection mode may suffer from strong self absorption and saturation effects, which lead to broadening and modifications of the spectral shape and altering of peak ratios, for instance [22, 23]. Ligand K-edge spectra are less affected by saturation effects. A special bulk sensitive detection mode can be utilized if thin films, heterostructures or multilayers are grown on luminescating substrates such as MgO, Al_2O_3, or $MgAl_2O_4$. Here, the visible light escaping from the substrate can be probed in transmission geometry by, e.g., using a GaAs photodiode. This way it may be possible to compare the surface sensitive XAS (TEY mode) with the bulk sensitive results from the luminescence yield (LY) [24]. in The XA-spectra can be formally divided into two parts. The approach discussed in the framework of this thesis can be also called near edge x-ray absorption spectroscopy (NEXAFS) or x-ray absorption near edge structure (XANES). Here. the excitation of an electron into the unoccupied states across a desired edge is probed. The other approach is called extended x-ray absorption fine structure (EXAFS). The EXAFS region is located at photon energies well above the corresponding XANES threshold, where the electron is emitted into the continuum and its scattering with the environment of the absorber leads to characteristic features comprising information about the local structure.

Emission of the excited electron well above an absorption threshold into the continuum is also a prerequisite for normal x-ray emission spectroscopy (NXES) (c.f. Fig. 1.2 right). The x-ray emission can be analyzed element-selective and reflect the partial densities of states, convoluted by lifetime broadening [25]. In combination with valence band x-ray photoelectron spectroscopy (XPS) or ultraviolet photoelectron spectroscopy (UPS), NXES is a powerful tool to investigate the occupied density of states of a compound in question, in particular in correlation with *ab initio* electronic structure calculations. If x-ray emission is measured resonantly, i.e. across a absorption edge, so called resonant x-ray emission spectroscopy (RXES) may be used to tackle resonant inelastic x-ray scattering (RIXS) features, e.g. local charge transfer excitations or optical weakly accessible bands such as *dd*-transitions of transition metal cations in transition metal oxides [20, 26].

Since $RE ScO_3$ are highly insulating crystals, we performed the XAS in TFY mode,

the (photon-in, photon-out) (N)XES spectra are not affected by charging effects. In particular, we utilized a combination of oxygen K-edge XAS and (N)XES to probe the occupied partial and unoccupied density of states and to determine the band gap of these ternary oxides in dependence of the rare earth.

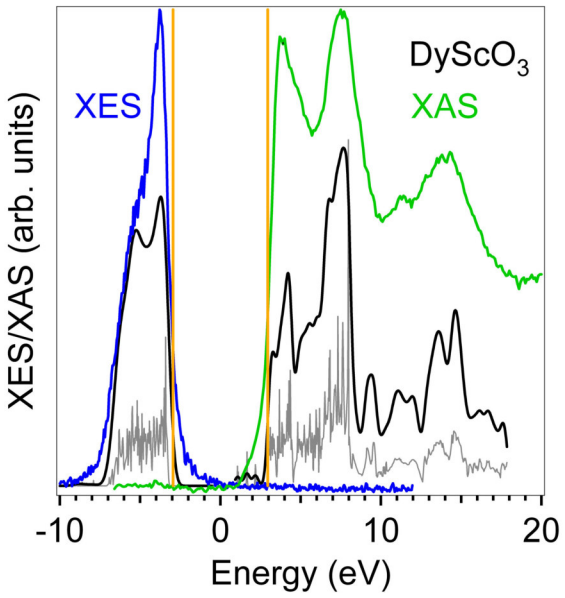

Figure 1.3: O K XAS (green) and O K XES (blue) of $DyScO_3$. LDA+U (Local Density Approximation + "Hubbard U") calculations (grey) below experimental data were convoluted with 0.7 (XES) and 0.4 eV (XAS) Gaussian to consider experimental broadening (black) [**H1,H2**].

Fig.1.3 displays the O K edge XAS and O $2p \rightarrow$ O $1s$ XES of $DyScO_3$ as an example. The spectra of the other $REScO_3$ crystals were performed under equivalent conditions. For reasons of comparison the energies of the O K XAS and XES were shifted by 530 eV, i.e. the binding energy of the O $1s$ XPS peak. This combination is a good approach to specify band gaps of wide gap charge transfer insulators as $REScO_3$, since the band gap is formed by Sc $3d$ and RE $5d$ states hybridized with O $2p$. A further advantage is that these experiments can be performed under the same conditions in a rather short time for various samples. The band gaps were determined by extracting the calculated highest occupied and lowest unoccupied states from the calculated spectra. This prevents a wrong determination of the gap due to some states present near Fermi energy which stem from defects. The slope of these lines (represented by

	$PrScO_3$	$NdScO_3$	$SmScO_3$	$EuScO_3$	$GdScO_3$	$TbScO_3$	$DyScO_3$
this work	5.7 eV	5.6 eV	5.6 eV	5.7 eV	5.8 eV	6.1 eV	5.9 eV
Cicerrella[27]	5.7 eV	5.5 eV	5.4 eV		5.2 eV	5.6 eV	5.3 eV
Lim *et al.* [5]			5.5-6.0 eV		6.5 eV		
Afanasev *et al.* [28]					5.6 eV		5.7 eV
Lucovsky *et al.* [6]					5.8 eV		

Table 1.2: Band gaps of rare-earth scandates (in eV) as found in this work **[H2]** (the upper line) in comparison with previously reported values. Since we applied the identical equivalent experimental conditions, the relative error bars are ± 0.1-0.2 eV; the absolute error could be larger.

the orange lines in Fig. 1.3) was used to derive the band gaps of the other crystals. Since for $GdScO_3$ and $SmScO_3$ *ab initio* electronic structure calculations were also performed, the above described approach could be cross checked, ensuring a uniform determination of the band gap for each $RE ScO_3$ crystal. Hence, we obtain a rather good approximation of the band gap with this combination of XAS and XES at the oxygen K edge.

Table 1.2 compares the results obtained from the applied combination of XAS and XES with previously reported values stemming from different approaches, i.e. ultraviolet absorption [27], ellipsometry measurements [5, 6], and a combination of internal photoemission and photoconductivity measurements [28]. While the ellipsometry experiments of Lim *et al.* yield partly significantly higher values for the band gap compared to the XAS-XES combination [5], UV absorption [27] indicates slightly lower values for the band gap. Overall decent to very good agreement is achieved compared to the other experiments. Interestingly, the obtained band gap variation does not follow typical structural differences of $RE ScO_3$ as function of the rare earth ion. First, we want to point out that the most basic structural parameters (lattice constants a and/or c or unit cell volume) are monotonically decreasing with larger RE ion [15]. We can also exclude that the band gap variation correlates with the Goldschmidt factor, also known as tolerance factor: a larger RE-ion leads to a lower tolerance factor. A direct correlation to the Sc-O-Sc bond angles is not found as well. Finally, from Sc $L_{2,3}$ XAS, changes in local symmetry or crystal field can be neglected, and are unlikely

the reason for the observed changes of the optical band gap.

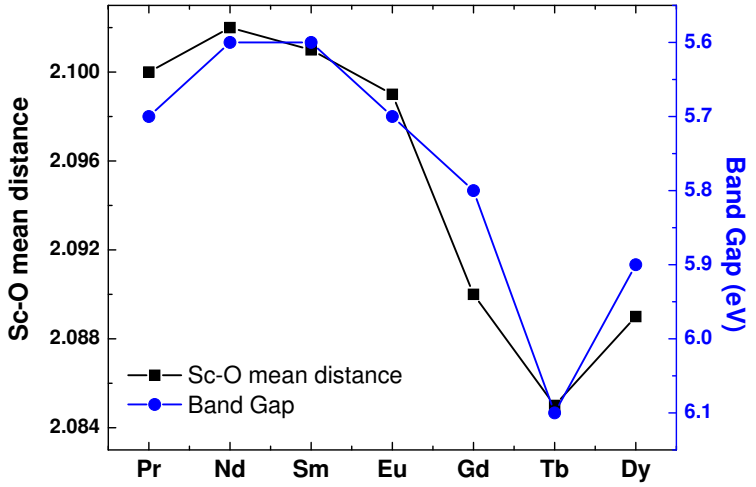

Figure 1.4: Sc-O mean distance of $REScO_3$ in comparison with the experimental band gaps [**H2**]. The structural parameters have been extracted from Liferovich *et al.* [15].

Interestingly, we find a clear correlation of the Sc-O mean distance which can be qualitatively established (Fig. 1.4). For a qualitative discussion of this finding it is important to consider that the RE 4f states are split much larger than the band gap and do not participate in the build up of the latter. Hence, the band gap seems to be dominated by the strength of the O $2p$ - Sc $3d$ interaction, inversely following a non-trivial variation of the Sc-O mean distance, rather than from structural parameters as briefly discussed above. A remarkable observation is that a Sc-O mean distance variation of up to 0.4% leads to tenfold "amplified" band-gap variation of 4.2%. In conclusion, we demonstrated that the optical band gap of the ternary oxides $REScO_3$ is dominated by the strength of the O$2p$ - Sc $3d$ interaction. For this the $GdFeO_3$-like distortion of the perovskite, influencing the mean Sc - O distances, plays a major role. The unusual result that relative Sc-O mean distance variations lead to tenfold amplified variations of the optical band gap values may stimulate further complementary experimental and theoretical work on this class of materials.
For a more detailed study of the electronic structure of $REScO_3$ (RE = Pr, Nd, Sm, Eu, Gd, Tb, and Dy) including a combinatoral x-ray spectroscopic approach, magnetic measurements, neutron and x-ray diffraction analysis, and theoretical LDA+U

electronic structure calculations the interested reader is referred to publications [**H1**] and [**H2**].

1.2 The colossal magneto resistance manganites $La_{1-x}Sr_xMnO_3$

Hole doped manganese oxides with the perovskite structure and composition $RE_{1-x}A_xMnO_3$ (where RE and A denote a trivalent rare earth atom and a divalent alkaline earth metal atom, respectively) display a remarkably rich phase diagram as a function of temperature, magnetic field and doping that is due to the complex interplay of charge, spin, orbital and lattice degrees of freedom. This competition of different phases on the nanoscale has been the subject of many studies during the last decade [29–31]. The variety of properties is often due to different localization of $3d$ electrons giving rise to intra atomic correlation effects of varying strength. Moreover, the orbital degeneracy compatible with a given crystal space group can be lifted by Jahn-Teller distortions. In a cubic crystal the Jahn-Teller distortion leads to a lowering of the symmetry and, thus, a splitting of the e_g level. Its occupation, determined by doping and energetic position, strongly influences the hybridisation between the Mn $3d$ and the O $2p$ states, which in turn is crucial for the colossal magnetoresistance (CMR), a huge negative change in the electrical resistance induced by an applied magnetic field [32, 33], observed in these compounds. CMR effects can be significantly stronger than the giant magneto resistance (GMR) effect observed in a number of multilayers and superlattices comprising an alternating stack of ferromagnetic and non-magnetic metallic layers (Peter Grünberg and Albert Fert, Physics Nobel Prize 2007) [34, 35]. Furthermore, the superparamagnetic limit might be pushed to higher storage density by the use of nanostructured $La_{1-x}Sr_xMnO_3$ as read head in hard disks [36], moreover $La_{0.7}Sr_{0.3}MnO_3$ is of interest for magnetic tunnel junctions due to its nearly 100% spin polarization (half metallic ferromagnetism) and a high Curie temperature of around 350 K [37, 38].

The long-standing double exchange (DE) model provides a qualitatively correct approach of the CMR effect in manganites [39]. In order to develop also an improved quantitative understanding, several theoretical and experimental results have been performed and more complex, although not necessarily mutually exclusive, mecha-

nisms such as short range ordered Jahn-Teller distortions in the local environment of the magnetic atom with resulting electron localization and polaron formation [40, 41], charge and orbital ordering [42], and phase separation [43, 44] have been discussed. The band structure of $LaMnO_3$ and $La_{1-x}A_xMnO_3$ (A=Ca, Sr, Ba) has been also studied theoretically by several local spin density approximation (LSDA) studies [45, 46]. A number of experimental spectroscopic techniques, such as x-ray absorption spectroscopy (XAS), x-ray photoelectron spectroscopy (XPS), or angle resolved photoemission spectroscopy (ARPES) and have been applied to $La_{1-x}A_xMnO_3$ (A=Ca, Sr) [37, 47]. In a recent ARPES study Lev *et al.* found that the rhombohedral distortion influences the CMR via affecting the electron hopping and hence the double exchange in $La_{1-x}Sr_xMnO_3$ [48].

Here, we study the magnetic properties of $La_{1-x}Sr_xMnO_{3+\delta}$ (x=0.12±0.02, 0.17±0.02, and 0.36±0.02; δ close to 0) single crystals by means of SQUID magnetometry and XMCD at the Mn $L_{2,3}$ edges **[H3]**. Since its discovery in the late 1980's by Schütz *et al.* [49] and the development of the so called sum rules [50, 51] nowadays this technique is widely used to tackle the magnetic properties of novel materials. This stems partly from the growing availability of tunable, polarized, high brilliance X-rays, i.e. synchrotron radiation, and partly from the fact that XMCD offers a unique possibility to analyze the magnetic moments element specifically as well as separated into their spin and orbital contributions. Since the XMCD approach has been used for the magnetic characterization of many materials in the framework of this thesis it will be introduced briefly. Following the dipole selection rules, the spin is conserved during the absorption process. For XMCD circularly polarized light is used which means $\Delta m_l = \pm 1$. In combination with the spin orbit splitting of core levels ($j = l \pm s$), preferentially either majority or minority spin carriers are excited to unoccupied states in dependence of the light helicity [52].

Fig. 1.5 displays a scheme of possible $2p \rightarrow 3d$ transitions when excited with right circularly (σ^+) light. Out of the $2p_{3/2}$ ($2p_{1/2}$) states preferentially spin-up (spin-down) electrons are excited into the unoccupied 3d levels ($\mid m_l, m_s >$) (c.f. upper line in Fig. 1.5), that contribute to the respective $\mid m_j >$ states according to the Clebsch-Gordon coefficients. According to Fermis golden rule the absorption coefficients are proportional to the density of unoccupied states above the Fermi level. Thus, the photoelectron serves as a probe of the spin and orbital polarisation of these states, which is very important for the investigation and characterisation of magnetic materials and

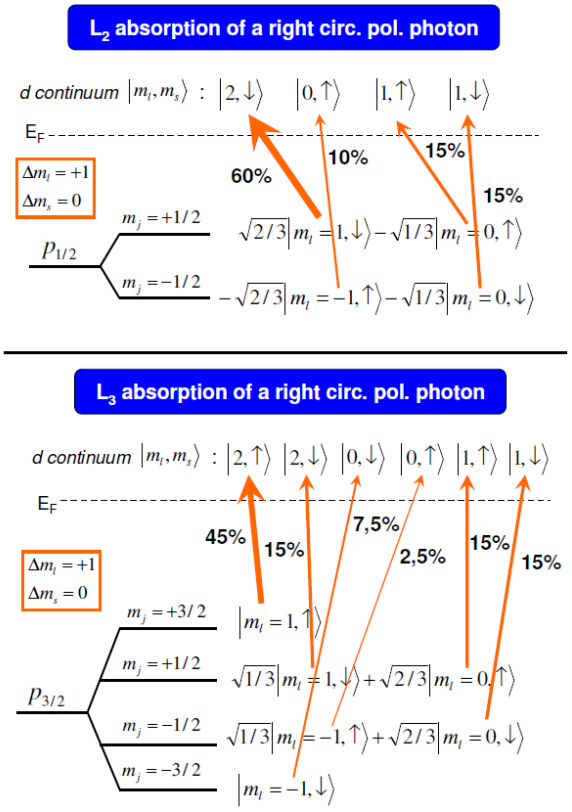

Figure 1.5: Schematic plot of a transition metal $L_{2,3}$ edge ($2p \rightarrow 3d$) transition with right circularly polarized light (according to [53]). For right circularly polarized light the magnetization of the sample is assumed to be antiparallel to the photon wave vector, allowed transitions follow the dipole selection rules for σ^+ light ($\Delta m_s = 0$, $\Delta m_l = +1$). Reproduced from Taubitz [18].

their magnetic moments.

Figure 1.6 displays the XMCD spectrum obtained at 80 K and applied magnetic fields of 0.7 T from $La_{0.87\pm0.02}Sr_{0.12\pm0.02}MnO_{3+\delta}$ **[H3]**. Moreover, charge transfer multiplet calculations assuming a cubic symmetry for the systems are shown as well. For all samples the same parameters were used, but the mixing of Mn^{3+} and Mn^{4+} spectra was derived from the formal valence state determined by the amount of Sr doping. The charge transfer from the ligand oxygen to the Mn site ($3d^nL \rightarrow 3d^{n+1}L^{-1}$) is included in the calculations. The best agreement with the experiment could be achieved with amounts of approximately 50% and 30% for Mn^{4+} and Mn^{3+}, respectively.

The XMCD spectrum shows distinct spectral features at the Mn L_3 edge near 643 eV

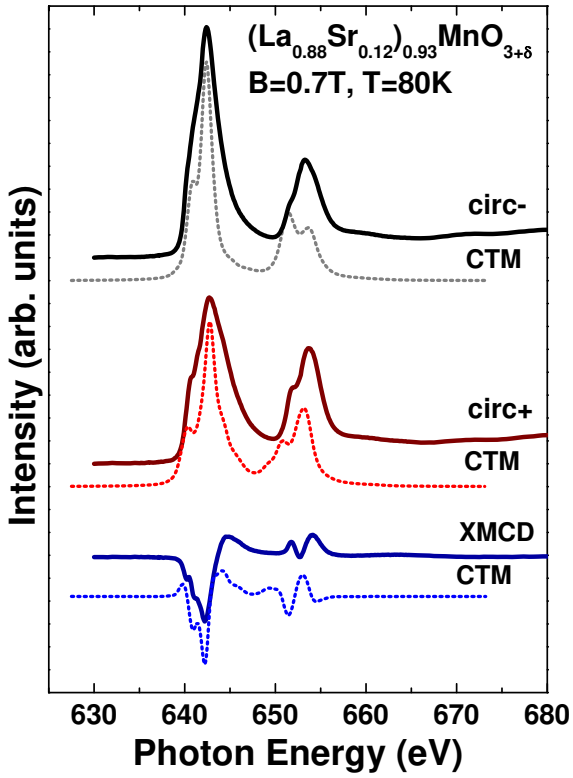

Figure 1.6: XMCD spectra of $La_{0.87\pm0.02}Sr_{0.12\pm0.02}MnO_{3+\delta}$ with 0.7 T applied magnetic field at 80 K in comparison with charge transfer multiplet (CTM) calculations [**H3**].

and the L_2 edge around 654 eV. The main L_3 edge feature has two shoulders to lower photon energy (641.5 eV and 640.5 eV). At higher photon energy a broad shoulder is present (around 645 eV). The main feature of the L_2 edge at 653.0 eV has a shoulder at 654.0 eV and a feature at 641.5 eV. A very small feature appears at 650.5 eV. The calculations are in overall satisfactory agreement with the experiment, but there are some notable differences. In the positive circularly polarized spectra the main peak at 653.5 eV at the Mn L_2-edge is underestimated for all samples, whereas the prepeak located around 651 eV is overestimated in the simulations. Furthermore, the $2p-3d$ spin orbit splitting is underestimated approximately by 1 eV. The separation between the L_3 and the L_2 edge is caused by the $2p$ spin-orbit coupling. The Mn L_2-edge prepeak present in the experimental spectra at 651 eV is hardly visible in the simulations. The prepeak structure of the Mn L_3-edge at 641 eV is not completely

rendered. The different mixing of Mn valence states is overestimated by the calculations in comparison to the experiment. The less pronounced fine structure in the experiment might be considered due to a metallic character of the samples. However, it has been demonstrated before for a very similar system, namely $La_{0.7}Sr_{0.3}MnO_3$, that dynamical screening leads to a superposition of the electronic structure of initial and final states.[54] Hence, the $2p$-hole and the $3d$-hole have radial wave functions which overlap significantly, and the corresponding Mn $L_{2,3}$ XAS are ruled mainly by (localized) multiplet effects. Nevertheless, the calculation allows to estimate values for the crystal field (1.4 eV), and the charge transfer amount (Mn^{4+}: 50%, Mn^{3+}: 30%) giving the described agreement with the experiment. This leads to averaged 3.9 holes per Mn ion, which we also used for the sum rule analysis of the experimental spectra.

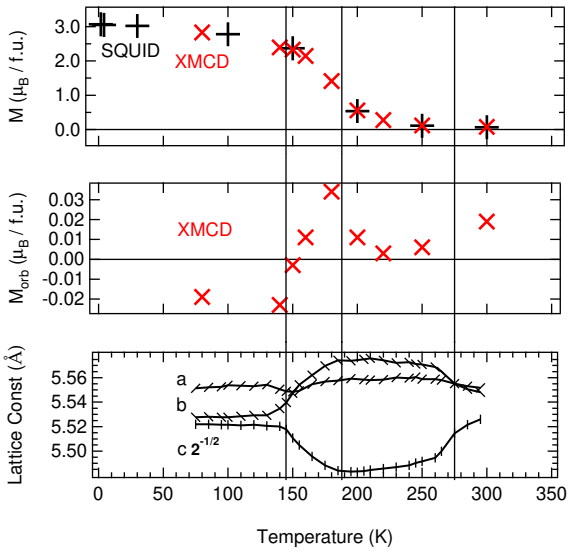

Figure 1.7: Total magnetic moment and Mn magnetic moment from XMCD (top panel), orbital magnetic moment (middle panel), and lattice parameters (those have been extracted from Pinsard *et al.* [55]) (bottom panel) $La_{0.87\pm0.02}Sr_{0.12\pm0.02}MnO_{3+\delta}$. Extracted from Raekers [56].

Figure 1.7 compares the total and orbital magnetic moment at the Mn site of $La_{0.87\pm0.02}Sr_{0.12\pm0.02}MnO_{3+\delta}$ determined from the XMCD spectra, the total magnetic moment from SQUID measurements with the lattice parameter of $La_{0.875}Sr_{0.125}MnO_3$ from Pinsard *et al.* [55] on a temperature scale. Three transition temperatures are marked. From 145 K to 188 K the structural transition from a ferromagnetic orthorhombic O′* to another orthorhombic paramagnetic O′ phase occurs. During this

transition the orbital magnetic moment changes from $\sim -0.02\ \mu_B$/f.u. at 145 K to $\sim 0.04\ \mu_B$/f.u. at 188 K. Remarkably, we find a negative orbital moment in the O$'^*$ phase which is approximately the half of the positive moment in the O$'$ phase at 188 K. This may be due to the structural changes and indicates the occupation of orbitals with different orbital quantum number m_l. Which orbitals are occupied in the different structural phases cannot be interpreted exactly, because the quantitative value of the orbital moment is not very reliable due to quenching. Below 145 K another type of orbital ordering seems to be present than above 145 K. The structural change from 145 K to 188 K (T_C) is seen in the lattice parameters and corresponds directly to the orbital moment. Such complex behavior of the orbital magnetic moment of orbitally degenerated 3d transition metal ions has been theoretically proposed earlier [57], including the possibility of sign reversal of the orbital moment via interaction with the ligand states in different structural and orbitally ordered or disordered phases [58, 59]. A more detailed discussion of the spin and orbital moments found at the Mn sites of $La_{1-x}Sr_xMnO_{3+\delta}$ (x=0.12±0.02, x=0.17±0.02, and x=0.36±0.02; δ close to 0), with special emphasis concerning the spin sum rule correction in combination with charge transfer multipet simulations can be found in reference [**H3**].

1.3 The layered multiferroic oxide $LuFe_2O_4$

Multiferroic materials exhibit more than one primary ferroic phase simultaneously. Ferroic degrees of freedom may include long range elastic, electric or magnetic order, for instance [60]. Since the prominent paper of Hill [61] in the year 2000 multiferroicity is often referred to the coexistence of a ferroelectric and a magnetic (antiferro-, ferri-, or ferromagnetic) long range order. If a magnetic field induces an electric field and/or vice versa the material is also magnetoelectric [60]. Besides studying fundamental aspects these materials might be also interesting for new device applications.

A number of different mechanisms may lead to the simultaneous appearance of ferroelectric and long range magnetic order. Some important examples include the **lone-pair mechanism** in $BiFeO_3$ [62], ferroelectricity induced via structural instability (**geometrical ferroelectricity**) [63], the creation of multiferroic **interfaces**, e.g. $CoFe/BaTiO_3$ [64] or $Fe_3O_4/BaTiO_3$ [65], or by designing multiferroic **superlattices** such as $(LuFeO_3)_m/(LuFe_2O_4)_1$ [66].

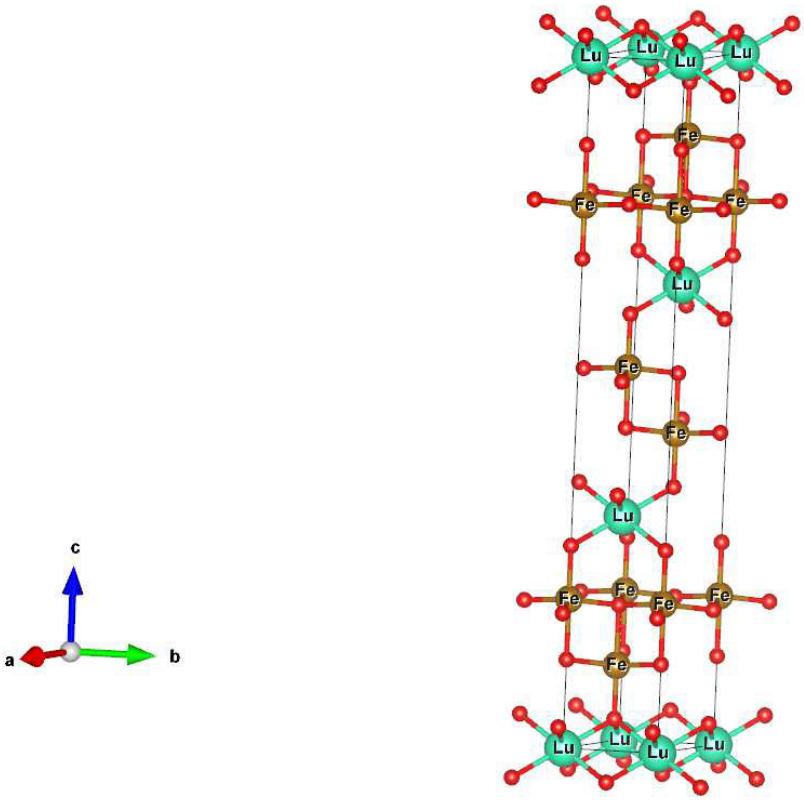

Figure 1.8: Crystal structure of $LuFe_2O_4$ with Lu (turquoise spheres), Fe (orange spheres), and oxygen (small red spheres). The crystal structure has been visualized using the VESTA software [67], structural data from Isobe *et al.* [68].

$LuFe_2O_4$ itself exhibits multiferroic behavior which has been associated with an electric polarization induced via a frustrated **charge ordering** [69]. $LuFe_2O_4$ crystallizes in a trigonal crystal lattice (space group $R\bar{3}m$) with lattice parameters with a = 3.4406Å and c = 25.2800Å [68]. The underlying structure consists of W-like hexagonal $Fe_2O_{2.5}$ and U-like $LuO_{1.5}$ layers [70] (c.f. Fig. 1.8). It has been proposed that the long range electric polarization is induced via the W-like lattice building up a honeycomb lattice below 330 K [69]. Despite $LuFe_2O_4$ has been subject to many investigations the proposed polar nature is still under debate [71, 72]. On the other side also the magnetic properties of $LuFe_2O_4$ are not understood completely. $LuFe_2O_4$ exhibits spin ordering below an ordering temperature of T_N = 240K [69], however, different models based on *ab initio* electronic structure calculations concerning the spin-charge ordering, leading to the observed magnetoelectric coupling have been pro-

posed. Whereas one model suggests a $\sqrt{3} \times \sqrt{3}$ ground state [73], another study finds a frustrated spin ground state with a ferromagnetic spin ordering [74]. By performing XMCD across the Fe $L_{2,3}$ edges of a $LuFe_2O_4$ single crystal we could confirm the latter model [**H4**]. We also carried out further x-ray spectroscopic investigations by means of XPS and XES along with theoretical first principles calculations, leading to valuable information about the correlation strength between the Fe $3d$ ions and the Lu $4f$ ions in $LuFe_2O_4$. Further information can be found in reference [**H4**].

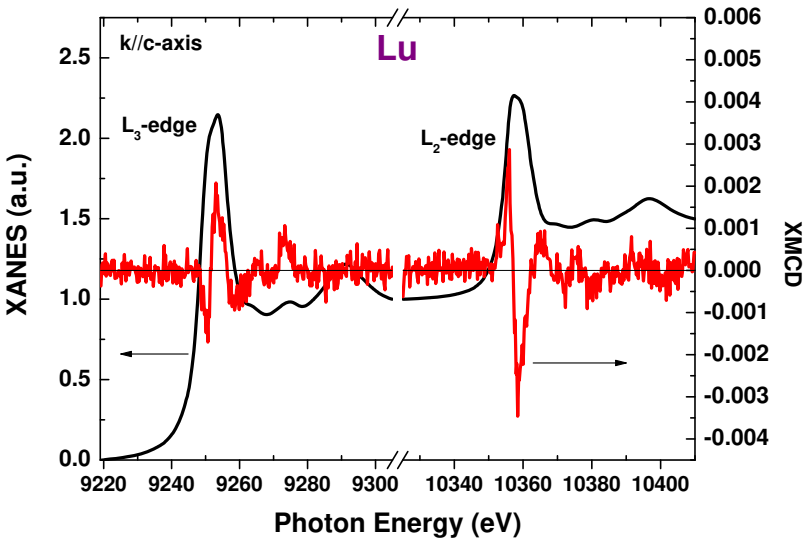

Figure 1.9: XMCD across the Lu $L_{2,3}$ edges of $LuFe_2O_4$ recorded at a temperature of 150 K and with the crystal c-axis parallel to the e-vector of the incoming light.

Furthermore, complementary XMCD investigations in the hard x-ray regime including the Fe K and Lu $L_{2,3}$ edges have been done (Fig. 1.9). The Fe K edge can be used to record element specific hysteresis loops, which resemble those measured by SQUID magnetometry, hence demonstrating that the magnetism of $LuFe_2O_4$ is dominated by the Fe ions [17]. XMCD across the Lu $L_{2,3}$ edges yields a very small but unambiguously measurable dichroic signal. Sum rule analysis determines a spin moment of -0.018 μ_b/Lu atom (parallel aligned to the Fe magnetic moments) and an orbital moment of +0.011 μ_b/Lu atom, which is opposite in sign compared to the Fe orbital moment [17].

Ultrathin iron oxide films

Ferrites with spinel structure of type AB_2O_4, where A nd B are divalent or trivalent transition metal cations (depending on the cation distribution on different sub-lattices also the inverse spinel is possible with identical formal stoichiometry) are of special interest due to a number intriguing magnetic properties such as high Curie temperature above room temperature and significant saturation moments stemming from a ferrimagnetic ground state making them potential candidates for a number of applications in spintronics, electronics but also in the fields of electrocatalysis or as supercapacitor, for instance. The most prominent example of a ferrite with inverse spinel structure is magnetite (Fe_3O_4). This fact stems from various aspects as the high Curie temperature (860 K) for bulk material with a magnetic saturation moment of $4.07\mu_B$ per formula unit [75], the Verwey transition taking place at around 120 K for bulk material [76, 77], as well as the predicted 100% spin polarization of Fe_3O_4 [78] making this halfmetallic material interesting for future spintronic devices such as spin valves or magnetic tunnel junctions [79, 80]. Consequently, here, we extend the research to ultrathin films of compound ferrites. These materials attract much attention concerning different aspects of spintronic devices, e.g., spin filters [81], and more recently in the emerging field of spin caloritronics [82, 83].

The interface between Fe_3O_4 and substrate, however, has to be very abrupt concerning both stoichiometry and morphology (roughness) to obtain these properties. Understanding the magnetic properties of spinel thin films requires a detailed control of epitaxial strain as well as its microstructure. Detailed knowledge of the surface morphology is particularly relevant for these thin films, required in advanced applications such as spin filters or others [85–87]. In addition, the film structure (inverse spinell) and ordering has to be of high quality with equal distribution of Fe^{3+} on A and B sites and Fe^{2+} exclusively on B sites. It has been demonstrated that the electronic and magnetic properties of Fe_3O_4 films can be tailored for strained Fe_3O_4 films. Strained Fe_3O_4 films can be formed using $SrTiO_3(001)$ as support due to the lattice mismatch

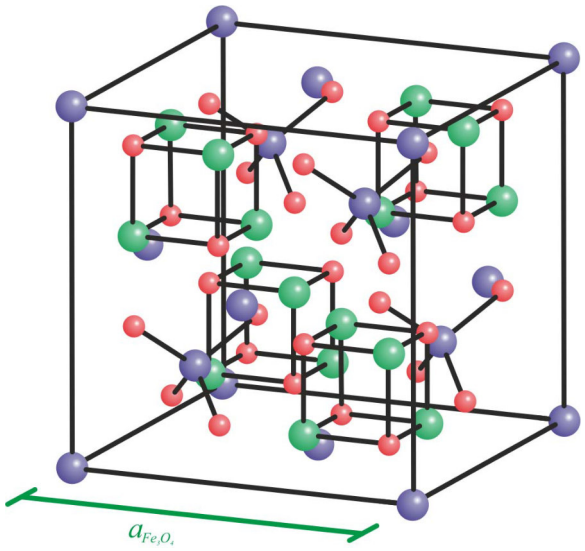

Figure 1.10: Schematic representation of the inverse spinell magnetite (Fe_3O_4) unit cell with equal distribution of Fe^{3+} on the A and B sites and Fe^{2+} exclusively on B sites (extracted from [84]).

of 7.5% [8]. Further modifications of the magnetic behaviour of Fe_3O_4 films can be obtained if the magnetite film is combined with an antiferromagnetic film (e.g. NiO, CoO). In this case the hysteresis loop is shifted due to the so-called exchange bias effect which has been reported for Fe_3O_4/NiO multilayers [88]. All these interesting effects rely on the order of the magnetite film structure and its interface. We investigated the structural properties including strain and morphology of magnetite single layers as well as Fe_3O_4/NiO bi-layers in detail [89–91].

1.4 Electronic and magnetic properties of epitaxial Fe_3O_4(001)/NiO bi-layers

Besides the structural properties we also studied the electronic and magnetic properties by employing a set of suitable experimental approaches [**H5**]. Magnetite thin films with thicknesses between 5 and 30 nm grown on MgO(001) and $SrTiO_3$(001) supports, with and without antiferromagnetic NiO buffer layer, have been examined. Magnetic hysteresis loops recorded with help of the magneto optical Kerr effect (MOKE) reveal

strongly enhanced coercive fields and a 45° rotation of the magnetic easy axis (⟨100⟩ in-plane direction) for all layers investigated in comparison to Fe_3O_4/MgO(001) (easy axis along ⟨110⟩ in-plane direction). Potential reasons include the formation of multiple domains, the presence of anti phase boundaries and/or a spin flip coupling at the interface between the oxides which has been investigated before by Krug *et al.* [92].

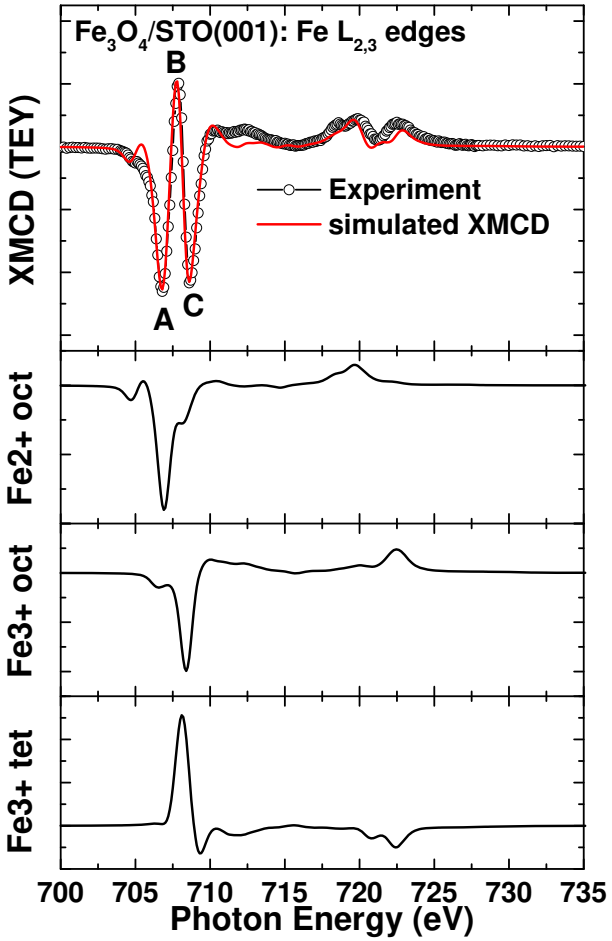

Figure 1.11: XMCD spectrum with corresponding charge transfer simulation of a 33 nm thick magnetite film grown on $SrTiO_3(001)$. The overall simulated result (red) comprises appropriate fractions of the charge transfer simulations performed for Fe^{2+} (octahedral) and Fe^{3+} (octahedral and tetrahedral) shown in the lower panels. For more details see [**H5**].

To clarify the electronic structure and valence states in the interface near region hard x-ray photoemission spectroscopy (HAXPES) under variation of excitation energy has

been performed on some samples, showing a bit of Fe^{3+} excess towards the surface near layers, in particular in case of thin layers below ∼10nm thickness. Valence band spectra taken at different excitation energies lead to the result of a lack of Fe t_{2g} down states in case of Fe_3O_4/NiO interface.
XAS and XMCD across the Fe $L_{2,3}$- and Ni $L_{2,3}$-edges carried out in the surface sensitive total electron yield exhibit a very weak Ni dichroic signal which is an indication for the absence of a $NiFe_2O_4$ interlayer, as this should lead to an enhanced dichroic signal at the Ni $L_{2,3}$ edges. Fe $L_{2,3}$ spectra confirm a lack of Fe^{2+} ions at the surface of the films with thicknesses of the magnetite layer up to around 10-12 nm found also by the Fe 2*p* HAXPES measurements. Above this thickness there we find cationic distributions much closer to the optimal Fe_3O_4 stoichiometry, with a general tendency of some excess of octahedral coordinated trivalent iron ions. The cationic distributions have been extracted from the XMCD spectra with help of corresponding charge transfer multiplet simulations [23]. Fig. 1.11 presents one example. A detailed analysis can be found in publication [**H5**].

1.5 High quality $Ni_xFe_{3-x}O_4$ thin films produced via diffusion

Dependent on the rather different values for the bandgap available in literature, $NiFe_2O_4$ and $CoFe_2O_4$ are a semiconducting or insulating ferrimagnet with inverse spinel structure which are discussed as part of magneto electric heterostructures [4, 93], for instance. The spin dependent band gap enables the use of $NiFe_2O_4$ ultrathin films as building blocks in novel spin-filter devices [94, 95]. The spin filter performance, however, depends on both, the stoichiometry and the structure of the ultrathin $NiFe_2O_4$ films since these properties determine their magnetic properties. These aspects are also of great importance for application of ultrathin $NiFe_2O_4$ films in the field of spincaloritronics where they serve as supports for ultrathin metallic films (e.g., Pt films or other metals with large spin orbit coupling) which are used to detect spin currents [96]. Another well promising approach to influence the underlying properties is tuning the chemical composition, and hence cationic distribution and inversion parameter, by synthesizing thin films of type $Ni_xFe_{3-x}O_4$. Indeed, $Ni_xFe_{3-x}O_4$ thin films prepared by reactive co-sputtering showed a tunable electric conductivity and

a lower saturation magnetization with increasing Ni content [97]. Often pulsed laser deposition (PLD) is used to grow $NiFe_2O_4$ films [98] while reactive molecular beam epitaxy (RMBE) is also used for other ferrite films [96].

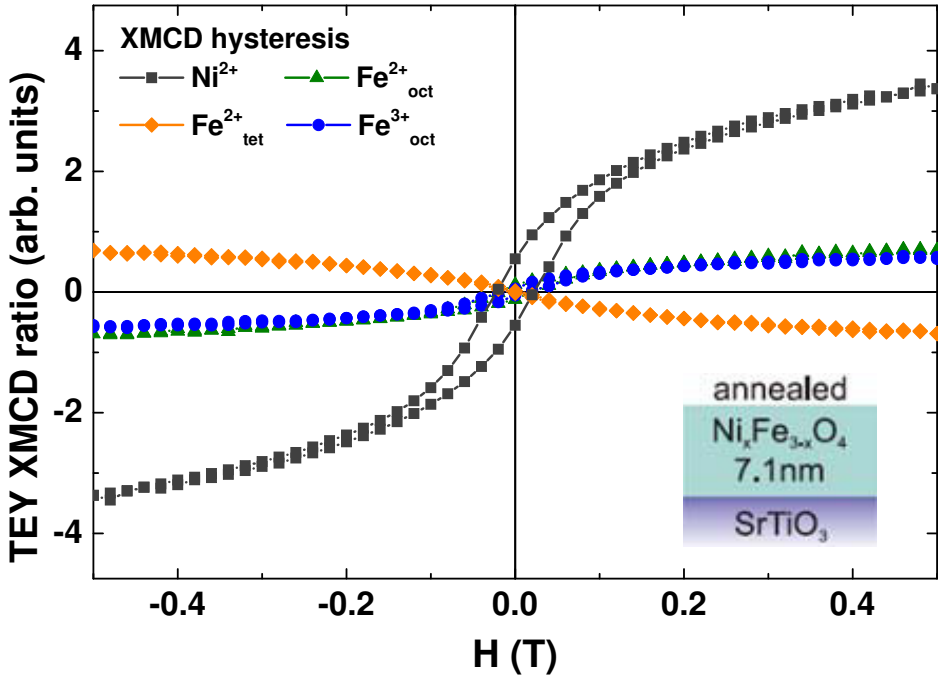

Figure 1.12: Element- and site-specific XMCD hysteresis loops of the Ni L_3 and Fe L_3 intensities of an intermixed $Ni_{1-x}Fe_{3-x}O_4$ thin film after a sequence of post deposition annealing steps. For more details see text and [**H6**].

Recently, we demonstrated an alternative pathway to form ferrite films on $SrTiO_3(001)$. Starting with an Fe_3O_4/NiO bilayer, we formed NFO by post deposition annealing (PDA) due to interlayer diffusion [**H6**]. For this purpose, Fe_3O_4/NiO-bilayers were grown by RMBE onto $SrTiO_3(001)$ supports and then mounted into the HAXPES experimental chamber at beamline I09 of the Diamond synchrotron radiation facility. The experimental setup allowed annealing up to 800°C and recording LEED patterns between the post deposition steps, which were carried out in a molecular oxygen background atmosphere of $5 \cdot 10^{-6}$ mbar at 400°C, 600°C, and 800°C. LEED patterns confirm the disappearance of the superstructure typical for magnetite, soft and hard x-ray photoelectron spectroscopy performed after each annealing step are used to determine the cation distribution from the Fe $2p$ and Ni $2p$ spectra. These results were

complemented by XRR and XRD analysis confirming the intermixing of the initial NiO and Fe_3O_4 layers. X-ray magnetic circular dichroism (XMCD) experiments in combination with multiplet calculations were used to analyse the cation distribution on the different lattice sites. Finally, element and site specific XMCD-hysteresis loops demonstrate the antiferromagnetic coupling of the octahedral and tetrahedral coordinated Fe^{3+} ions, which is mediated via superexchange interaction, (c.f. Fig.1.12) for the intermixed $Ni_{1-x}Fe_{3-x}O_4$ thin film, and an overall open hysteresis with a coercive field typical for high quality $NiFe_2O_4$ thin films grown by pulsed laser deposition [97] and $NiFe_2O_4$ bulk crystals [99]. In summary, paper **[H6]** demonstrates the possibility to synthesize $Ni_{1-x}Fe_{3-x}O_4$ thin films of high crystallographic quality by thermal interdiffusion of distinct Fe_3O_4/NiO-bilayers grown on $SrTiO_3(001)$, which might be used to tailor $Ni_{1-x}Fe_{3-x}O_4$ thin films with desired stoichiometry and bad gap, respectively.

Zero dimensional nanomaterials: $NaREF_4$ (RE = Rare Earth) and magnetic molecules

1.6 The nanoparticles $NaREF_4$ (RE = Eu and Gd)

The exact knowledge of the inherent electronic effects at the interface of inorganic core/shell nanoparticles is of utmost importance as they can be applied to multiple applications in catalysis, optics and magnetism [100]. In particular, rare earth (RE) based nanoparticles of type $NaREF_4$ have attracted a lot of attention in the last few years due to their upconverting luminescent properties [101]. These particles have a number of superior luminescent, electronic and chemical properties making them highly promising candidates for quantum dots or (medical) magnetic resonance imaging [102]. However, a combination of multiple functions and properties not obtainable in individual materials or nanoparticles is highly desirable. Nearly monodisperse nanocrystals of sodium rare-earth metal fluorides ($NaREF_4$), in particular $NaYF_4$ and $NaGdF_4$ are thoroughly investigated for biolabeling applications and for magnetic resonance imaging (MRI), since they also exhibit high chemical stability and good optical transparency over a wide wavelength range [103, 104]. In particular, $NaGdF_4$ exhibits a high magnetic moment due to the seven unpaired electrons in the ground state ($^8S_{7/2}$). Since there is a relatively large energy gap between the ground state and the lowest excited level ($^6P_{7/2}$) the luminescence is taking place in the ultraviolet regime. On the other hand the Eu^{3+}-ion shows pure red emission in many host materials such as $NaEuF_4$, if the concentration of Eu^{3+}-ion is high enough, since this leads to quenched multiphonon relaxation except those stemming from the $^5D_0$ level [**H7**]. Since trivalent europium ions are usually in a low spin ground state, hence

carrying no magnetic moment, a combination with $NaGdF_4$ particles, e.g. by doping of Eu^{3+} ions into $NaGdF_4$ could be an interesting approach to combine the magnetic properties of $NaGdF_4$ with the high quantum yield of the Eu^{3+} ions in the red spectral region. However, at lower Eu^{3+} concentrations, also other transitions at lower wavelengths are observed, lowering the efficiency of the red emission significantly. Therefore, β-$NaEuF_4/NaGdF_4$ core-shell nanocrystals with narrow size distribution have been synthesized and thoroughly studied as to their structural, optical, chemical, and magnetic properties.

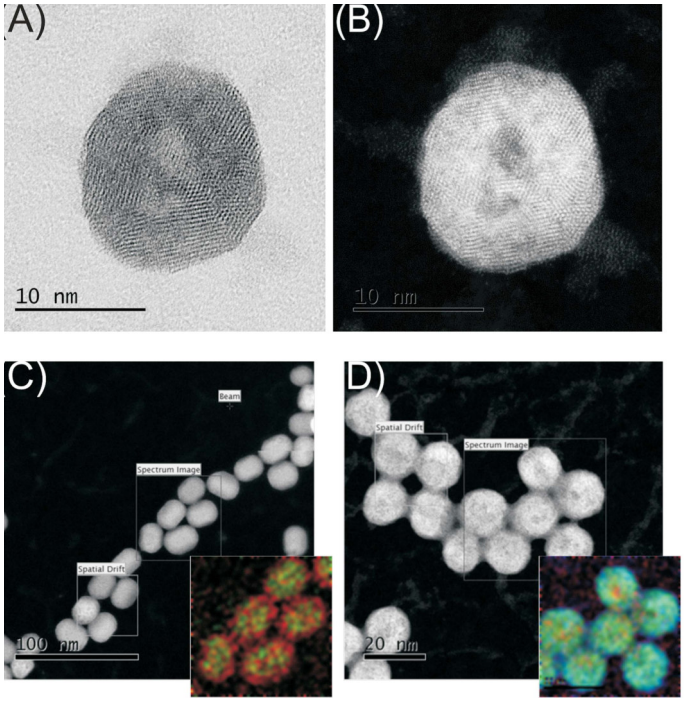

Figure 1.13: (A) Bright field (BF), (B) and high angular annular dark field (HAADF) HR-TEM images of 20 nm $NaEuF_4/NaGdF_4$ core-shell nanoparticles with a 3 nm $NaEuF_4$ core and 8 nm $NaGdF_4$ shell. (C) Scanning transmission electron microscope-electron energy loss spectrscopy (STEM-EELS) images of 22 nm $NaEuF_4/NaGdF_4$ core-shell nanoparticles with a 18 nm $NaEuF_4$ core and 2 nm $NaGdF_4$ shell. (D) STEM-EELS images of 20 nm $NaEuF_4/NaGdF_4$ core-shell nanoparticles with a 3 nm $NaEuF_4$ core and $NaGdF_4$ shell and false color maps of Eu (green), Gd (red), F (orange) and O (blue) concentration.

The morphology of the nanoparticles was characterized by transmission electron mi-

croscopy (TEM). The images were recorded by Jan Neethling using a double Cs corrected JEOL ARM 200F transmission electron microscope at the Centre for HRTEM, Nelson Mandela Metropolitan University, Port Elizabeth, South Africa. The nanoparticles are nearly monodisperse and either close to spherical in shape [**H7**]. High resolution imaging shows the particles to be crystalline with interplanar spacings, the HAADF imaging of the particles showed indications of a core-shell type structure in some nanoparticles (c.f. Fig. 1.13 A and B). However, it appears that parts of the small core (3 nm) and hence fractions of the Eu^{3+}-ions have been released into the $NaGdF_4$-shell. In particular the STEM-EELS mapping of the 18 nm $NaEuF_4$ core nanoparticles with a 2 nm $NaGdF_4$ shell (Fig. 1.13C) exhibits good indication of the desired core shell structure.

X-ray powder diffraction and electron paramagnetic resonance (EPR) measurements confirm the HRTEM results, luminescence spectra of the nanoparticles with large core only exhibit emission intensities at 591, 614 and 691 nm corresponding to $^5D_0 \rightarrow ^7F_1$, $^5D_0 \rightarrow ^7F_2$, and $^5D_0 \rightarrow ^7F_4$ intra-4f shell transitions [**H7**]. Another focus is set to the characterization of the magnetic properties. Here, we find a butterfly shaped hysteresis loop for the nanoparticles comprising a 3nm $NaEuF_4$ core. This effect can be qualitatively explained by Monte Carlo simulations based upon the Heisenberg model considering magnetic anisotropy at the interface between the $NaEuF_4$ core and the surrounding $NaGdF_4$ shell. We also performed element specific XMCD experiments across the Eu $M_{4,5}$- and Gd $M_{4,5}$-edges. A small but distinct negative XMCD stemming from the Eu ions is found for both, pure $NaEuF_4$ and 18 nm $NaEuF_4$ core / 2 nm $NaGdF_4$ shell particles, the Eu moments are aligned parallel to those of Gd. The Eu moment can be assigned to a rather small Eu^{2+}-fraction present as well as to weak Eu^{3+} magnetism in case of the pure $NaEuF_4$ nanoparticles. For the core-shell particles only weak Eu^{3+} XMCD-signal could be detected. For a deeper analysis of the multifunctional β-$NaEuF_4$/$NaGdF_4$ core-shell nanoparticles the interested reader is referred to reference [**H7**].

1.7 Electronic and magnetic properties of various Single Molecular Magnets

1.7.1 Iron-based magnetic polyoxometalates of type $\{(M)M_5\}_{12}Fe_{30}^{III}$ (M = Mo^{VI}, W^{VI})

Polyoxometalates (POMs) are polyatomic ions, where metal ions are bridged with oxygen atoms, building up clusters [105, 106]. These clusters are usually built up by molybdenum and tungsten in their highest oxidation state (VI). Possible applications of POMs include the usage as heterogeneous catalyst [107] or the possibility to tune their electronic and magnetic interactions [108].

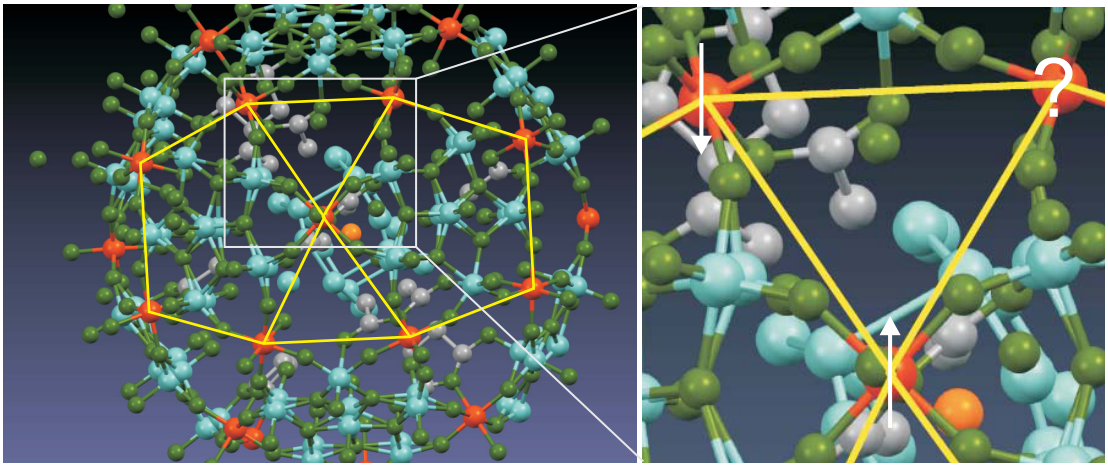

Figure 1.14: Left: Scheme of $\{Mo_{72}Fe_{30}\}$-acetate, the molecule is shown in the ball and stick representation. The Fe atoms (red) carry the magnetic moments and are ordered on an icosidodecahedral surface (indicated by the yellow lines). Mo atoms (turquois) are also present at the ball surface and interconnected by oxygen atoms (green). The crystal structure visualisation has been made employing the Mercury software [109], using the crystallographic data made available by Müller *et al.* [110]. Right: Magnification of a part of the icosidodecahedral arrangement of the Fe atoms, illustrating the triangular lattice leading to frustrated magnetism and competing spin phases in Fe_{30}-molecules.

Here, in particular the giant neutral Keplerate-type molecules with $\{Mo_{72}Fe_{30}\}$ and $\{W_{72}Fe_{30}\}$ core exhibit a number of intriguing magnetic properties. The 30 Fe^{III} ions are symmetrically placed on an icosidodecahedral surface, building a mesoscopic

kagomé lattice, especially at low temperatures [111], leading to competing spin phases in a frustrated magnetic system [112] (c.f. Fig. 1.14).
In paper [**H8**] we address two different aspects and close two gaps in knowledge as to the $\{Mo_{72}Fe_{30}\}$ and $\{W_{72}Fe_{30}\}$ molecules. Firstly, we made use of element specific XAS across the O K edge of the molecules, which reflects the unoccupied density of states, and compared the O K XAS with first-principles electronic structure calculations. We found a good agreement between the experimental results with the calculations leading to the conclusion that there is almost no band gap but Fe t_{2g} states near Fermi energy, hence both molecules are semi-metallic. Sum rule analysis of Fe $L_{2,3}$-XMCD recorded on $\{W_{72}Fe_{30}\}$ yields a bit lower magnetic moment ($\sim$52 μ_b/f.u.) compared to SQUID measurements ($\sim$60 μ_b/f.u.). A comprehensive discussion of potential reasons for this discrepancy can be found in [**H8**]. One reason might be a beginning x-ray photoinduced photoreduction process of the Fe^{3+}-ions towards Fe^{2+}, which is also indicated by charge transfer multiplet simulations of the Fe $L_{2,3}$-XAS and XMCD, suggesting 85% to be trivalent and 15% to be bivalent, although we reduced the photon flux to 1-2% of the full flux ($\sim 10^{12}$ photons per second) of beamline 8.0.1, Advanced Light Source, Lawrence Berkeley Laboratory, to minimize potential radiation damage effects.

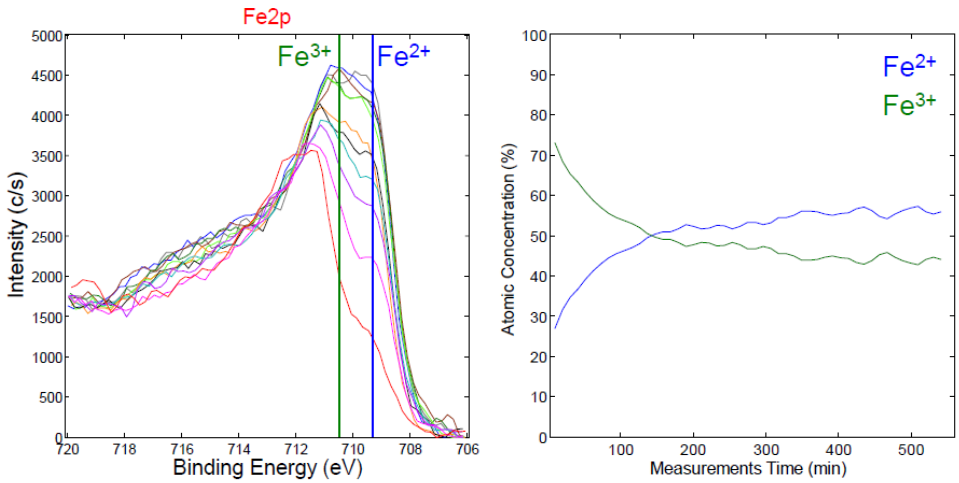

Figure 1.15: Left: Fe $2p_{3/2}$ core level spectra of $\{Mo_{72}Fe_{30}\}$-acetate, each scan took approximately 10 minutes. Right: ratio of percentages of Fe^{2+} and Fe^{3+} estimated from the corresponding binding energies.

Secondly, we investigated the soft x-ray-induced Fe^{3+} to Fe^{2+} photoreduction in more

detail. X-ray photoelectron spectroscopy performed with a monochromatized Al anode ($E_{exc} = 1486.6$ eV) indicates a gradual transition from a pure Fe^{3+} state to Fe^{2+} over time (c.f. Fig. 1.15). The 3+ and 2+ fractions (Fig. 1.15, right panel) were roughly estimated by the ratio of the peaks present at the corresponding binding energies (709.4 eV for Fe^{2+}, 710.6 eV for Fe^{3+}). More detailed information was extracted from systematic investigation of the observed shift x-ray induced Fe^{3+} to Fe^{2+} photoreduction by means of x-ray absorption spectroscopy across the Fe $L_{2,3}$-edges [**H8**]. $\{Mo_{72}Fe_{30}\}$ and $\{W_{72}Fe_{30}\}$ molecules with different ligands (charge neutral acetate and SO_4^{2-} were investigated. The percentages of bivalent and trivalent Fe ions were analyzed by full multiplet simulations after each XAS-scan, which lead to qualitative similar results compared to the Fe $2p_{3/2}$ XPS results shown in Fig. 1.15 but significant more precise results compared to the rather superficial analysis carried out with the x-ray photoelectron spectra. An exponential Fe^{3+} to Fe^{2+} photoreduction is found for both, the acetate and the SO_4^{2-} ligands, however, the photoreduction rate is considerably lower in case of molecules with the negatively charged SO_4^{2-} ligands. One potential reason maybe that the negative charge builds up a negative repulsive potential, slowing down the electron-transfer towards the Fe^{3+} ions. More details as the experiments and the theoretical approaches can be found in reference [**H8**].

1.7.2 Magnetic ground-state studies of star-shaped Single Molecule Magnets

Magnetic, molecular materials comprising nanosized building blocks are of special interest for chemists and physicists seeking new molecule-based materials. In particular, new molecule-based magnets are, among others, candidates for high density storage devices in quantum computing. Since the discovery of the famous Mn12-Ac cluster 25 years ago [113], a number of different molecular magnets, leading to a rich variety of intramolecular exchange interactions or magnetic anisotropy have been discovered [114–116]. One of the most interesting class of molecules exhibiting single molecule magnet (SMM)-behavior are the so-called star-shaped molecules, i.e. the core comprises one central ion and three peripheral ions. Besides others, star-shaped molecules with Cr_4-core [117], a Mn_4-core **[H9]**, a Fe_4 core [118], a Ni_4 core [119], or the spin-frustrated $CrMn_3$-complex **[H10]** have been synthesized and characterized. More recently, star-shaped macrocyclic complexes with Cu_3Tb core [120–122] which show slow relaxation of magnetization, a prerequisite for SMM behavior, have been synthesized. Complexes comprising both, $3d$ transition metal and $4f$ rare earth ions, are investigated intensely in the last few years [122, 123]. In particular, Tb^{III} and Dy^{III} ions are of special interest due to their high single ion anisotropies [124]. Here, we show the magnetic properties, investigated by means of XMCD of some of the above mentioned star-shaped molecules in more detail.

1.7.2.1 Star-shaped molecules with transition metal cores

In contrast to most other transition metal ions, manganese ions are often characterized by ground states with high magnetic moments. Manganese based complexes comprising Jahn-Teller distorted Mn-ions are highly promising candidates for high-spin molecules [125]. Hence, a number of molecules comprising up to 84 manganese ions have been synthesized [126], displaying huge spin ground states and magneto-anisotropy. On the other side, hexanuclear manganese complexes showed higher blocking temperatures and open magnetic hysteresis [127], which are prerequisites for applications like ultra-dense magnetic data storage. For a better understanding of the magnetic coupling mechanisms on the inter-atomic length scale, we performed comprehensive experimental and theoretical studies on two star-shaped manganese-containing high spin molecules **[H9, H10]**.

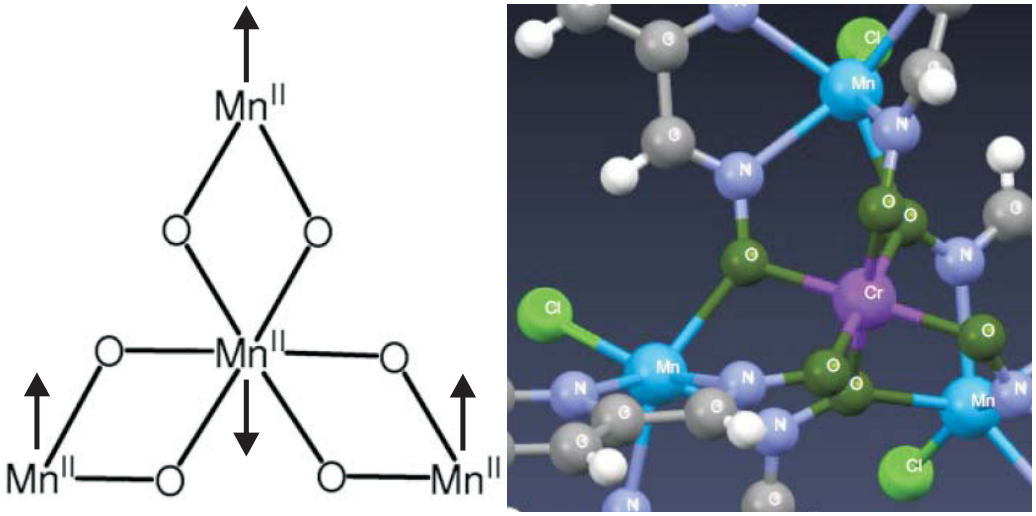

Figure 1.16: Left: Schematic representation of the star-shaped molecule with Mn_4^{II} core, the antiferromagnetic coupling of the central ion with the outer ions leads to an overall ferrimagnetic coupling with high saturation moment [H9]. Right: The replacement of the central ion by Cr leads to an intriguing interplay of strong anisotropy and frustration in a chemically very similar molecule [H10]. The crystal structure visualisation has been made employing the Mercury software [109], using the crystallographic data made available by Khanra et al. [128].

3d transition metal based molecules with star-shaped core often exhibit ferromagnetic coupling, i.e. the interaction between the nearest-neighbor transition metal ions is antiferromagnetic, leading to an effective ferromagnetic coupling of the outer ions (c.f. Fig. 1.16, left), making star-shaped molecules highly interesting candidates in the context of synthesizing high-spin molecules. A molecule comprising four divalent manganese ions leads to a very large net moment of $10\mu_b$/f.u. [**H9**]. Another interesting option to influence the magnetic properties of star shaped molecules is to replace the central ion by another transition metal, that means bringing single-ion anisotropy and frustration into chemically very similar molecules. Magnetic frustration in magnetic molecules can lead to: i) non-trivially degenerated ground state [129], ii) low lying non-magnetic excitation leading to iii) jumps and/or plateaus in magnetization curves [112, 130]). We investigated very intriguing consequences by replacing the central manganese ion by chromium, leading to a ($CrMn_3$) core (see also right panel of Fig. 1.16) [**H10**].

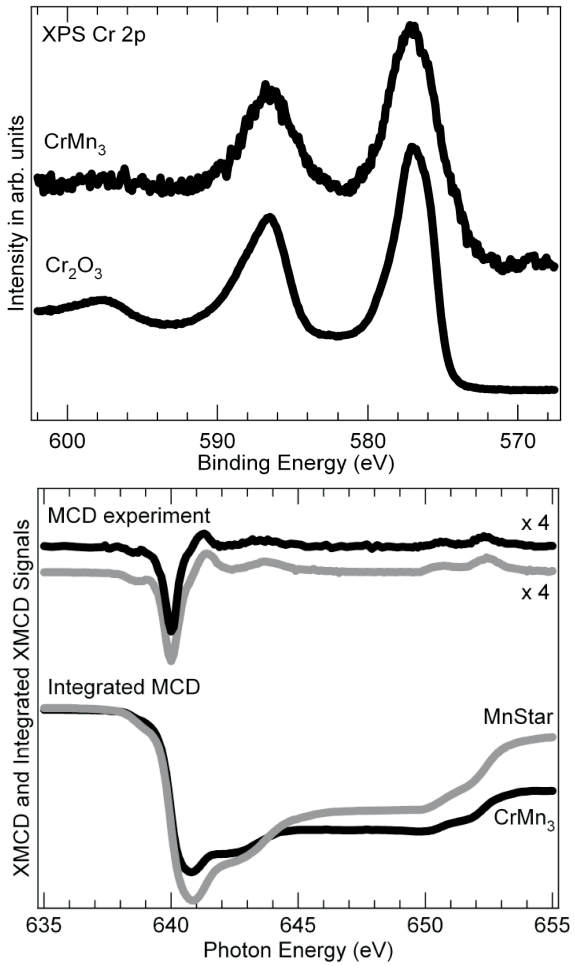

Figure 1.17: Top: Cr 2p core-level XPS of the $CrMn_3$ molecule. The corresponding spectrum of trivalent Cr_2O_3 is also shown. Bottom: Comparison of the experimental XMCD spectra of the Mn_4 and the $CrMn_3$ molecules. Both spectra were performed in an magnetic field of 5T and at a temperature of 5K.

To elucidate the magnetic properties element specific, we employed XMCD to the Cr $L_{2,3}$ (the $CrMn_3$-molecule) and Mn $L_{2,3}$ edges (both molecules). As to the Cr, the Cr $2p$ core level XPS resembles that of Cr_2O_3 as to the binding energies of Cr $2p_{3/2}$ and Cr $2p_{1/2}$, indicating trivalent Cr ions (c.f. Fig. 1.17, top panel), whereas for manganese a divalent Mn^{2+} valence state is found (not shown here). The interested reader is refereed to references [**H10**,[131]] for further details.

Looking at the XMCD a small negative XMCD-signal is recorded at the Cr^{3+} edge,

which indicates that there is no significant contribution of the Cr ions compared to Mn [**H10**] at T = 5 K and in an external magnetic field of B = 5 T strength, which is a rather astonishing result at first glance. A second highly interesting result is the obviously relative high orbital contribution to the Mn magnetic moment in case of the $CrMn_3$-molecule, as reflected in the non-vanishing integral of the XMCD signal (Fig. 1.17, bottom panel) [**H10**]. In contrast, the Mn^{2+} ions of the (chemically very similar) Mn_4 molecule carry no or a neglectable orbital magnetic moment, as expected for divalent Mn ions ($3d^5$ configuration) [**H9**]. This result is supported by the fact that high field EPR measurements yielded a gyromagnetic g-factor of 2.05 [128], hence indicating a positive orbital angular momentum. Furthermore, these XMCD-results can, in conjunction with Heisenberg simulations, explain the magnetization curve of the $CrMn_3$ molecule recorded by SQUID. At low fields up to around 2 T the Cr moments appear to be aligned antiparallel to the Mn moments, at 14 T ferromagnetic ordering with an overall saturation moment of 18 μ_b/f.u. is found [**H10**]. These results can be regarded as an example of strong anisotropy and frustration probed by XMCD. Finally, electronic structure calculations (density functional theory) confirm that the spins of the central ion, and not of one of the outer ions, are aligned anti-parallel to those of the other ions in the magnetic ground state (at T = 0 K and B = 0 T) for both, the Mn_4 and the $CrMn_3$ molecule. More details about our comprehensive work of the Mn_4 and $CrMn_3$ molecules can be found in references [**H9**] and [**H10**].

Besides the Mn-based molecules we also probed a very similar iron-based star-shaped complex by means of complementary x-ray spectroscopic approaches. This specific Fe based single-molecule magnet with exact chemical formula $C_{30}H_{66}Fe_4N_6O_{12}$, H_2L = *N*-methyldiethanolamine, is of particular interest due to a number of intriguing progress in terms of deposition on a gold surface, exhibiting an open magnetic hysteresis loop at low temperature [132] and quantum tunneling of the magnetization by employing suitable ligand chemistry [133]. Our work is motivated by the fact that there are some different reports as to the Fe valence state, both predominantly Fe^{2+} [134] and Fe^{3+} [132] valence states have been found in previous works.
Therefore, we performed a comprehensive study of the Fe_4 molecule by means of XMCD and XPS. For the XMCD experiments, the intensity of the incoming x-rays was reduced to 1% or less of the full intensity of the undulator based SIM-beamline of the Swiss Light Source, Paul Scherrer Institute. Under these conditions a pure Fe^{3+}

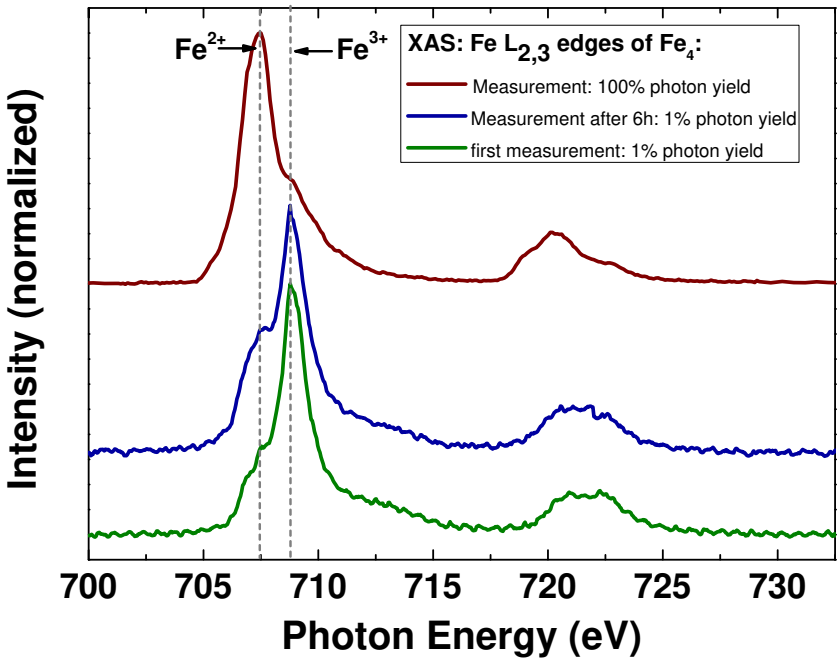

Figure 1.18: Fe $L_{2,3}$ isotropic x-ray absorption spectra taken on a fresh spot of the sample with 1% beamline flux (bottom, olive), after 6h of exposure (center, dark blue), and the XAS on a fresh spot with 100% beamline flux (top, wine).

valence state is found [**H11**]. Furthermore, sum rule analysis in conjunction with charge transfer multiplet simulations yields a saturation moment of almost exactly 10 μ_b/f.u. at a temperature of 0.6 K and an external magnetic field of 6.5 T, hence confirming earlier SQUID results and the ferromagnetic ordering of the four Fe^{3+} ions, which is analogous to that found for the Mn_4 molecule [**H9**]. When recording XAS across the Fe $L_{2,3}$ edges with full intensity of the beamline, a pure Fe^{2+} valence state is found already after one XAS-scan (c.f. Fig. 1.18). Hence, one has to lower the intensity of the incoming beam drastically to avoid radiation damage on this Fe_4 based complex, the sensitivity is significantly higher than that found for the Fe_{30} molecules [**H8**]. We also could investigate the Fe^{3+} to Fe^{2+} x-ray induced transition by performing Fe $2p$ XPS core levels and analyzing the Fe $2p_{3/2}$ binding energies and charge transfer satellites with help of suitable reference spectra as function of recording time [**H11**].

1.7.2.2 Element specific determination of macrocyclic 3d-4f complexes with Cu_3Tb core

Here we investigate the internal magnetic structure of the propylene linked macrocycles $[Cu_3^{II}Tb^{III}(\mathbf{L^{Pr}})(NO_3)_2(MeOH)(H_2O)_2](NO_3)\cdot 3H_2O$ (nickname $Cu_3Tb(\mathbf{L^{Pr}})$), and its butylene linked analogue, $[Cu_3^{II}Tb^{III}(\mathbf{L^{Bu}})(NO_3)_2(MeOH)(H_2O)](NO_3)\cdot 3H_2O$ (nickname $Cu_3Tb(\mathbf{L^{Bu}})$). These two molecules are rare examples of complexes comprising transition metal and rare earth ions prepared with a macrocyclic ligand which exhibit well promising indications of single molecule magnet behavior [120, 121]. Fig. 1.19 presents the structure of the propylene linked complex with $Cu^{II}Tb^{III}$ core. In order to proof the ferromagnetic coupling indicated by SQUID and to record element specific magnetization curves, XMCD across the Cu $L_{2,3}$ and Tb $M_{4,5}$ edges of both complexes was performed in external fields up to 13.5 T.

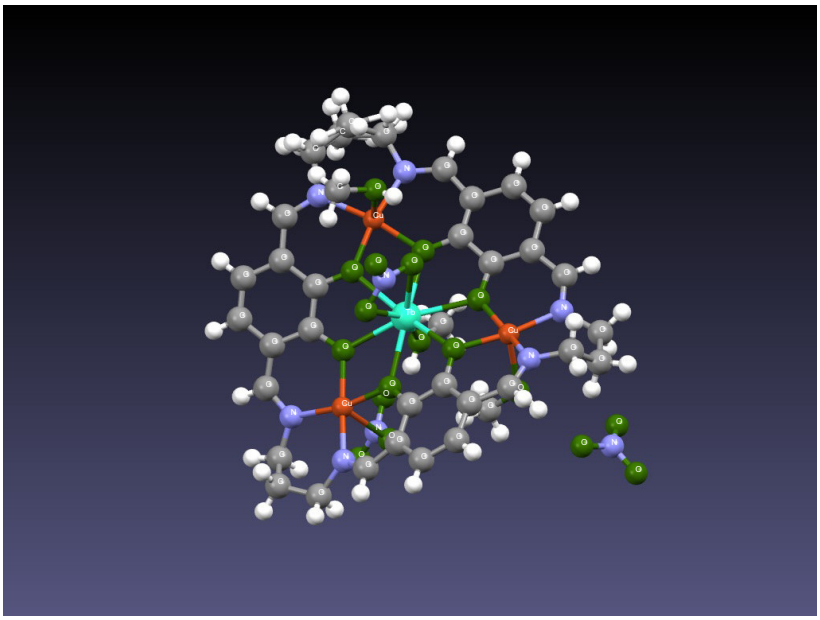

Figure 1.19: Structure of the tetrametallic $3d-4f$ macrocyclic complex $Cu_3Tb(\mathbf{L^{Pr}})$[120]. Turquise: the central Tb^{III} ion; dark orange: Cu^{II} ions. The molecule structure visualisation has been made using the Mercury software [109].

The top panels of Figure 1.20 display the dichroic XA-spectra, the resulting XMCD signals and their integrals for the $Cu_3Tb(\mathbf{L^{Pr}})$ complex performed at B = 13.5 T and T = 3 K. One can clearly see the ferromagnetic coupling of the moments of the

outer copper ions with that of the central terbium ion. Also the bivalent Cu and the trivalent Tb valence states can be unambiguously identified by the multiplet structure of the XAS. We also performed sum rule analysis yielding a particular high orbital contribution to the Tb moment. The results determined for the overall magnetic properties are in line with SQUID results for both complexes, if the exact value of the spin-quadrupole coupling is known, which is in particular important for $4f$ lanthanide ions, Tb in the current case. A detailed discussion of the sum rule analysis, also employing suitable complementary ligand field simulations, can be found in reference [**H12**].

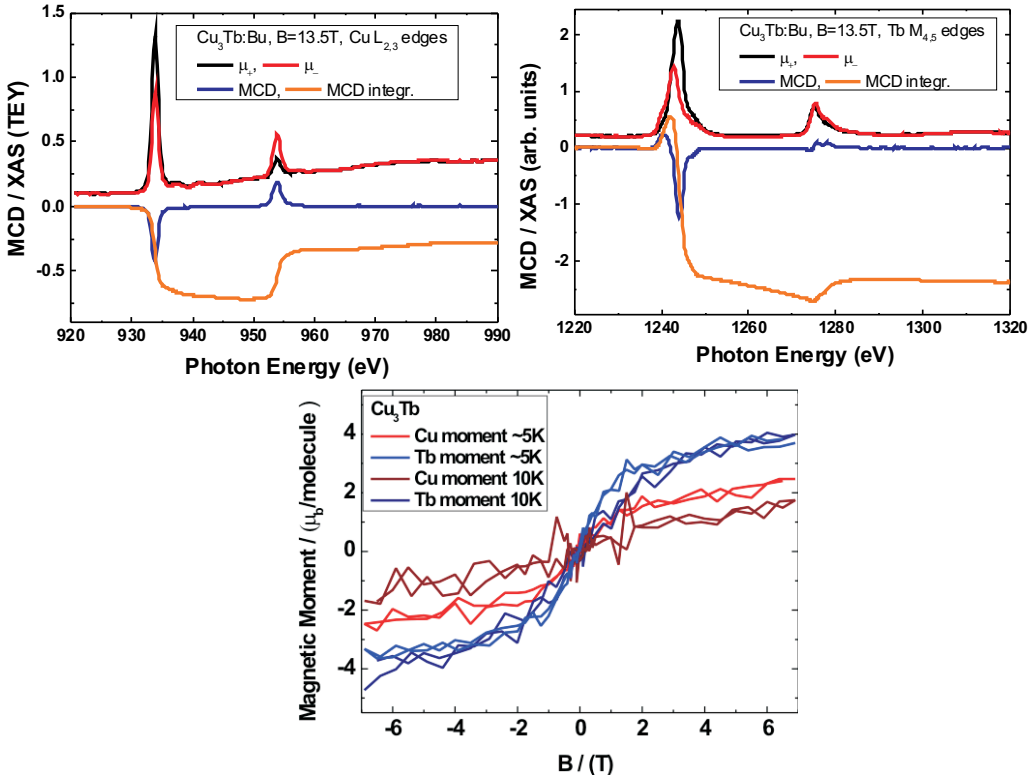

Figure 1.20: Top: Dichroic XA-spectra across the Cu $L_{2,3}$ (left) and Tb $M_{4,5}$ (right) edges of $Cu_3Tb(\mathbf{L^{Pr}})$. The resulting XMCD signals and their integrals are also shown. The experiments were performed at B = 13.5 T and T = 3 K. Bottom: Element specific magnetization curves of the $Cu_3Tb(\mathbf{L^{Pr}})$ complex recorded at the Cu L_3 and Tb M_5 resonances at temperatures of 5 K and 10 K.

Finally, we were able to record element specific magnetization curves of the $Cu_3Tb(\mathbf{L^{Pr}})$

molecule at temperatures of 5 K and 10 K (c.f. Fig. 1.19 bottom). Whereas the contribution of the Cu ions to the overall magnetic moment of the molecule becomes significantly lower with increasing temperature, the Tb moment remains constant within the accuracy of the experiment. This result reflects a weak coupling between the $3d$ Cu and the $4f$ Tb ions in the $Cu_3Tb(\mathbf{L^{Pr}})$ complex [**H12**].

In summary, it has been demonstrated that x-ray spectroscopic approaches are a very useful tool to investigate the chemical and magnetic properties of magnetic molecules. For instance, the results obtained by x-ray crystallography and integral magnetometry approaches can be substantially extended by the element and chemical sensitive information that can be extracted from core level XPS and XAS measurements. As shown for the molecules with Fe_{30} and Fe_4 core, a lot of attention has be paid concerning the investigation of any potential beginning of x-ray induced damage effects if working with these metallo-organic complexes [**H8, H11**]. On the other side, if carried out carefully, x-ray induced changes like the studied Fe^{3+} to Fe^{2+} photoreduction can be investigated in detail [**H8, H11**].

XMCD in the soft x-ray regime covering the transition metal $L_{2,3}$ and rare earth $M_{4,5}$ edges has been employed to tackle the internal magnetic structure of some molecules in question. This technique enables not only to extract the magnetic properties element specific but also separated into the spin and orbital contribution to the overall magnetic moment via the already mentioned sum rules. We could determine an unusual high Mn orbital moment for the Mn^{2+} ions in the Mn_3Cr molecule [**H10**] and successfully characterize the chemical and magnetic properties of a number of other single molecule magnets with star shaped core [**H9, H11, H12**] at low temperatures. We also performed element specific magnetization curves for $3d-4f$ macrocyclic Cu_3Tb molecules revealing a weak $3d-4f$ coupling in these complexes [**H12**].

Summary and Outlook

In the framework of this habilitation thesis a number of $3d$ transition metal and $4f$ rare earth compounds ranging from highly insulating ternary oxides of type $REScO_3$ via ferrite thin film to single molecule magnets have been studied by means of complementary x-ray spectroscopic approaches. In combination with structural investigations, magnetic measurements and suitable theoretical calculations a detailed picture of the electronic and magnetic structure of the materials in question could be developed.

In particular, photoelectron spectroscopy (PES) enables to study the chemical composition as well as the valence states of the constituents of a compound. Furthermore, PES is a probe of the total occupied density of states (tDOS). Soft x-ray absorption spectroscopy is very sensitive to the local ligand field and the valence state of a $3d$ transition metal and rare earth ion, extending this technique to XMCD opens an avenue for an element-specific investigation of the magnetic properties. Here, in particular with respect to the magnetic molecules experiments in the sub-Kelvin regime are of utmost interest to probe the internal magnetic structure of potential single molecule magnets even closer to the ground state [135].

Whereas XAS across ligand K edges (e.g. O K edge) is a tool to obtain partial information about the unoccupied density of states, x-ray emission spectroscopy (XES) yields the partial, element specific, occupied density of states. A combinatorial approach of O K edge XAS and (non-resonant) XES can be used to obtain information about the band gap in insulating oxides. During the last 10-15 years, resonant inelastic x-ray scattering (RIXS) in the soft x-ray regime has become a powerful approach to probe electron-hole excitations. In particular the spectral resolution has been improved from around 1 eV to the sub 10 meV range for transition metal L edge spectra [136], enabling the detailed study of $d-d$- or $f-f$-excitations, spin-flip transitions, magnons or even phononic excitations in complex correlated materials. This development will be sup-

ported by the emergence of diffraction-limited synchrotron radiation sources (DLSR) delivering a highly focused, very intense light beam with extremely high brilliance. The tight focal spot will enable x-ray spectroscopic experiments with significantly improved spectral resolution and on the sub-μm lateral scale. Even nano-focussed novel operando approaches to study emergent states and their underlying phase transitions in transition metal oxides and other complex materials are coming into sight [137]. The same accounts for imaging approaches such as greatly improved Photoelectron Emission Microscopy (PEEM), Scanning Transmission X-ray Microscopy (STXM), or coherent x-ray imaging approaches (for example ptychographic imaging in forward direction or under Bragg condition) [138].

Besides intensity, tunability, and brilliance the time structure of the synchrotron radiation is increasingly used to investigate structural phase transitions or magnetization dynamics by stroboscopic pump-probe experiments. The next generation sources for ultrashort (femtosecond to attosecond timescale) and extremely intense x-ray pulses are realized by means of free electron lasers (XFELs). An alternative approach is the variable pulse length storage ring planned at the BESSY II storage ring which will provide simultaneously pulses of 15 ps and 1.7 ps length [139], hence closing the gap between the DLSR and the ultrashort pulses produced by the XFELs.

These sources lead to entire new opportunities to investigate the structural, electronic or magnetic phase transitions in complex new advanced materials, e.g. by means of time-resolved diffraction, spectroscopic or imaging experiments which may include both, single shot and stroboscopic techniques [140]. For instance, one can think about tackling the dynamics of phase transitions in CMR-manganites, high T_c-superconductors, multiferroic materials or magnetic molecules on the ultrafast time scale with unprecedented precession, leading to new knowledge of emergent states and cooperative ordering phenomena poorly understood up to now.

List of Figures

List of Tables

References

[1] M. Dawber, K. M. Rabe, and J. F. Scott. Physics of thin-film ferroelectric oxides. *Rev. Mod. Phys.*, **77**:1083–1130, 2005. doi: https://doi.org/10.1103/RevModPhys.77.1083.

[2] H. Fu and R. E. Cohen. Polarization rotation mechanism for ultrahigh electromechanical response in single-crystal piezoelectrics. *Nature*, **403**:281–283, 2000. doi: 10.1038/35002022.

[3] J. Zaanen, G. A. Sawatzky, and J. W. Allen. Band gaps and electronic structure of transition-metal compounds. *Phys. Rev. Lett.*, **55**:418–421, 1985. doi: 10.1103/PhysRevLett.55.418.

[4] R. V. Chopdekar, V. K. Malik, A. Fraile Rodríguez, L. Le Guyader, Y. Takamura, A. Scholl, D. Stender, C. W. Schneider, C. Bernhard, F. Nolting, and L. J. Heyderman. Spatially resolved strain-imprinted magnetic states in an artificial multiferroic. *Phys. Rev. B*, **86**:014408, 2012. doi: 10.1103/PhysRevB.86.014408.

[5] S.-G. Lim, S. Kriventsov, T. N. Jackson, J. H. Haeni, D. G.Schlom, A. M. Balbashov, R. Uecker, P. Reiche, J. L. Freeouf, and G.Lucovsky. Dielectric functions and optical bandgaps of high-K dielectrics for metal-oxide-semiconductorfield-effecttransistors by far ultraviolet spectroscopic ellipsometry. *J. Appl. Phys.*, **91**:4500–4505, 2002. doi: 10.1063/1.1456246.

[6] G. Lucovsky, J. G. Hong, C. C. Fulton, Y. Zou, R. J. Nemanich, H. Ade, D. G. Schlom, and J. L. Freeouf. Spectroscopic studies of metal high-k dielectrics: transition metal oxides and silicates, and complex rare earth/transition metal oxides. *phys. stat. sol. (b)*, **241**:2221–2235, 2004. doi: 10.1002/pssb.200404938.

[7] H. M. Christen, G. E. Jellison, I. Ohkubo, S. Huang, M. E. Reeves, E. Cicerrella, J. L. Freeouf, Y. Jia, and D. G. Schlom. Dielectric and optical properties of

epitaxial rare-earth scandate films and their crystallization behavior. *Appl. Phys. Lett.*, **88**:262906, 2006. doi: 10.1063/1.2213931.

[8] P. Delugas, V. Fiorentini, A. Filippetti, and G. Pourtois. Cation charge anomalies and high-kappa dielectric behavior in $DyScO_3$: Ab initio density-functional and self-interaction-corrected calculations. *Phys. Rev. B*, **75**:115126, 2007. doi: 10.1103/PhysRevB.75.115126.

[9] P. Kužel, F. Kadlec, J. Petzelt, J. Schubert, and G. Panaitov. Highly tunable $SrTiO_3/DyScO_3$ heterostructures for applications in the terahertz range. *Appl. Phys. Lett.*, **91**:232911, 2007. doi: 10.1063/1.2822409.

[10] R. Uecker, B. Velickov, D. Klimm, R. Bertram, M. Bernhagen, M. Rabe, M. Albrecht, R. Fornari, and D. G. Schlom. Properties of rare-earth scandate single crystals (Re=Nd-Dy). *J. Cryst. Growth*, **310**:2649–2658, 2008. doi: 10.1016/j.jcrysgro.2008.01.019.

[11] K. J. Choi, M. Biegalski, Y. L. Li, A. Sharan, J. Schubert, R. Uecker, P. Reiche, Y. B. Chen, X. Q. Pan, V. Gopalan, L.-Q. Chen, D. G. Schlom, and C. B. Eom. Enhancement of Ferroelectricity in Strained $BaTiO_3$ Thin Films. *Science*, **306**: 1005–1009, 2004. doi: 10.1126/science.1103218.

[12] K. Rahmanizadeh, G. Bihlmayer, M. Luysberg, and S. Blügel. First-principles study of intermixing and polarization at the $DyScO_3/SrTiO_3$ interface. *Phys. Rev. B*, **85**:075314, 2012. doi: 10.1103/PhysRevB.85.075314.

[13] D. Kan, R. Aso, R. Sato, M. Haruta, H. Kurata, and Y. Shimakawa. Tuning magnetic anisotropy by interfacially engineering the oxygen coordination environment in a transition metal oxide. *Nat. Mat.*, **15**:432–437, 2016. doi: 10.1038/NMAT4580.

[14] Y. L. Tang, Y. L. Zhu, X. L. Ma, A. Y. Borisevich, A. N. Morozovska, E. A. Eliseev, W. Y. Wang, Y. J. Wang, Y. B. Xu, Z. D. Zhang, and S. J. Pennycook. Observation of a periodic array of flux-closure quadrants in strained ferroelectric $PbTiO_3$ films. *Science*, **348**:547–551, 2015. doi: 10.1126/science.1259869.

[15] R. P. Liferovich and R. H. Mitchell. A structural study of ternary lanthanide orthoscandate perovskites. *J. Sol. Stat. Chem.*, **177**:2188–2197, 2004. doi: 10.1016/j.jssc.2004.02.025.

[16] R. Uecker, H. Wilke, D. G. Schlom, B. Velickov, P. Reiche, A. Polity, M. Bernhagen, and M. Rossberg. Spiral formation during Czochralski growth of rare-earth scandates. *J. Cryst. Growth*, **295**:84–91, 2006. doi: 10.1016/j.jcrysgro.2006.07.018.

[17] C. Derks. *Characterization of* $RScO_3$*,* $LuFe_2O_4$ *and* $M_{72}Fe_{30}$ *based molecules by x-ray spectroscopic techniques.* PhD Thesis, Universität Osnabrück, 2012. URL `https://repositorium.ub.uni-osnabrueck.de/handle/urn:nbn:de:gbv:700-2013040810750`.

[18] C. Taubitz. *Investigation of the magnetic and electronic structure of Fe in molecules and chalcogenide systems.* PhD Thesis, Universität Osnabrück, 2010. URL `https://repositorium.ub.uni-osnabrueck.de/handle/urn:nbn:de:gbv:700-201006096312`.

[19] K. Küpper. *Electronic and magnetic properties of transition metal compounds: An x-ray spectroscopic study.* PhD Thesis, Universität Osnabrück, 2005. URL `https://repositorium.ub.uni-osnabrueck.de/handle/urn:nbn:de:gbv:700-2005071510`.

[20] F. M. F. de Groot. High resolution x-ray emission and x-ray absorption spectroscopy. *Chem. Rev.*, **101**:1779–1808, 2001. doi: 10.1021/cr9900681.

[21] J. Stöhr. *NEXAFS Spectroscopy.* Springer, Berlin, 1992.

[22] J. Stöhr and H.C. Siegmann. *Magnetism - From Fundamentals to Nanoscale Dynamics.* Springer, 2006.

[23] F.M.F. de Groot and Kotani. *Core Level Spectroscopy of Solids.* Francis & Taylor, 2008.

[24] M. Kallmayer, H. J. Elmers, B. Balke, S. Wurmehl, F. Emmerling, G. H. Fecher, and C. Felser. Magnetic properties of $Co_2Mn_{1-x}Fe_xSi$ Heusler alloys. *J. Phys. D: Appl. Phys.*, **39**:786–792, 2006. doi: 10.1088/0022-3727/39/5/S03.

[25] E. J. Nordgren, S. M. Butorin, L. C. Duda, J. H. Guo, and J. E.Rubensson. *Soft X-ray Flourescence Spectroscopy for Materials Science and ChemicalPhysics:In Advanced Series of Physical Chemistry - Vol. 12A - ChemicalApplicationsof Synchrotron Radiation*. World Scientific, 2002.

[26] A. Kotani and S. Shin. Resonant inelastic x-ray scattering spectra for electrons in solids. *Rev. Mod. Phys.*, **73**:203–246, 2001. doi: 10.1103/RevModPhys.73.203.

[27] E. Cicerrella. *Dielectric functions and optical bandgaps of high-K dielectrics by farultravioletspectroscopic ellipsometry*. PhD thesis, OGI School of Science & Engineering at Oregon Health & Science University, 2006.

[28] V. V. Afanas'ev, A. Stesmans, C. Zhao, M. Caymax, T. Heeg, J.Schubert, Y. Jia, D. G. Schlom, and G. Lucovsky. Band alignment between (100)Si and complex rare earth/transition metaloxides. *Appl. Phys. Lett.*, **85**:5917–5919, 2004. doi: 10.1063/1.1829781.

[29] A. J. Millis. Lattice effects in magnetoresistive manganese perovskites. *Nature*, **392**:147–150, 1998. doi: 10.1038/32348.

[30] M. B. Salamon and M. Jaime. The physics of manganites: Structure and transport. *Rev. Mod. Phys.*, **73**:583–628, 2001. doi: 10.1103/RevModPhys.73.583.

[31] Y. D. Chuang, A. D. Gromko, D. S. Dessau, T. Kimura, and Y. Tokura. Fermi surface nesting and nanoscale fluctuating charge/orbital orderingincolossal magnetoresistive oxides. *Science*, **292**:1509–1513, 2001. doi: 10.1126/science.1059255.

[32] R. von Helmolt and J. Wecker and B. Holzapfel and L. Schultz and K. Samwer. Giant negative magnetoresistance in perovskitelike $La_{2/3}Ba_{1/3}MnO_x$ ferromagnetic-films. *Phys. Rev. Lett.*, **71**:2331–2334, 1993. doi: 10.1103/PhysRevLett.71.2331.

[33] S. Jin, T. H. Tiefel, M. McCormack, R. A. Fastnacht, R. Ramesh, and L. H. Chen. Thousandfold Change in Resistivity in Magnetoresistive La-Ca-Mn-O Films. *Science*, **264**:413–415, 1994. doi: 10.1126/science.264.5157.413.

[34] M. N. Baibich, J. M. Broto, A. Fert, N. Van Dau, F. Petroff, P. Eitenne, G. Creuzet, A. Friederich, and A. Chazelas. Giant magnetoresistance of (001)Fe/(001)Cr magnetic superlattices. *Phys. Rev. Lett.*, **61**:2472–2475, 1988. doi: 10.1103/PhysRevLett.61.2472.

[35] G. Binasch, P. Grünberg, F. Saurenbach, and W. Zinn. Enhanced magnetoresistance in layered magnetic structures with antiferromagnetic interlayer exchange. *Phys. Rev. B*, **39**:4828–4830, 1989. doi: 10.1103/PhysRevB.39.4828.

[36] D. Ruzmetov, Y. Seo, L. J. Belenky, D. M. Kim, X. L. Ke, H. P. Sun, V. Chandrasekhar, C. B. Eom, M. S. Rzchowski, and X. Q. Pan. Epitaxial magnetic perovskite nanostructures. *Adv. Mater.*, **17**:2869, 2005. doi: 10.1002/adma.200501240.

[37] J. H. Park, E. Vescovo, H. J. Kim, C. Kwon, R. Ramesh, and T.Venkatesan. Direct evidence for a half-metallic ferromagnet. *Nature*, **392**:794–796, 1998. doi: 10.1038/33883.

[38] W. E. Pickett and J. S. Moodera. Half metallic magnets. *Physics Today*, **54**: 39–44, 2001. doi: 10.1063/1.1381101.

[39] C. Zener. Interaction between the D-shells in the Transition Metals .2. FerromagneticCompoundsof Manganese with Perovskite Structure. *Phys. Rev.*, **82**: 403–405, 1951. doi: 10.1103/PhysRev.82.403.

[40] A. J. Millis, P. B. Littlewood, and B. I. Shraiman. Double exchange alone does not explain the resistivity of $\mathrm{la}_{1-x}\mathrm{sr}_x\mathrm{mno}_3$. *Phys. Rev. Lett.*, **74**:5144–5147, 1995. doi: 10.1103/PhysRevLett.74.5144.

[41] J. M. De Teresa, M. R. Ibarra, P. A. Algarabel, C. Ritter, C.Marquina, J. Blasco, J. Garcia, A. Del Moral, and Z. Arnold. Evidence for magnetic polarons in the magnetoresistive perovskites. *Nature*, **386**:256–259, 1997. doi: 10.1038/386256a0.

[42] Y. Murakami, H. Kawada, H. Kawata, M. Tanaka, T. Arima, Y. Moritomo, and Y. Tokura. Direct observation of charge and orbital ordering in $La_{0.5}Sr_{1.5}MnO_4$. *Phys. Rev. Lett.*, **80**:1932–1935, 1998. doi: 10.1103/PhysRevLett.80.1932.

[43] A. Moreo, S. Yunoki, and E. Dagotto. Solid state physics - phase separation scenario for manganese oxides and related materials. *Science*, **283**:2034–2040, 1999. doi: 10.1126/science.283.5410.2034.

[44] N. Mathur and P. Littlewood. Mesoscopic texture in manganites. *Phys. Today*, **56**:25–30, 2003. doi: 10.1063/1.1554133.

[45] T. Saitoh, A. E. Bocquet, T. Mizokawa, H. Namatame, A. Fujimori, M. Abbate, Y. Takeda, and M. Takano. Electronic structure of $La_{1-x}Sr_xMnO_3$ studied by photoemission and x-ray-absorption spectroscopy. *Phys. Rev. B*, **51**:13942–13951, 1995. doi: 10.1103/PhysRevB.51.13942.

[46] P. Ravindran, A. Kjekshus, H. Fjellvåg, A. Delin, and O. Eriksson. Ground-state and excited-state properties of $LaMnO_3$ from full-potential calculations. *Phys. Rev. B*, **65**:064445, 2002. doi: 10.1103/PhysRevB.65.064445.

[47] N. Mannella, W. L. Yang, X. J. Zhou, H. Zheng, J. F. Mitchell, J. Zaanen, T. P. Devereaux, N. Nagaosa, Z. Hussain, and Z.-X. Shen. Nodal quasiparticle in pseudogapped colossal magnetoresistive manganites. *Nature*, **438**:474–478, 2005. doi: 10.1038/nature04273.

[48] L. L. Lev, J. Krempaský, U. Staub, V. A. Rogalev, T. Schmitt, M. Shi, P. Blaha, A. S. Mishchenko, A. A. Veligzhanin, Y. V. Zubavichus, M. B. Tsetlin, H. Volfová, J. Braun, J. Minár, and V. N. Strocov. Fermi Surface of Three-Dimensional $La_{1-x}Sr_xMnO_3$ Explored by Soft-X-Ray ARPES: Rhombohedral Lattice Distortion and its Effect on Magnetoresistance. *Phys. Rev. Lett.*, 114:237601, 2015. doi: 10.1103/PhysRevLett.114.237601.

[49] G. Schütz, W. Wagner, W. Wilhelm, P. Kienle, R. Zeller, R.Frahm, and G. Materlik. Absorption of circularly polarized x-rays in iron. *Phys. Rev. Lett.*, **58**:737–740, 1987. doi: 10.1103/PhysRevLett.58.737.

[50] P. Carra, B. T. Thole, M. Altarelli, and X. Wang. X-ray circular dichroism and local magnetic fields. *Phys. Rev. Lett.*, **70**:694–697, 1993. doi: 10.1103/PhysRevLett.70.694.

[51] C. T. Chen, Y. U. Idzerda, H.-J-Lin, N. V. Smith, G. Meigs, E. Chaban, G. H. Ho, E. Pellegrin, and F. Sette. Experimental Confirmation of the X-Ray Magnetic Circular Dichroism Sum Rules for Iron and Cobalt. *Phys. Rev. Lett.*, **75**: 152–155, 1995. doi: 10.1103/PhysRevLett.75.152.

[52] H. Ebert. Magneto-optical effects in transition metal systems. *Rep. Prog. Phys.*, **59**:1665–1735, 1996.

[53] Cz. Kapusta, P. Fischer, and G. Schütz. Magnetic X-ray absorption spectroscopy. *J. Alloys Comp.*, **286**:37–46, 1999. doi: 10.1016/S0925-8388(98)00977-3.

[54] O. Wessely, P. Roy, D. Åberg, C. Andersson, S. Edvardsson, O. Karis, B. Sanyal, P. Svedlindh, M. I. Katsnelson, R.Gunnarsson, D. Arvanitis, and O. Eriksson. Initial and final state effects in the x-ray absorption process of $La_{1-x}Sr_xMnO_3$. *Phys. Rev. B*, **68**:235109, 2003. doi: 10.1103/PhysRevB.68.235109.

[55] L. Pinsard, J. Rodriguez-Carvajal, A. H. Moudden, and A. Anane. Jahn-Teller effect and ferromagnetic ordering in $La_{0.875}Sr_{0.125}MnO_3$: A reentrant behaviour. *Physica B*, **234-236**:856–858, 1997. doi: 10.1016/S0921-4526(96)01130-1.

[56] Michael Raekers. *An x-ray spectroscopic study of novel material for electronic applications.* PhD Thesis, Universität Osnabrück, 2009. URL `https://repositorium.ub.uni-osnabrueck.de/handle/urn:nbn:de:gbv:700-2009061010`.

[57] B. Hoppe and L. L. Hirst. Ordering of spin and orbital moments in a lattice of 3d ions coupled by superexchange. *J. Phys. C: Solid State Phys.*, **16**:1919–1932, 1983. doi: 10.1088/0022-3719/16/10/021.

[58] I. Galanakis, P. M. Oppeneer, P. Ravindran, L. Nordström, P. James, M. Alouani, H. Dreysse, and O. Eriksson. Sign reversal of the orbital moment via ligand states. *Phys. Rev. B*, **63**:172405, 2001. doi: 10.1103/PhysRevB.63.172405.

[59] S. V. Trukhanov. Peculiarities of the magnetic state in the system $La_{0.70}Sr_{0.30}MnO_{3-?}$ ($0 \leq \gamma \leq 0.25$). *J. Exp. Theor. Phys.*, **100**:95–105, 2005. doi: 10.1134/1.1866202.

[60] M. Fiebig, T. Lottermoser, D. Meier, and M. Trassin. The evolution of multiferroics. *Nat. Rev. Mat.*, **1**:16046, 2016. doi: 10.1038/natrevmats.2016.46.

[61] N. A. Hill. Why are there so few magnetic ferroelectrics? *J.Phys. Chem. B*, **104**:6694–6709, 2000. doi: 10.1021/jp000114x.

[62] J. Wang, J.B. Neaton, H. Zheng, V. Nagarajan, S. B. Ogale, B. Liu, D. Viehland, V. Vaithyanathan, D.G. Schlom, U.V. Waghmare, N.A. Spaldin, K.M. Rabe, M. Wuttig, and R. Ramesh. Epitaxial $BiFeO_3$ Multiferroic Thin Film Heterostructures. *Science*, **299**:1719–1722, 2003. doi: 10.1126/science.1080615.

[63] B. B. van Aken, T. T. M. Palstra, A. Filippetti, and N. A. Spaldin. The origin of ferroelectricity in magnetoelectric $YMnO_3$. *Nat. Mat.*, **3**:164–170, 2004. doi: 10.1038/nmat1080.

[64] H. E. Lahtinen, K. J. A. Franke, and S. van Dijken. Electric-field control of magnetic domain wall motion and local magnetization reversal. *Sci. Rep.*, **2**: 258, 2012. doi: 10.1038/srep00258.

[65] S. Geprägs, D. Mannix, M. Opel, S. T. B. Goennenwein, and R. Gross. Converse magnetoelectric effects in $Fe_3O_4/BaTiO_3$ multiferroic hybrids. *Phys. Rev. B*, **88**: 054412, 2013. doi: 10.1103/PhysRevB.88.054412.

[66] J. A. Mundy, C. M. Brooks, M. E. Holtz, J. A. Moyer, H. Das, A. F. Rébola, J. T. Heron, J. D. Clarkson, S. M. Disseler, Z. Liu, A. Farhan, R. Held, R. Hovden, E. Padgett, Q. Mao, H. Paik, R. Misra, L. F. Kourkoutis, E. Arenholz, A. Scholl, J. A. Borchers, W. D. Ratcliff, R. Ramesh, C. J. Fennie, P. Schiffer, D. A. Muller, and D. G. Schlom. Atomically engineered ferroic layers yield a room-temperature magnetoelectric multiferroic. *Phys. Rev. B*, **537**:523–527, 2016. doi: 10.1038/nature19343.

[67] K. Momma and F. Izumi. VESTA 3 for three-dimensional visualization of crystal, volumetric and morphology data. *J. Appl. Crystallogr.*, **44**:1272–1276, 2011. doi: 10.1107/S0021889811038970.

[68] M. Isobe, N. Kimizuka, J. Iida, and S. Takekawa. Structure of $lufecoo_4$ and $lufe_2o_4$. *Acta Cryst.*, **C46**:1917–1918, 1990. doi: 10.1107/S0108270190004784.

[69] N. Ikeda. Ferroelectricity from iron valence ordering in the charge-frustrated system $LuFe_2O_4$. *Nature*, **436**:1136–1138, 2005.

[70] J. Kim, S.B. Kim, C.U. Jung, and B.W. Lee. Magnetic Anisotropy in $LuFe_2O_4$ Single Crystal. *IEEE Transactions on Magnetics*, **45**:2608–2609, 2009. doi: 10.1109/TMAG.2009.2018912.

[71] J. de Groot, T. Mueller, R. A. Rosenberg, D. J. Keavney, Z. Islam, J.-W. Kim, and M. Angst. Charge Order in $LuFe_2O_4$: An Unlikely Route to Ferroelectricity. *Phys. Rev. Lett.*, **108**:187601, 2012. doi: 10.1103/PhysRevLett.108.187601.

[72] L. Ding, F. Orlandi, D. D. Khalyavin, A. T. Boothroyd, D. Prabhakaran, G. Balakrishnan, and P. Manuel. Coupling between Spin and Charge Order Driven by Magnetic Field in Triangular Ising System LuFe2O4+{\delta}. *Crystals*, **8**:88, 2018. doi: 10.3390/cryst8020088.

[73] H. J. Xiang and M. H. Whangbo. CCharge order and the origin of giant magnetocapacitance in $LuFe_2O_4$. *Phys. Rev. Lett.*, **98**:246403, 2007. doi: 10.1103/PhysRevLett.98.246403.

[74] A. Nagano, M. Naka, J. Nasu, and S. Ishihara. Electric polarisation, magnetoelectric effect, and orbital state of a layered iron oxide with frustrated geometry. *Phys. Rev. Lett.*, **99**, 2007. doi: 10.1103/PhysRevLett.99.217202.

[75] P. Weiss and R. Forrer. La saturation absolue des ferromagnétiques et les lois d'approche en fonction du champ et de la température. *Ann. Phys.*, **10**:279 – 372, 1929. doi: 10.1051/anphys/192910120279.

[76] E.J.W. Verwey. Electronic Conduction of Magnetite (Fe_3O_4) and its Transition Point at Low Temperatures. *Nature*, **144**:327–328, 1939. doi: 10.1038/144327b0.

[77] M.S. Senn, J.P. Wright, and J.P. Attfield. Charge order and three-site distortions in the Verwey structure of magnetite. *Nature*, **481**:173–176, 2012. doi: 10.1038/nature10704.

[78] M. I. Katsnelson, V.Yu. Irkhin, L. Chioncel, A.I. Lichtenstein, and R.A. de Groot. Half-metallic ferromagnets: From band structure to many-body effects. *Rev. Mod. Phys.*, **80**:315–378, 2008. doi: 10.1103/RevModPhys.80.315.

[79] R. Bliem, E. McDermott, P. Ferstl, M. Setvin, O. Gamba, J. Pavelec, M.A. Schneider, M. Schmid, U. Diebold, P. Blaha, L. Hammer, and G.S. Parkinson. Subsurface cation vacancy stabilization of the magnetite (001) surface. *Science*, **346**:1215–1218, 2014. doi: 10.1126/science.1260556.

[80] J.M. Byrne, N. Klueglein, C. Pearce, K.M. Rosso, E. Appel, and A. Kappler. Redox cycling of fe(ii) and fe(iii) in magnetite by fe-metabolizing bacteria. *Science*, **347**:1473–1476, 2015. doi: 10.1126/science.aaa4834.

[81] J.-B. Moussy. From epitaxial growth of ferrite thin filmsto spin-polarized tunnelling. *J. Phys. D: Appl. Phys.*, **46**:143001, 2013. doi: 10.1088/0022-3727/46/14/143001.

[82] C. Klewe, M. Meinert, A. Böhnke, K. Kuepper, E. Arenholz, A. Gupta, J.-M. Schmalhorst, T. Kuschel, and G. Reiss. Physical characteristics and cation distribution of $NiFe_2O_4$ thin films prepared by reactive co-sputtering . *J. Appl. Phys.*, **115**:123903, 2014. doi: 10.1063/1.4869400.

[83] T. Kuschel, C. Klewe, J.-M. Schmalhorst, F. Bertram, O. Kuschel, T. Schemme, J. Wollschläger, S. Francoual, J. Strempfer, A. Gupta ans M. Meinert, G. Gerhard, D. Meier, and G. Reiss. Static Magnetic Proximity Effect in $Pt/NiFe_2O_4$ and Pt/Fe Bilayers Investigated by X-Ray Resonant Magnetic Reflectivity. *Phys. Rev. Lett.*, **115**:097401, 2015.

[84] Florian Bertram. *The structure of ultrathin iron oxide films studied by x-ray diffraction*. PhD Thesis, Universität Osnabrück, 2013. URL `https://repositorium.ub.uni-osnabrueck.de/handle/urn:nbn:de:gbv:700-2013060310882`.

[85] J. A. Moyer, S. Lee, P. Schiffer, and L. W. Martin. Magnetically disordered phase in epitaxial iron-deficient Fe_3O_4 thin films. *Phys. Rev. B*, **91**:064413, 2015. doi: 10.1103/PhysRevB.91.064413.

[86] G.S. Parkinson. Iron oxide surfaces. *Surf. Sci. Rep.*, **71**:272–365, 2016. doi: 10.1016/j.surfrep.2016.02.001.

[87] S. Hwang, Q. Meng, P.-F. Chen, K. Kisslinger, J. Cen, A. Orlov, Y. Zhu, E.A. Stach, Y.-H. Chu, and D. Su. Strain Coupling of Conversion-type Fe_3O_4 Thin

Films for Lithium Ion Batteries . *Angew. Chem.: Int. Ed.*, **56**:7813–7816, 2017. doi: 10.1002/anie.201703168.

[88] C. Gatel, E. Snoeck, V. Serin, and A. R. Fert. Epitaxial growth and magnetic exchange anisotropy in Fe_3O_4/NiO bilayers grown on MgO(001) and Al_2O_3(0001). *Eur.Phys. Journ. B*, **45**:157–168, 2005. doi: 10.1140/epjb/e2005-00073-y.

[89] T. Schemme, O. Kuschel, F. Bertram, K. Kuepper, and J. Wollschläger. Structure and morphology of epitaxially grown Fe_3O_4/NiO bilayers on MgO(001). *Thin Solid Films*, **589**:526–533, 2015. doi: 10.1016/j.tsf.2015.06.018.

[90] O. Kuschel, W. Spiess, T. Schemme, J. Rubio-Zuazo, K. Kuepper, and J. Wollschläger. Real-time monitoring of the structure of ultrathin Fe_3O_4 films during growth on Nb-doped $SrTiO_3$(001). *Appl. Phys. Lett.*, **111**:041902, 2017. doi: 10.1063/1.4995408.

[91] O. Kuschel, N. Pathé, T. Schemme, K. Ruwisch, J. Rodewald, R. Buss, F. Bertram, T. Kuschel, K. Kuepper, and J. Wollschläger. Impact of Strain and Morphology on Magnetic Properties of Fe_3O_4/NiO Bilayers Grown on Nb:$SrTiO_3$(001) and MgO(001). *Materials*, **11**:1122, 2018. doi: 10.3390/ma11071122.

[92] I. P. Krug, F. U. Hillebrecht, M. W. Haverkort, A. Tanaka, L. H. Tjeng, H. Gomonay, A. Fraile-Rodríguez, F. Nolting, S. Cramm, and C. M. Schneider. Impact of interface orientation on magnetic coupling in highly ordered systems: A case study of the low-indexed Fe_3O_4/NiO interfaces. *Phys. Rev. B*, **78**:064427, 2008. doi: 10.1103/PhysRevB.78.064427.

[93] H. Zheng, J. Wang, S. E. Lofland, Z. Ma, L. Mohaddes-Ardabili, T. Zhao, L. Salamanca-Riba, S. R. Shinde, S. B. Ogale, F. Bai, D. Viehland, Y. Jia, D. G. Schlom, M. Wuttig, A. Roytburd, and R. Ramesh. Multiferroic $BaTiO_3$-$CoFe_2O_4$ Nanostructures. *Science*, **303**:661–663, 2004. doi: 10.1126/science.1094207.

[94] U. Lüders, M. Bibes, K. Bouzehouane, E. Jacquet, J. P. Contour, S. Fusil, J.-F. Bobo, J. Fontcuberta, A. Barthélémy, and A. Fert. Spin filtering through ferrimagnetic $NiFe_2O_4$ tunnel barriers. *Appl. Phys. Lett.*, **88**:082505, 2006. doi: 10.1063/1.2172647.

[95] S. Matzen, J. B. Moussy, P. Wei, C. Gatel, J. C. Cezar, M. A. Arrio, Ph. Sainctavit, and J. S. Moodera. Structure, magnetic ordering, and spin filtering efficiency of $NiFe_2O_4$(111) ultrathin films. *Appl. Phys. Lett.*, **104**:182404, 2014. doi: 10.1063/1.4871733.

[96] J. A. Moyer, C. A. F. Vaz, E. Negusse, D. A. Arena, and V. E. Henrich. Controlling the electronic structure of $Co_{1-x}Fe_{2+x}O_4$ thin films through iron doping. *Phys. Rev. B*, **83**:035121, 2011. doi: 10.1103/PhysRevB.83.035121.

[97] C. Jin, Q. Zhang, W. B. Mi, E. Y. Jiang, and H. L. Bai. Tunable magnetic and electrical properties of polycrystalline and epitaxial $Ni_xFe_{3-x}O_4$ thin films prepared by reactive co-sputtering. *J. Phys. D: Appl. Phys.*, **43**:385001, 2010. doi: 10.1088/0022-3727/43/38/385001.

[98] M. Hoppe, S. Döring, M. Gorgoi, S. Cramm, and M. Müller. Enhanced ferrimagnetism in auxetic $NiFe_2O_4$ in the crossover to the ultrathin-film limit. *Phys. Rev. B*, **91**:054418, 2015. doi: 10.1103/PhysRevB.91.054418.

[99] A. Shan, X. Wu, J. Lu, C. Chen, and R. Wang. Phase formations and magnetic properties of single crystal nickel ferrite ($NiFe_2O_4$) with different morphologies. *CrystEngComm*, **17**:1603–1608, 2015. doi: 10.1039/c4ce02139h.

[100] X. Sun, N. Frey Huls, A. Sigdel, and S. Sun. Tuning Exchange Bias in Core/Shell FeO/Fe_3O_4 Nanoparticles. *Nano Lett.*, **12**:246–251, 2012. doi: 10.1021/nl2034514.

[101] M. Haase and H. Schäfer. Upconverting Nanoparticles. *Angew. Chem. Int. Ed.*, **50**:5808–5829, 2011. doi: 10.1002/anie.201005159.

[102] C. C. Lin, Z. R. Xiao, G. Y. Guo, T. S. Chan, and R. S. Liu. Versatile Phosphate Phosphors $ABPO_4$ in White Light-Emitting Diodes: Collocated Characteristic Analysis and Theoretical Calculations. *J. Am. Chem. Soc.*, **132**:3020–3028, 2010. doi: 10.1021/ja9092456.

[103] R. Komban, J. P. Klare, B. Voss, J. Nordmann, H.-J. Steinhoff, and M. Haase. An Electron Paramagnetic Resonance Spectroscopic Investigation on the Growth Mechanism of $NaYF_4$:Gd Nanocrystals. *Angew. Chem. Int. Ed.*, **51**:6506, 2012. doi: 10.1002/anie.201201025.

[104] O. S. Kwon, H. S. Song, J. Conde, H. I. Kim, N. Artzi, and J. H. Kim. Dual-Color Emissive Upconversion Nanocapsules for Differential Cancer Bioimaging In Vivo. *ACS Nano*, **10**:1512–1521, 2016. doi: 10.1021/acsnano.5b07075.

[105] A. Müller and P. Gouzerh. From linking of metal-oxide building blocks in a dynamic library to giant clusters with unique properties and towards adaptive chemistry. *Chem. Soc. Rev.*, **51**:7431–7463, 2012. doi: 10.1039/c2cs35169b.

[106] S. Garai, H. Bögge, A. Merca, O. A. Petina, A. Greg, P. Gouzerh, E. T. K. Haupt, I. A. Weinstock, and A. Müller. Densely Packed Hydrophobic Clustering: Encapsulated Valerates Form a High-Temperature-Stable $\{Mo_{132}\}$ Capsule System. *Angew. Chem. Int. Ed.*, **55**:6634–6637, 2016. doi: 10.1002/anie.201601140.

[107] A. Patel, N. Narkhede, S. Singh, and S. Pathan. Keggin-type lacunary and transition metal substituted polyoxometalates as heterogeneous catalysts: A recent progress. *Catalysis Reviews*, **58**:337–370, 2016. doi: 10.1080/01614940.2016.1171606.

[108] N.I. Gumerova and A. Rompel. *Nat. Rev. Chem.*, **2**:UNSP 0112, 2018. doi: 10.1038/s41570-018-0112.

[109] C.F. Macrae, I.J. Bruno, J. A. Chisholm, P.R. Edgington, P. McCabe, E. Pidcock, L. Rodriguez-Monge, R. Taylor, J. van de Streek, and P.A. Wood. Mercury CSD 2.0 - New Features for the Visualization and Investigation of Crystal Structures. *J. Appl. Cryst.*, **41**:466–470, 2008. doi: 10.1107/S0021889807067908.

[110] A. Müller, S.K. Das, H. Bögge, M. Schmidtmann, A. Botar, and A. Patrut. Generation of cluster capsules (i_h) from decomposition products of a smaller cluster (keggin-t_d) while surviving ones get encapsulated: species with core-shell topology formed by a fundamental symmetry-driven reaction. *Chem. Commun.*, **7**:657–658, 2001. doi: 10.1039/b009518b.

[111] A. Müller, S.K. Das, P. Körgeler, H. Bögge, M. Schmidtmann, V. Schunemann A.X. Trautwein, E. Krickemeyer, and W. Preetz. Linking icosahedral, strong molecular magnets $\{Mo_{72}^{VI}Fe_{30}^{III}\}$ to layers - a solid-state reaction at room temperature. *Angew. Chem. Int. Ed.*, **39**:1612–1614, 2000. doi: 10.1002/(SICI)1521-3773(20000502)39:9⟨1612::AID-ANIE1612⟩3.0.CO;2-L.

[112] C. Schröder, H. Nojiri, J. Schnack, P. Hage, M. Luban, and P. Kögerler. Competing spin phases in geometrically frustrated magnetic molecules. *Phys. Rev. Lett.*, **94**:017205–017209, 2005. doi: 10.1103/PhysRevLett.94.017205.

[113] R. Sessoli, D. Gatteschi, A. Caneschi, and M.A. Novak. Magnetic bistability in a metal-ion cluster. *Nature*, **365**:141–143, 1993. doi: 10.1038/365141a0.

[114] M.N. Leuenberger and D. Loss. Quantum computing in molecular magnets. *Nature*, **410**:789–793, 2001. doi: 10.1038/35071024.

[115] O. Kahn. *Molecular MAgnetism*. VCH, New York, 1999.

[116] H. Wende, M. Bernien, J. Luo, C. Sorg, N. Ponpandian, J. Kurde, J. Miguel, M. Piantek, X. Xu, P. Eckhold, W. Kuch, K. Baberschke, P. M. Panchmatia, B. Sanyal, P. M. Oppeneer, and O. Ericksson. Substrate-induced magnetic ordering and switching of iron porphyrin molecules. *Nat. Mater.*, **6**:516–520, 2007. doi: 10.1038/nmat1932.

[117] H. U. Güdel and U. Hauser. Exchange Interactions in Tris[cis-di-μ-hydroxo-bis(ethylenediamine)chromium(III)]chromium(III) Tris-(dithionate) Octahydrate. *Inorg. Chem.*, **19**:1325–1328, 1980.

[118] K. Petukhov, M. S. Alam, H. Rupp, S. Strömsdörfer, P. Müller, A. Scheurer, R. W. Saalfrank, J. Kortus, A. Postnikov, M. Ruben, L. K. Thompson, and J. M. Lehn. Stm spectroscopy of magnetic molecules. *Coord. Chem. Rev.*, **253**: 2387–2398, 2009. doi: 10.1016/j.ccr.2009.01.024.

[119] V. Pavlishchuk, F. Birkelbach, T. Weyhermüller, K. Wieghardt, and P. Chaudhuri. Polynuclear Complexes of the Pendent-Arm Ligand 1,4,7-Tris(acetophenoneoxime)-1,4,7-triazacyclononane. *Inorg. Chem.*, **41**:4405–4416, 2002. doi: 10.1021/ic011322m.

[120] H. L. C. Feltham, R. Clérac, A .K. Powell, and S. Brooker. A Tetranuclear, Macrocyclic 3d-4f Complex Showing Single-Molecule Magnet Behavior. *Inorg. Chem.*, **50**:4232–4234, 2011. doi: 10.1021/ic2003639.

[121] H. L. C. Feltham, R. Clérac, L. Ungur, L. F. Chibotaru, A. K. Powell, and S. Brooker. By Design: A Macrocyclic 3d-4f Single-Molecule Magnet with

Quantifiable Zero-Field Slow Relaxation of Magnetization. *Inorg. Chem.*, **52**: 3236–3240, 2013. doi: 10.1021/ic302735j.

[122] H. L. C. Feltham, S. Dhers, M. Rouzieres, R. Clérac, A. K. Powell, and S. Brooker. A family of fourteen soluble stable macrocyclic [$Ni_3^{II}Ln^{III}$] heterometallic 3d-4f complexes. *Inorg. Chem. Front.*, **2**:982–990, 2015. doi: 10.1039/c5qi00130g.

[123] F. J. Kettles, V. A. Milway, F. Tuna amd R. Valiente amd L. H. Thomas, W. Wernsdorfer, S. T. Ochsenbein, and M. Murrie. Exchange Interactions at the Origin of Slow Relaxation of the Magnetization in $TbCu_3$ and $DyCu_3$ Single-Molecule Magnets. *Inorg. Chem.*, **53**:8970–8978, 2014. doi: 10.1021/ic500885r.

[124] J. D. Rinehart and J. R. Long. Exploiting single-ion anisotropy in the design of f-element single-molecule magnets. *Chem. Sci.*, **2**:2078–2085, 2011. doi: 10.1039/c1sc00513h.

[125] D .N. Hendrickson, G. Christou, H. Ishimoto, J. Youu, E. K. Brechin, A. Yamaguchi, E. M. Rumberger, S. M. J. Aubin, Z. Sun, and G. Aromi. Molecular Nanomagnets. *Mol. Cryst. Liq. Cryst.*, **376**:301–313, 2002. doi: 10.1080/10587250210781.

[126] S. K. Ritter. Single-Molecule Magnets evolve. *Chemical & Engineering News*, **82**:29–32, 2004. doi: 10.1021/cen-v082n050.p029.

[127] W. Wernsdorfer and R. Sessoli. Quantum phase interference and parity effects in magnetic molecular clusters. *Science*, **284**:133–135, 1999. doi: 10.1126/science.284.5411.133.

[128] S. Khanra, B. Biswas, C. Golze, B. Büchner, V. Kataev, T. Weyhermüller, and P. Chaudhuri. A spin-frustrated star-shaped heterotetranuclear ($Cr^{III}Mn_3^{II}$) species and its magnetic and HF-EPR measurements. *Dalton Trans.*, **2007**: 481–487, 2007. doi: 10.1039/b613293f.

[129] O. Kahn. Competing spin interactions and degenerate frustration for discrete molecular species. *Chem. Phys. Lett.*, **265**:109–114, 1997. doi: 10.1016/S0009-2614(96)01424-8.

[130] J. Schnack, H. Nojiri, P. Körgeler, G. J. T. Cooper, and L. Cronin. Magnetic characterization of the frustrated three-leg ladder compound $[(CuCl_2tachH_3Cl]Cl_2$. *Phys. Rev. B*, **70**:174420, 2004. doi: 10.1103/PhysRevB.70.174420.

[131] Manuel Prinz. *X-ray spectroscopic and magnetic investigations of selected manganese-containing molecular high-spin complexes*. PhD Thesis, Universität Osnabrück, 2009. URL `https://repositorium.ub.uni-osnabrueck.de/handle/urn:nbn:de:gbv:700-2009071011`.

[132] M. Mannini, F. Pineider, P. Sainctavit, C. Danieli, E. Otero, C. Sciancalepore, A. M. Talarico, M.-A. Arrio, A. Cornia, D. Gatteschi, and R. Sessoli. Magnetic Memory of a Single-Molecule Quantum Magnet Wired to a Gold Surface. *Nat. Mater.*, **8**:194–197, 2009. doi: 10.1038/NMAT2374.

[133] M. Mannini, F. Pineider, C. Danieli, F. Totti, L. Sorace, , P. Sainctavit, M.-A. Arrio, E. Otero, J. Joly, J. C. Cezar, A. Cornia, and R. Sessoli. Quantum tunnelling of the magnetization in a monolayer of oriented single-molecule magnets. *Nature*, **468**:417–421, 2010. doi: 10.1038/nature09478.

[134] A. Takacs, M. Neumann, A. V. Postnikov, K. Kuepper, A. Scheurer, S. Sperner, R. W. Saalfrank, and K. C. Prince. Electronic structure study by means of x-ray spectroscopy and theoretical calculations of the "ferric star" single molecule magnet. *J. Chem. Phys.*, **124**:044503, 2006. doi: 10.1063/1.2155340.

[135] J.-P. Kappler, E. Otero, W. Li, L. Joly, G. Schmerber, B. Muller, F. Scheurer, F. Leduc, B. Gobaut, L. Poggini, G. Serrano, F. Choueikani, E. Lhotel, A. Cornia, R. Sessoli, M. Mannini, M.-A. Arrio, Ph. Sainctavit, and P. Ohresser. Ultralow-temperature device dedicated to soft X-ray magnetic circular dichroism experiments. *J. Synchrotron Rad.*, **25**:1727–1735, 2018. doi: 10.1107/S1600577518012717.

[136] J. Dvorak, I. Jarrige, V. Bisogni, S. Coburn, and W. Leonhardt. Towards 10 meV resolution: The design of an ultrahigh resolution soft X-ray RIXS spectrometer. *Rev. Sci. Instrum.*, **87**:115109, 2016. doi: 10.1063/1.4964847.

[137] A. Streun, T. Garvey, L. Rivkin, V. Schlott, T. Schmidt, P. Willmott, and A. Wrulich. SLS-2 – the upgrade of the Swiss Light Source. *J. Synchrotron Rad.*, **25**:631–641", 2018. doi: 10.1107/S1600577518002722.

[138] C. G. Schroer, I. Agapov, W. Brefeld, R. Brinkmann, Y.-C. Chae, H.-C. Chao, M. Eriksson, J. Keil, X. Nuel Gavaldà, R. Röhlsberger, O. H. Seeck, M. Sprung, M. Tischer, R. Wanzenberg, and E. Weckert. PETRA IV: the ultralow-emittance source project at DESY. *Journal of Synchrotron Radiation*, **25**:1277–1290, 2018. doi: 10.1107/S1600577518008858.

[139] A. Jankowiak, W. Anders, T. Atkinson, H. Ehmler, A. Föhlisch, P. Goslawski, K. Holldack, J. Knobloch, P. Kuske, D. Malyutin, A. Matveenko, R. Müller, A. Neumann, K. Ott, M. Ries, M. Ruprecht, A. Schälicke, A. Velez, and G. Wüstefeld. The BESSY VSR project for short X-ray pulse production. *Proceedings of IPAC2016, Busan, Korea*, pages 2833–2836, 2016.

[140] T. Tschentscher, C. Bressler, J. Grünert, A. Madsen, A. P. Mancuso, M. Meyer, A. Scherz, H. Sinn, and U. Zastrau. Photon beam transport and scientific instruments at the european xfel. *Appl. Sci.*, **7**:592, 2017. doi: 10.3390/app7060592.

List of articles included in this habilitation thesis

Chapter 1

[**H1**] M. Raekers, K. Kuepper, S. Bartkowski, A. V. Postnikov, M. Prinz, K. Potzger, S. Zhou, A. Arulraj, N. Stüßer, R. Uecker, W. L. Wang, and M. Neumann. *Electronic and magnetic structure of $RScO_3$ (R = Sm,Gd,Dy) from x-ray spectroscopies and first-principles calculations*, Phys. Rev. B **79**, 125114 (2009), doi: 10.1103/PhysRevB.79.125114.

[**H2**] C. Derks, K. Kuepper, M. Raekers, A. V. Postnikov, R, Uecker, W. L. Yang, and M. Neumann. *Band gap variation in RScO 3 (R=Pr, Nd, Sm, Eu, Gd, Tb, and Dy): X-ray absorption and O K-edge x-ray emission spectroscopies*, Phys. Rev. B **86**, 155124 (2012), doi: 10.1103/PhysRevB.86.155124.

[**H3**] K. Kuepper, M. Raekers, C. Taubitz, M. Uhlarz, C. Piamonteze, F. M. F. de Groot, E. Arenholz, V. R. Galakhov, Ya. M. Mukovskii, and M. Neumann. *The x-ray magnetic circular dichroism spin sum rule for $3d^4$ systems: Mn^{3+} ions in colossal magnetoresistance manganites*, J. Phys.: Condens. Matter **24**, 435602 (2012), doi: 10.1088/0953-8984/24/43/435602.

[**H4**] K. Kuepper, M. Raekers, C. Taubitz, M. Prinz, C. Derks, M. Neumann, A. V. Postnikov, F. M. F. deGroot, C. Piamonteze, D. Prabakharan and S. J. Blundell. *Charge order, enhanced orbital moment, and absence of magentic frustration in layered multiferroic $LuFe_2O_4$*, Phys. Rev. B **80**, 220409(R) (2009), doi: 10.1103/PhysRevB.80.220409.

Chapter 2

[**H5**] K. Kuepper, O. Kuschel, N. Pathé, T. Schemme, J. Schmalhorst, A. Thomas, E. Arenholz, M. Gorgoi, R. Ovsyannikov, S. Bartkowski, G. Reiss, and J. Wollschläger. *Electronic and magnetic structure of epitaxial NiO/Fe_3O_4 heterostructures grown on MgO(001) and Nb-doped $SrTiO_3$(001)*, Phys. Rev. B **94**, 024401 (2016), doi: 10.1103/PhysRevB.94.024401.

[**H6**] O. Kuschel, R. Buess, J. Wöllermann, K. Balinski, W. Spiess, T. Kuschel, A.T. N'Diaye, J. Wollschäger, and K. Kuepper. *From NiO/Fe_3O_4 bilayers to $NiFe_2O_4$-like thin films through interdiffusion*, Phys. Rev. B **94**, 094423 (2016), doi: 10.1103/PhysRevB.94.094423.

Chapter 3

[**H7**] L. Schneider, T. Rinkel, B. Voß, A. Chrobak, J. P. Klare, J. Neethling, J. Olivier, D. Schnaniel, E.-E. Bendeif, F. Bondino, E. Magnano, I. Píš. K. Balinski, J. Wollschläger, H.-J. Steinhoff, M. Haase, and K. Kuepper. *Characterization of multifunctional β-$NaEuF_4/NaGdF_4$ core-shell nanoparticles with narrow size distribution*, Nanoscale **8**, 2832 (2016), doi: 10.1039/c5nr06915g.

[**H8**] K. Kuepper, C. Derks, C. Taubitz, M. Prinz, L. Joly and J. P. Kappler, A. Postnikov, W. L. Yang, T. V. Kuznetsova, and P. Ziemann. *Electronic structure nd soft-X-ray-induced photoreduction studies of iron-based magnetic polyoxometalates of type$\{(M)M_5\}_{12}Fe_{30}^{III}$ (M=Mo^{VI}, W^{VI})*, Dalton Transactions **42**, 7924 (2013), doi: 10.1039/c3dt32759k.

[**H9**] S. Khanra, K. Kuepper, T. Weyermüller, M. Prinz, M. Raekers, S. Voget, A. V. Postnikov, F. M. F. De Groot, S. J. George, M. Coldea, M. Neumann, and P. Chaudhuri. *Star-Shaped molecule of $Mn(II)_4O_6$ Core with an St=10 High-Spin State: A Theoretical and Experimental Study with XPS, XMCD, and Other Magnetic Methods*, Inorg. Chem. **47**, 4605 (2008), doi: 10.1021/ic7023007.

[**H10**] M. Prinz, K. Kuepper, C. Taubitz, M. Raekers, B. Biswas, T. Weyhermüller, M. Uhlarz, J. Wosnitza, J. Schnack, A. V. Postnikov, C. Schröder, S. J. George, M. Neumann, and P. Chaudhuri. *A star-shaped heteronuclear $Cr^{III}Mn_3^{II}$ species and its electronic and magnetic structure: Spin frustration studied by XMCD,*

high field magnetic measurements and theoretical simulations, Inorg. Chem. **49**, 2093 (2010), doi: 10.1021/ic9012119.

[**H11**] K. Kuepper, C. Taubitz, D. Taubitz, U. Wiedwald, A. Scheurer, S. Sperner, R. W. Saalfrank, J. P. Kappler, L. Joly, and P. Ziemann. *Magnetic Ground State and Systematic X-ray Photoreduction Studies of an Iron-based Star-Shaped Complex*, J. Phys. Chem. Lett. **2**, 1491 (2011), doi: 10.1021/jz2005013.

[**H12**] K. Balinski, L. Schneider, J. Wöllermann, A. Buling, L Joly, C. Piamonteze, H. L. C. Feltham, S. Brooker, A. K. Powell, B. Delley, and K. Kuepper. *Element specific determination of the magnetic properties of two macrocyclic tetranuclear 3d-4f complexes with Cu_3Tb core by means of X-ray magnetic circular dichroism (XMCD)* , Phys. Chem. Chem. Phys. **20**, 21286-21293 (2018), doi: 10.1039/C7CP08689J.

Chapter 1

Publication H1

[**H1**] M. Raekers, K. Kuepper, S. Bartkowski, A. V. Postnikov, M. Prinz, K. Potzger, S. Zhou, A. Arulraj, N. Stüßer, R. Uecker, W. L. Wang, and M. Neumann. *Electronic and magnetic structure of $RScO_3$ (R = Sm,Gd,Dy) from x-ray spectroscopies and first-principles calculations*, Phys. Rev. B **79**, 125114 (2009), doi: 10.1103/PhysRevB.79.125114.

Electronic and magnetic structure of $R\mathrm{ScO_3}$ (R=Sm,Gd,Dy) from x-ray spectroscopies and first-principles calculations

M. Raekers,[1,*] K. Kuepper,[2,†] S. Bartkowski,[1] M. Prinz,[1] A. V. Postnikov,[3] K. Potzger,[2] S. Zhou,[2] A. Arulraj,[4] N. Stüßer,[4] R. Uecker,[5] W. L. Yang,[6] and M. Neumann[1,‡]

[1]*Department of Physics, University of Osnabrück, D-49069 Osnabrück, Germany*

[2]*Institute of Ion Beam Physics and Materials Research, Forschungszentrum Dresden-Rossendorf, P.O. Box 51 01 19, D-01314 Dresden, Germany*

[3]*Laboratoire de Physique des Milieux Denses, Unversité Paul Verlaine, 1 Boulevard Arago, F-57078 Metz, France*

[4]*Department of Magnetism, Hahn-Meitner-Institut, Berlin, Glienicker Strasse 100, 14109 Berlin, Germany*

[5]*Institute for Crystal Growth, Max-Born-Street 2, D-12489 Berlin, Germany*

[6]*Advanced Light Source, Lawrence Berkeley National Laboratory, Berkeley, California 94720, USA*

(Received 19 November 2008; revised manuscript received 28 January 2009; published 23 March 2009)

The electronic structures of $\mathrm{SmScO_3}$, $\mathrm{GdScO_3}$, and $\mathrm{DyScO_3}$ are investigated by means of x-ray photoelectron spectroscopy, x-ray emission spectroscopy (XES), and x-ray absorption spectroscopy (XAS). A strong hybridization between Sc 3*d* and O 2*p* is found, and a contribution of the rare-earth 5*d* states to this hybridization is not excluded. The band gaps of the compounds are determined by combining XES and XAS measurements. For $\mathrm{SmScO_3}$, $\mathrm{GdScO_3}$, and $\mathrm{DyScO_3}$ the band gaps were determined to be 5.6, 5.8, and 5.9 eV, respectively. Magnetization versus temperature measurements reveal antiferromagnetic coupling at 2.96 ($\mathrm{SmScO_3}$), 2.61 ($\mathrm{GdScO_3}$), and 3.10 K ($\mathrm{DyScO_3}$). For $\mathrm{DyScO_3}$ a Rietveld refinement of a 2 K neutron-diffraction data set gives the spin arrangement of Dy in the *Pbnm* structure (Shubnikov group: $Pb'n'm'$).

DOI: 10.1103/PhysRevB.79.125114 PACS number(s): 77.84.Bw, 32.30.Rj, 71.20.−b, 71.15.Mb

I. INTRODUCTION

Perovskites of the type RMO_3, where R^{3+} represents a trivalent rare-earth metal and M is a trivalent or mixed-valent transition-metal ion, exhibit an enormous variety of physical properties.[1] During the last decade the so-called manganites have attracted much attention due to their unusual magnetic transport phenomena resulting in the colossal magnetoresistance (CMR) effect.[2,3] These compounds are also promising candidates for various potential applications, e.g., for hard disk drive reading heads or in the rapidly growing field of magnetic random access memory (MRAM). On the other hand, ferroelectric perovskites such as $\mathrm{KTaO_3}$, $\mathrm{KNbO_3}$, $\mathrm{LiNbO_3}$, or $\mathrm{BaTiO_3}$ have been subjected to intense studies due to their unusual dielectric properties and the possibility to switch the electrical polarization.[4] This leads to the idea that information can be also stored using the electrical polarization state of a ferroelectric material (FeRAM).[5,6] A practical realization of such devices demands to prepare high quality thin films with thickness of the micron scale in order to operate switches at few volts whereas the coercive voltages in these materials are at the order of kV per centimeter. These materials may also be used in somewhat related applications mentioned above, such as the next-generation semiconductor components (to replace the $\mathrm{SiO_2}$ gate dielectric). With the continued scaling of the gate oxide to below 2 nm, leakage currents due to tunneling became very high. Therefore it is necessary to increase the thickness of the gate dielectrics without reduction in the associated capacitance. This can be achieved with materials which exhibit a high dielectric constant k. Lucovsky *et al.*[7] found that increases in k are generally accompanied by decreases in the optical band gap E_g, the conduction-band offset energy with respect to Si E_B, and the effective electron tunneling mass m_{eff}.[7] Hence the adjustment of the electronic band structure plays an important role in tuning the high-k materials.[7] In the last years a number of high-k compounds were observed.[8] The ternary oxide scandates $\mathrm{SmScO_3}$, $\mathrm{GdScO_3}$, and $\mathrm{DyScO_3}$ are promising candidates to serve as high-k dielectrics in future applications.[9,10] Furthermore these materials are utterly interesting substrates for the production of highly strained ferroelectric thin films. Thin ferroelectric films often show strong epitaxial strain effects, e.g., the change in critical temperatures, crystal structure, and thus ferroelectric properties as a consequence to the growth on a substrate with defects or different lattice parameters. These strains can deteriorate the required thin-film properties but also be used to control and optimize the desired ferroelectric properties if one finds a suitable high quality substrate. During the last few years the family of scandates such as $\mathrm{SmScO_3}$, $\mathrm{GdScO_3}$, or $\mathrm{DyScO_3}$ has bridged the gap of suitable substrates, thus widening the scope for strain tailoring of the films and allowing to explore experimentally some of the desired predictions and properties.[6,11–13] Very recently it has been shown that $\mathrm{SrTiO_3/DyScO_3}$ multilayers can be also used for modulation of the permittivity in terahertz range.[14]

Due to all the above-described experimental progress and potential applications, proper theoretical approaches to describe and predict the variety of properties in ferroelectric materials such as the scandates are highly desirable. Hence, these materials are subject to numerous first-principles studies for almost two decades now. Such calculations within density-functional theory (DFT) offer a very powerful possibility to describe the structural, magnetic, and electronic structures of ferroelectrics in deep detail. However, there are some known limitations and inaccuracies. In particular in presence of rare-earth 4*f* orbitals, the widely used local density approximation (LDA) and, to some extent, also the gen-

eralized gradient approximation (GGA) lead to a qualitatively incorrect description of the $4f$ energy placement. A related problem is that the structural properties, due to wrongly estimated localization of the $4f$ states, are often described improperly. There are a number of approaches in order to minimize or overcome these limitations. Some works include a Hubbard U parameter in order to consider the Coulomb repulsion between the highly localized $4f$ electrons. Some very recent works apply hybrid exchange functionals that combine fixed amounts of Hartree-Fock and LDA or GGA functionals to rare-earth oxides as CeO_2 or ferroelectric oxides such as $BaTiO_3$.[15,16]

Concerning the scandates, up to now only some electronic structure calculations for $DyScO_3$ have been reported.[17] From the experimental point of view only a few ultraviolet ellipsometry data, x-ray absorption spectroscopy (XAS) data, and a combination of internal photoemission and photoconductivity studies are available up to now.[7,18,19] However, in order to achieve a proper description of the electronic properties of rare-earth-based ferroelectric oxides (such as the scandates investigated here) a comparison with suitable experiments is of utmost importance. The techniques of x-ray photoelectron spectroscopy (XPS), XAS, and x-ray emission spectroscopy (XES) are powerful tools of unique precision in order to directly probe the total and partial densities of states (tDOS and pDOS, respectively) of ferroelectric materials.[20–22] Therefore we perform a detailed electronic structure investigation of $SmScO_3$, $GdScO_3$, and $DyScO_3$ by combining the complementary experimental techniques of XPS, XES, and XAS. We compare our experiments with first-principles electronic structure calculations. Furthermore we probe the magnetic structure of these samples by means of a superconducting quantum interference device (SQUID) and neutron powder diffraction.

II. EXPERIMENTAL AND THEORETICAL DETAILS

High quality $SmScO_3$, $GdScO_3$, and $DyScO_4$ single crystals were grown by the conventional Czochralski technique by Uecker *et al.*[23] The XAS and XES on these samples were performed at room temperature at beamline 8.0.1 at the Advanced Light Source, Berkeley, California, USA, using the soft x-ray fluorescence (SXF) end station of the University of Tennessee at Knoxville.[24] Linearly polarized light with polarization in the horizontal plane was incident on the sample whose surface was in the vertical plane. The emission was measured along the electric vector of the incident light in the horizontal plane, that is, at a scattering angle of 90°. This geometry minimizes diffuse elastic scattering from the surface since the Brewster angle in the soft x-ray range is usually very close to 45° so that the reflectivity for $\vec{p}$ light is very close to zero. The light was incident at 30° to the sample normal. Photons with an energy of 65–1400 eV were provided to the end station via a spherical 925 lines/mm grating monochromator. The rare-earth $4f \rightarrow 3d$, Sc $3d \rightarrow 2p$, and O $2p \rightarrow 1s$ XES were obtained with a 1500 lines/mm, 10-m-radius grating. The excitation energies for the x-ray emission (XE) spectra were set to 420.2 eV for the Sc $L_{2,3}$ edge and to 542.1 eV for the O K edge. The rare-earth $M_{4,5}$ edges were exited with 1141 (Sm), 1260 (Gd), and 1360 eV (Dy). Since the SXF detector cannot analyze photons with energies over 1000 eV, the latter spectra were recorded in second order of the spectrometer. The overall resolution of the beamline plus spectrometer was set to around 0.7 eV for the oxygen and scadium spectra and to around 1 eV for the rare-earth XES. The resolution can be obtained from the full width at half maximum (FWHM) of the corresponding elastic recombination peaks. Absorption was measured in total fluorescence yield with a channeltron. The entrance and exit slits were set to 40 μm resulting in an overall resolution of 0.4 eV.

The XPS valence bands (VBs) were recorded at the Department of Physics, University of Osnabrück, Germany, using a PHI 5600ci multitechnique spectrometer with monochromatic Al $K_\alpha = 1486.6$ eV radiation with FWHM $= 0.3$ eV. The overall resolution of the spectrometer is 1.5% of the pass energy of the analyzer; 0.45 eV in the present case. The spectra were calibrated using the line of adsorbed carbon (C $1s = 285.0$ eV) as a reference. Since $R\mathrm{ScO}_3$ ($R = \mathrm{Sm}, \mathrm{Gd}, \mathrm{Sc}$) are insulators the sample surfaces were neutralized with a constant electron current from a soft electron gun during the measurements in order to compensate charging effects. For clean surfaces the samples were cleaved and measured in ultrahigh vacuum ($\approx 10^{-9}$ mbar).

Magnetization versus temperature measurements have been performed by means of a superconducting quantum interference device (SQUID) [Quantum Design magnetic property measurement system (MPMS) XL] at the Institute for Ion Beam Physics and Materials Research, Forschungszentrum Rossendorf.

Neutron powder diffraction of the compound $DyScO_3$ taken in a cylindrical vanadium container (diameter of 8mm) was recorded with the focusing diffractometer E6 at the Berlin Neutron Scattering Center (BENSC). The E6 diffractometer is equipped with a horizontally and vertically bent monochromator consisting of 105 pyrolytic graphite crystals ($20 \times 20 \times 2$ mm^3) mounted on a 15×7 matrix leading to a relatively high flux at the sample position. The incident wavelength was 2.442 Å. The data were collected at 2 and 300 K. The integration of the Debye-Scherrer rings measured on a two-dimensional (2D) detector resulted in intensity versus scattering angle 2Θ for each temperature. Crystal (magnetic) structure was further analyzed by Rietveld refinements employing the program GSAS.[25] An absorption correction for the cylindrical sample was carried out using GSAS for which a wavelength-dependent coefficient of 1.138 was used. A smoothly varying background was defined by extrapolating a fixed number of background points.

The electronic structure calculations were performed with the (linearized) full-potential augmented plane wave method—see, e.g., Ref. 26—of the density-functional theory, as implemented in the WIEN2K code.[27] For the exchange-correlation potential, we used the generalized gradient approximation in the form of Perdew-Burke-Ernzerhof.[28,29] In order to describe the effects of intra-atomic correlation beyond the conventional LDA or GGA treatment, we have taken into account the spin-orbit interaction and orbital-dependent potential, notably LDA+U (Ref. 30) (or rather GGA+U in our case), specifically in the "LDA+U(SIC)"

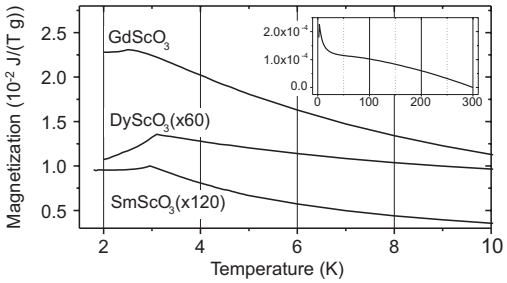

FIG. 1. *M-T* curves for $SmScO_3$, $GdScO_3$, and $DyScO_3$. The measurement was performed under an applied flux of $\mu_0 H=0.5$ T after cooling from 300 K in the same field. The magnification factor is indicated. The inset shows the high-temperature range for $DyScO_3$. The constant *M* offset at 300 K has been subtracted.

flavor of the WIEN2K implementation, with the correction added in the 4*f* shell of a rare earth. Even as the *U* and *J* values in the LDA+*U* formalism can be, in principle, estimated from first-principles calculations,[31] it is a more practical routine to use them as adjustable phenomenological parameters. In the present context, we were guided by the placement of occupied (majority-spin) *R* 4*f* states in the x-ray (photo)emission spectra, relative to other valence-band states. This sole criterion was, however, conflicting with the (experimentally founded) condition to have the band gap free from the minority-spin 4*f* states. In order to satisfy this second criterion, we preferred to use somehow elevated *U* values that resulted in a slightly overbonded majority-spin *R* 4*f* states. Our values of choice are $U=0.6$ Ry (8.2 eV) for Gd 4*f* and $U=0.8$ Ry (10.8 eV) for $SmScO_3$ and $DyScO_3$ as used in the following discussion (in part giving the reference to the results obtained with other *U* values as well). The *J* value was kept equal to 0.05 Ry (0.68 eV). The calculations were done in antiferromagnetic ordering which is explained in detail in Sec. III. These calculations are compared with experimental results of paramagnetic phase. In the comparison between the calculated tDOS and XPS results (Fig. 4) we present ferromagnetic calculations with $U=0.4$ Ry additionally to the antiferromagnetic calculation with $U=0.6$, 0.8 Ry. The rare-earth 4*f* states shift with the *U* value. The smaller *U* values give the right energy positions of occupied 4*f* states in the valence band but a too low (within the band gap) placement of their vacant counterparts. The nominal (as determined) crystal structure was used[32] (4 f.u./unit cell, all rare-earth positions being equivalent). The densities of states (DOSs) have been calculated with the *k* mesh $3\times2\times2$ over the Brillouin zone and have been smeared in the following figures for a more clear comparison with experimental spectra.

III. RESULTS AND DISCUSSION

A. Magnetic properties

First we want to discuss magnetic properties by means of magnetic measurements. Magnetization versus temperature SQUID measurements are presented in Fig. 1. We expected the materials $SmScO_3$, $GdScO_3$, and $DyScO_3$ to exhibit similar magnetic order such as the corresponding rare-earth (3+) oxides, i.e., antiferromagnetism at low Néel temperatures. E.g., for Dy_2O_3, this temperature is 1.2 K.[33] Note that discussions about the kind of magnetic ordering in $GdScO_3$ occurred in the past.[34] By our measurements basically the transition temperature of the substrates were obtained prior to neutron-diffraction measurement. The field-cooled *M-T* curves were measured at a field *H* determined by $\mu_0 H=0.5$ T. The field was applied parallel to the single crystal surface. Cusps typical for the onset of antiferromagnetic order occur at 2.96 ($SmScO_3$), 2.61 ($GdScO_3$), and 3.10 K ($DyScO_3$). While the former two substrates exhibit Brillouin-type behavior in the high-temperature range (not shown), the latter deviates significantly, exhibiting a large plateau (Fig. 1, inset). The peak for $GdScO_3$ is much broader than for the other samples. Moreover, $GdScO_3$ exhibits a much larger magnetization and thus behaves similar to Gd_2O_3.[34]

Exemplarily, $DyScO_3$ was investigated with respect to its microscopic magnetic structure by means of neutron diffraction. The room-temperature (300 K) data set could be indexed with an orthorhombic lattice with space group *Pbnm*. In the 2 K data set several peaks in addition to those present in the 300 K data were observed (Fig. 2). These peaks could be indexed with the propagation vector $k=0$ and are due to the antiferromagnetic arrangement of the spins of Dy in the low-temperature magnetic structure of $DyScO_3$. Of the four possible spin arrangements of the antiferromagnetic type only that with the magnetic group symmetry (Shubnikov groups: *Pbnm′* and *Pb′n′m′*) explains the presence of all the peaks of the 2 K data set. Symmetry analysis of the arrangement of the spin of Dy in the *Pbnm* structure of $DyScO_3$ indicates the following two possibilities. The first possibility is that the spin components of Dy belong to *G* mode with *y* component and *A* mode with *x* component (representation Γ_8) and in the second possibility *G* mode with *x* component and *A* mode with *y* component (representation Γ_5).[35] A Rietveld refinement of the 2 K neutron-diffraction data set gives a good fit only with the second possibility (Shubnikov group: *Pb′n′m′*). In Fig. 2 the crystal structure and the magnetic structure (spin arrangement) of $DyScO_3$ at 2 K are shown.

B. Calculated densities of states

Here we want to describe the calculated densities of states for three systems, obtained in true orthorhombic distorted perovskite structure (Fig. 3). Instead of the experimentally established noncollinear ferromagnetic structure depicted (for DyScO3) in Fig. 2, we considered its most straightforward collinear simplification, with spin moments of *R* centers set antiparallel between the nearest neighbors (both in the *ab* plane and along the *c* axis of Fig. 2). As the *R* magnetic moments are quite localized (and really negligible, below 0.01 μ_B, on Sc and O sites), the plotted partial DOS of the antiferromagnetic structure are practically indistinguishable from those in the ferromagnetic phase, which are used for comparison with room-temperature experiments.

It should be noted that we used the *U* value for the LDA+*U* calculation of 0.6 Ry for $GdScO_3$ and 0.8 Ry for $SmScO_3$ and $DyScO_3$. Its detailed tuning can be subjected to

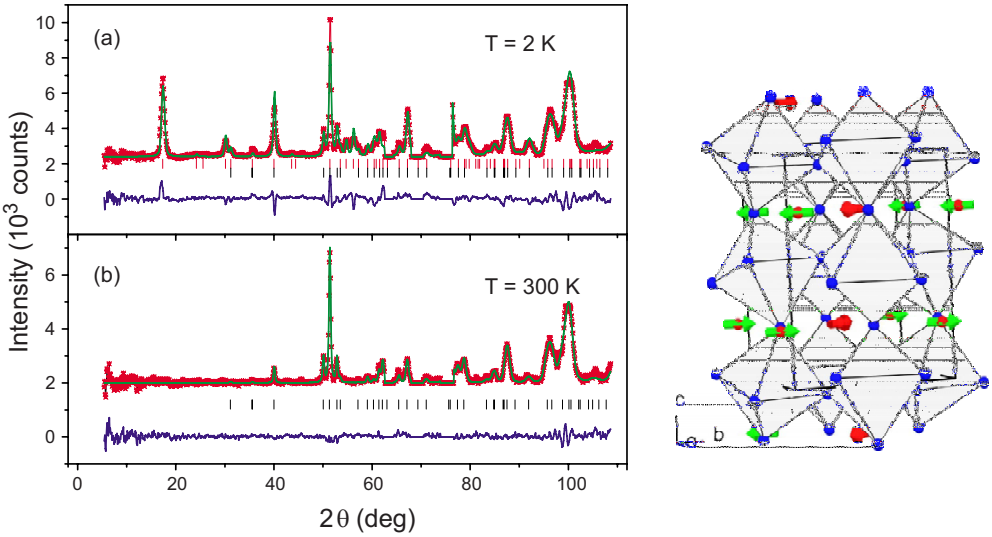

FIG. 2. (Color online) Neutron-diffraction and crystal (magnetic) structures of $DyScO_3$. Results of the Rietveld refinement of the (a) 2 and (b) 300 K neutron powder diffraction data of $DyScO_3$. The crystal and the magnetic structure (arrangement of arrows representing magnetic moments at Dy sites) is also shown.

careful analysis and argument. As stated above, we chose a compromise between the position of $R4f$ states in the valence band and the need to the band gap free of the $R4f$ states. Emphasizing a typically "semiempirical" character of the U values in practical calculations, we note that the examples are known where the U values have been evaluated over a range of rare-earth compounds. E.g., Larson *et al.*[36] cited a range of U values gradually varying from 7.47 (CeN) to 10.94 eV (LuN) in a row of rare-earth nitrides. Our values are close to those cited in Ref. 36, with a noticeable difference that we were primarily guided by the criteria named in Sec. II. Summarizing the results over different U, we note that the larger U values, understandably, move the (vacant) minority-spin $4f$ states out of the band gap, as desired.

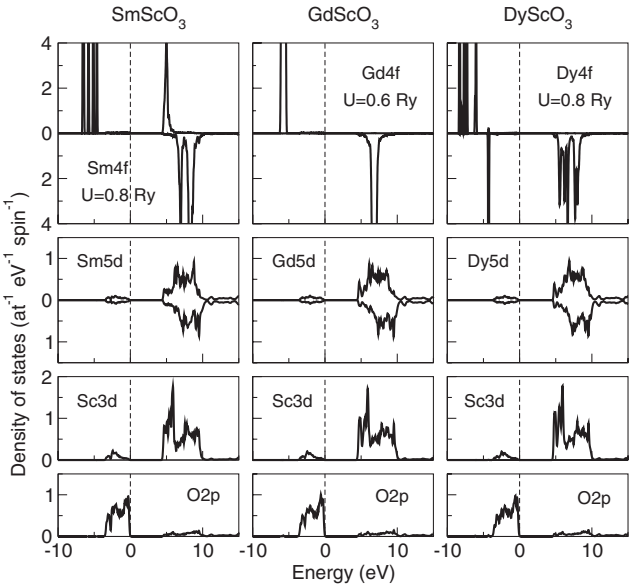

FIG. 3. Selected partial DOS in $SmScO_3$, $GdScO_3$, and $DyScO_3$. The zero of energy scale is set to the top of the valence band. For Sc $3d$ and O $2p$, only one component of spin-resolved DOS is shown, which is indistinguishable from the other. Sc site is nonmagnetic by symmetry. O $2p$ stands for a mean value (per atom) over four inequivalent oxygen sites.

However, this happens at the expense of lowering the majority-spin Dy $4f$ well below its experimentally expected position. This problem illustrates the shortcoming and crudeness of the LDA+U approach: with a single tunable parameter it is difficult to accommodate the correct placement of $4f$ states relative to the valence band involving other atoms, and an introduction of further tunable U parameters (e.g., for Sc $3d$ and O $2p$ states) would sacrifice physical transparence.

With this in mind, we note in Fig. 3 that occupied $R4f$ states are (intentionally) placed just below the valence band, which is formed predominantly by O $2p$, with a small admixture of $R5d$ and Sc $3d$ in the range between 0 and −3 eV. However, due to the orbital-dependent potential taken into account, the $4f$ peak remains narrow only for Gd (around −6 eV) with its half-filled shell, whereas for Sm (from −4.5 to −7 eV) and Dy (from −4.5 to −8.5 eV) it reveals a system of energy levels, yielding a non-negligible hybridization with the valence band (majority-spin states) and the conduction band (minority-spin states). Apart from the details of this hybridization, the Sc $3d$ partial DOS and the $R5d$ DOS are almost identical throughout the three compounds (occupied: from 0 to −4 eV; unoccupied: 4.5–10 eV). For the comparison with the experimental data (Figs. 4–6) the Fermi level is shifted by ~−2.5 eV into the band gap. That the experimental Fermi level lies in the calculated gap can be due to a very small amount of defects.

C. X-ray spectroscopic experiments and discussion

Next we want to discuss the XPS valence-band spectra of $SmScO_3$, $GdScO_3$, and $DyScO_3$ (Fig. 4). The experiments are compared with the results of *ab initio* band-structure calculations, namely, the total density of states from a GGA

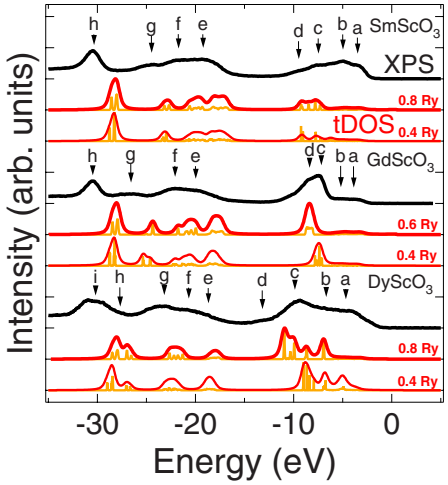

FIG. 4. (Color online) XPS valence bands (black thick lines) of $SmScO_3$ (top), $GdScO_3$ (middle), and $DyScO_3$ (bottom). The convoluted and weighted tDOS with different U values and the corresponding nonconvoluted tDOS are shown below the XPS. The calculations are shifted by −2.5 eV for comparison with experiment.

calculation which gives the best agreement with the experiment. The excitation (N-1 electrons) during the XPS process is not included in the calculations (N electrons). Hence the localized states at ~−30 and ~−20 eV in the calculations are located closer to the Fermi level than in the XPS measurement. Moreover, the multiplet effects are not included. The valence-band region is constituted by R 4f, 5p, 5d and Sc 3p, 3d, 4s and O 2p, 2s states. These states have different photoionization cross sections, which should be taken into account for weighting the corresponding DOS contributions to yield the simulated spectrum. Specifically, we took the relative photoionization cross-section values, corresponding to the excitation energy of 1486.6 eV, from Scofield.[37] The weights tabulated therein, which refer to each respective electronic shell as a whole, were normalized to a single electron and then multiplied with partial densities of states and with the number of atoms of each type in the unit cell, giving the calculated spectral intensity which is compared to the experiment. Then the calculated total density of states was convoluted with a 0.45 eV Gaussian and a 0.5 eV Lorentzian for experimental and lifetime broadening, respectively.

The valence-band region of $SmScO_3$ is composed of eight distinct features, a–h. Features a, b, and c at −3.5, −5.0, and −7.5 eV on the energy loss scale are followed by a shoulder d at −9.5 eV. The O 2p states are located from −3 to −5 eV, while the Sm 4f multiplet is found in features b, c, and d. The next group of features (e, f, and g) is located at −19.5, −21.5, and −24.5 eV. In this region the O 2s states take place around −23 eV and the Sm 5p multiplet reaches from −19 to −25 eV. At −30.5 eV feature h appears which corresponds to Sc 3p states. The experiment is very well reproduced by the calculation with U=0.4 Ry besides the intensities of Sm 4f multiplet features b, c, and d. For U =0.8 Ry the calculated Sm 4f states are less splitted and appear too far away from the Fermi level.

The XPS valence-band region of $GdScO_3$ also consists of eight features, a–h. The four features close to the Fermi level are a, b, c, and d at −4.0, −5.5, −7.5, and −8.5 eV. The O 2p states are located from −3 to −5.5 eV (a and b), while the Gd 4f states are relatively localized from −7.5 to −8.5 eV (c and d). Features e and f are located at −20.0 and −22.0 eV, followed by relatively small feature g at −26.5 eV. The O 2s states are at around −22 eV, and the Gd 5p multiplet reaches from −18 to −26 eV. Sc 3p feature h takes place at −30.5 eV. Features a–d close to the Fermi level are in very good agreement with both calculations. The intensities of features e and f are reversed in the calculation with respect to experiment, whereas the g and h features are reproduced well.

Finally the XPS valence-band $DyScO_3$ consists of nine features, a–i. Features a, b, and c are located at −4.5, −7.0, and −9.0 eV, followed by a shoulder at −13.0 eV (d). From −3 to −5 eV the O 2p states take place. The Dy 4f multiplet is comprised of features b, c, and d. Features e, f, and g take place at −18.5, −20.5, and −23.0 eV. O 2s states are located at around −22 eV. Sc 3p feature i at −30.5 eV has prepeak h at −27.5 eV. The Dy 5p multiplet reaches from −18.5 to −27.5 eV. The three features a, b, and c near the Fermi level are reproduced by the calculation with U=0.8 Ry a little bit too far away from the Fermi level, but the calculation with U=0.4 Ry is in perfect agreement. Multiplet feature d is missing in calculations. Features e, f, and g are calculated as two separated peaks. Feature i and prepeak h are in very good agreement with the calculation. In general the shape of the XPS measurement is reproduced by the calculations in a satisfactory way. However, there are some differences in detail. The comparison for $GdScO_3$ and $DyScO_3$ shows a difference at the group of features around −20 eV. The com-

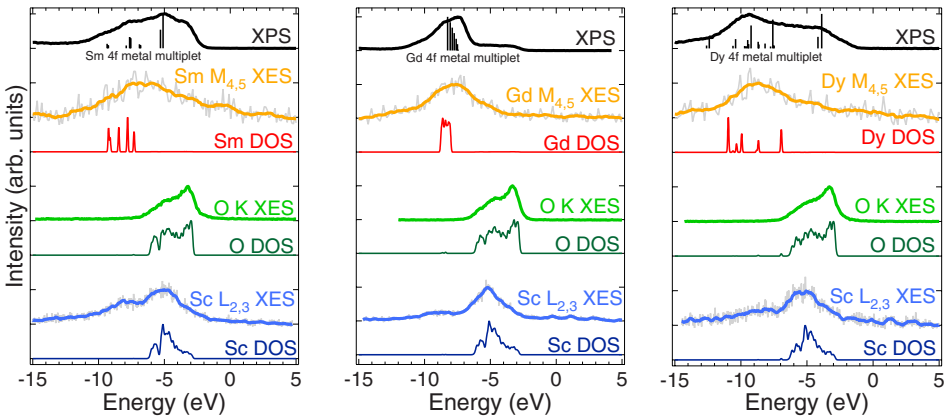

FIG. 5. (Color online) XPS valence bands and experimental R $M_{4,5}$, O K, and Sc $L_{2,3}$ XE spectra (thick lines). The corresponding calculated partial DOSs (thin lines) are also shown and are shifted by −2.5 eV for comparison with experiment. Calculations of R metals in the Russel-Saunders spin-orbit coupling scheme from Lang *et al.*[38] are plotted below the $RScO_3$ XPS spectra.

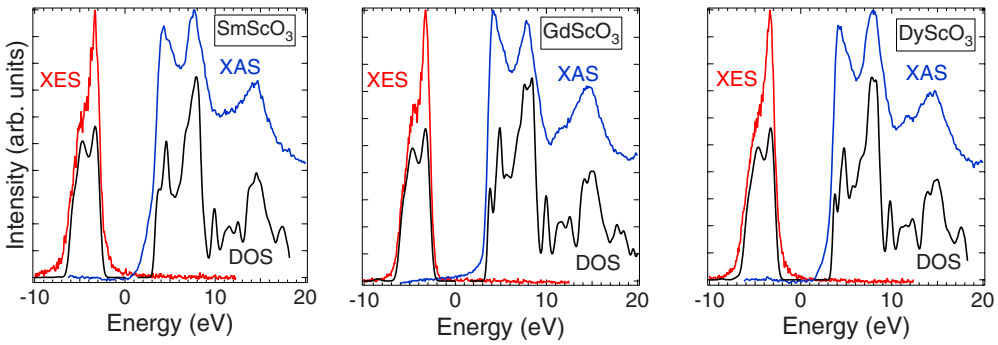

FIG. 6. (Color online) O*K* XAS (blue) and XES (red) of $SmScO_3$, $GdScO_3$, and $DyScO_3$. LDA+*U* calculations below experimental data were convoluted with 0.7 (XES) and 0.4 eV (XAS) Gaussian for experimental broadening. The calculated unoccupied states are shifted upwards by 1.4 eV for $SmScO_3$, 1.6 eV for $GdScO_3$, and 1.5 eV for $DyScO_3$.

parison of the states closer to the Fermi level reveals differences for $SmScO_3$ by rendering the rare-earth 4*f* multiplet in position and splitting. Also the $DyScO_3$ calculations with $U=0.8$ Ry show the 4*f* states shifted away from the Fermi level. The position of the rare-earth 4*f* states is influenced by the choice of the *U* parameter. Other differences arise from the fact that the calculations did not include multiplet effects which are more important for rare-earth atoms than for oxygen and scandium atoms.

Now we turn to a detailed comparison between XPS valence-band, XES, and pDOS of the calculations. In the left panel of Fig. 5 the XE spectra of Sm $M_{4,5}$, O *K*, and Sc $L_{2,3}$ are displayed with corresponding partial DOS from the GGA+*U* calculations. Below the XPS valence-band spectra of $RScO_3$, the rare-earth 4*f* multiplet calculations of Lang *et al.*[38] are plotted. These calculations are using the Russel-Saunders spin-orbit coupling scheme for comparison with XPS valence-band spectra of trivalent rare-earth metals. Comparable calculations were done by Gerken.[39] The XE spectra have been plotted on a common energy scale with the XPS valence band by using corresponding XPS core level binding energies for calibration (Sm 3*d*: 1109.5 eV; O 1*s*: 530.0 eV; and Sc 2*p*: 401.5 eV). The $M_{4,5}$ XE spectrum consists of Sm 4*f* features from −2 to −11 eV with a maximum at −6 eV. The calculated partial DOS has four features from −7 to −10 eV. This multiplet structure is better rendered by the multiplet calculation of trivalent Sm 4*f* states, which also shows the main peak at −5 eV.

The O *K* XE spectrum has two features at −3.0 and −5.0 eV. These features agree with the calculated O 2*p* states. The −5.0 eV feature is due to hybridization of O 2*p* and Sc 3*d* levels. The Sc $L_{2,3}$ XE spectrum is comprised of three features at −3.0, −5.0, and −8.0 eV. The −3.0 eV is due to the hybridization between O 2*p* and Sc 3*d*, and the −5 eV feature is the main feature of Sc 3*d* levels. The third feature at −8.0 eV is not covered by the calculation because it is due to the spin-orbit splitting of Sc 2*p* of ~4 eV. But this cannot completely explain the shape and energetic position of this feature. It is not clear if there is another feature due to an interaction between Sc and Sm which might be a *d* state coupling that was formerly found for complex oxides.[7,8,32]

Also the XE spectra of $GdScO_3$ are compared with the XPS valence-band and pDOS calculations (Fig. 5, middle panel). The calculation of trivalent Gd 4*f* multiplets from Lang *et al.*[38] is plotted below the XPS valence-band spectrum. XPS core level energies have been used to get a common energy scale (Gd 3*d*: 1189.5 eV; O 1*s*: 530.0 eV; and Sc 2*p*: 401.5 eV). The Gd $M_{4,5}$ XE spectra are comprised of an intense feature at −8.0 eV with a shoulder at −6.0 eV. The main feature is rendered by the band-structure calculation as Gd 4*f* states. This is also in comparison with the multiplet calculation of trivalent Gd 4*f* states. The O *K* XES has a O 2*p* main feature at −3.5 eV with a shoulder at −5.0 eV which is due to hybridization between O 2*p* and Sc 3*d*. The calculations show O 2*p* levels around −5 eV. The Sc $L_{2,3}$ XE spectrum consists of three features: a Sc 3*d* feature at −5.0 eV with a shoulder at −3.5 eV, which is due to hybridization between Sc 3*d* and O 2*p*, and a small shoulder from −7.5 to −10 eV which is due to spin-orbit splitting of the Sc 2*p*(~4 eV). As discussed before an interaction between Sc and Gd is possible but weaker than for $SmScO_3$. The calculation shows the Sc 3*d* features at −3.5 and −5.0 eV, but the feature around −9 eV is missing.

In the right panel of Fig. 5 the XES experiments of $DyScO_3$ are shown, along with the band-structure-calculated partial densities of states. The common energy scale is achieved by use of the XPS core level energies (Dy 3*d*: 1296.0 eV; O 1*s*: 530.0 eV; and Sc 2*p*: 401.5 eV). Multiplet calculations of trivalent Dy 4*f* states[38] are plotted below the XPS VB spectrum. The Dy $M_{4,5}$ XE spectra are comprised of four Dy 4*f* features at −5.0, −7.0, −9.0, and −13.0 eV. The three features from −5.0 to −9.0 eV are calculated with lower energy, and the feature at −13.0 eV is missing in the calculation which is due to not included multiplet effects. In the O *K* XE spectrum the O 2*p* main feature at −3.5 eV with a Sc 3*d* hybridization shoulder from −5.0 to −7.0 eV is in perfect agreement with the calculation. The Sc $L_{2,3}$ spectrum consists of a peak at −5.0 eV with a shoulder at −3.5 eV and a smaller peak at −8.0 eV. As discussed for the other samples the −8.0 eV peak is due to the spin-orbit splitting of Sc 2*p*. The interaction between Sc and Dy might be smaller than for $SmScO_3$ but larger than for $GdScO_3$. The calculation renders the peaks at −3.5 and −5.0 eV.

Apart from the appearance of *R* 4*f* states, the electronic structures of $SmScO_3$, $GdScO_3$, and $DyScO_3$ are very similar. The 4*f* levels, dominating the valence band, are located at −7.5 eV for Gd. For the Sm and the Dy compounds the

R 4*f* levels are more multiplet splitted in the range from −6 to −10 eV for Sm and from −5 to −9 eV for Dy. The band-structure calculations show some difference to the *R* 4*f* states due to multiplet splitting of 4*f* states. This is visible by comparing multiplet calculations for trivalent rare-earth 4*f* states with the experimental data.

The O and Sc states for which multiplet splitting is less important are in good agreement with the band-structure calculations. At around −5 eV there are O 2*p* states which are hybridized with Sc 3*d*. An interaction between Sc and *R* atoms might be present in the Sc $L_{2,3}$ XE spectra at around −8 eV. Such a hybridization was found for $DyScO_3$ and $GdScO_3$ by Lucovsky *et al.*[7] and for $AScO_3$ perovskite alloys by Halilov *et al.*[40]

Now we want to discuss the unoccupied states with help of O 1*s* x-ray absorption (XA) spectra and calculated O pDOS convoluted with a 0.4 eV Gaussian for experimental broadening (Fig. 6). The XA spectra are shifted by the binding energy of the O 1*s* XPS peak (530 eV) for comparison with the calculations. In the range of 1–20 eV unoccupied Sc 3*d* states and *R* 5*d* states hybridized via oxygen are present.[7] Three intense features are assigned to Sc 3*d* at 4 eV, Dy 5*d* at 14 eV, and a Sc *R* mixed *d* state at 7.5 eV. At 5 and 11 eV smaller features are visible which are due to splitting of the main features by an uniaxial crystal distortion.

Finally we want to determine the band gaps of the samples by combining the O 1*s* XA spectra and the O *K* XE spectra (Fig. 6). The DOS from the first-principles calculations is also shown for comparison. There are different methods in literature to obtain band gaps which are comparable with the method that is used here. Very similar is the approach made by Dong *et al.*,[41] where the onset of the O 1*s* XAS and O *K* edge XES peaks was taken to determine the band gap of ZnO. Another possibility is given by Hüfner *et al.*[42] where the band gap of NiO is determined between Fermi level of XPS and maximum of the first peak of a bremsstrahlung isochromat spectroscopy (BIS) spectrum. The advantages of XAS and XES compared with band-structure calculations are that a small density of states at the edge of the band gap are taken into account, the experiments are made under very similar conditions in a short time range, and the precise relative calibration of XAS and XES. A disadvantage is the element-specific band gap, but due to the delocalization of the O 2*p* electrons this method is applicable.

As the band gap is formed by rare-earth 4*f*, 5*d*, and scandium 3*d* states hybridized with O 2*p*, the LDA+*U* correction "naturally" increases the band gap, as is known from many *ab initio* studies of correlated oxides. The values of band gaps resulting from band-structure calculations should not be taken too seriously because of empirical adjustment of the *U* value. Still, it is comfortable, having proceeded from, primarily, the adjustment of the 4*f* peak positions in the XP spectra, to arrive at values for the band gaps which are in the range of the results from optical experiments. Also the shape of the calculations is in very good agreement with the shape of the XAS and XES experiments. This yields the conviction that the overall description of the underlying band structure is correct.

In Fig. 6 the band gap of the calculations is enlarged by shifting the unoccupied states (1.4 eV for $SmScO_3$, 1.6 eV for $GdScO_3$, and 1.5 eV for $DyScO_3$) to achieve perfect agreement with the XA spectra and the XE spectra. To determine the band gap in the experiment the highest occupied and the lowest unoccupied states of the enlarged calculations are used so one can overcome the too small band gap of the calculations. The calculated and experimental values are compared with ultraviolet absorption results,[18] ellipsometry measurements,[7,43] and a combination of internal photoemission and photoconductivity measurements[19] in Table I. The values determined by XAS and XES are slightly higher than the results from UV spectroscopy from Cicerella,[18] but the agreement with Lucovsky *et al.*[7] and Afanas'ev *et al.*[19] is very good. Ellipsometry measurements of Lim *et al.*[43] for $GdScO_3$ give higher results for the band gap than other methods, while the transmission spectrum in the same paper show the absorption onset below 6 eV, which is in agreement with the present results.

TABLE I. Band gaps of rare-earth scandates from this work (LDA+*U*; experiment) in comparison with values from literature.

	$SmScO_3$ (eV)	$GdScO_3$ (eV)	$DyScO_3$ (eV)
Cicerella (Ref. 18)	5.4	5.2	5.3
Lim *et al.* (Ref. 43)	5.5–6.0	6.5	
Afanas'ev *et al.* (Ref. 19)		5.6	5.7
Lucovsky *et al.* (Ref. 7)		5.8	
LDA+*U*	4.2	4.2	4.4
experiment	5.6	5.8	5.9

This partly different results can be understood if one takes into account the differences of the techniques and their interpretation. The band gap is defined as the energetic difference between the highest occupied and the lowest unoccupied level in the ground state. In experiments the initial state is usually the ground state, while the final state differs for various techniques. For XPS and XES the final state is a *N*-1 electron state where one electron has left the atom. During the XAS process the electron stays in the atom and the final state is a *N* electron state. A different charge of the final states in XPS and XAS processes implies a need to introduce a correction in order to permit a superposition of both in the common energy scale. The correction becomes larger the more "dense" the core states are. Consequently the difference (correction) is large in *R* 4*f* but negligible in O 2*p* (weak localization) and in Sc 3*d* (empty *d* shell), the states which essentially flank the band gap.

IV. CONCLUSIONS

In conclusion the electronic structure of $SmScO_3$, $GdScO_3$, and $DyScO_3$ is investigated with XPS, XAS, XES, and band-structure calculations (WIEN2K). Magnetism versus temperature measurements reveal antiferromagnetic coupling at 2.96 ($SmScO_3$), 2.61 ($GdScO_3$), and 3.10 K ($DyScO_3$). For $DyScO_3$ a Rietveld refinement of a 2 K neutron-diffraction data set gives a spin arrangement of Dy in the

Pbnm structure (Shubnikov group: *Pb′n′m′*). The XPS valence band is dominated by the *R* 4*f* multiplet structure corresponding to a trivalent state. XES measurements show that the oxygen 2*p* and Sc 3*d* levels are strongly hybridized. The rare-earth 5*d* states may contribute slightly to this hybridization. The band gaps of the compounds are determined by combining XES and XAS measurements. For $SmScO_3$, $GdScO_3$, and $DyScO_3$ the band gaps were 5.6, 5.8, and 5.9 eV, respectively.

ACKNOWLEDGMENTS

Part of this work has been performed at the Advanced Light Source (ALS), Lawrence Berkeley National Laboratory, Berkeley, USA, which is operated under Contract No. DE-AC03-76SF00098. M.R. gratefully acknowledges financial support from the GRK695: Nonlinearities of optical materials. Financial support by the Ph.D. program (Lower Saxony) is gratefully acknowledged by M.P.

*mraekers@uos.de

†Present address: University of Ulm, Institut für Festkörperphysik, Albert-Einstein-Allee 11, D-89069 Ulm, Germany. karsten.kuepper@uni-ulm.de

‡mneumann@uos.de

[1] S. Maekawa, T. Tohyama, S. E. Barnes, S. Ishihara, and W. K. Khaliullin, *Physics of Transition Metal Oxides* (Springer, Berlin, 2004).

[2] R. von Helmolt, J. Wecker, B. Holzapfel, L. Schultz, and K. Samwer, Phys. Rev. Lett. **71**, 2331 (1993).

[3] S. Jin, T. H. Tiefel, M. McCormack, R. A. Fastnacht, and R. R. H. Chen, Science **264**, 413 (1994).

[4] M. Dawber, K. M. Rabe, and J. F. Scott, Rev. Mod. Phys. **77**, 1083 (2005).

[5] H. Fu and R. E. Cohen, Nature (London) **403**, 281 (2000).

[6] K. J. Choi *et al.*, Science **306**, 1005 (2004).

[7] G. Lucovsky, J. G. Hong, C. C. Fulton, Y. Zou, R. J. Nemanich, H. Ade, D. G. Scholm, and J. L. Freeouf, Phys. Status Solidi B **241**, 2221 (2004).

[8] G. D. Wilk, R. M. Wallace, and J. M. Anthony, J. Appl. Phys. **89**, 5243 (2001).

[9] C. Zhao *et al.*, Appl. Phys. Lett. **86**, 132903 (2005).

[10] K. H. Kim, D. B. Farmer, J.-S. M. Lehn, P. Venkateswara Rao, and R. G. Gordon, Appl. Phys. Lett. **89**, 133512 (2006).

[11] J. Schubert, O. Trithaveesak, A. Petraru, C. L. Jia, R. Uecker, P. Reiche, and D. G. Schlom, Appl. Phys. Lett. **82**, 3460 (2003).

[12] J. H. Haeni *et al.*, Nature (London) **430**, 758 (2004).

[13] G. Catalan, A. Janssens, G. Rispens, S. Csiszar, O. Seeck, G. Rijnders, D. H. A. Blank, and B. Noheda, Phys. Rev. Lett. **96**, 127602 (2006).

[14] P. Kužel, F. Kadlec, J. Petzelt, J. Schubert, and G. Panaitov, Appl. Phys. Lett. **91**, 232911 (2007).

[15] J. L. F. Da Silva, M. V. Ganduglia-Pirovano, J. Sauer, V. Bayer, and G. Kresse, Phys. Rev. B **75**, 045121 (2007).

[16] D. I. Bilc, R. Orlando, R. Shaltaf, G.-M. Rignanese, J. Íñiguez, and P. Ghosez, Phys. Rev. B **77**, 165107 (2008).

[17] P. Delugas, V. Fiorentini, A. Filippetti, and G. Pourtois, Phys. Rev. B **75**, 115126 (2007).

[18] E. Cicerella, Ph.D. thesis, OGI School of Science & Engineering at Oregon Health & Science University, 2006.

[19] V. V. Afanas'ev, A. Stesmans, C. Zhao, M. Caymax, T. Heeg, J. Schubert, Y. Jia, D. G. Schlom, and G. Lucovsky, Appl. Phys. Lett. **85**, 5917 (2004).

[20] A. Moewes, A. V. Postnikov, B. Schneider, E. Z. Kurmaev, M. Matteucci, V. M. Cherkashenko, D. Hartmann, H. Hesse, and M. Neumann, Phys. Rev. B **60**, 4422 (1999).

[21] K. Kuepper, A. V. Postnikov, A. Moewes, B. Schneider, M. Matteucci, H. Hesse, and M. Neumann, J. Phys.: Condens. Matter **16**, 8213 (2004).

[22] K. Kuepper, B. Schneider, V. Caciuc, M. Neumann, A. V. Postnikov, A. Ruediger, A. A. Grabar, and Y. M. Vysochanskii, Phys. Rev. B **67**, 115101 (2003).

[23] R. Uecker, B. Velickov, D. Klimm, R. Bertam, M. Bernhagen, M. Rabe, M. Albrecht, R. Fornan, and D. G. Schlom, J. Cryst. Growth **310**, 2649 (2008).

[24] J. J. Jia *et al.*, Rev. Sci. Instrum. **66**, 1394 (1995).

[25] A. C. Larson and R. B. Von Dreele, *GSAS: General Structural Analysis System* (LANSCE, Los Alamos National Laboratory, Los Alamos, NM, 1994).

[26] D. J. Singh, *Planewaves, Pseudopotentials and the LAPW Method* (Kluwer Academic, Boston, 1994).

[27] P. Blaha, K. Schwarz, G. K. H. Madsen, D. Kvasnicka, and J. Luitz, *An Augmented Plane Wave + Local Orbitals Program for Calculating Crystal Properties* (Karlheinz Schwarz, Techn. Universität Wien, Austria, 2001).

[28] J. P. Perdew, K. Burke, and M. Ernzerhof, Phys. Rev. Lett. **77**, 3865 (1996).

[29] J. P. Perdew, K. Burke, and M. Ernzerhof, Phys. Rev. Lett. **78**, 1396 (1997) Erratum.

[30] V. I. Anisimov, F. Arysetiawan, and A. I. Lichtenstein, J. Phys.: Condens. Mat. **9**, 767 (1997).

[31] V. I. Anisimov and O. Gunnarsson, Phys. Rev. B **43**, 7570 (1991).

[32] R. P. Liferovich and R. H. Mitchell, J. Solid State Chem. **177**, 2188 (2004).

[33] H. Bonrath, K. H. Heliwege, K. Nicolay, and G. Weber, Phys. Kondens. Mater. **4**, 382 (1966).

[34] G. R. Stewart, J. A. Barclay, and W. A. Steyert, Solid State Commun. **29**, 17 (1979).

[35] E. F. Bertaut, Acta Crystallogr., Sect. A: Cryst. Phys., Diffr., Theor. Gen. Crystallogr. **24**, 217 (1968).

[36] P. Larson, W. R. L. Lambrecht, A. Chantis, and M. van Schilfgaarde, Phys. Rev. B **75**, 045114 (2007).

[37] J. H. Scofield, J. Electron Spectrosc. Relat. Phenom. **8**, 129 (1976).

[38] J. K. Lang, Y. Baer, and P. A. Cox, J. Phys. F: Met. Phys. **11**, 121 (1981).

[39] F. Gerken, J. Phys. F: Met. Phys. **13**, 703 (1983).

[40] S. V. Halilov, M. Fornari, and D. J. Singh, Phys. Rev. B **69**, 174107 (2004).

[41] C. L. Dong, C. Persson, L. Vayssieres, A. Augustsson, T. Schmitt, M. Mattesini, R. Ahuja, C. L. Chang, and J.-H. Guo, Phys. Rev. B **70**, 195325 (2004).
[42] S. Hüfner, P. Steiner, I. Sander, M. Neumann, and S. Witzel, Z. Phys. B: Condens. Matter **83**, 185 (1991).
[43] S.-G. Lim, S. Kriventsov, T. N. Jackson, J. H. Haeni, D. G. Schlom, A. M. Balbashov, R. Uecker, P. Reiche, J. L. Freeouf, and G. Lucovsky, J. Appl. Phys. **91**, 4500 (2002).

Publication H2

[**H2**] C. Derks, K. Kuepper, M. Raekers, A. V. Postnikov, R, Uecker, W. L. Yang, and M. Neumann. *Band gap variation in RScO 3 (R=Pr, Nd, Sm, Eu, Gd, Tb, and Dy): X-ray absorption and O K-edge x-ray emission spectroscopies*, Phys. Rev. B **86**, 155124 (2012), doi: 10.1103/PhysRevB.86.155124.

Band-gap variation in $R\mathrm{ScO_3}$ (R = Pr, Nd, Sm, Eu, Gd, Tb, and Dy): X-ray absorption and O K-edge x-ray emission spectroscopies

C. Derks,[1,*] K. Kuepper,[2,†] M. Raekers,[1] A. V. Postnikov,[3] R. Uecker,[4] W. L. Yang,[5] and M. Neumann[1]

[1]*Department of Physics, University of Osnabrück, D-49069 Osnabrück, Germany*

[2]*University of Ulm, Institut für Festkörperphysik, Albert-Einstein-Allee 11, D-89069 Ulm, Germany*

[3]*LCP-A2MC, Université de Lorraine, 1 Bd Arago, F-57078 Metz, France*

[4]*Institute for Crystal Growth, D-12489 Berlin, Germany*

[5]*Advanced Light Source, Lawrence Berkeley National Laboratory, Berkeley, California 94720, USA*

(Received 2 August 2012; published 12 October 2012)

The electronic structure of rare-earth scandates $R\mathrm{ScO_3}$ (R: newly studied Pr, Nd, Eu, and Tb, compared with previously studied Sm, Gd, and Dy) was analyzed by a combined use of O K absorption and emission spectroscopies and Sc L-edge absorption spectroscopy. This permitted the estimation of band gaps by use of a method that differed from optical measurements. The band-gap variation over the series in dependence on the rare-earth ion is analyzed, and a correlation between the Sc-O mean distance and the band gap is found and discussed.

DOI: 10.1103/PhysRevB.86.155124 PACS number(s): 77.84.Bw, 32.30.Rj, 71.20.−b

I. INTRODUCTION

Transition-metal-based perovskites exhibit a vast variety of unique physical characteristics, e.g., transport properties. Among the best known examples of such systems are cuprates with their high-temperature superconductivity),[1] manganites (colossal magneto resistance),[2] or cobaltates (displaying rich magnetic phase diagrams and high-spin to low-spin transitions).[3] More recently, superconducting iron pnictides[4] and multiferroic perovskites like $\mathrm{BiFeO_3}$ (showing ferromagnetic and ferroelectric ordering phenomena)[5] have attracted much attention. On the other hand, dielectric and ferroelectric "d^0-perovskites" like $\mathrm{BaTiO_3}$, $\mathrm{LaTiO_3}$, or $\mathrm{SrTiO_3}$ are subject to intense research activities due to their remarkable dielectric properties and the possibility to control the electrical polarization, which is a required prerequisite for constructing a ferroelectric memory (FeRAM).[6] Studying these materials has significantly changed, within the past three decades, our fundamental understanding of electron correlation effects. Basically, transition-metal oxides can be classified into two type of insulators: Mott-Hubbard insulators (whose band gap is ruled by the repulsive potential U_{dd} between the 3d electrons) and charge-transfer insulators, in which the energy between the filled ligand p bands and the unoccupied upper 3d states (Δ_{pd}) dominates the band gap.[7] In this relation, two issues of interest may be outlined: (i) by analyzing detailed trends in the band-gap variation, try to learn more about the nature of correlation in the material(s) in question, and (ii) use the detected trends to tailor the optical band gap in wide-gap oxidic insulators to desired values for possible applications, e.g., as a high-k gate dielectric or a transparent conducting oxide.[8] Among a number of other wide-gap oxides, the scandates of type $R\mathrm{ScO_3}$ (R = Pr, Nd, Sm, Eu, Gd, Tb, and Dy) are particularly promising candidates for replacing $\mathrm{SiO_2}$ as the gate dielectric;[9–12] moreover, they can be used as a model system for applications in the terahertz regime.[13] Furthermore, these scandium-based pervovskites belong to the best available thin-film substrates for the epitaxial growth of high-quality thin films. This allows a so-called strain tailoring of ferroelectric, ferromagnetic, or multiferroic perovskite thin films by choosing different $R\mathrm{ScO_3}$,[14–17] including a prediction of the band-gap reduction at the interface of $\mathrm{DyScO_3}$ and $\mathrm{SrTiO_3}$.[18] A sophisticated description of the electronic structure is of utmost importance to understand complex properties of $R\mathrm{ScO_3}$ itself and its interaction to other materials. However, only a limited knowledge about their electronic structure has been available until now. Delugas *et al.*[12] performed *ab initio* investigations on $\mathrm{DyScO_3}$, and Lucovsky *et al.*[10] published some oxygen x-ray absorption spectra. Raekers *et al.* published a work on the electronic structure of $\mathrm{SmScO_3}$, $\mathrm{GdScO_3}$, and $\mathrm{DyScO_3}$.[19] To our knowledge, this was the only work so far which combined x-ray spectroscopic techniques with *ab initio* electronic structure calculations. In the present work, our aim is to extend the electronic structure studies on the $R\mathrm{ScO_3}$ series onto further rare-earth scandates, namely $\mathrm{PrScO_3}$, $\mathrm{NdScO_3}$, $\mathrm{EuScO_3}$, and $\mathrm{TbScO_3}$. We focus on discussing the variation of the optical band gap in dependence of the rare-earth ion R in these charge-transfer compounds.

II. EXPERIMENTAL AND THEORETICAL DETAILS

High-quality $R\mathrm{ScO_3}$ (R = Pr, Nd, Sm, Eu, Gd, Tb, and Dy) bulk single crystals have been grown from the melt by the conventional Czochralski technique because of their congruent melting behavior.[14,20] Due to their exceptionally high melting temperature (>2000 °C) and the occurrence of spiral formation, these crystals required very carefully adjusted growth conditions. Thus, bulk crystals 18–33 mm in diameter and about 50 mm in length were obtained in high perfection [e.g., the rocking curve mapping of the 220 reflection of a square 0.5-inch $\mathrm{DyScO_3}$ wafer showed an average full width at half maximum (FWHM) of 20 arcsec].

The x-ray absorption spectroscopy (XAS) and x-ray emission spectroscopy (XES) experiments on these samples were performed at room temperature at beamline 8.0.1 at the Advanced Light source (Berkeley, California, USA), using the soft x-ray fluorescence (SXF) end station of the University of Tennessee at Knoxville.[21] Linearly polarized light with horizontal plane was incident on the sample, whose surface was in the vertical plane. The emission was measured along the electric vector of the incident light in the horizontal plane,

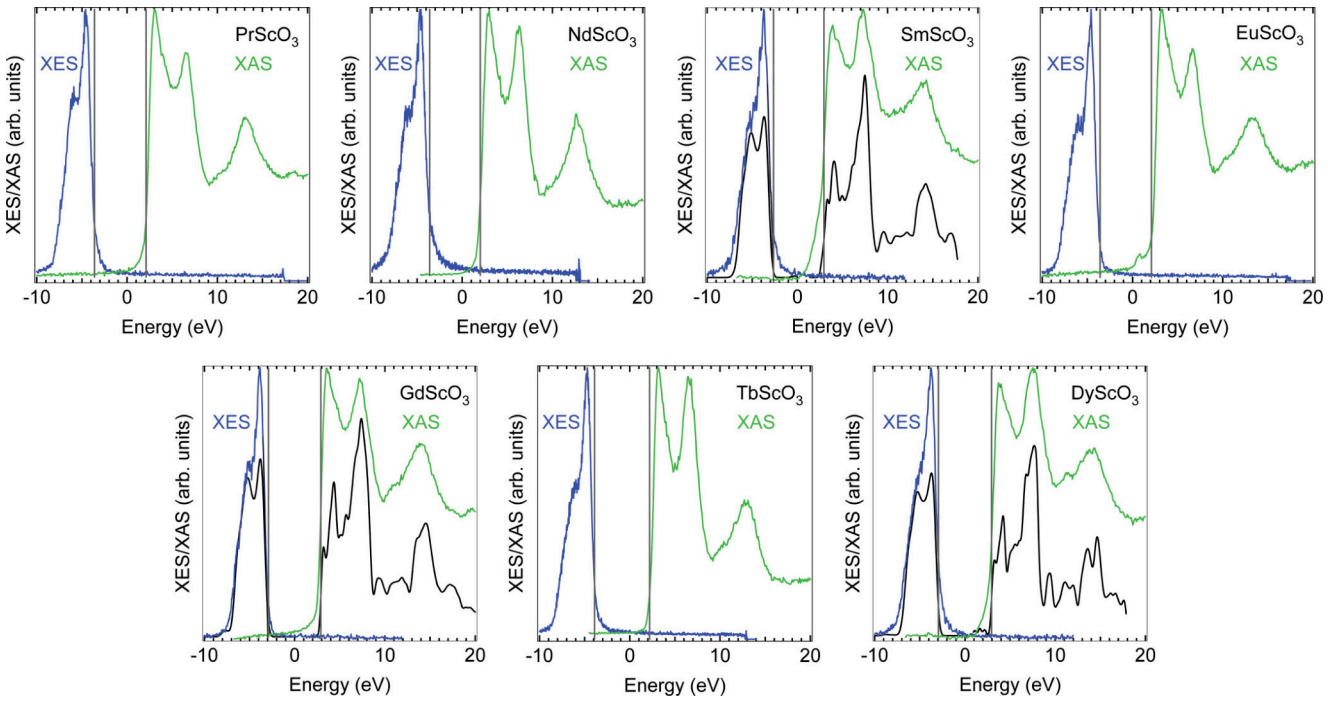

FIG. 1. (Color online) O K XAS (green) and XES (blue) of $PrScO_3$, $NdScO_3$, $SmScO_3$, $EuScO_3$, $GdScO_3$, $TbScO_3$, and $DyScO_3$. LDA + U calculations (black) below experimental data were convoluted with 0.7 (XES) and 0.4 eV (XAS) Gaussian for experimental broadening. The calculated unoccupied states are shifted upward by 1.4 eV for $SmScO_3$, 1.6 eV for $GdScO_3$, and 1.5 eV for $DyScO_3$.

that is, at a scattering angle of 90°. This geometry minimizes diffuse elastic scattering from the surface, since the Brewster angle in the soft x-ray range is usually very close to 45°, so the reflectivity for p light is very close to zero. The light was incident at 30° to the sample normal. Photons with the energy of 65 to 1400 eV were provided to the end station via a spherical 925 lines/mm grating monochromator. X-ray absorption at the Sc $L_{2,3}$ and O K edges was measured in total fluorescence yield with a channeltron. The entrance and exit slits of the spherical grating monochromator were both set to 40 μm, resulting in an overall resolution of 0.4 eV. The O $2p \rightarrow 1s$ x-ray emission spectra were obtained with a 1500 lines/mm, 10-m radius grating. The excitation energies for the x-ray emission spectra were set to 539.6 eV for the O K edge, which corresponds to the first XAS minimum after the two main peaks. The overall "beamline-plus-spectrometer" resolution was estimated to be of about 0.7 eV for the oxygen spectra. The resolution can be obtained from the width of the corresponding elastic recombination peaks at FWHM.

III. RESULTS AND DISCUSSION

Figure 1 shows the O K XAS and x-ray emission spectra for all compounds, whereby the spectra of $SmScO_3$, $GdScO_3$, and $DyScO_3$ have been extracted from Raekers *et al.*[19] The O K x-ray absorption spectra were shifted by the binding energy of the O 1s XPS peak (530 eV) in order to enable an easier comparison of the results. The corresponding O K x-ray emission were shifted by an equal amount on the energy scale. To get the band gaps without resorting to new first-principles calculations, we extrapolated the theoretical highest occupied and lowest unoccupied states by lines in the spectra of $SmScO_3$, $GdScO_3$, and $DyScO_3$.[19] This was done because the measurements show some states near the band gap which in fact stem from defects. The slope of these lines was used to get the band gaps of the other four samples, which were all measured under equivalent conditions. More details of this specific procedure can be found at Raekers *et al.*.[19] By using these lines in combination with the measurements, we got the band gaps listed in Table I without

TABLE I. Band gaps of rare-earth scandates (in eV) as found in the present work (the upper line) in comparison with previously reported values. Since we applied the identical equivalent experimental conditions, the relative error bars are ±0.1–0.2 eV; the absolute error could be larger.

	$PrScO_3$	$NdScO_3$	$SmScO_3$	$EuScO_3$	$GdScO_3$	$TbScO_3$	$DyScO_3$
Experiment	5.7	5.6	5.6	5.7	5.8	6.1	5.9
Cicerrella[22]	5.7	5.5	5.4		5.2	5.6	5.3
Lim *et al.*[9]			5.5–6.0		6.5		
Afanas'ev *et al.*[23]					5.6		5.7
Lucovsky *et al.*[10]					5.8		

considering the states which are induced by crystal defects. They are in good agreement with band gaps which were determined by other methods, like ellipsometry,[9,10] ultraviolet absorption,[22] or a combination of internal photoemission and photoconductivity.[23] The applied combination of x-ray absorption spectroscopy and x-ray emission spectroscopy at the O K edge leads to good approximations for wide-gap charge-transfer insulators, since a relatively weak density of states close to the highest occupied states and/or the lowest unoccupied can be probed with a relatively precise calibration of the spectra.

To further confirm the nature of charge order, we plotted the Sc L_α and the O K_α x-ray emission spectra of SmScO$_3$, GdScO$_3$, and DyScO$_3$ in Fig. 2, calibrated to the binding energy scale (adapted from Ref. 19). The O K x-ray emission spectra reflect wide O $2p$ bands for these compounds. The shoulders of the Sc L_α x-ray emission spectroscopy and O K x-ray emission spectroscopy are aligned with the main peaks of the O K and Sc L_α, respectively. This indicates strong $3d$-$2p$ hybridization, the highest occupied states being dominated by occupied O $2p$, similar to recently reported results on ZnF$_2$[24] or on late transition-metal dicyanamides.[25] On the other side, the lowest unoccupied states are ruled by unoccupied Sc $3d$ hybridized with empty O $2p$, as discussed in some previous works.[10,19]

Moreover, structural differences may be a potential reason for the observed band-gap variation, since the Δ_{pd} value substantially depends on the metal-oxygen-metal (M−O−M) angle, which is, in turn, closely related to the size of the rare-earth ion R.[26] A larger rare-earth ion in general leads to a lower tolerance factor (also called Goldschmidt factor) and, hence, to an increasing deviation from the ideal 180° M−O−M bond angle. This decreases the p-d electron hopping, usually resulting in a larger band gap. In Fig. 4 we present a number of structural parameters of RScO$_3$ extracted from Liferovich *et al.*[27] along with a plot of the experimentally determined band gaps.

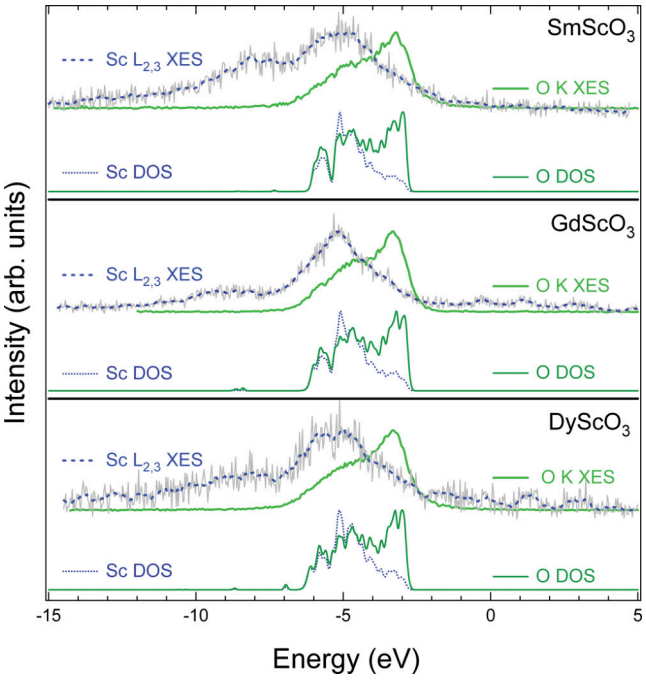

FIG. 2. (Color online) Experimental O K (blue) and Sc $L_{2,3}$ (green) XES spectra of SmScO$_3$, GdSco$_3$, and DyScO$_3$ (extracted from Raekers *et al.*[19]).

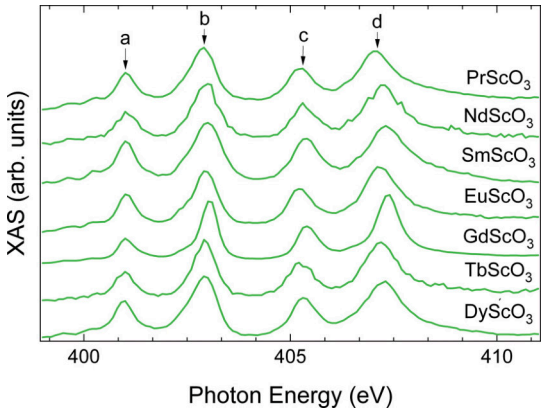

FIG. 3. (Color online) Sc $L_{2,3}$ XAS spectra of RScO$_3$.

The electronic structure of the systems in question is, in a nutshell, that of "conventional," "ionic" perovskite-type oxides: The formal valences are compensated $R^{3+}Sc^{3+}O_3^{2-}$, so the Sc $3d$ and R $5d$ states form the conduction bands and O $2p$—the valence band. In reality (as typical for many perovskites), the bonding is partially covalent, so a non-negligible, albeit small, admixture of O $2p$ can be established in the conduction band, and that of Sc $3d$—in the valence band. This is evidenced by first-principles calculations (see also Fig. 6 of Raekers *et al.*[19]) and by the present experimental outcome.

We enter now a somehow more detailed discussion of the band-gap changes summarized in Table I. Figure 3 shows the Sc $L_{2,3}$ x-ray absorption spectra of all RScO$_3$ crystals. The spectra consist of four main peaks labeled a–d. Peaks a and b are the main features of the L_3 edge, whereas the L_2 edge comprises peaks c and d. The main features of all spectra are quite similar between themselves and to those of the related compound LaScO$_3$.[28] The peaks a and c can be related to dipole allowed transitions into the unoccupied Sc $3d$ t_{2g}-like states; the peaks b and d represent the empty e_g-like states. However, we want to note that the energy splitting between peaks a and b (c and d) does not, in general, not even for d^0 systems, correspond directly to the crystal field parameter $10Dq$,[29] even if the latter is somehow involved in this interplay. The energy splitting measured between peaks a and b (c and d) as well as

TABLE II. Measured interpeak distances (in eV ± 0.2 eV) in the Sc $L_{2,3}$ XAS spectra of Fig. 3.

	a–b	c–d	a–c	b–d
PrScO$_3$	1.9	1.8	4.3	4.2
NdScO$_3$	2.0	1.9	4.3	4.2
SmScO$_3$	2.0	1.9	4.4	4.3
EuScO$_3$	1.9	1.9	4.2	4.2
GdScO$_3$	2.0	2.0	4.4	4.4
TbScO$_3$	1.9	2.0	4.2	4.3
DyScO$_3$	1.9	2.0	4.3	4.4

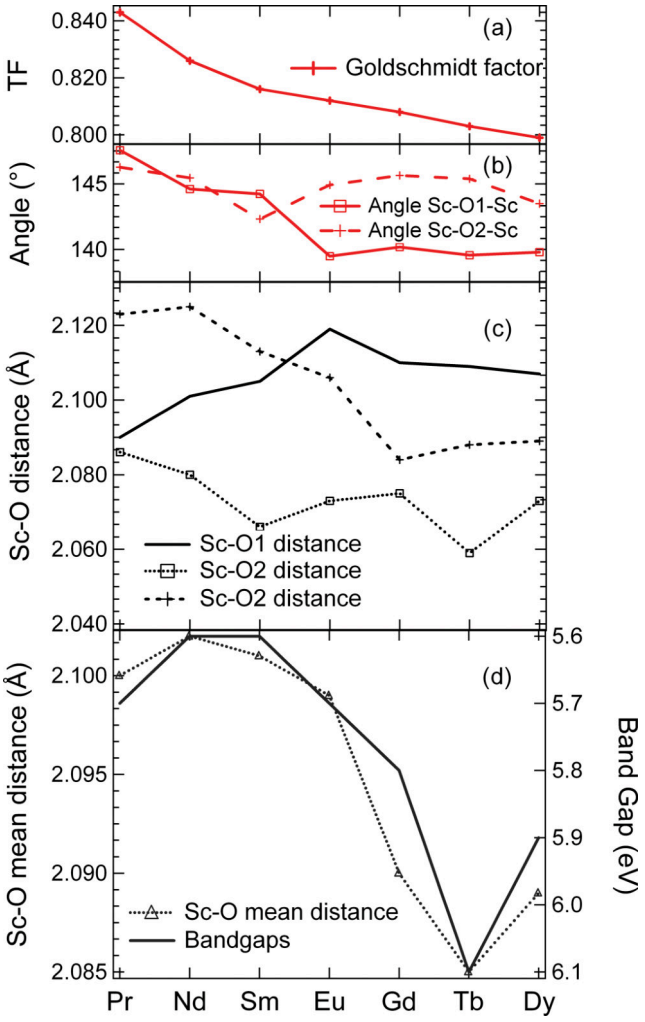

FIG. 4. (Color online) (a) Tolerance factor (Goldschmidt factor) for $R\mathrm{ScO_3}$, (b) Sc−O−Sc bond angles of $R\mathrm{ScO_3}$, (c) distances between Sc and the two oxygen spectra, and (d) Sc−O mean distance and experimental band gaps. All structural parameters have been extracted from Liferovich *et al.*.[27]

between peaks a and c (b and d) are summed up in Table II. No major differences within the experimental resolution are found, indicating a quite similar local crystal field environment of the $\mathrm{ScO_6}$ octahedra in all the $R\mathrm{ScO_3}$ crystals. Therefore, the changes in local symmetry or crystal field strength are not likely to be the reason for the observed changes of the optical band gap. Besides the tolerance factor [Fig. 4(a)] and the Sc−O−Sc bond angles [Fig. 4(b)], we also show the distances between Sc and the two oxygen sites, $\mathrm{O_1}$ and $\mathrm{O_2}$, respectively [Fig. 4(c)]. At this point we want to mention that the trend of the most basic structural parameter of the lattice constant (a and/or c or unit cell volume), is monotonically decreasing.[27] Finally, the Sc−O mean distance is also shown [Fig. 4(d)]. Interestingly, the investigated variation of the band gap does not correlate with the Sc−O−Sc bond angle for $R\mathrm{ScO_3}$. On the other hand, a clear correlation between the band gap and the Sc−O mean distance can be qualitatively established. For a simple discussion of this finding, two aspects are important: (i) the "native" Sc $3d$ states are not partially occupied, so no Jahn–Teller effect comes about to induce the distortion of the $\mathrm{ScO_6}$ octahedra; (ii) the R $4f$ states are split much larger than the band gap and do not "contaminate" the edges of the latter. The band gap is, therefore, primarily influenced by the strength of the O $2p$–Sc $3d$ interaction that moves the barycenters of the valence band and the conduction bands apart, from which, further, the (half-) width of each of these bands must be subtracted. As it seems, the band widths are not markedly dependent on structure parameters of individual compounds, whereas the band gap (revealing, as it seems, the strength of O $2p$–Sc $3d$ interaction) inversely follows a nontrivial variation of the mean Sc−O distance, as R changes; see Fig. 4. A remarkable observation is that the variations of bond length of $\pm 0.4\%$ give rise to "amplified" band-gap variations of $\pm 4.2\%$.

Apparently, the real trend is much richer in details, because the deformation of $\mathrm{ScO_6}$ octahedra is accompanied by non-negligible variations of Sc−O−Sc bond lengths (see Fig. 4). However, the latter do not fall onto any noticeable trend in the electronic structure. Also, as mentioned before, no obvious correlation exists with the size of the R ion.

IV. CONCLUSIONS

The band gaps determined by x-ray absorption spectroscopy and x-ray emission spectroscopy give data which are in good agreement with different results from the literature. The $\mathrm{GdFeO_3}$-like distortion of the perovskite structure plays a key role in the formation of the band gap, because the Sc−O distances are influenced by the distortion. Our unusual finding that relative variations of bond length along the row result in tenfold amplified variations of the band-gap values will hopefully stimulate additional theory efforts on this class of materials.

ACKNOWLEDGMENTS

Part of this work was performed at the Advanced Light Source (ALS), Lawrence Berkeley National Laboratory, Berkeley, USA, which is operated under Contract No. DE-AC03-76SF00098. M.R. and C.D. gratefully acknowledges financial support from the GRK695: Nonlinearities of optical materials. K.K. thanks SFB 569 for financial support.

*cderks@uos.de
†kkuepper@uos.de; present address: Department of Physics, University of Osnabrück, D-49069 Osnabrück, Germany

[1] E. Dagotto, Rev. Mod. Phys. **66**, 763 (1994).
[2] A. P. Ramirez, J. Phys.: Condens. Matter **9**, 8171 (1997).
[3] M. A. Korotin, S. Y. Ezhov, I. V. Solovyev, V. I. Anisimov, D. I. Khomskii, and G. A. Sawatzky, Phys. Rev. B **54**, 5309 (1996).
[4] D. C. Johnston, Adv. Phys. **59**, 803 (2010).
[5] S.-W. Cheong and M. Mostovoy, Nat. Mater. **6**, 13 (2007).
[6] M. Dawber, K. M. Rabe, and J. F. Scott, Rev. Mod. Phys. **77**, 1083 (2005).

[7]J. Zaanen, G. A. Sawatzky, and J. W. Allen, Phys. Rev. Lett. **55**, 418 (1985).
[8]W. S. Choi, M. F. Chisholm, D. J. Singh, T. Choi, G. E. Jellison, and H. N. Lee, Nat. Commun. **3**, 689 (2012).
[9]S.-G. Lim, S. Kriventsov, T. N. Jackson, J. H. Haeni, D. G. Schlom, A. M. Balbashov, R. Uecker, P. Reiche, J. L. Freeouf, and G. Lucovsky, J. Appl. Phys. **91**, 4500 (2002).
[10]G. Lucovsky, J. G. Hong, C. C. Fulton, Y. Zou, R. J. Nemanich, H. Ade, D. G. Scholm, and J. L. Freeouf, Phys. Status Solidi B **241**, 2221 (2004).
[11]H. M. Christen, G. E. Jellison, I. Ohkubo, S. Huang, M. E. Reeves, E. Cicerrella, J. L. Freeouf, Y. Jia, and D. G. Schlom, Appl. Phys. Lett. **88**, 262906 (2006).
[12]P. Delugas, V. Fiorentini, A. Filippetti, and G. Pourtois, Phys. Rev. B **75**, 115126 (2007).
[13]P. Kužel, F. Kadlec, J. Petzelt, J. Schubert, and G. Panaitov, Appl. Phys. Lett. **91**, 232911 (2007).
[14]R. Uecker, B. Velickov, D. Klimm, R. Bertam, M. Bernhagen, M. Rabe, M. Albrecht, R. Fornan, and D. G. Schlom, J. Crystal Growth **310**, 2649 (2008).
[15]K. J. Choi, M. Biegalski, Y. L. Li, A. Sharan, J. Schubert, R. Uecker, P. Reiche, Y. B. Chen, X. Q. Pan, V. Gopalan, L.-Q. Chen *et al.*, Science **306**, 1005 (2004).
[16]J. H. Haeni, P. Irvin, W. Chang, R. Uecker, P. Reiche, Y. L. Li, S. Choudhury, W. Tian, M. E. Hawley, B. Craigo, A. K. Tagantsev *et al.*, Nature (London) **430**, 758 (2004).
[17]G. D. Wilk, R. M. Wallace, and J. M. Anthony, J. Appl. Phys. **89**, 5243 (2001).
[18]K. Rahmanizadeh, G. Bihlmayer, M. Luysberg, and S. Blügel, Phys. Rev. B **85**, 075314 (2012).
[19]M. Raekers, K. Kuepper, S. Bartkowski, M. Prinz, A. V. Postnikov, K. Potzger, S. Zhou, A. Arulraj, N. Stüßer, R. Uecker *et al.*, Phys. Rev. B **79**, 125114 (2009).
[20]R. Uecker, H. Wilke, D. G. Schlom, B. Velickov, P. Reiche, A. Polity, M. Bernhagen, and M. Rossberg, J. Cryst. Growth **295**, 84 (2006).
[21]J. J. Jia, T. A. Callcott, J. Yurkas, A. W. Ellis, F. J. Himpsel, M. G. Samant, G. Stöhr, D. L. Ederer, J. A. Carlisle, E. A. Hudson *et al.*, Rev. Sci. Instrum. **66**, 1394 (1995).
[22]E. Cicerrella, Ph.D. thesis, OGI School of Science & Engeneering at Oregon Health & Science University, 2006.
[23]V. V. Afanas'ev, A. Stesmans, C. Zhao, M. Caymax, T. Heeg, J. Schubert, Y. Jia, D. G. Schlom, and G. Lucovsky, Appl. Phys. Lett **85**, 5917 (2004).
[24]P. Olalde-Velasco, J. Jiménez-Mier, J. D. Denlinger, Z. Hussain, and W. L. Yang, Phys. Rev. B **83**, 241102 (2011).
[25]D. O. Demchenko, A. Y. Liu, E. Z. Kurmaev, L. D. Finkelstein, V. R. Galakhov, A. Moewes, S. G. Chiuzbăian, M. Neumann, C. R. Kmety, and K. L. Stevenson, Phys. Rev. B **69**, 205105 (2004).
[26]T. Arima, Y. Tokura, and J. B. Torrance, Phys. Rev. B **48**, 17006 (1993).
[27]R. P. Liferovich and R. H. Mitchell, J. Solid State Chem. **177**, 2188 (2004).
[28]T. Higuchi, Y. Nagao, J. Liu, F. Iguchi, N. Sata, T. Hattori, and H. Yugami, J. Appl. Phys. **104**, 076110 (2008).
[29]F. M. F. de Groot, J. C. Fuggle, B. T. Thole, and G. A. Sawatzky, Phys. Rev. B **42**, 5459 (1990).

Publication H3

[**H3**] K. Kuepper, M. Raekers, C. Taubitz, M. Uhlarz, C. Piamonteze, F. M. F. de Groot, E. Arenholz, V. R. Galakhov, Ya. M. Mukovskii, and M. Neumann. *The x-ray magnetic circular dichroism spin sum rule for $3d^4$ systems: Mn^{3+} ions in colossal magnetoresistance manganites*, J. Phys.: Condens. Matter **24**, 435602 (2012), doi: 10.1088/0953-8984/24/43/435602.

The x-ray magnetic circular dichroism spin sum rule for $3d^4$ systems: Mn^{3+} ions in colossal magnetoresistance manganites

2012 J. Phys.: Condens. Matter 24 435602

J. Phys.: Condens. Matter **24** (2012) 435602 (7pp) doi:10.1088/0953-8984/24/43/435602

The x-ray magnetic circular dichroism spin sum rule for $3d^4$ systems: Mn^{3+} ions in colossal magnetoresistance manganites

K Kuepper[1,9], M Raekers[2], C Taubitz[2], M Uhlarz[3], C Piamonteze[4], F M F de Groot[5], E Arenholz[6], V R Galakhov[7], Ya M Mukovskii[8] and M Neumann[2]

[1] Helmholtz-Zentrum Dresden-Rossendorf, Institute of Ion Beam Physics and Materials Research, PO Box 51 01 19, D-01314 Dresden, Germany
[2] Department of Physics, University of Osnabrück, D-49069 Osnabrück, Germany
[3] Helmholtz-Zentrum Dresden-Rossendorf, High Magnetic Field Laboratory, PO Box 51 01 19, D-01314 Dresden, Germany
[4] Swiss Light Source, Paul Scherrer Institut, CH-5232 Villigen PSI, Switzerland
[5] Department of Inorganic Chemistry and Catalysis, Utrecht University, Sorbonnelaan 16, 3584 CA Utrecht, The Netherlands
[6] Advanced Light Source, Lawrence Berkeley National Laboratory, Berkeley, CA 94720, USA
[7] Institute of Metal Physics, Russian Academy of Sciences—Ural Division, 620990 Yekaterinburg, Russia
[8] National Science and Technology University 'MISiS', 119049 Moscow, Russia

E-mail: karsten.kuepper@uos.de

Received 5 January 2012, in final form 16 August 2012
Published 4 October 2012
Online at stacks.iop.org/JPhysCM/24/435602

Abstract

The colossal magnetoresistance manganites $La_{0.87\pm0.02}Sr_{0.12\pm0.02}MnO_{3+\delta}$, $La_{0.78\pm0.02}Sr_{0.17\pm0.02}MnO_{3+\delta}$, and $La_{0.66\pm0.02}Sr_{0.36\pm0.02}MnO_{3+\delta}$ (δ close to 0) were investigated by using soft x-ray magnetic circular dichroism (XMCD) and magnetometry. Very good agreement between the values for the average Mn magnetic moments determined with these two methods was achieved by correcting the XMCD spin sum rule results by means of charge transfer multiplet calculations, which also suggest a charge transfer of ~50% for Mn^{4+} and ≃30% for Mn^{3+}. The magnetic moment was found to be localized at the Mn ions for $x = 0.17$ and 0.36 at 80 K and for $x = 0.12$ in the temperature range from 80 to 300 K. We discuss our findings in the light of previously published data, confirming the validity of our approach.

(Some figures may appear in colour only in the online journal)

1. Introduction

X-ray magnetic circular dichroism (XMCD) is one of the most versatile techniques for the study of the internal magnetic structure of magnetic materials. This stems from its element specificity as well as the unique possibility to separate spin and orbital contribution to the magnetic moment by applying the sum rules developed by Thole [1] and Carra [2]. In order to extract quantitative accurate results, core level spin–orbit coupling and core–valence exchange interactions have to be taken into account [3, 4]. The fundamental issue behind the correction factor is that assumptions used for the orbital sum rule are not fulfilled for the L edges of 3d systems. The reason is that the orbital sum rule implicitly assumes pure L_3 and L_2 edges. Due to the large 2p3d overlap integrals (a.k.a. multiplet effects), the L_3 and L_2 edges mix the $2p_{3/2}$ and $2p_{1/2}$ character and the orbital sum rule breaks down. To correct for the error

[9] Present address: Department of Physics, University of Osnabrück, D-49069 Osnabrück, Germany.

in the sum rule, an alternative procedure is used: (1) the spectrum is fitted with calculations; (2) the orbital moment for the theoretical ground state is determined; (3) the orbital sum rule is applied to the calculated spectra; (4) the error in the orbital sum rule is determined. Therefore, we do not actually use a correction factor, but rather a different procedure to determine the orbital moment. This procedure avoids the error in the orbital sum rule due to multiplet mixing of the *j*-character. These multiplet effects are critical in case of 3d transition metal oxides, in particular for $3d^4$ systems the error of the spin sum rule is very large [4]. Since many $3d^4$ systems exhibit intriguing magnetic properties, e.g. are Cr based ferromagnetic semiconductors [5] or magnetic molecules [6], $SrFeO_3$ based perovskites [7, 8], and in particular the manganese based colossal magnetoresistance perovskites $RE_{1-x}A_xMnO_3$ (where RE and A denote a trivalent rare earth atom and a divalent atom, respectively) [9–11]. Developing a better understanding of the precise internal magnetic structure of such materials and their interfaces [12–17] is of utmost importance.

Here we study a $3d^4$ and a CMR model system, namely $La_{0.87\pm0.02}Sr_{0.12\pm0.02}MnO_{3+\delta}$, $La_{0.78\pm0.02}Sr_{0.17\pm0.02}MnO_{3+\delta}$, and $La_{0.66\pm0.02}Sr_{0.36\pm0.02}MnO_{3+\delta}$ (δ close to 0) by means of XMCD, conventional magnetometry and multiplet simulations including corresponding spin sum rule correction. We demonstrate and validate the spin sum rule correction method developed by Piamonteze *et al* [4] for the particular delicate case of a $3d^4$ system leading to excellent agreement between the results obtained with different methods. Furthermore we compare our results with previously published data [13, 18], demonstrating that previously observed and reported differences using different methods may be resolved by our approach.

2. Experimental and theoretical details

Single crystals of $La_{0.87\pm0.02}Sr_{0.12\pm0.02}MnO_{3+\delta}$, $La_{0.78\pm0.02}Sr_{0.17\pm0.02}MnO_{3+\delta}$, and $La_{0.66\pm0.02}Sr_{0.36\pm0.02}MnO_{3+\delta}$ were grown in air by floating-zone method and details can be found in the work of Shulyatev *et al* [19]. Electron microprobe analysis at different points of the samples reveals a potential deviation from the nominal cation stoichiometry of around 2%, the growth or fritting in air leads to an oxygen content close to 3. A slightly increased oxygen concentration cannot be excluded. The XMCD measurements were performed at beamline 4.0.2 at the Advanced Light Source in Berkeley, California [20, 21], using the eight-pole electromagnet. The experiments were performed within a temperature range of 80–300 K and an external magnetic field of 0.7 T, which was aligned along the *c*-axis of the crystals. The polarity of the field was flipped at each data point measured. Spectra were taken in total electron yield (TEY). The x-ray incident angle was chosen 90° to the sample normal in order to minimize potential self-absorption and electron yield saturation effects. Magnetization measurements were performed with a commercial superconducting quantum interference device (SQUID) magnetometer (Quantum Design MPMS XL) at the High Magnetic Field Laboratory, Helmholtz-Zentrum Dresden-Rossendorf. The charge transfer multiplet calculations were performed using the TT-multiplet code [22, 23]. The Slater integrals and the spin–orbit couplings were calculated in spherical symmetry and reduced to 80% of the calculated values. Then an octahedral crystal field (10Dq) and an external magnetic field of $\mu_B H = 0.05$ eV along the *z*-direction were applied. Finally charge transfer states were considered. In order to enable a direct comparison between experiment and simulation, the calculated spectra have been normalized to 90% circular polarization by considering the transitions which can only be excited with a linear polarization vector with 10% weight. Furthermore, the calculated spectra have been convoluted with the overall experimental resolution (lifetime broadening plus spectrometer resolution).

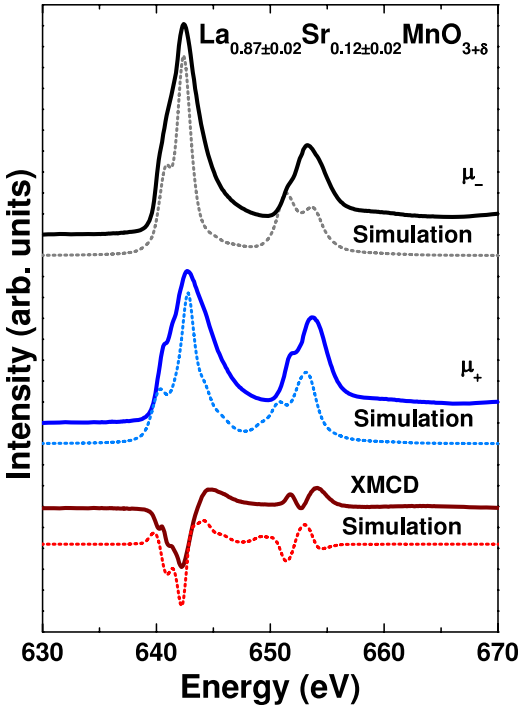

Figure 1. XMCD spectra of $La_{0.87\pm0.02}Sr_{0.12\pm0.02}MnO_{3+\delta}$ with 0.7 T applied magnetic field at 80 K in comparison with charge transfer multiplet calculations.

3. Results and discussion

Figures 1–3 display the XMCD spectra obtained at 80 K and applied magnetic fields of 0.7 T from $La_{0.87\pm0.02}Sr_{0.12\pm0.02}MnO_{3+\delta}$, $La_{0.78\pm0.02}Sr_{0.17\pm0.02}MnO_{3+\delta}$, and $La_{0.66\pm0.02}Sr_{0.36\pm0.02}MnO_{3+\delta}$. Moreover, charge transfer multiplet calculations assuming a cubic symmetry for the systems are shown as well. For all samples the same parameters were used, but the mixing of Mn^{3+} and Mn^{4+} spectra was derived from the formal valence state determined by the amount of Sr doping. The charge transfer from the ligand oxygen to the Mn site ($3d^nL \rightarrow 3d^{n+1}L^{-1}$) is included in the calculations. The best agreement with the experiment could be achieved with amounts of approximately 50% and 30% for Mn^{4+} and Mn^{3+}, respectively.

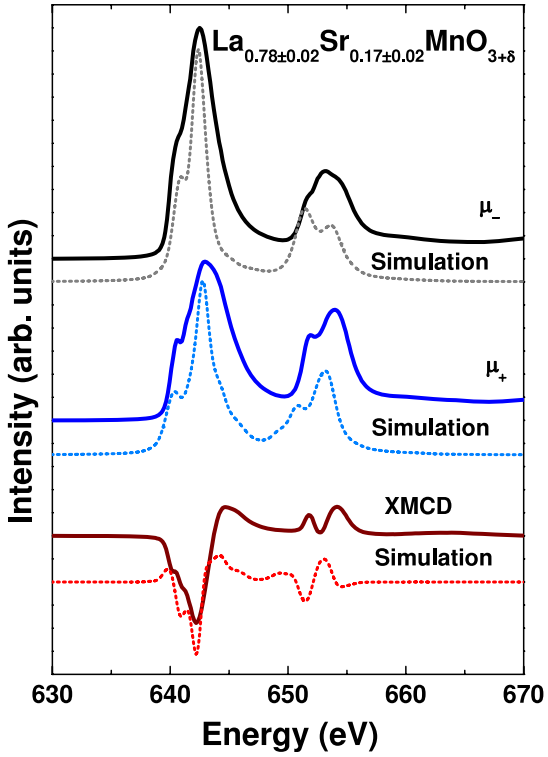

Figure 2. XMCD spectra of $La_{0.78\pm0.02}Sr_{0.17\pm0.02}MnO_{3+\delta}$ with 0.7 T applied magnetic field at 80 K in comparison with charge transfer multiplet calculations.

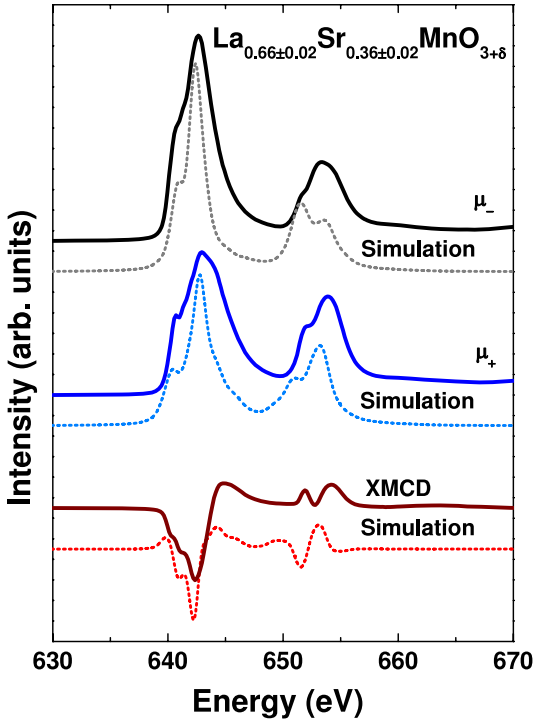

Figure 3. XMCD spectra of $La_{0.66\pm0.02}Sr_{0.36\pm0.02}MnO_{3+\delta}$ with 0.7 T applied magnetic field at 80 K in comparison with charge transfer multiplet calculations.

The XMCD spectra show distinct spectral features at the Mn L_3 edge near 643 eV and the L_2 edge around 654 eV. The main L_3 edge feature has two shoulders to lower photon energy (641.5 and 640.5 eV). At higher photon energy a broad shoulder is present (around 645 eV). The main feature of the L_2 edge at 653.0 eV has a shoulder at 654.0 eV and a feature at 641.5 eV. A very small feature appears at 650.5 eV. It is very similar for all three samples, but the intensities are slightly different. The feature at 654.0 eV is higher for the sample with a Sr concentration of $x = 0.12$ than for the sample with $x = 0.36$. The shoulder at 640.5 eV is slightly more pronounced for the sample with $x = 0.36$ than for the other two.

The calculations are in overall satisfactory agreement with the experiment, but there are some notable differences. In the positive circularly polarized spectra the main peak at 653.5 eV at the Mn L_2 edge is underestimated for all samples, whereas the prepeak located around 651 eV is overestimated in the simulations. Furthermore, the 2p–3d spin–orbit splitting is underestimated approximately by 1 eV in the simulations. The separation between the L_3 and the L_2 edge is caused by the 2p spin–orbit coupling. In many papers it is assumed that the 2p spin–orbit coupling has its atomic value. However, looking more closely into this issue there are many cases where the experimental difference between the L_3 and the L_2 edge differs from the theoretical value. The issue is complicated by the fine structure of the L_3 and L_2 edges, which makes it difficult to determine the L_3–L_2 splitting precisely. The clearest case is Cu(II), where both the L_3 and the L_2 edge contain a single peak. Experimental values for the 2p spin–orbit splitting range between 19.2 and 20.4 eV, against the theoretical value of 20.3 eV [24]. It is important to notice that the 2p spin–orbit coupling does not play a role in the further discussion of the spin and orbital moment. Instead the 3d spin–orbit coupling is at stake here and is a crucial aspect.

The Mn L_2 edge prepeak present in the experimental spectra at 651 eV is hardly visible in the simulations. The prepeak structure of the Mn L_3 edge at 641 eV is not completely rendered by the calculation. The different mixing of Mn valence states is overestimated by the calculations in comparison to the experiment. The less pronounced fine structure in the experiment might be considered due to a metallic character of the samples. However, it has been demonstrated before for a very similar system, namely $La_{0.7}Sr_{0.3}MnO_3$, that dynamical screening leads to a superposition of the electronic structure of initial and final states [25]. Hence, the 2p-hole and the 3d-hole have radial wavefunctions which overlap significantly, and the corresponding Mn $L_{2,3}$ XAS are ruled mainly by (localized) multiplet effects. Nevertheless, the calculation allows us to estimate values for the crystal field (1.4 eV), and the charge transfer amount (Mn^{4+}: 50%, Mn^{3+}: 30%) giving the described agreement with the experiment. This leads to averaged 3.9 holes per Mn ion, which we also used for the sum rule analysis of the experimental spectra. Furthermore, the nonresonant part of the spectra was subtracted by two step functions following the approach of Chen *et al* [26].

For $La_{0.87\pm0.02}Sr_{0.12\pm0.02}MnO_{3+\delta}$, $La_{0.78\pm0.02}Sr_{0.17\pm0.02}MnO_{3+\delta}$, and $La_{0.66\pm0.02}Sr_{0.36\pm0.02}MnO_{3+\delta}$ XMCD spectra

Table 1. Spin and orbital magnetic moment of $La_{0.87\pm0.02}Sr_{0.12\pm0.02}MnO_{3+\delta}$, $La_{0.78\pm0.02}Sr_{0.17\pm0.02}MnO_{3+\delta}$ and $La_{0.66\pm0.02}Sr_{0.36\pm0.02}MnO_{3+\delta}$ at various temperatures and with 0.7 T applied magnetic field extracted from XMCD spectra.

	T (K)	M_{spin} (μ_B)	M_{orb} (μ_B)
$La_{0.87\pm0.02}Sr_{0.12\pm0.02}MnO_{3+\delta}$	80	1.91	0.03 ± 0.01
$La_{0.78\pm0.02}Sr_{0.17\pm0.02}MnO_{3+\delta}$	80	2.21	0.02 ± 0.01
$La_{0.66\pm0.02}Sr_{0.36\pm0.02}MnO_{3+\delta}$	80	1.82	-0.02 ± 0.01
	140	1.54	-0.02 ± 0.01
	150	1.50	0.00 ± 0.01
	160	1.38	0.01 ± 0.01
	180	0.91	0.04 ± 0.01
	200	0.36	0.01 ± 0.01
	220	0.18	0.01 ± 0.01
	250	0.08	0.01 ± 0.01
	300	0.05	0.02 ± 0.01

were measured at temperatures between 80 and 300 K in applied magnetic fields of 0.7 T. The Mn $L_{2,3}$ XMCD spectra are plotted in figure 4. Above 180 K, the dichroism decreases significantly with temperature and nearly vanishes at 220 K while its shape is not changing. In table 1 the spin and orbital magnetic moments extracted using the sum rules are summarized. Since we already used a geometry minimizing self-absorption we did not correct the spectra for electron yield saturation effects. We want to point out that for other transition metal oxides, like Fe_2O_3 or Fe_3O_4 very different values for the electron escape depth have been reported [27, 28], which may influence any potential self-absorption correction in a crucial way.

Theoretically, the orbital sum rule is accurate, and we found only small orbital moments between -0.02 and 0.04 μ_B per Mn atom; similar absolute values have been reported before [12]. Hence the major contribution to the overall magnetization comes from the spin moment. In particular for the $x = 0.12$ sample a sign change of the orbital moment seems to be present at 160 K, which may correspond to a structural phase transition and a subsequent change of the orbital occupation of the 3d e_g level. Such complex behavior of the orbital magnetic moment of orbitally degenerated 3d transition metal ions has been theoretically proposed earlier [29], including the possibility of sign reversal of the orbital moment via interaction with the ligand states in different structural and orbitally ordered or disordered phases [30, 31]. However, on the other hand in many other systems a clear correlation between the spin and the orbital moment has been observed, suggesting at least a reduction of the orbital moment of one order of magnitude (while S is reduced by about two orders). Hence more experiments, in particular similar experiments with opposite helicity will be necessary to ultimately exclude the possibility of any spectral artifacts, e.g. like 'offsets' in the XMCD signal.

In figure 5 the magnetometry data are compared with the magnetic moments at the Mn atoms determined by XMCD and the sum rules. Since the spin sum rule is sensitive to a number of multiplet effects and core–valence interactions for $3d^4$ systems as Mn^{3+} ions, we employed the spin sum rule to our multiplet simulations first in order to derive the correction factor accounting for these effects [4]. Following the approach described by Piamonteze *et al* we find spin sum rule correction

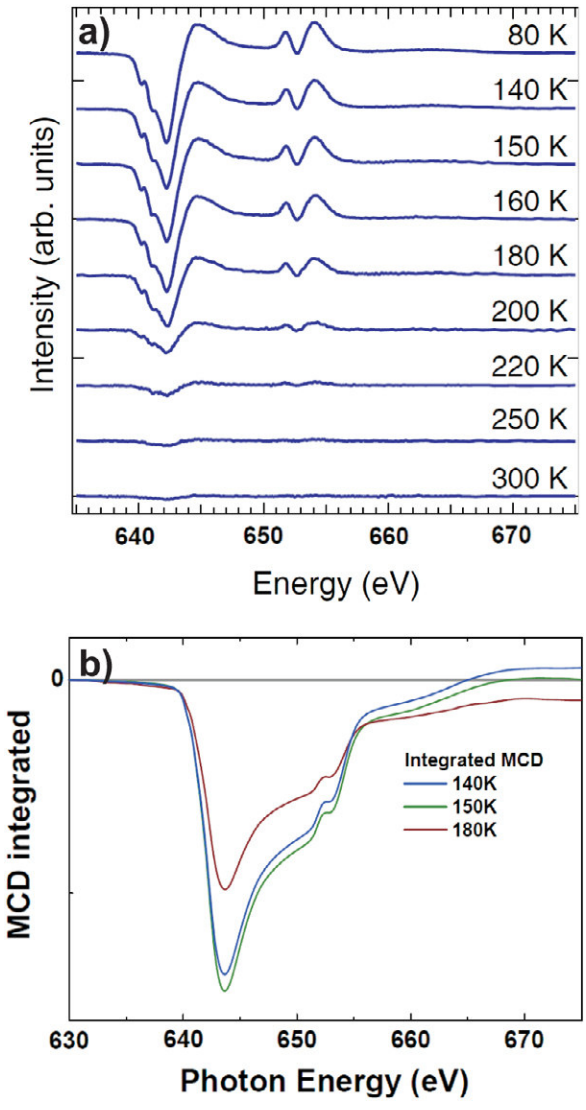

Figure 4. XMCD signals of $La_{0.87\pm0.02}Sr_{0.12\pm0.02}MnO_{3+\delta}$ with 0.7 T applied magnetic field at various temperatures from 80 to 300 K (a), integrals of three selected XMCD spectra (140, 150, and 180 K), demonstrating the sign reversal of the orbital moment (b).

factors of 0.6405 for Mn^{3+} and 0.6075 for Mn^{4+}. Employing these correction factors we find an almost perfect agreement between the overall moments derived from the XMCD sum

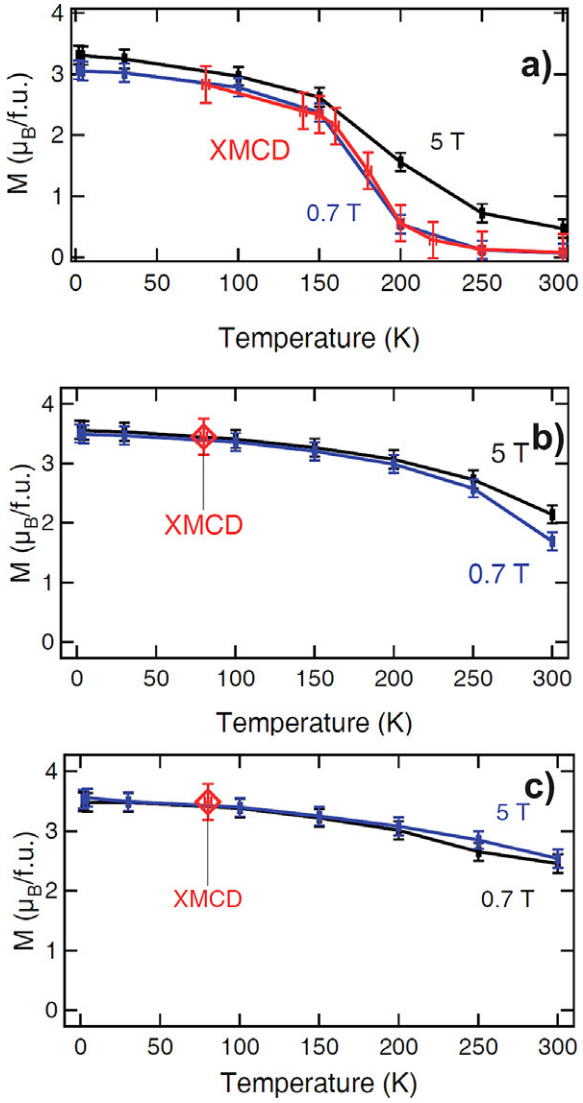

Figure 5. Comparison of magnetic moments of $La_{0.87\pm0.02}Sr_{0.12\pm0.02}MnO_{3+\delta}$ (a), $La_{0.78\pm0.02}Sr_{0.17\pm0.02}MnO_{3+\delta}$ (b), and $La_{0.66\pm0.02}Sr_{0.36\pm0.02}MnO_{3+\delta}$ (c) determined by SQUID and XMCD. The XMCD results were corrected as described in the text.

rules and the magnetometry result (see figure 5). Note that the 3d spin–orbit coupling (ls coupling) was reduced to 25% in the charge transfer multiplet simulations. A 3d-ls coupling of 100% leads to an error of around 10% of magnetic moments calculated from the XMCD spectra. Obviously, the Mn^{3+} ($3d^4$) configuration is in particular sensitive to the 3d-ls coupling, since the spin sum rule correction factor is strongly reduced with 100% 3d-ls coupling (0.5462), whereas the correction factor for Mn^{4+} ions remains almost unchanged (0.6066) compared to 25% 3d-ls coupling.

The magnetic moment derived from XMCD data can also be corrected following a second approach developed by Teramura *et al* [3]. Using that approach for Mn L edge XMCD has been very successful in deriving the magnetic moment in Mn based magnetic molecules [32]. The factor for Mn^{4+} and Mn^{2+} are 0.68 and 0.587, respectively. We have approximated the factor for Mn^{3+} as a linear combination of the factors for 2+ and 4+. We have also taken into account the charge transfer for Mn^{4+} and Mn^{3+} as used in the multiplet calculations. This approach leads within 1% deviation to the same results as the correction factors estimated from our multiplet simulations.

In figure 5(a) the magnetization of $La_{0.87\pm0.02}Sr_{0.12\pm0.02}MnO_{3+\delta}$, $La_{0.78\pm0.02}Sr_{0.17\pm0.02}MnO_{3+\delta}$, and $La_{0.66\pm0.02}Sr_{0.36\pm0.02}MnO_{3+\delta}$ is shown for temperatures from 1.8 to 300 K in fields of 0.7 and 5 T. The magnetic moment at the Mn atoms determined by XMCD at temperatures from 80 to 300 K at 0.7 T is also presented for comparison. With the corrections mentioned above an almost perfect agreement between magnetometry and XMCD could be achieved. The Curie temperature $T_C = 177$ K determined by Dabrowski *et al* [33] is also in agreement with our results. The comparison between magnetometry and XMCD at 80 K and 0.7 T for $La_{0.87\pm0.02}Sr_{0.12\pm0.02}MnO_{3+\delta}$, $La_{0.78\pm0.02}Sr_{0.17\pm0.02}MnO_{3+\delta}$, and $La_{0.66\pm0.02}Sr_{0.36\pm0.02}MnO_{3+\delta}$ is presented in figures 5(b) and (c), respectively. Here very good agreement between magnetometry and XMCD was achieved by the corrections mentioned above confirming the validity of our approach. We want to mention that we did not consider potential contributions from the other elements to the total magnetic moment here. Other XMCD studies on very similar samples revealed only low contributions of the oxygen atoms [12] and a small spin moment of less than 0.1 μ_B/La atom [34].

The maximal magnetization of the $La_{0.87\pm0.02}Sr_{0.12\pm0.02}MnO_{3+\delta}$, $La_{0.78\pm0.02}Sr_{0.17\pm0.02}MnO_{3+\delta}$, and $La_{0.66\pm0.02}Sr_{0.36\pm0.02}MnO_{3+\delta}$ samples for a temperature of 1.8 K and an applied field of 5.0 T is 3.31 μ_B/f.u. for $x = 0.12$. This value seems to be too small in comparison with a simple atomistic 'spin-only guess' for a completely ferromagnetic orientation of the spins, which gives 3.88 μ_B/f.u. with 12% Mn^{4+} (3 μ_B) and 88% Mn^{3+} (4 μ_B). For $x = 0.17$ we found for the same conditions 3.57 μ_B/f.u. which is larger than for $x = 0.12$, but again smaller than the theoretical value of 3.83 μ_B/f.u. For $x = 0.36$ the experiment is with 3.53 μ_B/f.u. much closer to the 'spin-only guess' with 3.64 μ_B/f.u.. Our results for $x = 0.12$ and 0.17 are in better agreement with neutron powder diffraction measurements [33] giving $\simeq$3.4 μ_B and $\simeq$3.5 μ_B for similar Sr concentrations. The too small values could be explained with cation deficiency and a slightly too high oxygen content which leads to lower magnetic moments [35], but also to a change of the Curie temperature. However, these results demonstrate that the influence of cation deficiency and oxygen content to the saturation magnetization is not larger than 15%.

With 3.1 oxygen atoms/f.u. and $\simeq$3.6 μ_B/Mn Bukowski *et al* [35] found a decreasing T_C by more than 20 K for a sample with $x = 0.185$. In the case of our sample with $x = 0.17$ we would achieve a transition temperature $T_C < 260$ K, which would be observed by our magnetization measurements (see figure 5, middle panel). Another explanation is given by Pinsard *et al* [36] finding a spin canting in a sample with $x = 0.125$ by means of neutron powder diffraction. This effect is explained with a strong coupling of Jahn–Teller distortion, ferromagnetic ordering and transport properties. For a higher Sr concentration the Jahn–Teller distortion becomes smaller

and the difference of the magnetization to the theoretical completely ferromagnetic ordered magnetization disappears. Such a spin canting was also observed by neutron powder diffraction by Xiong *et al* [37] in this Sr concentration range. They found the angle between spin and *c*-axis for $x = 0.11°$ to be $\simeq 77°$. For $x = 0.165\,40°$ and for $x = 0.185° \simeq 15°$ were determined. Our samples with low Sr concentration are in the range of the coupling between structural and magnetic properties ($0.11 \leq x \leq 0.185$) and the canted spin configuration leads to lower magnetizations than expected for a completely ferromagnetic spin orientation.

Finally we want to compare our results with similar XMCD studies reported in literature. Koide *et al* [13] performed a concentration dependent XMCD study on a series of $La_{1-x}Sr_xMnO_{3+\delta}$ polycrystals. They found discrepancies of 30–40% between the moments derived from the XMCD signal and their SQUID results. Applying our correction factors for Mn^{3+} and Mn^{4+} the error reduces to 10–15%. Whereas the spin sum rule results reveal markedly too low moments, they are too high if one includes the correction factors. The remaining discrepancy may be due to a somewhat inaccurate estimation of the number of holes (they estimated the error to be approx. 10% [13]) and due to inaccuracies stemming from the extraction of the moments from reference [13]. Nevertheless, the discrepancy between the magnetic moments probed by SQUID and XMCD reduces markedly for all samples with one exception ($x = 0.4$). Hence, our spin sum correction factor obviously also improves the results of other measurements performed earlier on similar manganite systems. On the other side Park *et al* [18] probed an $La_{0.3}Sr_{0.7}MnO_3$ thin film by means of XMCD and SQUID. Also they find differences between bulk and surface magnetism, which however is shown to be related to intrinsic properties of the film, e.g. surface stress or finite size effects. However, also for thin film systems, especially if they comprise more than one magnetic element, the application of a spin sum rule correction factor could be of advantage, as already motivated in the introduction.

4. Conclusions

In summary, the average magnetic moments for the compounds $La_{0.87\pm0.02}Sr_{0.12\pm0.02}MnO_{3+\delta}$, $La_{0.78\pm0.02}Sr_{0.17\pm0.02}MnO_{3+\delta}$, and $La_{0.66\pm0.02}Sr_{0.36\pm0.02}MnO_{3+\delta}$ (δ close to 0) were determined using SQUID measurements and XMCD using the spin sum rule correction approach by Piamonteze *et al* [4] and Teramura *et al* [3], taking into account the influence of charge transfer. With this combination of experiments and theory we demonstrate that the spin sum rule correction approach is applicable for the particularly delicate case of $3d^4$ systems, since the spin sum rule error is extremely large for these systems. For the samples with $x = 0.12$ and 0.17, indications for a canted spin configuration are found. The good agreement of the magnetic moment measured by SQUID magnetometry and that determined from XMCD for the single crystalline samples of $La_{0.87\pm0.02}Sr_{0.12\pm0.02}MnO_{3+\delta}$, $La_{0.78\pm0.02}Sr_{0.17\pm0.02}MnO_{3+\delta}$, and $La_{0.66\pm0.02}Sr_{0.36\pm0.02}MnO_{3+\delta}$ indicates that the magnetic moment is, to a large extent, localized at the Mn ions at 80 K. For $x = 0.12$, the localization is observed in the temperature range from 80 to 300 K.

Acknowledgments

Part of this work has been performed at the Advanced Light Source, ALS, Lawrence Berkeley National Laboratory, Berkeley, USA, which is operated under contract No. DE-AC02-05CH11231. The SQUID measurements have been supported by EuroMagNET under EU contract no. 228043. MR gratefully acknowledges financial support of the GRK695: Nonlinearities of optical materials. Financial support by the PhD program (Lower Saxony) is gratefully acknowledged by CT. MISiS is acknowledged by YaM. VRG thanks the Russian Foundation for Basic Research (project no. 11-02-00166) for financial support.

References

[1] Thole B T, Carra P, Sette F and van der Laan G 1992 *Phys. Rev. Lett.* **68** 1943
[2] Carra P, Thole B T, Altarelli M and Wang X 1993 *Phys. Rev. Lett.* **70** 694
[3] Teramura Y, Tanaka A and Jo T 1996 *J. Phys. Soc. Japan* **65** 1053
[4] Piamonteze C, Miedema P and de Groot F M F 2009 *Phys. Rev.* B **80** 184410
[5] Yamazaki Y *et al* 2011 *J. Phys.: Condens. Matter* **23** 176002
[6] Prinz M *et al* 2010 *Inorg. Chem.* **49** 2093
[7] Okamoto J *et al* 2005 *Phys. Rev.* B **71** 104401
[8] Galakhov V R, Kurmaev E Z, Kuepper K, Neumann M, McLeod J R, Moewes A, Leonidov I A and Kozhevnikov V 2010 *J. Phys. Chem.* C **114** 5154
[9] Millis A J 1998 *Nature* **392** 147
[10] Salamon M B and Jaime M 2001 *Rev. Mod. Phys.* **73** 583
[11] Chuang Y D, Gromko A D, Dessau D S, Kimura T and Tokura Y 2001 *Science* **292** 1509
[12] Pellegrin E, Tjeng L H, de Groot F, Hesper R, Sawatzky G A, Moritomo Y and Tokura Y 1997 *J. Electron Spectrosc. Rel. Phenom.* **86** 115
[13] Koide T *et al* 2001 *Phys. Rev. Lett.* **87** 257201
[14] Chakhalian J *et al* 2006 *Nature Phys.* **2** 244
[15] Arenholz E, van der Laan G, Yang F, Kemik N, Biegalski M D, Christen H M and Takamura Y 2009 *Appl. Phys. Lett.* **94** 072503
[16] Werner R *et al* 2010 *Phys. Rev.* B **82** 224509
[17] Yu P *et al* 2010 *Phys. Rev. Lett.* **105** 027201
[18] Park J-H, Vescovo E, Kim H-J, Kwon C, Ramesh R and Venkatesan T 1998 *Phys. Rev. Lett.* **81** 1953
[19] Shulyatev D, Karabashev S, Arsenov A, Mukovskii Y and Zverkov S 2002 *J. Cryst. Growth* **237** 810
[20] Young A T, Martynov V and Padmore H A 1999 *J. Electron Spectrosc. Relat. Phenom.* **101–103** 885
[21] Young A T, Arenholz E, Feng J, Padmore H, Marks S, Schlueter R, Hoyer E, Kelez C and Steier N 2002 *Surf. Rev. Lett.* **9** 549
[22] de Groot F M F 1994 *J. Electron Spectrosc. Relat. Phenom.* **67** 529
[23] de Groot F M F 2005 *Coord. Chem. Rev.* **249** 31
[24] Sarangi R, Aboelella N, Fujisawa K, Tolman W B, Hedman B, Hodgson K O and Solomon E I 2006 *J. Am. Chem. Soc.* **128** 8286
[25] Wessely O, Roy P, Åberg D, Andersson C, Karis S E, Sanyal B, Svedlindh P, Katsnelson M I, Arvanitis R D and Eriksson O 2003 *Phys. Rev.* B **68** 235109

[26] Chen C T, Idzerda Y U, Lin H-J, Smith N V, Chaban G M, Ho G H, Pellegrin E and Sette F 1995 *Phys. Rev. Lett.* **75** 152
[27] Gota S, Gautier-Soyer M and Sacchi M 2000 *Phys. Rev.* B **62** 4187
[28] Goering E, Gold S, Lafkioti M and Schütz G 2006 *Europhys. Lett.* **73** 97
[29] Hoppe B and Hirst L L 1983 *J. Phys. C: Solid State Phys.* **16** 1919
[30] Galanakis I, Oppeneer P M, Ravindran P, Nordström L, James P, Alouani M, Dreysse H and Eriksson O 2001 *Phys. Rev.* B **63** 172405
[31] Trukhanov S V 2005 *J. Exp. Theor. Phys.* **100** 95
[32] Khanra S *et al* 2008 *Inorg. Chem.* **47** 4605
[33] Dabrowski B *et al* 1999 *Phys. Rev.* B **60** 7006
[34] Kobayashi K, Iwazumi T, Suga S, Imada S, Muro T, Tokura Y and Moritomo Y 1997 *Physica* B **237** 41
[35] Bukowski Z, Dabrowski J, Mais J, Klamut P W, Kolesnik S and Chmaissem O 2000 *J. Appl. Phys.* **87** 5031
[36] Pinsard L, Rodriguez-Carvajal J, Moudden A H and Anane A 1997 *Physica* B **234–236** 856
[37] Xiong X, Dabrowski B, Chmaissem O, Bukowski Z, Kolesnik S, Dybzinski R and Jorgensen J D 1999 *Phys. Rev.* B **60** 10186

Publication H4

[**H4**] K. Kuepper, M. Raekers, C. Taubitz, M. Prinz, C. Derks, M. Neumann, A. V. Postnikov, F. M. F. deGroot, C. Piamonteze, D. Prabakharan and S. J. Blundell. *Charge order, enhanced orbital moment, and absence of magentic frustration in layered multiferroic* $LuFe_2O_4$, Phys. Rev. B **80**, 220409(R) (2009), doi: 10.1103/PhysRevB.80.220409.

PHYSICAL REVIEW B **80**, 220409(R) (2009)

Charge order, enhanced orbital moment, and absence of magnetic frustration in layered multiferroic $LuFe_2O_4$

K. Kuepper,[1,*] M. Raekers,[2,†] C. Taubitz,[2] M. Prinz,[2] C. Derks,[2] M. Neumann,[2,‡] A. V. Postnikov,[3] F. M. F. de Groot,[4] C. Piamonteze,[5] D. Prabhakaran,[6] and S. J. Blundell[6]

[1]*Institute of Ion Beam Physics and Materials Research, Forschungszentrum Dresden-Rossendorf, P.O. Box 51 01 19, D-01314 Dresden, Germany*

[2]*Department of Physics, University of Osnabrück, D-49069 Osnabrück, Germany*

[3]*LPMD, Institute Jean Barriol and Paul Verlaine University, Metz, France*

[4]*Department of Inorganic Chemistry and Catalysis, Utrecht University, Sorbonnelaan 16, 3584 CA Utrecht, Netherlands*

[5]*Swiss Light Source, Paul Scherrer Institut, 5232 Villigen PSI, Switzerland*

[6]*Department of Physics, Clarendon Laboratory, University of Oxford, Parks Road, Oxford OX1 3PU, United Kingdom*

(Received 13 November 2009; published 18 December 2009)

Electronic and magnetic properties of the charge ordered phase of $LuFe_2O_4$ are investigated by means of x-ray spectroscopic and theoretical electronic structure approaches. $LuFe_2O_4$ is a compound showing fascinating magnetoelectric coupling via charge ordering. Here, we identify the spin ground state of $LuFe_2O_4$ in the charge ordered phase to be a 2:1 ferrimagnetic configuration, ruling out a frustrated magnetic state. An enhanced orbital moment may enhance the magnetoelectric coupling. Furthermore, we determine the densities of states and the corresponding correlation potentials by means of x-ray photoelectron and emission spectroscopies, as well as electronic structure calculations.

DOI: 10.1103/PhysRevB.80.220409 PACS number(s): 75.80.+q, 71.20.−b, 78.70.Dm, 78.70.En

Multiferroic transition metal oxides, i.e., compounds in which more than one ferroic phase coexist, have gained enormous attention during the last few years.[1–4] Besides a number of perovskites and related compounds,[2,5,6] the charge frustrated layered compound $LuFe_2O_4$ has attracted intense interest due to its fascinating ferroelectric and magnetoelectric properties.[7,8] $LuFe_2O_4$ has a rhombohedral crystal structure (space group $R\bar{3}m$). The underlying layered structure consists of W-like hexagonal $Fe_2O_{2.5}$ and U-like $LuO_{1.5}$ layers.[9] The W layers comprise two triangular nets of Fe ions; the resulting electric polarization is induced via a frustrated charge ordering of Fe^{2+} and Fe^{3+} ions on the resulting honeycomb lattice below 330 K.[10–12] Below 240 K a long-range ferrimagnetic order sets in.[7] The fact that the ferroelectricity is caused by correlated electrons from the Fe ions leads to unusual properties and unique capabilities of $LuFe_2O_4$. A large response of the dielectric constant by applying small magnetic fields has been found, opening a possible route for future devices.[8] Phase transitions from the charge ordered (CO) phase have been very recently associated with a nonlinear current-voltage behavior and an electric-field-induced phase transition, which might be of interest for potential electric-pulse-induced resistive switching applications.[13,14]

The large magnetoelectric coupling has been attributed to an intricate interplay between charge and spin degrees of freedom with the crystal lattice and external electrical and magnetic fields to some extent on a short-range order.[15–19] However, there is still some confusion about the nature of spin-charge coupling in $LuFe_2O_4$. In particular a model finding a $\sqrt{3}\times\sqrt{3}$ CO ground state[20,21] is challenged by simulations implying that the electrical polarization in $LuFe_2O_4$ is due to spin-charge coupling and a spin frustrated magnetic ground state in a chain CO state.[22,23] On the other hand the first model finds a ferrimagnetic spin ground state where Fe^{2+} and 1/3 of Fe^{3+} make up the majority spin, and 2/3 of Fe^{3+} make up the minority spin.

X-ray magnetic circular dichroism (XMCD) is a very powerful tool to investigate the internal magnetic structure of the compound in question, including the unique possibility to separate the magnetic moments into their spin and orbital contributions. We applied XMCD to the Fe L edge in the charge ordered phase around 270 K and compare these results to corresponding full multiplet calculations. Furthermore, we performed x-ray photoelectron spectroscopy (XPS) and x-ray emission spectroscopy (XES) studies of the valence band. These results are compared to first-principles band-structure calculations in order to determine the Coulomb repulsion correlation strength between the Fe 3d and Lu 4f ions in $LuFe_2O_4$. High-quality single crystals were grown using a four-mirror floating zone furnace, as described elsewhere.[24]

Core levels and valence band were recorded by means of XPS, using a PHI5600ci multitechnique spectrometer with monochromatic Al $K\alpha$ radiation with an overall resolution of about 0.3 eV. The XMCD, XAS, and XES measurements were performed at beamlines 4.0.2 and 8.0.1 at the Advanced Light Source in Berkeley, California. In order to get a sample surface free of contamination the crystal was cleaved *in situ* just prior to the XPS and XMCD experiments. In case of the bulk sensitive XES the sample was rinsed with isopropanol before mounting the sample into the transfer chamber. The *ab initio* electronic structure calculations were performed using the (linearized) full-potential augmented plane-wave method[25] of the density-functional theory, as implemented in the WIENK2K code.[26] The Fe $L_{2,3}$ XAS and XMCD are compared to full multiplet simulations which were carried out with the *TT*-multiplets program package.[27,28]

Figure 1 displays the Fe 2p XPS of $LuFe_2O_4$ along with the spectra of reference compounds, namely, FeO (Fe^{2+}),

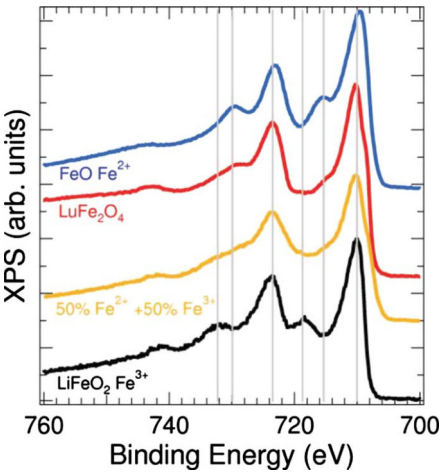

FIG. 1. (Color online) Fe $2p$ XPS of $LuFe_2O_4$, FeO (Fe^{2+} reference), and $LiFeO_2$ (Fe^{3+} reference).

$LiFeO_2$ (Fe^{3+}), and a 1:1 superposition of both reference spectra, representing a result for a nominally $Fe^{2.5+}$ based oxide since XPS is significantly more sensitive to the electronic configuration (charge transfer) than to the local symmetry. All spectra were recorded directly after cleaving the samples in ultrahigh vacuum in order to avoid any surface contamination. The Fe $2p_{3/2}$ peak of $LuFe_2O_4$ at 710 eV has a shoulder at 709 eV, which is due to the mixed Fe valence state in this compound. The Fe $2p_{1/2}$ peak is located at 705 eV. From the chemical shift of the Fe main peaks one cannot easily determine the valence state of Fe, following the usual procedure, because of the smallness of the shift. The satellites give better information about the valence state of the Fe ions. In the Fe^{2+} reference sample two satellites are present at 716 and 730 eV. The satellites of the Fe^{3+} reference are located at 718 and 732 eV. The $LuFe_2O_4$ Fe $2p$ spectrum shows clearly the presence of both types of satellites, yielding in fact a very good agreement with the superimposed (0.5 Fe^{2+}+0.5 Fe^{3+}) reference spectrum.

The electronic structure of occupied states was investigated by XPS of the valence band and XES from Fe $3d \rightarrow$ Fe $2p$ and O $2p \rightarrow$ O $1s$. The results are presented in Fig. 2 in comparison with GGA+U calculations, in which the U value of 0.7 Ry was selected for Lu $4f$ and U=0.3 Ry for Fe $3d$, guided by the best agreement with the valence-band XPS in the placement of respective peaks. In the XPS spectrum two peaks of the Lu $4f$ multiplet are located at −7.5 and −9 eV. The structure from −3 to −6 eV is distributed to O $2p$ states hybridized with Fe $3d$ states, which is in comparison with the XES spectra of the Fe L and the O K edges. The small states close to the Fermi level (from 0 to −1 eV) can be interpreted as highest occupied Fe $3d$ (d_{xy},$d_{x^2-y^2}$) states of the divalent sites in comparison with band-structure calculations of Xiang and Whangbo.[20]

The band-structure calculations presented in Fig. 2 are in excellent agreement with the XES and XPS measurements. It should be noted that the present calculation ignores charge ordering and assumes a minimal single unit cell of seven atoms. We checked that, in agreement with earlier calculations, a tripled unit cell with different magnetic and charge

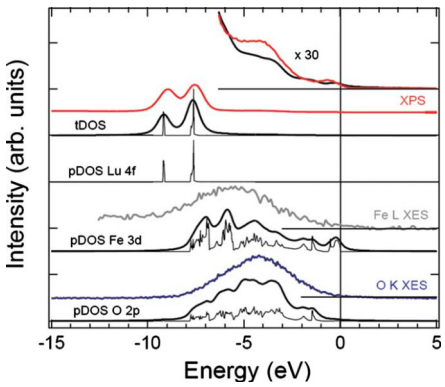

FIG. 2. (Color online) XPS valence band, Fe L edge, and O K edge XES in comparison with GGA+U calculations.

states over six Fe sites results in the opening of a band gap. However, a meaningful identification of all important features in the electronic structure is already possible on the basis of the single-cell calculation. The states close to the Fermi level in the XPS valence band can be identified as highest occupied Fe $3d$ states. Remarkable agreement is obtained between the XPS and the calculation in the range from −5 eV to the Fermi level as can be seen in the 30 times enlarged spectra in the top of Fig. 2. The strong hybridization between Fe $3d$ and O $2p$ becomes clear if one compares the peak structures of the calculated density of states of these states where the most intense Fe $3d$ states are located at −6 and −7 eV and the most intense O $2p$ states are located at −3.5 and −4.5 eV. Here, it is very clear that the states at higher binding energy (∼−6 eV) have a d character and the states at ∼−4 eV have a p character, as was found in Ref. 29 for $KTaO_3$ and $KNbO_3$. For two pronounced peaks identified with Fe $3d$ states at −7 and −6 eV, the lower is primarily formed by d_{z^2} and $d_{xy}+d_{x^2-y^2}$ states, of which the latter do equally contribute to the peak at −6 eV. This upper peak is otherwise built by the $d_{xz}+d_{yz}$ states. This agrees with the results of Xiang *et al.* In our calculation, the hybridization between Fe $3d$ and O $2p$ states seems slightly stronger than in previously published works; this strength must to some extent depend on the U value used. Note that the above labeling of the $3d$ orbitals is only approximative in the structure in question, as the spin and orbital diversification and related distortions would reduce the symmetry. The results give rise to different combinations of d orbitals—see Khomskii and Kugel.[30]

The hybridization between Fe $3d$ and O $2p$ states, *a priori* important for holding together the W layer, does not result in a substantial delocalization of magnetic moments, thus justifying our single-ion multiplet calculations. It can be concluded that magnetic density from Fe sites is only slightly spilled onto O in the W layer, not onto (equally close) O in the U layer. Note that this effect must be in fact somehow overestimated in the present calculation because of the ferromagnetic structure assumed, and in the genuine spin-charge mixed structure the localization of magnetic moments on the Fe sites should be stronger.

In Fig. 3 the XMCD spectra of the Fe L edge, measured in total electron yield (TEY) mode at ∼150 K, are presented in

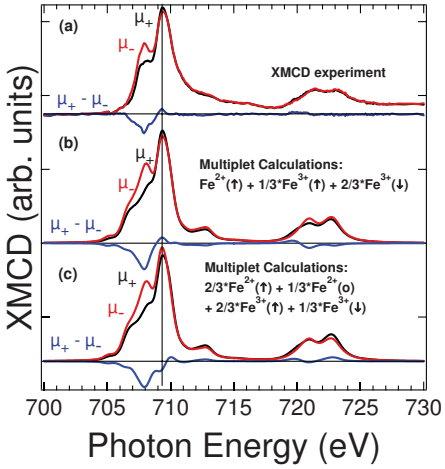

FIG. 3. (Color online) (a) Fe L edge XMCD performed at 150 K, and (b) and (c) ligand field multiplet simulations considering different possible spin orderings.

the upper part of the graph, with ligand multiplet calculations in C_{3i} symmetry plotted in the lower part of the graph for comparison. The sample was cleaved at an ambient pressure of around 5×10^{-5} mbar and a temperature of around 80 K (nitrogen precooling) before being transferred into the helium cryostat with a pressure of around 5×10^{-8} mbar. The c axis of the $LuFe_2O_4$ single crystal was aligned parallel to the external applied magnetic field (6 T).

The Fe^{2+} and Fe^{3+} peaks of the L_3 edge are located at 708 and 709.5 eV, respectively. The Fe^{3+} contribution is somewhat higher than 50% (due to the relatively high ambient pressure during cleaving the sample), and we had to take into account an additional Fe^{3+} contribution in order to get the best fit to the XAS. A comparison of fluorescence yield to electron yield XAS measurements, not shown here, revealed a contribution of the additional Fe^{3+} signal in the TEY spectra of about 50% compared to the bulk signal. This signal has been assumed not to contribute to the XMCD signal. The Fe L_2-edge peaks are located at 721 and 723 eV with a shoulder at 720 eV. The experimental dichroic signal at the L_2 edge is very small, but the calculated dichroism at the L_2 edge is in agreement with experiment. The L_3 edge shows a clear dichroism at the Fe^{2+} peak, whereas a smaller dichroism at Fe^{3+} is of the opposite sign. This is a clear indication of all Fe^{2+} sites being in the majority-spin state, while 1/3 of the Fe^{3+} spin being in majority and 2/3 in minority. This configuration is also used for the multiplet calculations shown in Fig. 3(b) and gives a very good agreement with the experiments besides the shoulder at 707 eV, which is overestimated by the calculation. In particular the reversal sign in the XMCD between 708 and 709.5 eV visible in the experimental data is perfectly reproduced by the simulations. We also calculated a frustrated spin configuration according to Nagano *et al.*[22] The results are shown in Fig. 3(c). As one can see there are significant differences between the measured spectra and the simulations, indicating that the Fe ions are not in a spin frustrated ground state.

This nonfrustrated spin configuration results in a saturation magnetic moment of the spin moment of $4\mu_B-(2/3)5\mu_B+(1/3)5\mu_B=2.33\mu_B$/f.u., considering a purely ionic configuration. The maximal orbital moment for Fe^{2+} in a trigonal bipyramidal crystal field and in high spin state is $m_{orb}=\pm2\mu_B$/f.u. for the occupation of d_{xy} or $d_{x^2-y^2}$. Fe^{3+} in high spin state has no orbital moment due to completely filled spin-up states and completely empty spin-down states. This results in a maximal total magnetic moment of $m_{tot}=2.33\mu_B$/f.u.$+2\mu_B$/f.u.$=4.33\mu_B$/f.u. In our experiment the spin and orbital sum rules give a spin magnetic moment equal to $1.1\mu_B$/f.u. and an orbital moment of $0.76\mu_B$/f.u. The simulated spectra and the expectation values obtained from the multiplet program were used to calculate a correction factor of 0.55 for the spin sum rule. The simulated spectra and the expectation values obtained from the multiplet program were used to calculate a correction factor to the effective spin sum rule. The correction factor found is 0.55, which also corrects for the non-negligible value of the magnetic dipole term (T_z) found to be 0.1 from the Fe^{2+} simulations. The relatively high orbital moment can be explained by the anisotropy induced by the bipyramidal local environment, and it can be also determined from the multiplet calculation of Fe^{2+}. The orbital moment is the reason for the spin-lattice interaction, and the magnetic easy axis is set by the orbital moment, which is fixed in the lattice by the electron configuration. Thus, this result clearly supports the model finding a $\sqrt{3}\times\sqrt{3}$ CO ground state including significant intersheet spin-exchange interactions.[20,21]

In conclusion, we performed an electronic structure investigation of the charge frustrated multiferroic $LuFe_2O_4$ with special emphasis on the charge ordered phase at room temperature, leading to a detailed picture of the electronic and magnetic properties. We identified the electronic states of the valence band by means of valence-band XPS and XES, and GGA+U first-principles calculations. Fe L-edge XMCD and multiplet simulations demonstrate a strong coupling between the charge order and the magnetic structure of $LuFe_2O_4$. Furthermore, the quite large orbital moment found may enhance the magnetoelectric coupling.

Part of this work was performed at the Advanced Light Source (ALS), Lawrence Berkeley National Laboratory, Berkeley, USA, which is operated under Contract No. DE-AC03-76SF00098. M.R. gratefully acknowledges financial support of the GRK695: Nonlinearities of optical materials. C.T. and M.P. were supportedd by the Lichtenberg program of the Federal State of Lower Saxony.

*Present address: University of Ulm, Institut für Festkörperphysik, Albert-Einstein-Allee 11, D-89069 Ulm, Germany; karsten.kuepper@uni-ulm.de

†mraekers@uos.de

‡mneumann@uos.de

[1] N. A. Hill, J. Phys. Chem. B **104**, 6694 (2000).

[2] J. Wang *et al.*, Science **299**, 1719 (2003).

[3] M. Fiebig, J. Phys. D: Appl. Phys. **38**, R123 (2005).

[4] S.-W. Cheong and M. Mostovoy, Nature Mater. **6**, 13 (2007).

[5] N. Hur, S. Park, P. A. Sharma, J. S. Ahn, S. Guha, and S.-W. Cheong, Nature (London) **429**, 392 (2004).

[6] M. Sakai, A. Masuno, D. Kan, M. Hashisaka, K. Takata, M. Azuma, M. Takano, and Y. Shimakawa, Appl. Phys. Lett. **90**, 072903 (2007).

[7] N. Ikeda *et al.*, Nature (London) **436**, 1136 (2005).

[8] M. A. Subramanian, T. He, J. Chen, N. S. Rogado, T. G. Calvarese, and A. W. Sleight, Adv. Mater. **18**, 1737 (2006).

[9] J. Kim, S. B. Kim, C. U. Jung, and B. W. Lee, IEEE Trans. Magn. **45**, 2608 (2009).

[10] M. Isobe *et al.*, Acta Crystallogr., Sect. C: Cryst. Struct. Commun. **46**, 1917 (1990).

[11] Y. Yamada, K. Kitsuda, S. Nohdo, and N. Ikeda, Phys. Rev. B **62**, 12167 (2000).

[12] N. Ikeda *et al.*, Ferroelectrics **314**, 41 (2005).

[13] L. J. Zeng, H. X. Yang, Y. Zhang, H. F. Tian, C. Ma, Y. B. Qin, Y. G. Zhao, and J. Q. Li, EPL **84**, 57011 (2008).

[14] C. Li, X. Zhang, Z. Cheng, and Y. Sun, Appl. Phys. Lett. **93**, 152103 (2008).

[15] M. Angst *et al.*, Phys. Rev. Lett. **101**, 227601 (2008).

[16] X. S. Xu *et al.*, Phys. Rev. Lett. **101**, 227602 (2008).

[17] W. Wu *et al.*, Phys. Rev. Lett. **101**, 137203 (2008).

[18] C.-H. Li, F. Wang, Y. Liu, X.-Q. Zhang, Z.-H. Cheng, and Y. Sun, Phys. Rev. B **79**, 172412 (2009).

[19] J. Wen, G. Xu, G. Gu, and S. M. Shapiro, Phys. Rev. B **80**, 020403(R) (2009).

[20] H. J. Xiang and M.-H. Whangbo, Phys. Rev. Lett. **98**, 246403 (2007).

[21] H. Xiang, E. Kan, S. Wei, M. Whangbo, and J. Yang, Phys. Rev. B **80**, 132408 (2009).

[22] A. Nagano, M. Naka, J. Nasu, and S. Ishihara, Phys. Rev. Lett. **99**, 217202 (2007).

[23] M. Naka, A. Nagano, and S. Ishihara, Phys. Rev. B **77**, 224441 (2008).

[24] J. Iida, S. Takekawa, and N. Kimizuka, J. Cryst. Growth **102**, 398 (1990).

[25] D. J. Singh, *Planewaves, Pseudopotentials and the LAPW Method* (Kluwer Academic Publishers, Boston, 1994), p. 115.

[26] P. Blaha, K. Schwarz, G. K. H. Madsen, J. Kvasnicka, and D. Luitz, *An Augmented Plane Wave+Local* Orbitals Program for Calculating Crystal Properties (Karlheinz Schwarz, Techn. Universität Wien, Wien, Austria, 2001).

[27] F. M. F. de Groot, J. Electron Spectrosc. Relat. Phenom. **62**, 111 (1993).

[28] F. M. F. de Groot and A. Kotani, *Core Level Spectroscopy of Solids*, Advances in Condensed Matter Science (CRC Press, Boca Raton, FL, 2008).

[29] A. Winiarski, T. Neumann, B. Mayer, G. Borstel, and M. Neumann, Phys. Status Solidi B **183**, 475 (1994).

[30] D. I. Khomskii and K. I. Kugel, Phys. Rev. B **67**, 134401 (2003).

Chapter 2

Publication H5

[**H5**] K. Kuepper, O. Kuschel, N. Pathé, T. Schemme, J. Schmalhorst, A. Thomas, E. Arenholz, M. Gorgoi, R. Ovsyannikov, S. Bartkowski, G. Reiss, and J. Wollschläger. *Electronic and magnetic structure of epitaxial NiO/Fe_3O_4 heterostructures grown on MgO(001) and Nb-doped $SrTiO_3$(001)*, Phys. Rev. B **94**, 024401 (2016), doi: 10.1103/PhysRevB.94.024401.

Electronic and magnetic structure of epitaxial Fe_3O_4(001)/NiO heterostructures grown on MgO(001) and Nb-doped $SrTiO_3$(001)

K. Kuepper,[1,*] O. Kuschel,[1] N. Pathé,[1] T. Schemme,[1] J. Schmalhorst,[2] A. Thomas,[2,3] E. Arenholz,[4] M. Gorgoi,[5] R. Ovsyannikov,[4] S. Bartkowski,[1] G. Reiss,[2] and J. Wollschläger[1]

[1]*Department of Physics and Center of Physics and Chemistry of New Materials, Osnabrück University, 49076 Osnabrück, Germany*

[2]*Center for Spinelectronic Materials and Devices, Physics Department, Bielefeld University, Universitätsstraße 25, 33615 Bielefeld, Germany*

[3]*Leibniz Institute for Solid State and Materials Research Dresden (IFW Dresden), Institute for Metallic Materials, Helmholtzstraße 20, 01069 Dresden, Germany*

[4]*Advanced Light Source, Lawrence Berkeley National Laboratory, California 94720, USA*

[5]*Helmholtz-Zentrum für Materialien und Energie GmbH, 12489 Berlin, Germany*

(Received 29 September 2015; revised manuscript received 25 April 2016; published 1 July 2016)

We study the underlying chemical, electronic, and magnetic properties of a number of magnetite-based thin films. The main focus is placed onto Fe_3O_4(001)/NiO bilayers grown on MgO(001) and Nb-$SrTiO_3$(001) substrates. We compare the results with those obtained on pure Fe_3O_4(001) thin films. It is found that the magnetite layers are oxidized and Fe^{3+} dominates at the surfaces due to maghemite (γ-Fe_2O_3) formation, which decreases with increasing magnetite layer thickness. For layer thicknesses of around 20 nm and above, the cationic distribution is close to that of stoichiometric Fe_3O_4. At the interface between NiO and Fe_3O_4 we find the Ni to be in a divalent valence state, with unambiguous spectral features in the Ni $2p$ core level x-ray photoelectron spectra typical for NiO. The formation of a significant $NiFe_2O_4$ interlayer can be excluded by means of x-ray magnetic circular dichroism. Magneto-optical Kerr effect measurements reveal significant higher coercive fields compared to magnetite thin films grown on MgO(001), and an altered in-plane easy axis pointing in the ⟨100⟩ direction. We discuss the spin magnetic moments of the magnetite layers and find that a thickness of 20 nm or above leads to spin magnetic moments close to that of bulk magnetite.

DOI: 10.1103/PhysRevB.94.024401

I. INTRODUCTION

Transition metal oxides display a remarkable variety of properties as functions of the complex interplay among the electron charge, spin, and orbital degree of freedom. Among many other transition metal oxides, as, for instance, perovskite-based manganites, ferrites, or cuprates, the oldest known magnetic material, namely magnetite (Fe_3O_4), is of special interest in current condensed matter and thin film physics. This fact stems partly from fundamental aspects as the high Curie temperature (860 K) for bulk material with a magnetic saturation moment of 4.07 μ_B per formula unit [1,2], the Verwey transition taking place at around 120 K [3,4], as well as the predicted 100% spin polarization of Fe_3O_4 [5], and partly from this material being of special interest for various applications in medicine, catalysis, and in particular future spintronic devices such as spin valves or magnetic tunnel junctions [6–9]. Recent approaches are pointing towards the synthesis of so-called all-oxide devices, e.g., by epitaxial growth of Fe_3O_4 on $SrTiO_3$(001) substrates to obtain the desired magnetite properties for further incorporation into $Fe_3O_4/La_{0.7}Sr_{0.3}MnO_3$ spin valves [10]. Another promising route to build a full oxide spin valve is to employ exchange bias between a ferro(i)magnetic and an antiferromagnetic oxide to manipulate the magnetization state of magnetite [11]. Such an exchange interaction can be realized by coupling of Fe_3O_4 with antiferromagnetic NiO in thin film heterostructures [11–13]. However, for the optimization of such potential all-oxidic devices as mentioned above, detailed characterization and understanding of the underlying structural, chemical, electronic, and magnetic properties of the thin films and the interfaces, e.g., between magnetite and the substrate or the antiferromagnetic NiO are indispensable.

The lattice mismatch between magnetite (bulk lattice constant 0.83963 nm) and the doubled MgO bulk lattice constant (0.42117 nm) is only 0.3%, making MgO an optimal candidate for epitaxial magnetite growth, which has been demonstrated many times using various deposition techniques [14–19]. There are quite a few works on Fe_3O_4/NiO bilayers and multilayers, mostly grown on MgO, investigating the structural properties of the heterostructures and the nature of exchange interaction between magnetite and (the antiferromagnetic) nickel oxide [13,20–22].

Thin magnetite films grown on $SrTiO_3$(001) allow tuning the conductivity via Nb doping, which is of interest for some important applications. Quite a few studies reveal altered magnetic properties such as a strongly increased coercive field compared to films grown on MgO [23,24]. Furthermore, Monti *et al.* recently report that the magnetic easy axis points along the in-plane ⟨100⟩ film directions [25] rather than the ⟨110⟩ directions for the easy axis mostly reported for $SrTiO_3$ [26] and MgO [19,27]. Despite the large lattice mismatch of −7.5% between the doubled $SrTiO_3$ bulk lattice constant (0.3905 nm) and magnetite, at least some of the thin films appear to grow almost relaxed on the $SrTiO_3$(001) surface [25,28], and hence the reason of the altered magnetic properties including the role of epitaxial strain and potential formation of antiphase domain boundaries (APBs) is still under discussion. As to coupled Fe_3O_4/NiO bilayers grown on $SrTiO_3$, up to now only Pilard *et al.* have reported on the magnetic properties of the Fe_3O_4/NiO interface [29].

*kkuepper@uos.de

They found evidence for a 1.5-nm-thick $NiFe_2O_4$ interfacial layer. An enhanced interfacial magnetization was also found by Krug *et al.*, who presented a rather complete study of the interfacial coupling of ultrathin NiO films grown on differently oriented Fe_3O_4 single crystals [30,31].

Since the orientation of the interface is of utmost importance for the magnetic properties in oxidic thin film systems, we want to perform a comprehensive study of Fe_3O_4(001)/NiO bilayers grown by reactive molecular beam epitaxy (RMBE) on MgO(001) and Nb-doped $SrTiO_3$(001) substrates, respectively. We investigate the electronic structure and the chemical composition by means of depth-selective hard x-ray photoelectron spectroscopy (HAXPES) and x-ray magnetic circular dichroism (XMCD) at the Fe $L_{2,3}$ and Ni $L_{2,3}$ edges. This complementary x-ray spectroscopic approach, along with magneto-optical Kerr effect (MOKE) measurements, allows us to develop a detailed picture of the overall electronic and magnetic structure of the magnetite-based bilayers in question. We compare our results with those obtained on pure magnetite thin films grown under equivalent conditions on Nb-$SrTiO_3$(001) and recent investigations reported in the literature.

II. EXPERIMENTAL AND THEORETICAL DETAILS

Preparation of the Fe_3O_4/NiO heterostructures and in situ characterization by means of low energy electron diffraction (LEED) and XPS have been performed in a multichamber ultra-high-vacuum system. The XPS system is equipped with a Phoibos HSA 150 hemispherical analyzer and an Al Kα anode (1486.6 eV), leading to an information depth ($\sim$3-nm mean free path) of about 5 nm in the case of magnetite. Prior to thin film deposition the MgO(001) and $SrTiO_3$ (doped with 0.05 wt% Nb) substrates were cleaned by heating them up to 400 °C at an oxygen partial pressure of 1×10^{-4} mbar for 1 h. Afterward the quality of the substrates was checked by LEED. In the next step NiO layers were deposited under an oxygen partial pressure of 1×10^{-5} mbar at a substrate temperature of 250 °C (in order to prevent any Mg interdiffusion in the case of MgO) [32]. After checking the quality of the NiO surfaces by LEED and XPS, the magnetite layers were grown on top of the NiO films at 250 °C and an oxygen partial pressure of 5×10^{-6} mbar. Subsequently LEED and XPS were performed in situ in order to check the magnetite surface reconstruction and chemical composition.

Then the samples were transported under ambient conditions for further characterization. MOKE measurements were conducted with a longitudinal setup and a HeNe laser. The Kerr rotation was measured with help of a photoelastic modulator (PEM). For the HAXPES experiments we used the HIKE endstation of the KMC-1 beamline of the BESSY II synchrotron facility [33]. Spectra were recorded at photon energies ranging from 2.2 to 9.6 keV, using the Si double-crystal monochromator with (111) orientation over the entire energy range. The samples were aligned at 3° grazing incidence to the incoming x-ray beam. The Scienta R4000 photoelectron analyzer was normal to the sample surface, and the analyzer resolotion was set to 0.25 eV. All HAXPES were taken at room temperature, as well as the XMCD spectra performed at the Fe $L_{2,3}$ and Ni $L_{2,3}$ edges at beamline 6.3.1 of the Advanced Light Source, Lawrence Berkeley Laboratory. We utilized total electron yield (TEY) as detection mode, which is mainly sensitive to the surface near region. The external magnetic field of 1.5 T was aligned parallel to the x-ray beam and reversed at each energy. The angle between sample surface and x-ray beam was 30°. The degree of circular polarization was about 55%.

TABLE I. Sample abbreviations (used in the text for brevity) and thin film thicknesses (in parentheses) as determined from x-ray reflectivity (XRR) experiments.

Sample	Substrate	Thin film layer(s)			
S1	$SrTiO_3$	Fe_3O_4	(12.3 nm)		
S2	$SrTiO_3$	Fe_3O_4	(21.5 nm)		
S3	$SrTiO_3$	Fe_3O_4	(33.0 nm)		
SN1	$SrTiO_3$	NiO	(5.0 nm)	Fe_3O_4	(6.2 nm)
SN2	$SrTiO_3$	NiO	(9.7 nm)	Fe_3O_4	(9.6 nm)
SN3	$SrTiO_3$	NiO	(10.3 nm)	Fe_3O_4	(20.7 nm)
M1	MgO	Fe_3O_4	(20.0 nm)		
MN1	MgO	NiO	(5.2 nm)	Fe_3O_4	(6.1 nm)
MN2	MgO	NiO	(11.5 nm)	Fe_3O_4	(10.5 nm)
MN3	MgO	NiO	(8.2 nm)	Fe_3O_4	(21.5 nm)

For the analysis of the Fe $L_{2,3}$ XMCD spectra, we performed corresponding model calculations within the atomic multiplet and crystal field theory, including charge transfer using the program CTM4XAS [34,35].

III. RESULTS AND DISCUSSION

The Fe_3O_4/NiO bilayers were synthesized using the same setup and using the same growth conditions described very recently by Schemme *et al.* [22]; see also the experimental section. All cleaned MgO(001) and $SrTiO_3$(001) substrates were checked by means of LEED for the expected (1 × 1) structure. Subsequently to each layer deposition, the NiO and magnetite layers were investigated for the typical NiO (1 × 1) LEED pattern and the characteristic $(\sqrt{2} \times \sqrt{2})R45°$ superstructure for Fe_3O_4. Ni $2p$ and Fe $2p$ XPS core levels confirm the formation of stoichiometric NiO and Fe_3O_4 deposited on MgO(001) and $SrTiO_3$(001). These data are discussed in detail along with a comprehensive structural analysis elsewhere [36]. Here we only sum up the results for the layer thicknesses (determined by x-ray reflectivity (XRR)) in Table I in order to report on the thickness dependence of the electronic structure and magnetic properties.

A. Electronic structure: Hard x-ray photoelectron spectroscopy (HAXPES)

In this section we want to clarify the chemical properties of the thin film surfaces and interfaces in detail. HAXPES measurements have been demonstrated to be a powerful tool for chemical depth profile and hence the characterization of buried layers and interfaces [37,38]. All HAXPES measurements presented in Figs. 1 to 3 are recorded in the geometry described in Sec. II. The probing or information depth (ID(95)) is defined as the depth from which 95% of the photoelectrons of the spectra come from. ID(95) can be derived by the following equation [39]: $ID(95) = \lambda_{IMFP}\cos(\alpha)\ln(1 - 95/100)$. Here α represents the off-normal emission angle. λ_{IMFP} is the inelastic mean free path of the

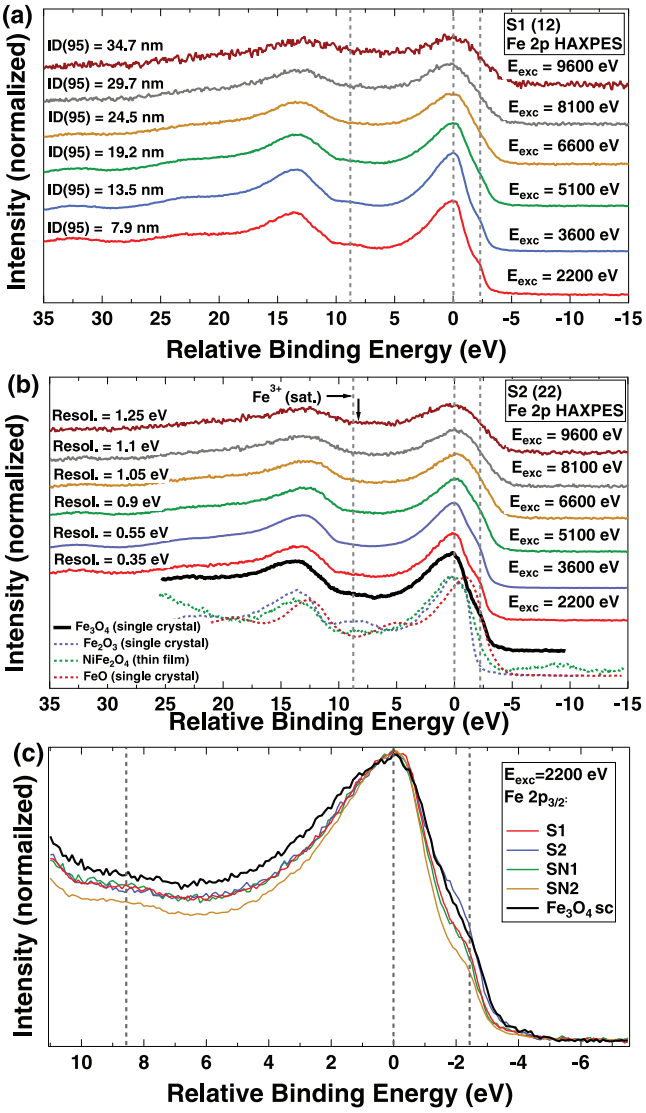

FIG. 1. Fe $2p$ HAXPES of samples **S1** (a) and **S2** (b) recorded at excitation energies between 2200 and 9600 eV. Reference spectra of FeO, Fe_3O_4, $NiFe_2O_4$, and Fe_2O_3 [42] are also shown for comparison. (c) Fe $2p_{3/2}$ core level of samples **S1**, **S2**, **SN1,** and **SN2** recorded at $E_{exc} = 2200$ eV.

photoelectrons. We derive λ_{IMFP} for the Fe_3O_4 top layers of the thin films and bilayers by employing the TTP-2 equation [40,41] and subsequently use the equation for calculating ID(95) to estimate the overall information depth. The resulting information depths for magnetite are denoted in Fig. 1(a) for each excitation energy, whereas in Fig. 1(b) the overall resolutions (beamline plus analyzer) of the spectra are given.

Figure 1 displays the Fe $2p$ spectra performed at excitation energies between 2200 and 9600 eV of samples **S1** and **S2**. The spectra have been normalized and rescaled to the Fe $2p_{3/2}$ maximum, so comparison between the spectra is straightforward. For stoichiometric Fe_3O_4 one expects the Fe $2p_{3/2}$ binding energy at around 710.6 eV (0 eV on the relative binding energy scale chosen here) and a structureless region between the Fe $2p_{3/2}$ and the Fe $2p_{1/2}$ peaks without satellite peak as previously reported [43], since the charge transfer satellites add up in such a way for a mixed valence state found in Fe_3O_4. As to sample **S1** (12 nm) [Fig. 1(a)] there appears to be an excess of trivalent ions observed by means of the more surface-sensitive 2200-eV photon energy. For $E_{exc} = 2200$ eV the typical Fe^{3+} charge transfer satellite is also visible at 8.5 eV above the Fe $2p_{3/2}$ maximum (see also gray vertical line, corresponding to a binding energy of around 719 eV). However, also a pronounced shoulder located around 2.2 eV at the low binding energy side (corresponding to 708.4 eV binding energy) is present, indicating the presence of a significant amount of divalent iron ions [44]. We find no indications of metallic iron, which should manifest itself at 707 eV and thus 3.6 eV below the Fe $2p_{3/2}$ maximum on the relative binding energy scale chosen here. At higher excitation energies the Fe^{3+} charge transfer satellite is not visible anymore and the overall Fe $2p$ spectral shape indicates a stoichiometric 2:1 ratio of Fe^{3+} to Fe^{2+} ratio.

For the thicker Fe_3O_4 film **S2** (22 nm), the Fe^{3+} charge transfer satellite is less pronounced, while the feature stemming from Fe^{2+} is more pronounced in the $E_{exc} = 2200$ eV spectrum of **S2** compared to that of **S1** [see also Fig. 1(c)]. Thus, the excess of Fe^{3+} in the surface near layers is significantly reduced in comparison with sample **S1**. At higher excitation energies (5100 eV and above) the Fe $2p$ spectra of **S1** resemble that of magnetite. The Fe^{2+} characteristic low binding energy shoulder becomes less visible due to the limited resolution of the spectra at higher excitation energies ($E_{exc} = 6600$ eV and above). It is also noteworthy that the Fe $2p$ spectra of sample **S2** taken at 8100 and 9600 eV also exhibit a weak Fe^{3+} charge transfer satellite, indicating a potential slight excess of Fe^{3+} close to or at the interface between the magnetite thin film and the $SrTiO_3$. No such features are visible in the corresponding spectra of sample **S1**.

Very recently, Taguchi *et al.* reported a very interesting Fe $2p$ HAXPES feature concerning a magnetite single crystal [45]. They found a double peak structure of the Fe $2p_{3/2}$ peak at higher excitation energies (approx. 6–8 keV) which is not present in the soft x-ray photoelectron spectra. They associate this effect with the two distinct Fe species and the charge modulation at the B site. The results are supported by complementary experiments on a magnetized 100-nm-thick Fe_3O_4 thin film [45]. On the other hand Müller *et al.* performed Fe $2p$ HAXPES with excitation energies of 3–5 keV on 15- to 20-nm-thick Fe_3O_4 thin films grown on ZnO and MgO [46], which are very similar to the results presented here. We do not observe the bulk electronic state found by Taguchi *et al.*, who employed excitation energies up to 9600 keV. As to the beamline and analyzer settings used (cf. Sec. II), the overall resolution of the spectra taken at $E_{exc} = 8100$ eV is ~1.1 eV [cf. Fig. 1(b)]. Taguchi *et al.* obtained spectra with significantly higher resolution (0.17 eV) at an excitation energy of 7.95 keV [45]. Hence, this might be one reason for not seeing the double peak in the spectra presented here, despite the two peaks being separated by ~1.5 eV [45]. Another reason for this discrepancy might be the thin film thickness, as the bulk-like features seem to be suppressed within a ~10-nm surface layer [45]. Detailed investigations of the bulk electronic structure of magnetite thin films in relation to thin film thickness, substrate, temperature, and magnetic state under consideration of the overall spectra resolution would be highly desirable.

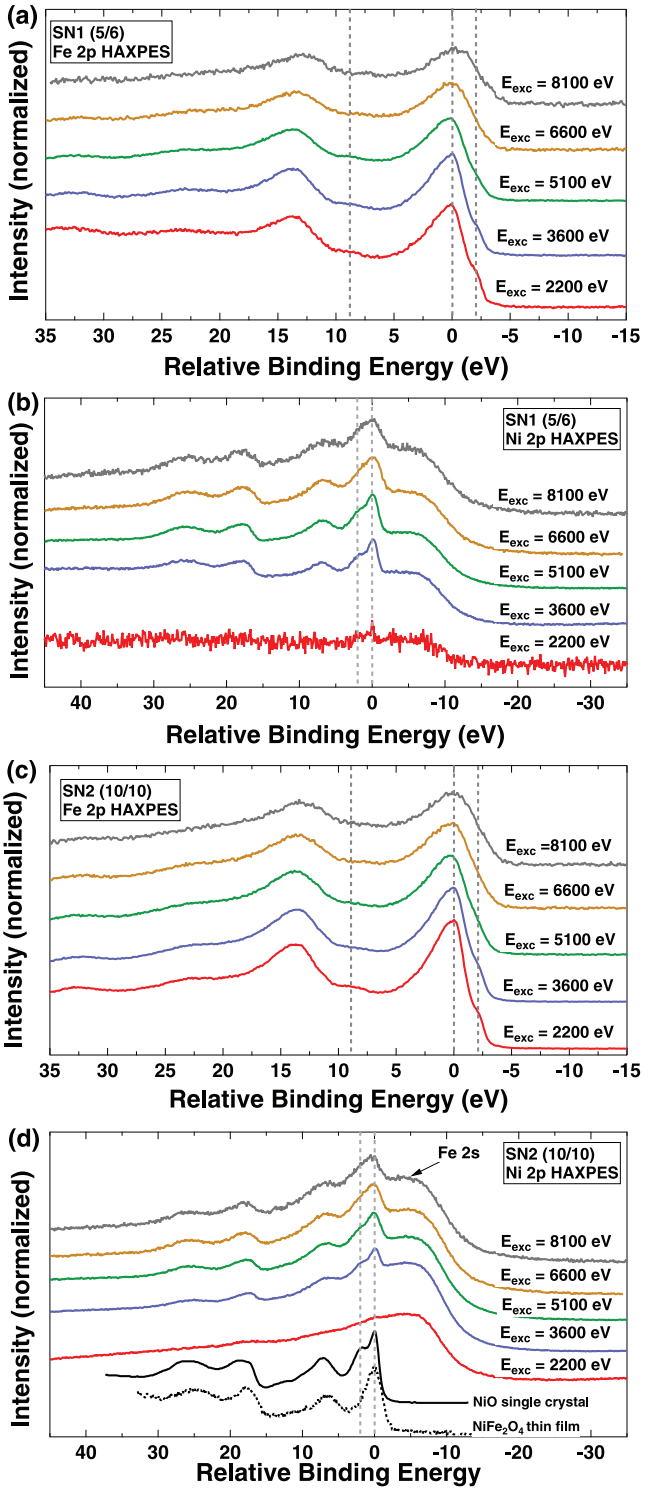

FIG. 2. HAXPE spectra of samples **SN1** and **SN2** recorded at excitation energies between 2200 and 8100 eV. (a) and (b) Fe $2p$ and Ni $2p$ HAXPES of sample **SN1**. (c) and (d) Fe $2p$ and Ni $2p$ HAXPES of sample **SN2**, reference spectra of NiO [47] and $NiFe_2O_4$ [42] are also shown for comparison.

Figure 2 depicts the Fe $2p$ and Ni $2p$ HAXPES of samples **SN1** and **SN2**. Similar to samples **S1** and **S2,** the Fe $2p$ spectra show a weak Fe^{3+} charge transfer satellite at $E_{exc} = 2200$ eV [Figs. 2(a) and 2(c)]. At higher excitation energies the spectra are identical to that of Fe_3O_4, even though in particular for sample **SN1** a weak Fe^{3+} charge transfer satellite is also present at higher excitation energies, indicating a small excess of trivalent ions at the interface between Fe_3O_4 and NiO [47]. The corresponding Ni $2p$ spectra are overlapped by broad Fe $2s$ states [Figs. 2(b) and 2(d)]. The overall shape of the Ni $2p$ spectra corresponds perfectly to that of NiO. Also the binding energies of the Ni $2p_{3/2}$ and Ni $2p_{1/2}$ main lines and the corresponding charge transfer satellites are typical for Ni^{2+}. Furthermore all Ni $2p$ spectra exhibit a prominent feature at the high binding energy side. The shoulder located 2 eV above the Ni $2p_{3/2}$ maximum [indicated by vertical lines in Figs. 2(b) and 2(d)] is a specific feature of bulk NiO [48], which has been associated with a nonlocal screening effect. The double structure is clearly visible in all Ni $2p$ spectra, even in the $E_{exc} = 2200$ eV spectrum of sample **SN1** due to the small Fe_3O_4 film thickness despite the rather poor signal-to-noise ratio. For sample **SN2** there is only the rather broad Fe $2s$ peak visible as the information depth is too low to probe the NiO layer at excitation energy 2200 eV.

The Fe $2p$ and Ni $2p$ HAXPES results confirm that stoichiometric Fe_3O_4 layers are formed on all samples investigated by HAXPES. Only small traces of Fe^{3+} excess might be found at the interface between Fe_3O_4 and $SrTiO_3$ of sample **S2** and the Fe_3O_4/NiO interface of sample **SN1**. At the surface of all magnetite top layers a certain degree of Fe^{3+} excess is found, indicating a potential maghemite (γ-Fe_2O_3) formation at the surface. It seems that thinner magnetite layers tend to enhance γ-Fe_2O_3 formation or, respectively, increase the amount of trivalent iron ions in the surface near layers. All Ni $2p$ spectra are, independent of the excitation energy, a quite perfect fingerprint of bulk NiO within the limits of this experiment. Hence, the formation of a $NiFe_2O_4$ interface layer or considerable amounts of $NiFe_2O_4$ islands or clusters can be excluded. Moreover, no Fe or Ni metallic contributions are investigated in the HAXPES spectra.

Next we will discuss the occupied total densities of states (tDOS) along the measured XPS valence band spectra (Fig. 3) in order to learn details about the electronic structure at the Fe_3O_4/NiO interface.

Figure 3(a) depicts the total densities of states of samples **S1**, **S2**, **SN1**, and **SN2** with those of Fe_3O_4, NiO, and $SrTiO_3$ single crystals. The latter spectra have been performed with a laboratory-based monochromatized Al Kα source (1486.6 eV). The valence band spectrum of sample **S2** is very similar to that of the Fe_3O_4 single crystal. For sample **S1** the region between 5 and 9 eV shows somewhat more intensity compared to single-crystal Fe_3O_4, likely due to contributions from the $SrTiO_3$ substrate. The valence band spectra of the double layers **SN1** and **SN2** are also quite similar to that of magnetite. However, in particular in the valence band of sample **SN1** there are a few differences in detail. It appears that feature A almost vanished in the valence band of sample **SN1**. As to theory [49,50], this feature stems mainly from t_{2g} spin-down states of octahedrally coordinated Fe cations. This trend is confirmed by the spectra taken at $E_{exc} = 3600$ eV [Fig. 3(b)]. Whereas feature A becomes weaker or vanishes in the XPS valence bands of samples **SN1** and **SN2**, feature B, representing the (localized) Ni $3d$ states of NiO becomes

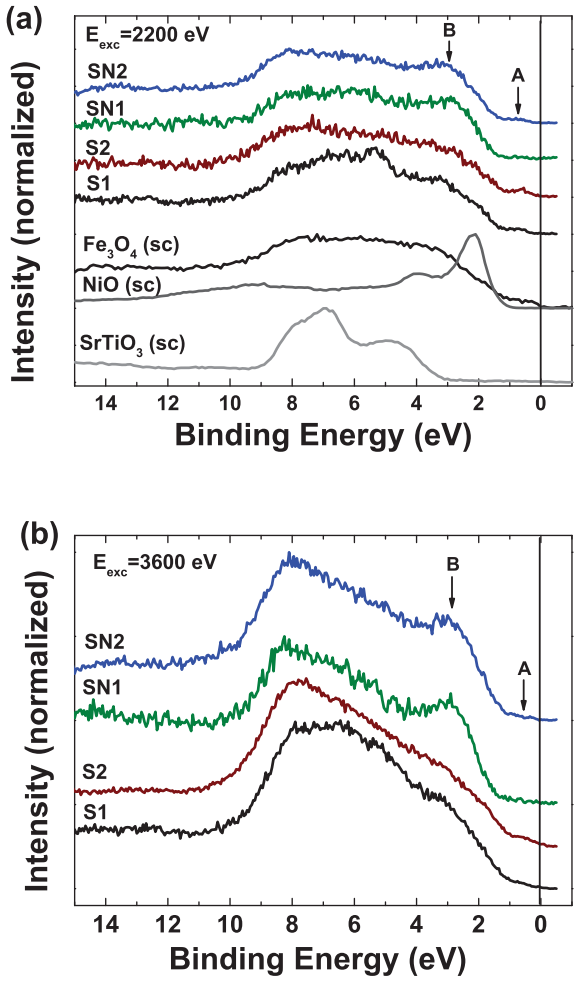

FIG. 3. HAXPES valence bands of samples **S1**, **S2**, **SN1,** and **SN2** recorded at excitation energies of 2200 eV (a) and 3600 eV (b). Reference spectra of $SrTiO_3$, NiO [47], and Fe_3O_4 are also shown for comparison.

stronger, confirming that also the interface and the underlying NiO layer is probed. The overall shape of the valence band spectra becomes different at excitation energy 3600 eV which is due to the different atomic cross sections at higher energies.

The valence band spectra presented in Fig. 3 recorded at $E_{exc} = 2200$ eV and 3600 eV can be understood as being a superposition of the electronic density of states of the Fe_3O_4 thin films, including the interfaces and partly the NiO buffer layers or the $SrTiO_3$ substrates, respectively. Therefore we cannot unambiguously discriminate between interface effects and size effects in the magnetite layer. We want to point out that a low density of states at the interface between Fe_3O_4 and NiO has been investigated before by growing ultrathin NiO layers onto an Fe_3O_4 single crystal and employing ultraviolet photoelectron spectroscopy (UPS) [51]. Another possible reason for the observed behavior is that thinner Fe_3O_4 films [e.g., 6 nm (sample **SN1**)] are different compared to somewhat thicker magnetite layers as to their electrical properties [52]. To further elucidate potential influences of different substrates or the presence of a buffer layer like NiO on the electronic structure near Fermi energy and hence the electrical properties, further complementary experiments such as resistivity measurements are highly desirable.

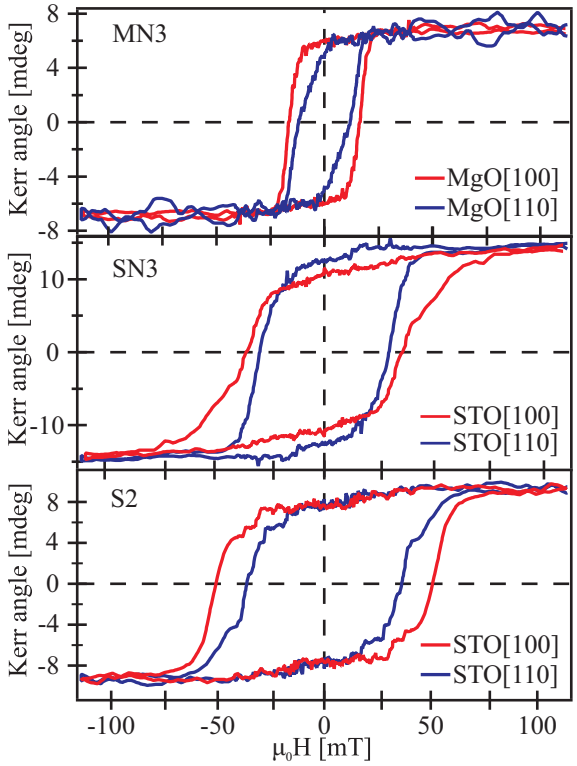

FIG. 4. Magnetization curves along the substrates [100] and [110] directions of samples **MN3** (top), **SN3** (center), and **S2** (bottom).

B. Magnetic properties: MOKE

Figure 4 depicts the magnetization curves for the ⟨100⟩ and ⟨110⟩ in-plane magnetic easy and hard directions of samples **MN3**, **SN3,** and **S2** probed by MOKE.

First, a significant increase of the coercive field is found compared to Fe_3O_4 films on MgO(001) [22]. This accounts in particular for the samples grown on Nb-$SrTiO_3$(001) substrates (**S2** and **SN3**). It is also noteworthy that a NiO buffer layer leads to an increase of the coercive field compared to corresponding Fe_3O_4 single layers in case of MgO(001) substrates but to a decrease of the coercive field in case of Nb-$SrTiO_3$(001) substrates. Whereas for Fe_3O_4/MgO(001) the magnetic in-plane easy axis (high coercive field) are aligned along the magnetite ⟨110⟩ direction [19,53,54], the other samples presented here have ⟨100⟩ in-plane magnetic easy axis as concluded from the higher coercive fields in these directions. The strong increase of the coercive field to around 50 mT in the easy magnetic direction as well as the rotated magnetic easy axis along the ⟨100⟩ in-plane directions have been recently also reported for thicker magnetite thin films (50–160 nm) grown by pulsed laser deposition on Nb-$SrTiO_3$(001) [25]. Obviously, a NiO buffer layer between the magnetite layer and the substrate seems to lead to a 45° rotated magnetic easy in-plane axis independent of the MgO or $SrTiO_3$(001) substrate compared to Fe_3O_4/MgO(001). Furthermore, assuming the one-domain Wohlfahrt-Stoner model, one would expect a

remanent magnetization M_r of $M_s/\sqrt{2}$ with respect to the saturation magnetization M_s for a hard magnetic direction due to geometric reasons. Smaller values of M_r, however, point to the formation of multiple domains. However, the remanence is about the same value in easy and hard directions for all three samples discussed here (cf. Fig. 4). Such an effect can be also seen for 20-nm thin magnetite films grown on $SrTiO_3$ (100) and $BaTiO_3$ (100) [54]. Potential reasons for this behavior concerning the magnetic easy axis rotation and remanent signal may stem from structural parameters such as interface structure and roughness or epitaxial strain [55], or from potential presence of antiphase domain boundaries (APBs), which may form during epitaxial thin film growth [25]. Another intriguing potential reason for the magnetic properties observed here is the fact that Krug *et al.* investigated an impact of the interface orientation on the magnetic coupling in particular in case of the (100) interface between NiO and magnetite [31]. They found a noncollinear orientation between the spin axis of the Fe_3O_4 and the NiO, which they associated with spin-flop coupling at the interface of ultrathin NiO films grown on (100)-oriented Fe_3O_4 single crystals [31]. A more complete study of the magnetic anisotropy, e.g., by means of angular resolved MOKE measurements and ferromagnetic resonance (FMR) experiments, is ongoing and will be presented elsewhere [36]. Moreover, the closer investigation of APB formation is an obstacle, and further work to understand and analyze the role of APBs by means of high-resolution TEM or LEEM/PEEM experiments during thin film growth would be desirable for thin magnetite films and heterostructures [25,31,56–59].

C. Magnetic properties: X-ray magnetic circular dichroism (XMCD)

Figure 5 presents the Ni $L_{2,3}$-edge x-ray Absorption (XA) spectra of sample **MN1** recorded at room temperature in an external magnetic field of ± 1.5T with circularly polarized light. The spectra show only a residual dichroic signal of 0.85%. The TEY detection mode is interface sensitive due to the $1/e$ probing depth [60]. Furthermore, the Ni $L_{2,3}$-XMCD should be rather strong in the case of a $NiFe_2O_4$ interlayer formation since in case of ultrathin films or spinel interfaces, a strongly enhanced magnetic moment due to proximity effects has been reported [61] and also found for ultrathin Fe_3O_4(110) films grown on NiO [30]. Krug *et al.* could even quantify the $NiFe_2O_4$ interlayer reconstruction to around one monolayer and deduced the Ni magnetic moments from the sum rules [30]. In contrast, the very weak Ni L_3-XMCD and within the experimental signal-to-noise ratio vanishing Ni L_2-XMCD (Fig. 5) indicate that there is no substantial formation of a $NiFe_2O_4$ interlayer or clusters at the interface between the Fe_3O_4(100) and the NiO layers studied in the present work. This result confirms the Ni $2p$ HAXPE spectra of samples **SN1** and **SN2**, as the corresponding Ni $2p$ HAXPES results of **SN1** and **SN2** indicate charge transfer satellites typical for NiO.

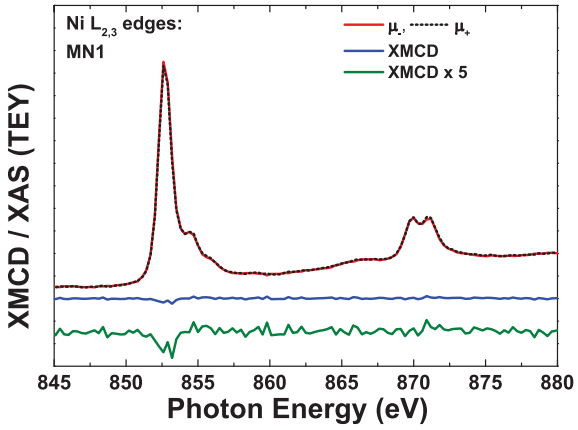

FIG. 5. Polarization-dependent x-ray absorption spectra performed at the Ni $L_{2,3}$ edges of samples **MN1** along with the resulting XMCD difference spectrum. The latter has been also multiplied by a factor of five for better visibility.

Turning to the Fe $L_{2,3}$ edges, Fig. 6(a) depicts the XA spectra taken at ± 1.5T of sample **MN1**, the resulting XMCD difference spectrum, and the integral of the XMCD. The lower panel of Fig. 6 shows the experimental XMCD of **MN1** along with the best fit obtained from an appropriate superposition of the single-ion charge-transfer multipet simulations plotted below.

The charge transfer multiplet spectra are calculated in the following way. In a first step, the Slater integrals and the spin-orbit couplings are calculated in spherical symmetry. The d–d and p–d integrals are reduced to 80% of their atomic value in order to account for screening, whereas the spin-orbit parameters are not reduced. Then crystal fields of $10Dq = 1.0$ eV (Fe^{2+}_{oct}, Fe^{3+}_{oct}) and -0.6 eV for the Fe^{3+}_{tet} using the crystal field approach of Kuiper *et al.*[62] as starting point. An exchange field $g\mu_B = 0.03$ eV is also applied. In a last step, charge transfer is considered. We find $\Delta = 6.0$ eV to lead to best agreement with the experimental data. We extract charge-transfer configurations of 89.7% $3d^6$ plus 10.3% $3d^7\underline{L}$ for Fe^{2+}_{oct}, 90.4% $3d^5$ plus 9.6% $3d^6\underline{L}$ for Fe^{3+}_{oct}, and an 89.6% $3d^5$ plus 10.4% $3d^6\underline{L}$ for Fe^{3+}_{tet}. At the Fe L_3 edge the calculated XMCD exhibits the typical three peaks expected for the inverse spinel structure of magnetite, indicating the antiferromagnetic alignment of the octahedrally coordinated Fe^{2+}_{oct} (feature A) and Fe^{3+}_{oct} (C) ions with the tetrahedrally coordinated Fe^{3+}_{tet} ions (B). The sum of the three calculated spectra, which may be shifted as to the energy scale since chemical bonding and band-like effects are not considered by the localized model [62], is used to fit the experimental spectra and estimate the cationic distribution of each magnetite thin film.

Figure 7(a) displays the Fe $L_{2,3}$ XMCD spectra and the corresponding fits for all samples discussed in this work. The cation distributions found are presented in a diagram [Fig. 7(b)]. We see that the iron cation distribution is significantly different from ideal magnetite for samples **S1**, **SN1**, and **MN1**, i.e., those samples with the thinnest iron oxide layers. These samples exhibit a lack of Fe^{2+}_{oct} but an excess of Fe^{3+}_{oct}. With increasing film thickness of the iron oxide layers the cation distribution converge towards that of stoichiometric Fe_3O_4, whereas a slight excess of Fe^{3+}_{oct} ions remains. The excess of Fe^{3+}_{oct} found in particular in the thinner films can likely be attributed to maghemite (γ-Fe_2O_3) formation. The thickness dependence points to the fact that

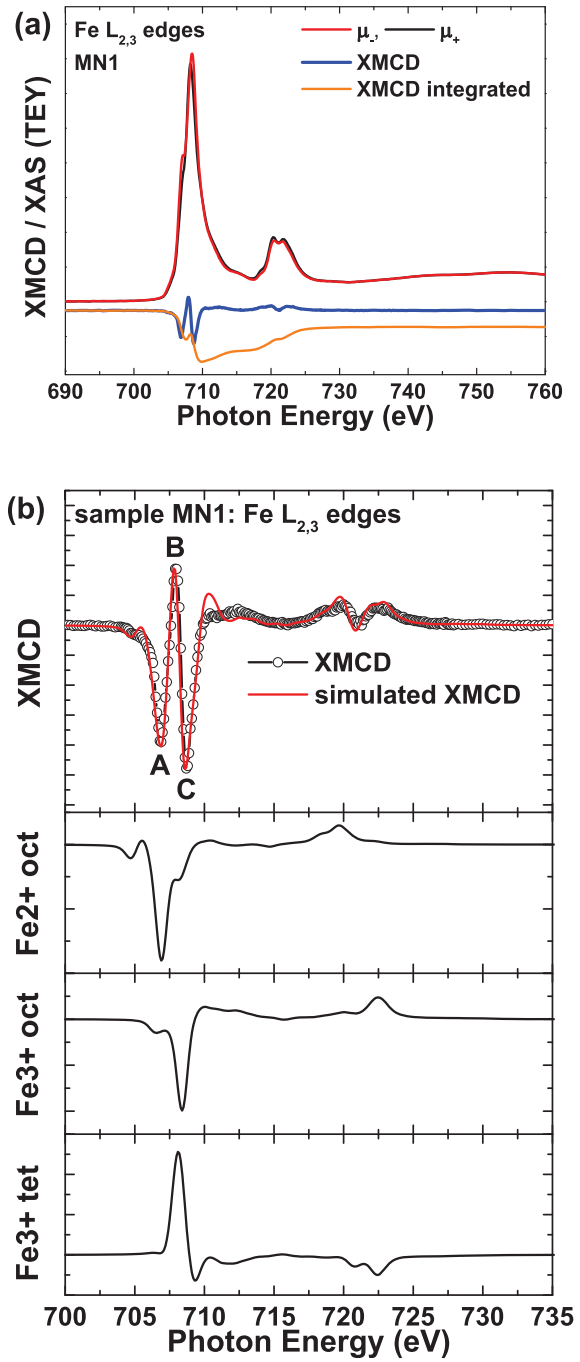

FIG. 6. (a) Polarization-dependent XA spectra performed at the Fe $L_{2,3}$ edges of sample **MN1** along with the resulting XMCD and its integral. (b) XMCD difference spectra and corresponding simulated fit as a result from summarizing the suitable amounts of the charge-transfer multiplet simulations of Fe^{2+} ions in octahedral coordination, and Fe^{3+} ions in octahedral and tetrahedral coordination, respectively.

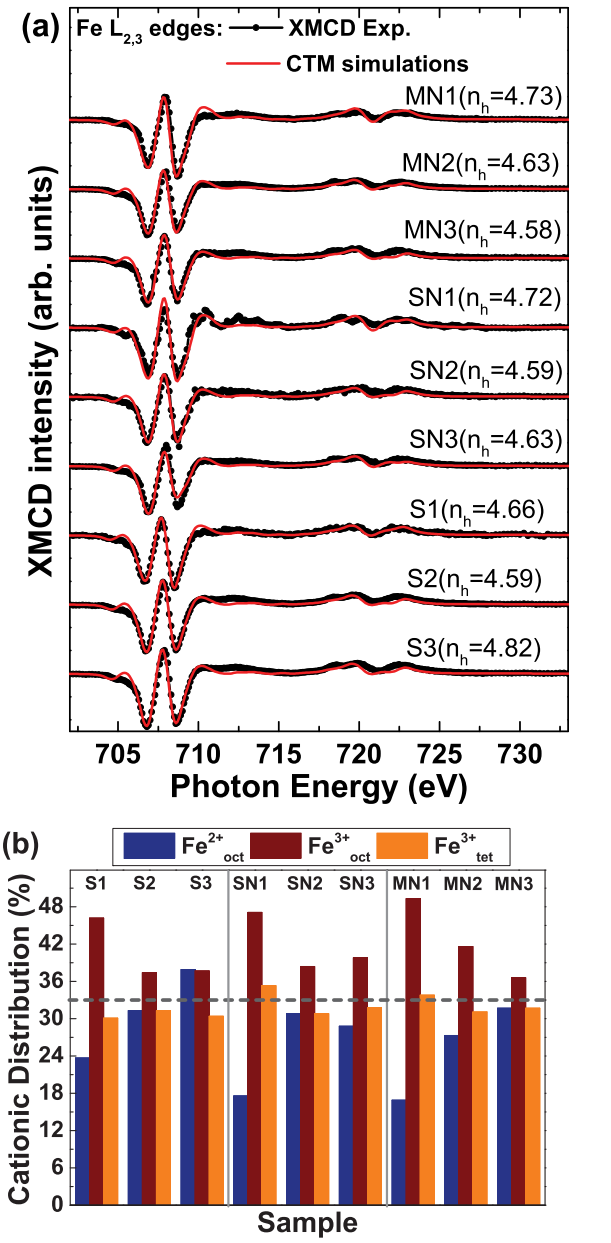

FIG. 7. (a) Fe $L_{2,3}$-XMCD spectra and the corresponding fits from CTM simulations for all samples investigated in this work. The average number of holes (n_h) per Fe atom as derived from the CTM simulations is also given in parentheses. (b) Cationic distribution of the divalent and trivalent iron ions in octahedral and tetrahedral coordinations as derived from the CTM simulations.

the maghemite is located at the thin film surfaces. Such an effect has been very recently investigated by Fleischer *et al.* [19,63], employing Raman spectroscopy. Fleischer *et al.* found on uncapped 4-nm Fe_3O_4 films on MgO(001) that most of the maghemite formation occurs within days under ambient conditions and then slows significantly down in the time frame of months [63]. As to the samples studied in this work, series **S** has been grown around 4 months and series **SN** and **MN** around 2–3 weeks prior to the XMCD experiments. The HAXPES experiments have been performed quite some time (over one year) after the thin film synthesis. Our experiments confirm a potential maghemite formation on the magnetite surfaces as to the cationic distribution determined from the XMCD experiments and the HAXPES spectra recorded at lower excitation energies. This applies in particular to the thin magnetite layers (~5 to 10 nm). However, thicker Fe_3O_4 thin

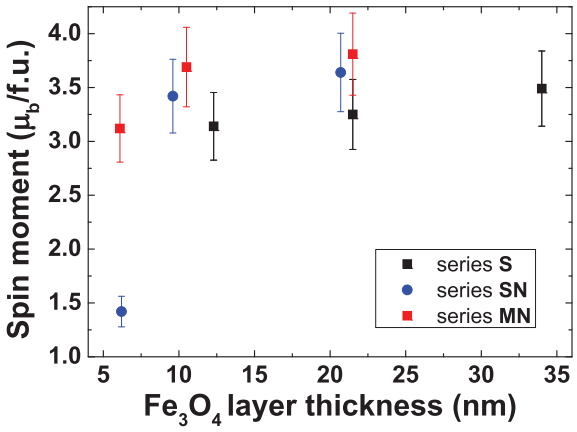

FIG. 8. Calculated magnetic spin moments in μ_B/f.u. from the XMCD spin sum rule.

films appear to be much more stable also at their surfaces. This is obvious a couple of months and over one year after synthesis (see, e.g., Fe $L_{2,3}$-XMCD analysis of samples **S2** and **S3** and HAXPES results of sample **S2**). Furthermore the total electron yield used to measure the XMCD spectra is known to be rather surface sensitive in the soft x-ray regime. For the Fe $L_{2,3}$ resonances of iron oxides the probing depth has been estimated to be around 0.8–3 nm [64,65]. As the thinnest magnetite layers investigated here are around 6 nm (**MN1** and **SN1**) we can assume that the XA and XMCD spectra stem from the first few nanometers and are not influenced by the substrate or the interface to the NiO buffer layer. Hence, we find a very different rate of maghemite formation within the first few 2–3 nm of the magnetite layers in dependence of the overall film thickness. Within the limits of the experiment, Fe_3O_4 layers with thickness $\geqslant$ 20 nm exhibit an almost stoichiometric magnetite cation distribution, independent from the substrate or the presence of a NiO buffer layer [see also Fig. 7(b)]. Similar results have been recently reported for magnetite thin films directly deposited in MgO(001) substrates [19].

Next we will discuss the magnetic spin moments determined by the spin sum rule. We limit our analysis to the spin magnetic moment which represents approximately 90% or more of the overall magnetic moment in iron oxides. We want to note that the orbital moment in magnetite is still under discussion in the literature [64,66,67], but a precise determination would require more intricate experiments and an extended energy range, which are beyond the scope of this work.

In order to extract the spin magnetic moments we use the spin sum rule developed by Chen *et al.* [68]. The number of holes are determined from the charge transfer multiplet simulations for each sample. We also account for the core hole interactions which mix the character of the L_3 and L_2 edges [69,70] by considering the spin sum rule correction factors obtained by Teramura *et al.* [69]. The spin magnetic moments are depicted in Fig. 8. One can see that an increasing magnetite layer thickness results in a higher spin moment. Samples **S2**, **SN3,** and **MN3** exhibit spin magnetic moments of 3.3, 3.6, and 3.8 μ_B/f.u., respectively. These results (excluding the orbital magnetic moment) are rather close to the bulk magnetic moment of Fe_3O_4 [1]. The thinner films have decreased spin moments, which might be partly due to maghemite formation on the very surface layer of these films. However, this cannot explain in particular the rather low spin moment found for sample **SN1** (which exhibits a very similar cationic distribution as sample **MN1**), 1.45 μ_B/f.u., which is the same value reported for a 2.5-nm Fe_3O_4 thin film on $BaTiO_3$ [71]. One possible reason for this might stem from epitaxial strain [36]. However, as well as sample **SN1,** also samples **SN2** and **SN3** show slight tensile strain [36] of less than 1% compared to the bulk value of Fe_3O_4 and have spin magnetic moments close to that found for the respective samples from series **MN**, and the latter ones exhibit slight compressive strain [36] of less than 1% in vertical direction. Another potential reason for this reduced spin moment might be connected with the higher roughness of the Fe_3O_4 layer, which is found to be 0.45 nm for sample **SN1**, since all other magnetite layers from series **SN** and **MN** have lower roughnesses of approximately 0.3 nm [36]. Finally, the formation of antiphase boundaries within magnetite thin films has been previously attributed to reduced magnetic moments [10,72]. The spin moment of sample **MN1** (3.1 μ_B/f.u.) is comparable to that very recently reported for Fe_3O_4(001) thin films grown on Ag(001) of similar thicknesses [65]. Except for sample **SN1,** we find significant higher spin magnetic moments for our thin films than observed for similar (001)-oriented Fe_3O_4 films grown on MgO(001) substrates [72].

IV. SUMMARY

In summary, we performed a comprehensive electronic and magnetic structure investigation of thin magnetite films and Fe_3O_4(001)/NiO bilayers grown on MgO(001) and Nb-$SrTiO_3$(001) by means of RMBE. In situ characterization using LEED and XPS shows formation of epitaxial and stoichiometric NiO layers and Fe_3O_4 thin films. Thicknesses of the NiO layers is varied between 6 and 12 nm and those of the Fe_3O_4 layers varied between 5 and 33 nm as to XRR measurements. Further electronic and chemical properties are tackled by HAXPES experiments with variable excitation energy. All thin films appear to comprise stoichiometric magnetite and NiO in deeper layers and at the interface. However, thinner Fe_3O_4 films (below 10 nm) tend to form Fe^{3+} on the very surface, likely in form of maghemite. MOKE magnetization curves show significant increased magnetic coercive field and that the in-plane magnetic axis are aligned in ⟨100⟩ in-plane directions, whereas the remanence has the same value along the magnetic easy and hard axes. Reasons for this magnetic behavior might be due to different reasons such as antiphase domain boundaries (APBs) or spin-flop coupling at the (100) interface between magnetite and NiO. We employ element-specific XMCD at the Fe $L_{2,3}$ edges to tackle the iron cationic distribution in detail. In agreement with the HAXPES we find a lack of Fe^{2+} at the surface of, in particular, the thinner magnetite layers investigated in the framework of this study. Thicker films are close to stoichiometric cation distribution also at their surface and exhibit spin magnetic moments close to that known from bulk material, whereas thinner samples ($<$10 nm) show only somewhat reduced spin moments. The only exception is the sample with 5-nm NiO and 6-nm Fe_3O_4

bilayers grown on Nb-$SrTiO_3$(001) (**SN1**); here a significantly reduced spin moment is found.

In conclusion we demonstrate that the interface of ferrimagnetic Fe_3O_4 and antiferromagnetic NiO leads to a low concentration of Fe t_{2g} spin-down states present directly at the interface. The γ-Fe_2O_3 formation seems to be less intense on the surface of thicker (uncapped) magnetite layers ($\geqslant$20 nm) than found for thin layers even in time frames of several months to one year under ambient conditions, which might be interesting for potential applications. The altered electronic and magnetic properties as the density of states near Fermi level, magnetic coercive field, and anisotropy deserve further future investigations. An improved understanding could open an avenue for tailoring the desired magnetic properties by choosing an appropriate set of substrate, layer thicknesses, and preparation parameters.

ACKNOWLEDGMENTS

Financial support by the Deutsche Forschungsgemeinschaft (DFG) (KU2321/2-1) is gratefully acknowledged. Part of this work has been performed at the Advanced Light Source, ALS, Lawrence Berkeley National Laboratory, Berkeley, USA, which is operated under Contract No. DE-AC03-76SF00098. We acknowledge Helmholtz-Zentrum Berlin for provision of synchrotron radiation beam time at beamline KMC-1 of Bessy II.

[1] P. Weiss and R. Forrer, Ann. Phys. (Paris) **12**, 279 (1929).
[2] P. I. Slick, *Ferromagnetic Materials: A Handbook on the Properties of Magnetically Ordered Substances,* edited by E. P. Wohlfarth (North-Holland Publishing Company, Amsterdam, 1980).
[3] E. J. W. Verwey, Nature (London) **144**, 327 (1939).
[4] M. S. Senn, J. P. Wright, and J. P. Attfield, Nature (London) **481**, 173 (2012).
[5] M. I. Katsnelson, V. Y. Irkhin, L. Chioncel, A. I. Lichtenstein, and R. A. de Groot, Rev. Mod. Phys. **80**, 315 (2008).
[6] I. Zutic, J. Fabian, and S. Das Sarma, Rev. Mod. Phys. **76**, 323 (2004).
[7] V. Drewello, M. Schäfers, O. Schebaum, A. A. Khan, J. Muenchenberger, J. Schmalhorst, G. Reiss, and A. Thomas, Phys. Rev. B **79**, 174417 (2009).
[8] R. Bliem, E. McDermott, P. Ferstl, M. Setvin, O. Gamba, J. Pavelec, M. A. Schneider, M. Schmid, U. Diebold, P. Blaha *et al.*, Science **346**, 1215 (2014).
[9] J. M. Byrne, N. Klueglein, C. Pearce, K. M. Rosso, E. Appel, and A. Kappler, Science **347**, 1473 (2015).
[10] J. A. Moyer, R. Gao, P. Schiffer, and L. W. Martin, Sci. Rep. **5**, 10363 (2015).
[11] H.-C. Wu, O. N. Mryasov, M. Abid, K. Radican, and I. V. Shvets, Sci. Rep. **3**, 1830 (2013).
[12] A. E. Berkowitz and K. Takano, J. Magn. Magn. Mater. **200**, 552 (1999).
[13] C. Gatel, E. Snoeck, V. Serin, and A. R. Fert, Eur. Phys. J. B **45**, 157 (2005).
[14] K. Balakrishnan, S. K. Arora, and I. V. Shvets, J. Phys. Condens. Matter **16**, 5387 (2004).
[15] G. E. Sterbinsky, J. Cheng, P. T. Chiu, B. W. Wessels, and D. J. Keavney, J. Vac. Sci. Technol. B **25**, 1389 (2007).
[16] F. Bertram, C. Deiter, O. Hoefert, T. Schemme, F. Timmer, M. Suendorf, B. Zimmermann, and J. Wollschläger, J. Phys. D: Appl. Phys. **45**, 395302 (2012).
[17] F. Bertram, C. Deiter, T. Schemme, S. Jentsch, and J. Wollschläger, J. Appl. Phys. **113**, 184103 (2013).
[18] J. A. Moyer, S. Lee, P. Schiffer, and L. W. Martin, Phys. Rev. B **91**, 064413 (2015).
[19] T. Schemme, N. Pathé, G. Niu, F. Bertram, T. Kuschel, K. Kuepper, and J. Wollschläger, Mater. Res. Express **2**, 016101 (2015).
[20] J. A. Borchers, R. W. Erwin, S. D. Berry, D. M. Lind, J. F. Ankner, E. Lochner, K. A. Shaw, and D. Hilton, Phys. Rev. B **51**, 8276 (1995).
[21] J. Keller, P. Miltényi, B. Beschoten, G. Güntherodt, U. Nowak, and K. D. Usadel, Phys. Rev. B **66**, 014431 (2002).
[22] T. Schemme, O. Kuschel, F. Bertram, K. Kuepper, and J. Wollschläger, Thin Solid Films **589**, 526 (2015).
[23] Y. Z. Chen, J. R. Sun, Y. N. Han, X. Y. Xie, J. Shen, C. B. Rong, S. L. He, and B. G. Shen, J. Appl. Phys. **103**, 07D703 (2008).
[24] A. D. Wei, J. R. Sun, Y. Z. Chen, W. M. Lü, and B. G. Shen, J. Phys. D: Appl. Phys. **43**, 205004 (2010).
[25] M. Monti, M. Sanz, M. Oujja, E. Rebollar, M. Castillejo, F. J. Pedrosa, A. Bollero, J. Camarero, J. L. F. Cuñado, N. M. Nemes *et al.*, J. Appl. Phys. **114**, 223902 (2013).
[26] S. Kale, S. M. Bhagat, S. E. Lofland, T. Scabarozi, S. B. Ogale, A. Orozco, S. R. Shinde, T. Venkatesan, B. Hannoyer, B. Mercey *et al.*, Phys. Rev. B **64**, 205413 (2001).
[27] A. Brandlmaier, S. Geprägs, M. Weiler, A. Boger, M. Opel, H. Huebl, C. Bihler, M. S. Brandt, B. Botters, D. Grundler *et al.*, Phys. Rev. B **77**, 104445 (2008).
[28] J. Rubio-Zuazo, L. Onandia, E. Salas-Colera, A. Munoz-Noval, and G. R. Castro, J. Phys. Chem. C **119**, 1108 (2015).
[29] M. Pilard, O. Ersen, S. Cherifi, B. Carvello, L. Roiban, B. Muller, F. Scheurer, L. Ranno, and C. Boeglin, Phys. Rev. B **76**, 214436 (2007).
[30] I. P. Krug, F. U. Hillebrecht, H. Gomonaj, M. W. Haverkort, A. Tanaka, L. H. Tjeng, and C. M. Schneider, Europhys. Lett. **81**, 17005 (2008).
[31] I. P. Krug, F. U. Hillebrecht, M. W. Haverkort, A. Tanaka, L. H. Tjeng, H. Gomonay, A. Fraile-Rodríguez, F. Nolting, S. Cramm, and C. M. Schneider, Phys. Rev. B **78**, 064427 (2008).
[32] N.-T. H. Kim-Ngan, A. G. Balogh, J. D. Meyer, J. Brötz, M. Zając, T. Ślęzak, and J. Korecki, Surf. Sci. **603**, 1175 (2009).
[33] M. Gorgoi, S. Svensson, F. Schaefers, G. Ohrwall, M. Mertin, P. Bressler, O. Karis, H. Siegbahn, A. Sandell, H. Rensmo *et al.*, Nucl. Instrum. Methods Phys. Res, Sect. A **601**, 48 (2009).
[34] F. M. F. de Groot, Coord. Chem. Rev. **249**, 31 (2005).
[35] E. Stavitski and F. M. F. de Groot, Micron **41**, 687 (2010).
[36] O. Kuschel, T. Schemme, N. Pathé, T. Kuschel, R. Buess, K. Kuepper, and J. Wollschläger (unpublished).
[37] R. Claessen, M. Sing, M. Paul, G. Berner, A. Wetscherek, A. Müller, and W. Drube, New J. Phys. **11**, 125007 (2009).

[38] M. Hoppe, S. Döring, M. Gorgoi, S. Cramm, and M. Müller, Phys. Rev. B **91**, 054418 (2015).
[39] C. J. Powell and A. Jablonski, Nucl. Instrum. Methods Phys. Res., Sect. A **601**, 54 (2009).
[40] S. Tanuma, C. J. Powell, and D. R. Penn, Surf. Interface Anal. **11**, 577 (1988).
[41] S. Tanuma, T. Shiratori, T. Kimura, K. Goto, S. Ichimura, and C. J. Powell, Surf. Interface Anal. **37**, 833 (2005).
[42] C. Klewe, M. Meinert, A. Boehnke, K. Kuepper, E. Arenholz, A. Gupta, J.-M. Schmalhorst, T. Kuschel, and G. Reiss, J. Appl. Phys. **115**, 123903 (2014).
[43] T. Yamashita and P. Hayes, Appl. Surf. Sci. **254**, 2441 (2008).
[44] M. C. Biesinger, B. P. Payne, A. P. Grosvenor, L. W. M. Lau, A. R. Gerson, and R. S. C. Smart, Appl. Surf. Sci. **257**, 2717 (2011).
[45] M. Taguchi, A. Chainani, S. Ueda, M. Matsunami, Y. Ishida, R. Eguchi, S. Tsuda, Y. Takata, M. Yabashi, K. Tamasaku *et al.*, Phys. Rev. Lett. **115**, 256405 (2015).
[46] A. Müller, A. Ruff, M. Paul, A. Wetscherek, G. Berner, U. Bauer, C. Praetorius, K. Fauth, M. Przybylski, M. Gorgoi *et al.*, Thin Solid Films **520**, 368 (2011).
[47] S. Uhlenbrock, C. Scharfschwerdt, M. Neumann, G. Illing, and H.-J. Freund, J. Phys. Condens. Matter **4**, 7973 (1992).
[48] D. Alders, F. C. Voogt, T. Hibma, and G. A. Sawatzky, Phys. Rev. B **54**, 7716 (1996).
[49] V. I. Anisimov, I. S. Elfimov, N. Hamada, and K. Terakura, Phys. Rev. B **54**, 4387 (1996).
[50] M. Fonin, R. Pentcheva, Y. S. Dedkov, M. Sperlich, D. V. Vyalikh, M. Scheffler, U. Rüdiger, and G. Güntherodt, Phys. Rev. B **72**, 104436 (2005).
[51] H.-Q. Wang, E. I. Altman, and V. E. Henrich, Appl. Phys. Lett. **92**, 012118 (2008).
[52] W. Eerenstein, T. T. M. Palstra, T. Hibma, and S. Celotto, Phys. Rev. B **66**, 201101 (2002).
[53] D. T. Margulies, F. T. Parker, and A. E. Berkowitz, J. Appl. Phys. **75**, 6097 (1994).
[54] J. Cheng, G. E. Sterbinsky, and B. W. Wessels, J. Cryst. Growth **310**, 3730 (2008).
[55] T. Schemme, A. Krampf, F. Bertram, T. Kuschel, K. Kuepper, and J. Wollschläger, J. Appl. Phys. **118**, 113904 (2015).
[56] D. T. Margulies, F. T. Parker, M. L. Rudee, F. E. Spada, J. N. Chapman, P. R. Aitchison, and A. E. Berkowitz, Phys. Rev. Lett. **79**, 5162 (1997).
[57] W. Eerenstein, T. T. M. Palstra, T. Hibma, and S. Celotto, Phys. Rev. B **68**, 014428 (2003).
[58] L. McGuigan, R. C. Barklie, R. G. S. Sofin, S. K. Arora, and I. V. Shvets, Phys. Rev. B **77**, 174424 (2008).
[59] K. P. McKenna, F. Hofer, D. Gilks, V. K. Lazarov, C. Chen, Z. Wang, and Y. Ikuhara, Nat. Commun. **5**, 5740 (2014).
[60] H. Ohldag, T. J. Regan, J. Stöhr, A. Scholl, F. Nolting, J. Lüning, C. Stamm, S. Anders, and R. L. White, Phys. Rev. Lett. **87**, 247201 (2001).
[61] B. B. Nelson-Cheeseman, R. V. Chopdekar, J. M. Iwata, M. F. Toney, E. Arenholz, and Y. Suzuki, Phys. Rev. B **82**, 144419 (2010).
[62] C. Kuiper, B. G. Searle, L.-C. Duda, R. M. Wolf, and P. J. van der Zaag, J. Electr. Spectr. Rel. Phenom. **86**, 107 (1997).
[63] K. Fleischer, O. Mauit, and I. V. Shvets, Appl. Phys. Lett. **104**, 192401 (2014).
[64] E. Goering, S. Gold, M. Lafkioti, and G. Schütz, Europhys. Lett. **73**, 97 (2006).
[65] G. F. M. Gomes, T. E. P. Bueno, D. E. Parreiras, G. J. P. Abreu, A. de Siervo, J. C. Cezar, H.-D. Pfannes, and R. Paniago, Phys. Rev. B **90**, 134422 (2014).
[66] D. J. Huang, C. F. Chang, H.-T. Jeng, G. Y. Guo, H.-J. Lin, W. B. Wu, H. C. Ku, A. Fujimori, Y. Takahashi, and C. T. Chen, Phys. Rev. Lett. **93**, 077204 (2004).
[67] L. Martín-García, R. Gargallo-Caballero, M. Monti, M. Foerster, J. F. Marco, L. Aballe, and J. de la Figuera, Phys. Rev. B **91**, 020408 (2015).
[68] C. T. Chen, Y. U. Idzerda, H.-J. Lin, N. V. Smith, G. Meigs, E. Chaban, G. H. Ho, E. Pellegrin, and F. Sette, Phys. Rev. Lett. **75**, 152 (1995).
[69] Y. Teramura, A. Tanaka, and T. Jo, J. Phys. Soc. Jpn. **65**, 4, 1053 (1996).
[70] C. Piamonteze, P. Miedema, and F. M. F. de Groot, Phys. Rev. B **80**, 184410 (2009).
[71] V. Hari Babu, R. K. Govind, K.-M. Schindler, M. Welke, and R. Denecke, J. Appl. Phys. **114**, 113901 (2013).
[72] J. Orna, P. A. Algarabel, L. Morellón, J. A. Pardo, J. M. de Teresa, R. López Antón, F. Bartolomé, L. M. García, J. Bartolomé, J. C. Cezar *et al.*, Phys. Rev. B **81**, 144420 (2010).

Publication H6

[**H6**] O. Kuschel, R. Buess, J. Wöllermann, K. Balinski, W. Spiess, T. Kuschel, A.T. N'Diaye, J. Wollschäger, and K. Kuepper. *From NiO/Fe_3O_4 bilayers to $NiFe_2O_4$-like thin films through interdiffusion*, Phys. Rev. B **94**, 094423 (2016), doi: 10.1103/PhysRevB.94.094423.

From Fe_3O_4/NiO bilayers to $NiFe_2O_4$-like thin films through Ni interdiffusion

O. Kuschel,[1] R. Buß,[1] W. Spiess,[1] T. Schemme,[1] J. Wöllermann,[1] K. Balinski,[1] A. T. N'Diaye,[2] T. Kuschel,[3,4] J. Wollschläger,[1,5,*] and K. Kuepper[1,5,†]

[1]*Department of Physics, Barbarastraße 7, Osnabrück University, 49076 Osnabrück, Germany*

[2]*Advanced Light Source, Lawrence Berkeley National Laboratory, California 94720, USA*

[3]*Center for Spinelectronic Materials and Devices, Department of Physics, Bielefeld University, 33615 Bielefeld, Germany*

[4]*Physics of Nanodevices, Zernike Institue for Advanced Materials, University of Groningen, 9747 AG Groningen, Netherlands*

[5]*Center of Physics and Chemistry of New Materials, Osnabrück University, 49076 Osnabrück, Germany*

(Received 9 February 2016; revised manuscript received 1 July 2016; published 20 September 2016)

Ferrites with (inverse) spinel structure display a large variety of electronic and magnetic properties, making some of them interesting for potential applications in spintronics. We investigate the thermally induced interdiffusion of Ni^{2+} ions out of NiO into Fe_3O_4 ultrathin films, resulting in off-stoichiometric nickel ferrite–like thin layers. We synthesized epitaxial Fe_3O_4/NiO bilayers on Nb-doped $SrTiO_3$(001) substrates by means of reactive molecular beam epitaxy. Subsequently, we performed an annealing cycle comprising three steps at temperatures of 400 °C, 600 °C, and 800 °C under an oxygen background atmosphere. We studied the changes of the chemical and electronic properties as result of each annealing step with help of hard x-ray photoelectron spectroscopy and found a rather homogeneous distribution of Ni and Fe cations throughout the entire film after the overall annealing cycle. For one sample we observed a cationic distribution close to that of the spinel ferrite $NiFe_2O_4$. Further evidence comes from low-energy electron diffraction patterns indicating a spinel-type structure at the surface after annealing. Site- and element-specific hysteresis loops performed by x-ray magnetic circular dichroism uncovered the antiferrimagnetic alignment between the octahedral coordinated Ni^{2+} and Fe^{3+} ions and the Fe^{3+} ion in tetrahedral coordination. We find a quite low coercive field of 0.02 T, indicating a rather low defect concentration within the thin ferrite films.

DOI: 10.1103/PhysRevB.94.094423

I. INTRODUCTION

Iron oxides are of special interest due to a number of astonishing properties dependent on the Fe valence state and the underlying crystallographic and electronic structure. Magnetite (Fe_3O_4) is among the most studied ferrites due to its ferrimagnetic ordered ground state with a saturation moment of $4.07\mu_B$ per formula unit and a high Curie temperature of 860 K for bulk material [1,2]. This magnetic ground state is accompanied by half metallicity; that is, only one spin orientation is present at the Fermi energy [3], making this material a potential candidate for future spintronic devices with 100% spin polarization [4,5]. Magnetite crystallizes in the cubic inverse spinel structure (equal distribution of Fe^{3+} on A and B sites and Fe^{2+} exclusively on B sites) with lattice constant $a = 0.8396$ nm (space group $Fd3m$). The oxygen anions form an fcc anion sublattice.

Often, Fe_3O_4 thin films are grown on cubic MgO(001) substrates by various deposition techniques [6–11] since the lattice mismatch between Fe_3O_4 and MgO(001) ($a = 0.42117$ nm) is only 0.3%, comparing the oxygen sublattices. A severe limit of epitaxial thin-film growth on MgO substrates is Mg^{2+} segregation into the Fe_3O_4 film if the substrate temperature is above 250 °C [12]. Mg-rich interfaces [13] and Mg interdiffusion have been studied in detail [14], having significant influence on interface roughness or antiphase boundaries. Thus, the underlying electronic and magnetic structure influences the properties of the magnetite thin film in question or the tunnel magnetoresistance in magnetic tunnel junctions with magnetite electrodes [15–18].

A potential approach to minimize or suppress Mg segregation, besides rather low substrate temperatures during magnetite growth, is an additional buffer layer, e.g., metallic iron [19] or NiO [20] between Fe_3O_4 and the substrate. This approach is also of interest with respect to the possibility of building a full oxidic spin valve making use of the exchange bias between the ferrimagnetic magnetite and the antiferromagnetic nickel oxide [20–22].

The usage of other substrates like $SrTiO_3$ could also prevent Mg interdiffusion. Despite the large lattice mismatch of −7.5% between the doubled $SrTiO_3$ bulk lattice constant (0.3905 nm) and magnetite, it is possible to grow epitaxial Fe_3O_4 films on the $SrTiO_3$(001) surface [23,24]. In particular, concerning coupled Fe_3O_4/NiO bilayers grown on $SrTiO_3$, so far only Pilard *et al.* have reported on the magnetic properties of the Fe_3O_4/NiO interface [25]. On the other hand, $NiFe_2O_4$ thin films are of huge interest nowadays since they are magnetic insulators or semiconductors. Therefore, they can be used as spin filters [26] or for thermal induction of spin currents via the spin Seebeck effect [27,28]. Furthermore, electrical charge transport and spin currents can be manipulated by the spin Hall magnetoresistance using $NiFe_2O_4$ thin films adjacent to nonmagnetic material [29].

Therefore, we study here the possibility to form nickel ferrite starting with a distinct Fe_3O_4/NiO bilayer grown on Nb-doped $SrTiO_3$(001). Knowledge about the modification of the underlying crystallographic, electronic, and magnetic structure by Ni interdiffusion is indispensable for potential applications. We also want to investigate fundamental aspects, especially of Ni^{2+} diffusion from a NiO buffer layer into a Fe_3O_4 top layer as well as NiO surface segregation through

*jwollsch@uos.de
†kkuepper@uos.de

the Fe_3O_4 film, since knowledge of diffusion processes in oxides still appears to be quite rudimentary for many systems.

We perform a systematic three-step annealing cycle of Fe_3O_4/NiO bilayers after synthesis and simultaneously investigating surface crystallographic and "bulk" electronic structure changes by means of low energy electron diffraction (LEED) and hard x-ray photoelectron spectroscopy (HAXPES). Furthermore, we carry out structural analysis before and after the overall annealing cycle employing x-ray reflectivity (XRR) and synchrotron-radiation-based x-ray diffraction (SR-XRD), as well as element- and site-specific x-ray magnetic circular dichroism (XMCD) after the overall annealing cycle to analyze the resulting magnetic properties in detail.

II. EXPERIMENTAL DETAILS

Two samples with ultrathin Fe_3O_4/NiO bilayers on conductive 0.05 wt% Nb-doped $SrTiO_3$(001) substrates have been prepared using the technique of reactive molecular beam epitaxy (RMBE). The substrates have been supplied with a polished surface and were annealed once at 400 °C for 1 h in an oxygen atmosphere of 1×10^{-4} mbar prior to deposition. Afterwards, the chemical cleanness and composition was proven by XPS, while the crystallinity of the surface was checked by LEED. Oxide films have been deposited by thermal evaporation from pure metal rods in low oxygen atmosphere. During film growth, the substrate was heated to 250 °C, while the oxygen pressure was kept at 1×10^{-5} mbar for NiO and 5×10^{-6} mbar for Fe_3O_4 to guarantee optimal oxidation condition. Deposition rates of 0.85 and 4.6 nm/min were used for the growth of NiO and Fe_3O_4 films, respectively, which was controlled by a quartz microbalance adjacent to the source. One sample was created with a 5.6-nm NiO film (sample A), and the other was created with a 1.5-nm NiO film (sample B). Thereafter, 5.5-nm-thick Fe_3O_4 films were deposited on the NiO films. Film stoichiometry and surface structure have been monitored *in situ* by x-ray photoelectron spectroscopy (XPS) using Al K_α radiation and LEED, respectively.

The samples were transported under ambient conditions to the Diamond Light Source (DLS) synchrotron, where the effects of annealing on the bilayer system were studied at beamline I09 by heating the samples in three steps at 400 °C, 600 °C, and 800 °C for 20 to 30 min in an oxygen atmosphere of 5×10^{-6} mbar to avoid reduction or further oxidation of the sample [30]. Prior to and after the annealing studies XRR measurements at 2.5 keV photon energy were performed to determine the film thickness. After each annealing step, the films were studied *in situ* by soft x-ray photoemission and HAXPES to clarify the chemical composition in the near-surface region and in the bulk region, respectively. In addition, LEED measurements were performed to check the crystallinity of the individual layers of the NiO/Fe_3O_4 bilayer.

For HAXPES an energy of $h\nu = 5934$ eV was used, creating photoelectrons with high kinetic energy, which allows a higher probing depth compared to soft x-ray photoemission ($h\nu = 1000$ eV).

The information depth D_I, from which 95% of the photoelectrons originate, is defined as

$$D_I(95) = -\lambda \cos\varphi \ln(1 - 95/100), \quad (1)$$

with the inelastic mean free path λ and the off-normal emission angle φ [31]. The maximum information depth for the Fe $2p$ core level for HAXPES and soft x-ray photoemission measurements is 22 and 2.5 nm, respectively, estimating λ with the Tanuma Powell and Penn algorithm (TPP-2M) formula [32]. As the beamline features a two-dimensional photoelectron detector, which can be operated in an angular mode, photoelectron spectra at different emission angles were acquired, each with an acceptance angle of $\sim7^\circ$.

Subsequently, structural analysis of the annealed films was performed using SR-XRD, while the resulting film thickness and layer structure of these films were determined by means of laboratory-based XRR using Cu K_α radiation. SR-XRD experiments have been carried out *ex situ* at PETRA III beamline P08 (DESY, Germany) using a photon energy of 15 keV. In both cases the measurements were performed in θ-2θ diffraction geometry. For the analysis of all XRR experiments an in-house-developed fitting tool based on the Parratt algorithm [33] and Névot-Croce roughness model [34] was used. The SR-XRD measurements were analyzed by calculating the crystal truncation rod (CTR) intensity within the full kinematic diffraction theory to fit the experimental diffraction data.

XMCD spectroscopy was performed at the Fe $L_{2,3}$ and Ni $L_{2,3}$ edges with the samples at room temperature at beamline 6.3.1 of the Advanced Light Source, Lawrence Berkeley Laboratory. We utilized total electron yield (TEY) as the detection mode. The external magnetic field of 1.5 T was aligned parallel to the x-ray beam and was switched for each energy. The angle between the sample surface and x-ray beam was chosen to be 30°. The resolving power of the beamline was set to $E/\Delta E \sim 2000$; the degree of circular polarization was about 55%. For the analysis of the Fe $L_{2,3}$ XMCD spectra, we performed corresponding model calculations within the atomic multiplet and crystal-field theory including charge transfer using the program CTM4XAS [35,36].

III. RESULTS

A. Surface characterization

In Figs. 1(a)–1(c) the LEED patterns of the cleaned substrate and the as-prepared NiO and Fe_3O_4 films are presented for sample A. Figures 1(d) and 1(e) show the LEED images recorded after the last annealing step of 800 °C for sample A and sample B, respectively.

After cleaning of the $SrTiO_3$ substrates the LEED pattern shows very sharp diffraction spots of a (1×1) surface with square structure and negligible background intensity [see Fig. 1(a)], indicating a clean (001)-oriented surface with long-range structural order. Additionally, XPS measurements show chemically clean substrates without carbon contamination (not shown here).

The LEED image recorded directly after RMBE of NiO also exhibits a quadratic (1×1) structure [see Fig. 1(b)], as expected for the NiO(001) surface unit cell. However, the pattern is rotated by 45° and is $\sim\sqrt{2}$ times larger than the pattern of the $SrTiO_3$(001) substrate. The broadening of the diffraction spots is most likely caused by defects due

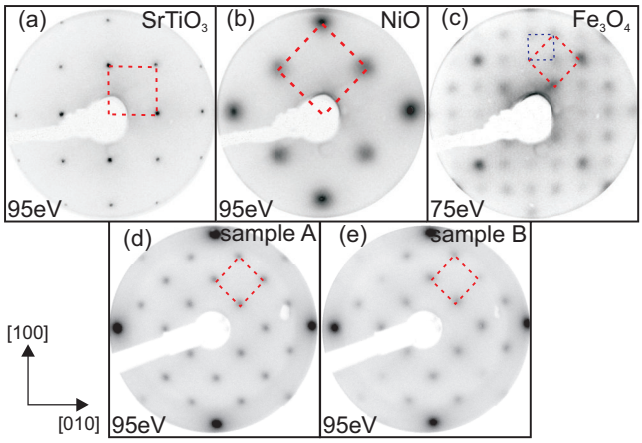

FIG. 1. LEED patterns for sample A recorded directly after (a) preparation of the $SrTiO_3$ substrate, (b) deposition of NiO, (c) deposition of Fe_3O_4, and (d) the last annealing step of 800 °C. For comparison, (e) shows the LEED pattern for sample B after the final annealing step. Marked with red squares are the respective (1×1) surface unit cells in reciprocal space. The blue square indicates the $(\sqrt{2}\times\sqrt{2})$R45° superstructure typical for magnetite.

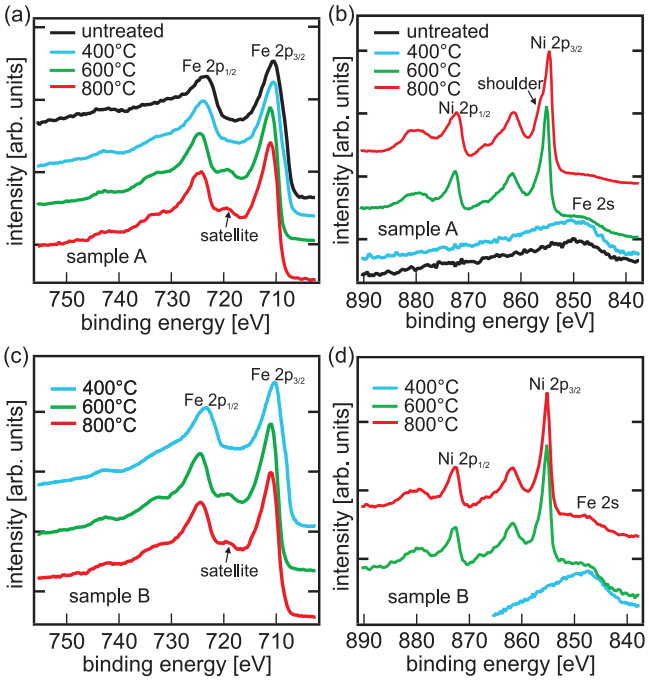

FIG. 2. Soft XPS spectra of (a) Fe 2p and (b) Ni 2p regions of sample A and (c) Fe 2p and (d) Ni 2p regions of sample B after each annealing step. For sample A the spectra of the untreated sample are shown exemplarily.

to relaxation processes induced by the high lattice misfit of −6.9% for NiO(001) compared to $SrTiO_3$(001).

The LEED pattern of the as-prepared Fe_3O_4 film [see Fig. 1(c)] reveals a quadratic (1×1) surface structure with almost doubled periodicity compared to NiO as the real-space lattice constant of the magnetite inverse spinel structure is about twice as large, giving a lattice misfit of only 0.5% for Fe_3O_4(001) on NiO(001). Furthermore, additional diffraction spots of a $(\sqrt{2}\times\sqrt{2})$R45° superstructure can be seen, which is characteristic of well-ordered Fe_3O_4(001) surfaces [37–39].

LEED results indicate a cube-on-cube growth for both NiO and Fe_3O_4 films. Additionally, the Ni 2p and Fe 2p XPS spectra recorded directly after preparation of each film (not shown here) exhibit a characteristic shape for Ni^{2+} and mixed Fe^{2+}/Fe^{3+} valence states, respectively. Thus, combining the results from XPS and LEED, we can conclude that the as-prepared films consist of stoichiometric Fe_3O_4/NiO bilayers.

Figure 2 shows the Fe 2p and Ni 2p core-level spectra of both samples after transport to DLS under ambient conditions (sample A) and after each annealing step using soft XPS.

After the first annealing step at 400 °C, the Fe 2p peak shape is similar to that of the untreated sample [see Fig. 2(a)]. No charge-transfer satellites are visible, indicating Fe_3O_4 stoichiometry and the presence of a mixed oxidation state [40,41]. For both samples, Fe $2p_{3/2}$ and Fe $2p_{1/2}$ peaks are located at binding energies of 710.4 (±0.2) and 723.8 (±0.2) eV, respectively, corresponding to the values for magnetite known from the literature [40]. Furthermore, no Ni 2p signal is visible for both samples due to the small information depth, demonstrating that Ni did not diffuse into the Fe_3O_4 film and that the Fe_3O_4 film was not deconstructed [see Figs. 2(b) and 2(d)]. Consequently, the first annealing step at 400 °C only removed surface contaminations from the transport, without effecting the initial layer structure of the sample.

After the annealing step at 600 °C, a distinctive satellite typical for trivalent iron becomes visible between the Fe $2p_{1/2}$ and Fe $2p_{3/2}$ peaks for sample A and sample B [see Figs. 2(a) and 2(c)]. Further, Fe $2p_{1/2}$ and Fe $2p_{3/2}$ are shifted to binding energies of 710.9 (±0.2) and 724.4 (±0.2) eV, respectively. The shift to higher binding energies and the satellite at ∼8 eV above the main peak confirm the presence of Fe^{3+} and a deficiency of divalent iron [40–42].

In contrast to lower annealing temperature, Ni 2p peaks becomes visible after the 600 °C annealing step. Both samples show an intense Ni 2p signal consisting of two main peaks accompanied by satellite peaks at ∼7 eV above their binding energies. The shape of the spectra and, in particular, the absence of a shoulder on the high-energy side of Ni $2p_{3/2}$ indicate that no NiO cluster has been formed at the surface of both samples [43,44]. The occurrence of such a shoulder ∼1.5 eV above the $2p_{3/2}$ peak is reported to be characteristic of NiO [45,46]. The binding energy of 855.2 (±0.2) eV of the Ni $2p_{3/2}$ peak also confirms the origin of $NiFe_2O_4$ and not of NiO [43,47]. Thus, both iron and nickel spectra obtained after annealing at 600 °C point to the formation of $NiFe_2O_4$ at the near-surface region of both samples as a result of intermixing.

The last annealing step at 800 °C influences the peak shape of neither the Fe 2p nor the Ni 2p spectra of sample B [see Figs. 2(c) and 2(d)], indicating a complete intermixing of the two layers already after the annealing at 600 °C. However, for sample A a NiO-specific shoulder on the high-energy side of Ni $2p_{3/2}$ appears [see Fig. 2(b)]. Further, a shift to lower binding energies takes place, resulting in a binding energy of 854.5 (±0.2) eV for Ni $2p_{3/2}$, indicating the presence of NiO at the surface [43]. Since there is no change in the Fe 2p spectra for sample A, we conclude that NiO clusters are formed at the surface of a $NiFe_2O_4$-like film.

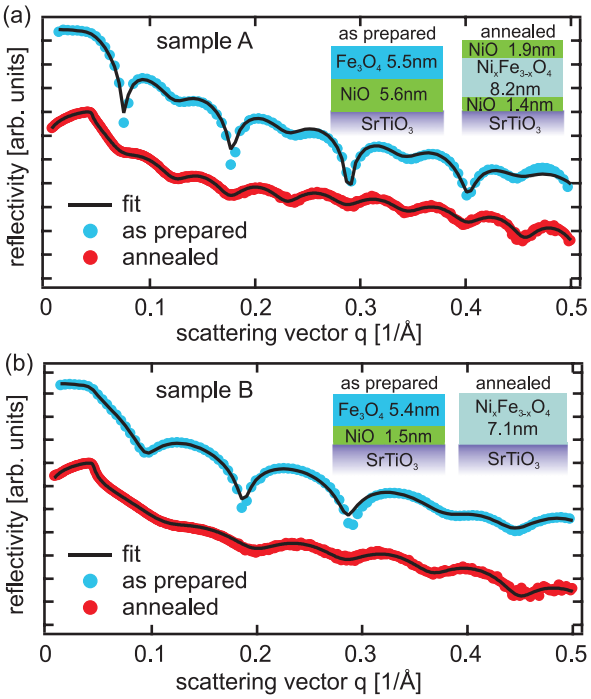

FIG. 3. Reflectivity curves and calculations from XRR measurements before and after the annealing experiments (a) for sample A and (b) for sample B. The insets show the underlying models.

LEED patterns of samples A and B recorded after the final annealing step are presented in Figs. 1(d) and 1(e). The diffraction pattern can be attributed to the (001)-(1×1) surface of nickel ferrite, which shows a lattice constant similar to that of magnetite [see Fig. 1(c)]. However, the $(\sqrt{2}\times\sqrt{2})$R45° superstructure indicative of magnetite is not observed after the final annealing step. Therefore, this result underpins the formation of nickel ferrite, as concluded before from XPS where Fe^{3+} is primarily observed. Furthermore, the LEED spots of sample A are sharper than the spots of sample B. We attribute this finding to the formation of a stoichiometric $NiFe_2O_4$ film for sample A, while the ferrite film is less ordered for sample B, in which the Ni content of the film is too low (see below). The formation of NiO islands concluded from our detailed XRR analysis cannot clearly be concluded from the LEED experiments since the diffraction peaks of the NiO film coincide with diffraction peaks from the nickel ferrite film due to the coincidence between the nickel ferrite lattice constant and the doubled NiO lattice constant.

B. XRR

Figure 3 shows the measured and calculated XRR intensities obtained at DLS prior to the annealing experiments for both samples. The XRR intensity obtained from sample A clearly shows the beating of two layers with almost identical thickness, while the intensity obtained from sample B points to two layers with very different thickness. In addition, the data show well-defined intensity oscillations for both samples, pointing to a double-layer structure and flat homogeneous interfaces and films. For the calculation of the intensity distributions and the exact layer structure a basic model was used, consisting of a magnetite film on top of a NiO layer on a $SrTiO_3$ substrate (insets of Fig. 3). In Table I the fit parameters, e.g., dispersion δ and rms roughness σ, are shown. Here, the obtained values for the dispersion of the as-prepared samples are within 1% of corresponding literature values [48].

The measured and calculated XRR intensities of the annealed samples as well as the model used are also presented in Fig. 3. For both samples the XRR shows clear intensity oscillations with a changed periodicity compared to the as-prepared films. Taking into account the electron densities and layer structures obtained from XRR, this effect can be attributed to an intermixing of the two initial oxide layers. In the case of sample A a three-layer model was necessary to describe the data after annealing [see Fig. 3(a)]. As concluded from the obtained dispersion δ, the first layer on top of the substrate is a thin nickel oxide layer, while the second layer is an 8.2-nm-thick nickel ferrite film [48]. The third layer on top of the nickel ferrite film consists of an oxide layer with a diluted dispersion δ and thus a reduced electron density. Taking into account the NiO formation on top of sample A seen in the soft XPS spectra, we can attribute the upper layer to NiO segregation to the surface. The low electron density of this layer indicates a deconstructed film or island formation on the surface.

For sample B, however, the XRR is modeled with a single homogeneous 7.1-nm-thick nickel ferrite film on top of the substrate [see Fig. 3(b)]. For both samples the thicknesses of the residual films almost coincide with the sum of the initial thicknesses of the Fe_3O_4 and NiO films.

The slight increase in the overall thickness can be attributed to a volume increase of ∼8% due to the formation of nickel ferrite.

TABLE I. Model parameters used for the XRR intensity calculations, with dispersion δ, surface roughness σ, and film thickness d.

	Substrate		Layer 1			Layer 2			Layer 3		
	δ	σ (Å)	δ	σ (Å)	d (nm)	δ	σ (Å)	d (nm)	δ	σ (Å)	d (nm)
Sample A											
As prepared[a]	1.48×10^{-4}	2.4	2.15×10^{-4}	1.7	5.6	1.65×10^{-4}	3.9	5.5			
Annealed[b]	1.50×10^{-5}	0.1	1.7×10^{-5}	6.0	1.4	1.58×10^{-5}	2.0	8.2	1.34×10^{-5}	3.0	1.9
Sample B											
As prepared[a]	1.48×10^{-4}	2.7	2.15×10^{-4}	1.9	1.5	1.65×10^{-4}	3.2	5.5			
Annealed[b]	1.50×10^{-5}	0.1	1.58×10^{-5}	1.0	7.1						

[a]Measured at a photon energy of 2500 eV.
[b]Measured at a photon energy of 8048 eV.

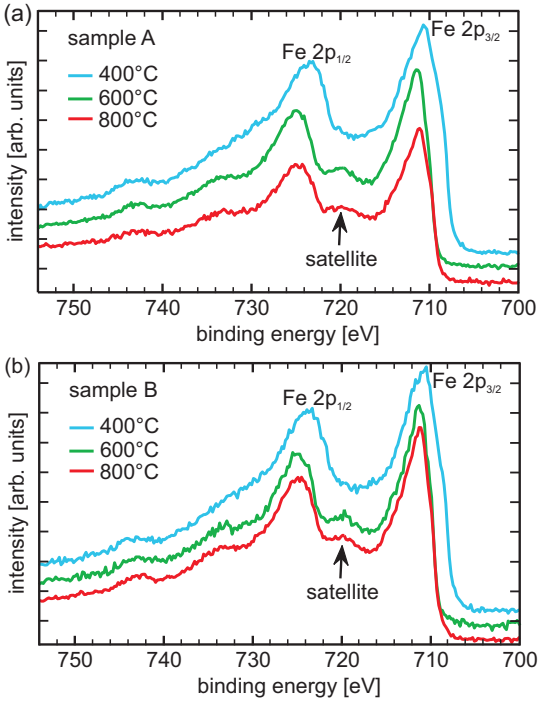

FIG. 4. HAXPES spectra of Fe $2p$ core level at 10° off-normal photoelectron emission after annealing at different temperatures (a) for sample A and (b) for sample B.

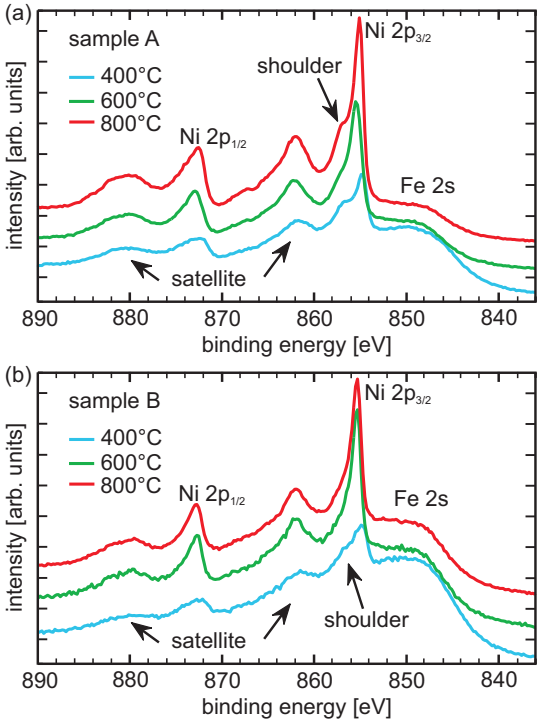

FIG. 5. HAXPES spectra of Ni $2p$ core level at 10° off-normal photoelectron emission after annealing at different temperatures (a) for sample A and (b) for sample B.

C. HAXPES

In contrast to soft x-ray photoemission, HAXPES measurements allow us to identify the valence states and chemical properties not only at the near-surface region but with bulk sensitivity due to higher excitation energy and thus increased information depth.

Figure 4 shows the HAXPES spectra for the Fe $2p$ core level, which is split into the Fe $2p_{1/2}$ and Fe $2p_{3/2}$ peaks (see soft XPS spectra, Fig. 2). Spectra recorded after each annealing step for both samples are presented. The shape of the spectra is determined by the relative fraction of Fe valence states, which is used to identify the material composition [40]. After the initial annealing step at 400 °C, there is no satellite peak visible between the two main peaks, indicating stoichiometric Fe_3O_4 for both samples. After the second and third annealing steps, at 600 °C and 800 °C, respectively, a satellite peak becomes visible between the two main peaks for both samples. As it resides on the side of the Fe $2p_{1/2}$ peak, it indicates a deficiency of Fe^{2+} ions in favor of Fe^{3+} ions compared to the initial magnetite stoichiometry. In addition, similar to the XPS results, an energy shift to higher binding energies can be seen after the second and third annealing steps, pointing to the formation of trivalent Fe^{3+} [40–42]. Thus, this behavior is in accordance with the results obtained from soft XPS spectra.

Figure 5 shows the photoelectron spectra for the Ni $2p_{1/2}$ and Ni $2p_{3/2}$ core level of both samples. After the annealing step at 400 °C the main Ni $2p_{3/2}$ peak is located at a binding energy of 854.5 (±0.2) eV, indicating NiO stoichiometry [43]. Further, for both samples, a shoulder on the high-binding-energy side of the Ni $2p_{3/2}$ peak is visible, which is also typical for NiO [43,47]. This shoulder almost completely disappears after annealing at 600 °C for both samples. Biesinger *et al.* [49] identified such a peak shape without a shoulder for the spinel-type material $NiFe_2O_4$. In addition, the Ni $2p_{3/2}$ peak is shifted to a higher binding energy of 855.0 (±0.2) eV, which is comparable to binding energy reported for Ni in $NiFe_2O_4$ stoichiometry [43]. The small mismatch between the measured value and the literature is due to an overlap of intensities originating from several layers with slightly different stoichiometries. In summary, similar to the soft XPS results, an exchange of Fe^{2+} ions with Ni^{2+} ions in the Fe_3O_4 spinel structure through interdiffusion seems to be likely [50].

For sample B, the peak shape does not change with the next annealing step at 800 °C [see Fig. 5(b)]. However, for sample A the shoulder on the high-binding-energy side re-appears, as observed for the initial bilayer system [see Fig. 5(a)]. Additionally, the Ni $2p_{3/2}$ peak is shifted to a lower binding energy, suggesting the formation of NiO-like structures, which is consistent with the NiO formation at the surface seen in the XRR and soft XPS measurements.

Furthermore, a quantitative analysis of the photoelectron spectra was performed to prove the formation of nickel ferrite. After subtracting a Shirley background, the intensities I_{Fe} and I_{Ni} of the Fe $2p$ peaks and the Ni $2p_{1/2}$ peak (due to the overlap with the Fe $2s$ peak, the Ni $2p_{3/2}$ peak has not been considered) have been numerically integrated. From these results, the relative photoelectron yield

$$Y_{Ni} = \frac{I_{Ni}/\sigma_{Ni}}{I_{Ni}/\sigma_{Ni} + I_{Fe}/\sigma_{Fe}} = \frac{N_{Ni}}{N_{Ni} + N_{Fe}C(\varphi)} \qquad (2)$$

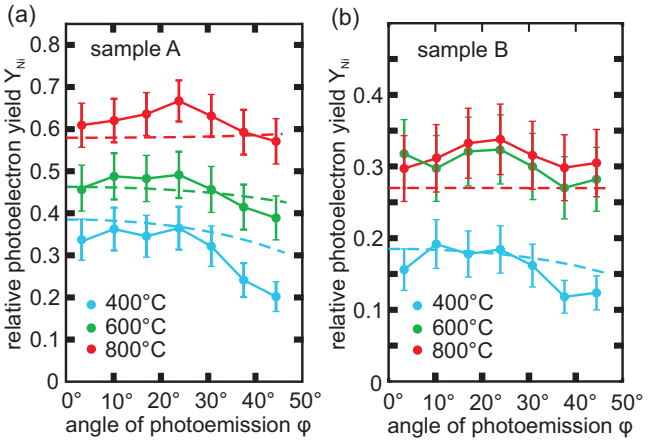

FIG. 6. Relative photoelectron yield at different off-normal emission angles (a) for sample A and (b) for sample B. The dashed lines show the calculated intensities using the models obtained from XRR analysis.

of Ni has been calculated, using the differential photoionization cross sections σ reported by Trzhaskovskaya *et al.* [51]. Newberg *et al.* [52] derived that this yield is equal to the atomic ratios but modified with a factor $C(\varphi)$ that depends on the angle of photoemission (neglecting photoelectron diffraction effects). The resulting yields from different detection angles are plotted in Fig. 6. The curves from the data of the first annealing steps show for both samples a decreasing yield for higher emission angles, as indicated by the blue dashed lines. This behavior points to an intact stack of oxide films due to a longer pathway of the photoelectrons for higher emission angles. The lines are calculated for a stack of two separated Fe_3O_4/NiO films using the thicknesses obtained from XRR analysis. With the successive annealing steps, the photoelectron yield from Ni increases, which indicates that there is diffusion of Ni into the Fe_3O_4 film and/or Fe into the NiO film.

Since there is no evidence of NiO in the Ni $2p$ HAXPES spectra after annealing at 600 °C, a model consisting of a stoichiometric 8.2-nm-thick $NiFe_2O_4$ on top of a 3.4-nm-thick NiO layer was used for sample A [green dashed line Fig. 6(a)].

With further annealing at 800 °C the intensity ratios [Fig. 6(a)] show a continuous increase of the nickel intensity. This indicates that more Ni atoms are diffusing/transported through the nickel ferrite layer to the very surface forming NiO as detected by XRR and soft XPS measurements. The photoelectron yield for this annealing step (dashed red line) was calculated using the layer structure and thicknesses obtained from the XRR analysis [see inset in Fig. 3(a)]. This model is based on a stoichiometric 8.2-nm-thick $Ni_xFe_{3-x}O_4$ film with $x = 1$ between two NiO films. The supposed segregation behavior of Ni and the formation of NiO at the surface could be explained by its lower surface energy of 0.863 J/m^2 compared to the surface energy of 1.235 J/m^2 for $NiFe_2O_4$(001) [53]. Thus, one would expect an inversion of the initial bilayer ordering with NiO under magnetite. However, during the diffusion process Ni is partly incorporated in the initial magnetite film, and stoichiometric $NiFe_2O_4$ is formed. After saturation of the nickel ferrite the residual Ni starts to form NiO at the surface. In our case, however, this process is obviously not completed due to kinetic effects, and residual NiO is still underneath the nickel ferrite.

In the case of sample B one can conclude that a single homogeneous film was already formed by the interdiffusion process after the second annealing step. Its stoichiometry does not change from the second to the third annealing step [see Fig. 6(b)]. The ratio of Ni and Fe, assuming a complete intermixing, can be determined from Eq. (2), as then the angular factor $C(\varphi) \equiv 1$. The amount of nickel and iron does not match the ratio of 1:2 for stoichiometric nickel ferrite and is 1:2.6 for sample B, indicating an excess of Fe atoms. The experimental data are in good agreement with the calculated behavior (dashed red line) for a homogeneously mixed single layer, which is also consistent with the model obtained from XRR. Thus, the resulting stoichiometry of sample B is $Ni_xFe_{3-x}O_4$, with $x = 0.83$.

The simulation of the photoelectron yield does not describe the measured data in full detail but gives an idea of the possible course. One limitation is that a model consisting of a stack of separated homogeneous layers was used. Thus, potential concentration gradients or clusters are not implemented in the simulation. Further, effects caused by x-ray photoelectron diffraction (XPD) are not considered. Nevertheless, the general trend is described well.

D. SR-XRD

Figure 7 shows SR-XRD measurements and calculated CTR intensity along the (00L) direction close to the perovskite $SrTiO_3(002)_P$ and spinel $(004)_S$ Bragg peaks for both samples after annealing. Here, L denotes the vertical scattering vector in reciprocal lattice units (r.l.u.) with respect to the lattice constant of the $SrTiO_3$(001) substrate. Indices P and S indicate

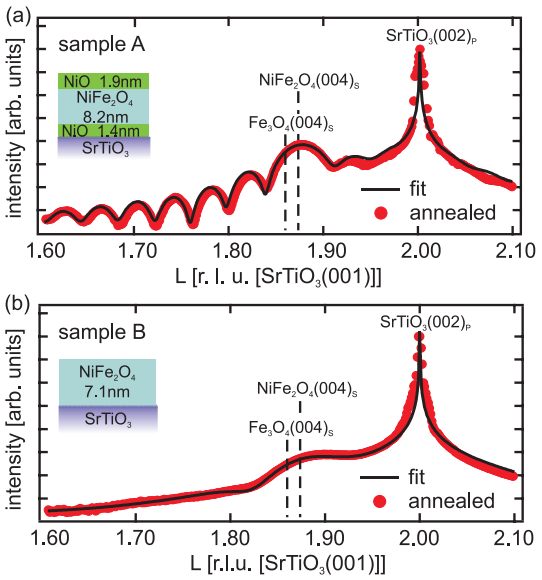

FIG. 7. SR-XRD measurements along the (00L) direction and calculated intensities. The insets show the layer structures used in the calculation. The model is similar to that obtained from the analysis of the XRR (see inset in Fig. 3).

the bulk notation for perovskite-type and spinel-type unit cells, respectively.

For both samples a clear peak from the $SrTiO_3(001)$ substrate at $L = 2$ and a broad Bragg peak originating from the oxide film around L $\approx$ 1.87 is observed. The structural parameters, e.g., vertical layer distances, are determined by analyzing the CTRs by applying full kinematic diffraction theory. The structural models obtained from the XRD analysis coincide with the layer models used for the XRR calculations of the annealed samples (see insets of Figs. 7 and 3).

For sample A the model consists of a $NiFe_2O_4$ layer between two thin NiO films (see inset in Fig. 7). The distinct oscillations close to the Bragg peak of the oxide film (Laue fringes) can be clearly attributed to the nickel ferrite layer, indicating a well-ordered homogeneous film of high crystalline quality. The diffracted intensity originating from the NiO results in a broad peak underneath the Bragg reflection of the nickel ferrite due to the small film thicknesses of the NiO films which cannot directly be seen by the bare eye in the experimental data. Furthermore, the vertical lattice constants obtained from curve fitting are $c_{\mathrm{NiO}} = 0.4177$ nm for the NiO films and $c_{NFO} = 0.8334$ nm for the $NiFe_2O_4$ layer. These results are in good agreement with the bulk values of $a_{\mathrm{NiO}}^{\mathrm{bulk}} = 0.4176$ nm and $a_{NFO}^{\mathrm{bulk}} = 0.8339$ nm, respectively.

For sample B the Laue oscillations completely vanish, pointing to inhomogeneities within the film [see Fig. 7(b)]. This effect is possibly caused by the excess of Fe atoms in the film, as observed by HAXPES. However, the peak width is in accordance with the $NiFe_2O_4$ thickness of 7.1 nm. In addition, the vertical lattice constant $c_{NFO} = 0.8304$ nm obtained from the calculations confirms the presence of a strongly distorted structure of the annealed film since it is notably lower than the value of bulk $NiFe_2O_4$.

E. XMCD

XMCD has been employed after the overall annealing cycle to analyze the resulting magnetic properties element specifically after annealing at 800 °C. Figure 8 depicts the XMCD spectra of samples A and B performed at the Fe $L_{2,3}$ and Ni $L_{2,3}$ edges, respectively. Both samples show a strong Ni dichroic signal [see Fig. 7(a)], and in order to extract the spin magnetic moments we use the spin sum rule developed by Chen *et al.* [54]. The number of holes is determined from the charge-transfer multiplet simulations for each sample. We also account for the core-hole interactions which mix the character of the L_3 and L_2 edges [55,56] by considering the spin sum rule correction factors obtained by Teramura *et al.* [55]. We find a Ni spin moment of 0.51 μ_B/Ni atom and an orbital contribution of 0.053μ_B/Ni atom, summing up to a total Ni moment of 0.56μ_B for sample A. In the case of sample B we derive $m_{\mathrm{spin}} = 0.91\mu_B$/Ni atom, $m_{\mathrm{orb}} = 0.122\mu_B$/Ni atom, and hence a total Ni moment of 1.03 μ_B/f.u.. The latter value is rather close to that recently found by Klewe *et al.* [57] on a stoichiometric $NiFe_2O_4$ thin film.

Turning to the Fe moments, we find strong indications that our heat and diffusion experiments lead to a $Ni_xFe_{3-x}O_4$ layer or cluster formation in both samples. Since we obtain $m_{\mathrm{spin}} = -0.028\mu_B$ $(+0.11\mu_B)$/Fe atom and $m_{\mathrm{orb}} = +0.015\mu_B$ $(+0.007\mu_B)$/Fe atom at the Fe sites of

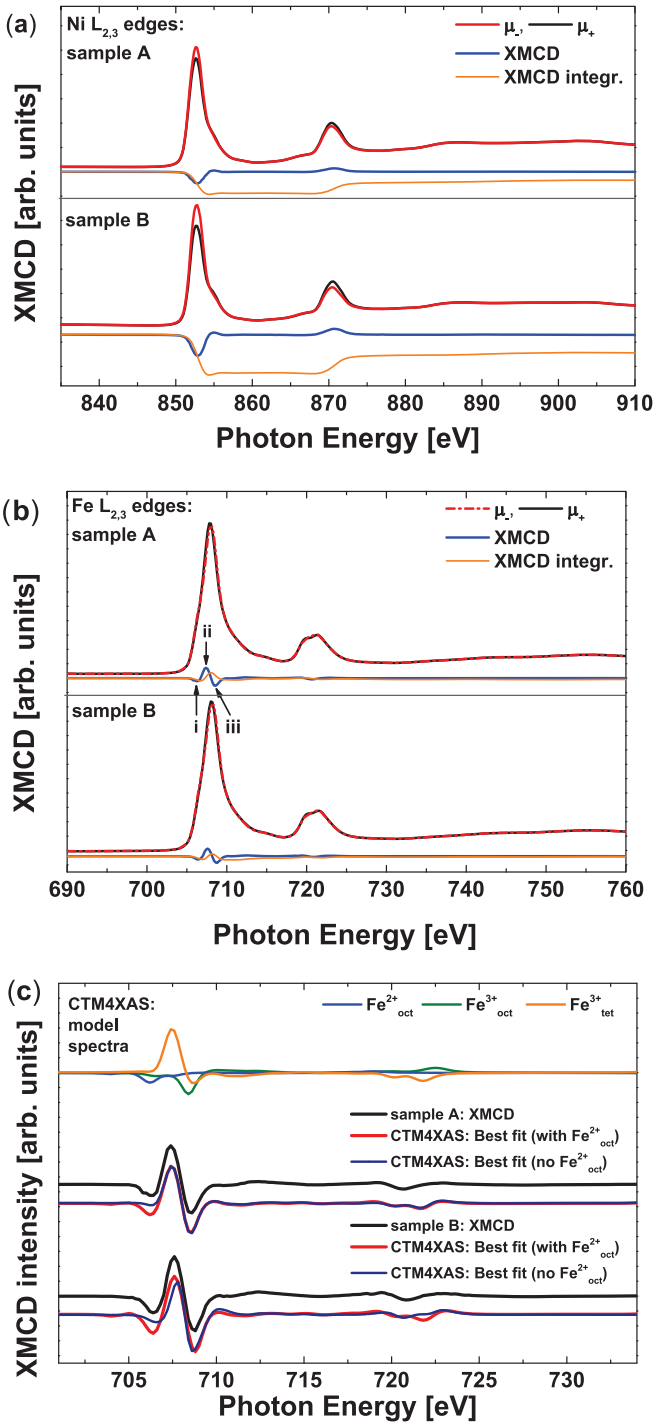

FIG. 8. (a) Ni $L_{2,3}$-XMCD spectra of samples A and B. (b) Fe $L_{2,3}$-XMCD spectra of samples A and B. (c) Experimental Fe $L_{2,3}$ edge XMCD of samples A and B and the corresponding XTM4XAS fits with and without considering octahedral coordinated Fe^{2+} ions.

sample A (sample B), we find very small net contributions to the overall magnetic moments. In comparison Klewe *et al.* [57] found an iron spin moment of around 0.1μ_B/Fe atom and a further orbital contribution of around 10%–15% of that value. This indicates an (almost complete) structural inversion of the prior bilayer system; that is, the iron ions occupy in equal parts

octahedral and tetrahedral positions within the crystal. Since the moments of these octahedrally and tetrahedrally coordinated cations are aligned antiparallel, the moments nearly cancel each other out in a perfect inverse spinel structure.

Figure 8(c) presents the charge-transfer multiplet calculations for the single iron cations in octahedral and tetrahedral coordination as well as the best fits to the experimental Fe $L_{2,3}$-XMCD spectra of samples A and B with (red) and without (blue) considering Fe^{2+}_{oct} ions. The resulting lattice site occupancies are 16.3% Fe^{2+}_{oct}, 32.2% Fe^{3+}_{oct}, and 51.5% Fe^{3+}_{tet} (42.6% Fe^{3+}_{oct} and 57.4% Fe^{3+}_{tet}) for sample A and 24.0% Fe^{2+}_{oct}, 31.5% Fe^{3+}_{oct}, and 44.5% Fe^{3+}_{tet} (55.6% Fe^{3+}_{oct} and 44.4% Fe^{3+}_{tet}) for sample B when including (not including) Fe^{2+}_{oct} ions in the respective fit. The result that, for sample A, over 50% are in Fe^{3+}_{tet} coordination as to the calculations also corresponds to the small negative spin moment determined by the spin sum rule.

From the overall multiplet fits [Fig. 8(c)] one can clearly see that feature *i* [Fig. 8(b)] is very small if Fe^{2+}_{oct} cations are not explicitly considered in the respective simulations. The origin of this feature in ferrites with inverse spinel structure other than magnetite is still not entirely understood [44,57,58]. In Fe $L_{2,3}$-XMCD spectra of both samples A and B peak *i* is significantly smaller than results obtained very recently for $NiFe_2O_4$ thin films grown by pulsed laser deposition (PLD) [44] but somewhat more intense than it is in the result of Klewe *et al.* [57]. Also, their corresponding multiplet simulation resembles our approach (not considering the Fe^{2+}_{oct} sites) rather well. The presence of peak *i* in the Fe $L_{2,3}$-XMCD of sample B can at least partly be explained by the lack of Ni^{2+}_{oct} ions as to the HAXPES measurements. Since peak *i* also occurs in XMCD experiments on bulk material [58], one can think about several additional reasons for the presence of some Fe^{2+}_{oct} ions. For instance, a small fraction of the Ni ions might be present in the form of Ni^{3+} or coordinated on tetrahedral sites as a result of the interdiffusion process. Despite the fact that Ni^{2+} prefers octahedral coordination, even measurements on $NiFe_2O_4$ bulk crystals indicate that a few of the Ni ions are on tetrahedral sites [58]. Furthermore, oxidation or reduction of a fraction of the Fe at the very surface of the thin films cannot be entirely excluded as the probing depth of the total electron yield is only around 2 nm at the Fe $L_{2,3}$ and Ni $L_{2,3}$ resonances of oxides [58,59].

For sample B we also recorded element-specific hysteresis loops at the Ni L_3 edge and the site-specific loops at Fe L_3 resonances for peaks i–iii [see Fig. 8(b)]. Figure 9 displays the resulting magnetization loops. One can see the ferrimagnetic ordering between the Fe^{3+}_{tet} cations and the other Fe and Ni cations. For all octahedrally coordinated cations we probe in-plane open magnetization curves, whereas the Fe^{3+}_{tet} cations exhibit a closed, paramagnetic magnetization curve. In the out-of-plane configuration we only probed the Ni sites (see insets in Fig. 9). Whereas recently reported values of the coercive field are on the order of $H_c = 0.1$ T or more for $NiFe_2O_4$ thin films [44,57,60], we find significantly lower values for hysteresis loops of the octahedrally coordinated cations [see Fig. 9(b)], although it is difficult to obtain exact values for H_c as the magnetization curves are pretty flat. We want to point out rather flat magnetization curves appear to be typical also for $NiFe_2O_4$ epitaxial thin films [61] and

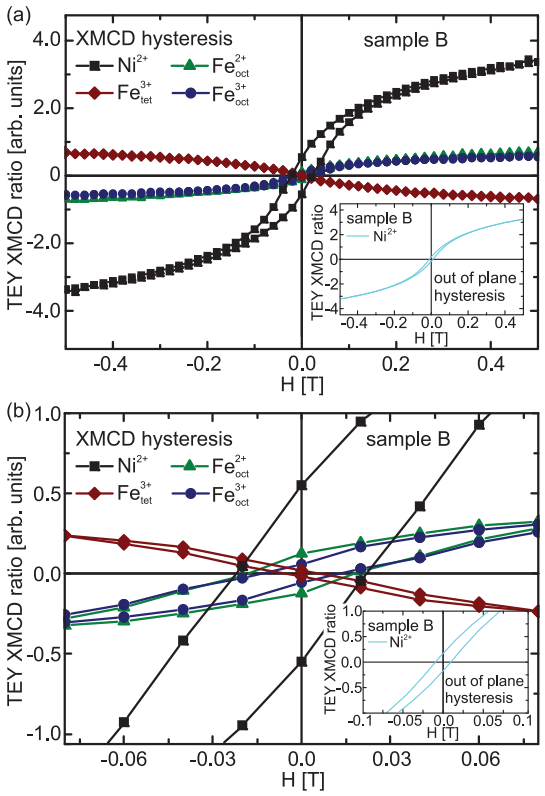

FIG. 9. (a) Element- and site-specific hysteresis loops of the Ni L_3 and Fe L_3 intensities of sample B. (b) Expanded view of the loops near $H = 0$ T. Insets show the Ni hysteresis loop measured in perpendicular (out-of-plane) geometry.

nanoparticles [62]. A number of things might be responsible for the observed discrepancy; a strongly increased H_c might be caused by exchange-coupled grains [60] or a high defect density [57], for instance. On the other hand, similar values for the coercive field measured here have been found for polycrystalline as well as epitaxial $Ni_xFe_{3-x}O_4$ thin films [61]. The bulk value of $NiFe_2O_4$ has been reported to be 0.01 T [62], which is closer to the values obtained here.

IV. SUMMARY AND CONCLUSIONS

We investigated the modification of the crystallographic, electronic, and magnetic properties of Fe_3O_4/NiO bilayers due to thermally induced interdiffusion of Ni ions out of the NiO layer into the magnetite film. We annealed two bilayers [sample A (B) initially comprises 5.6 nm (1.5 nm) NiO and 5.5 nm (5.4 nm) Fe_3O_4] in three steps of 20–30 min in an oxygen atmosphere of 5×10^{-6} mbar. LEED demonstrated the extinction of the magnetite-specific $(\sqrt{2}\times\sqrt{2})$R45° superstructure; however, a spinel-like (1×1) surface structure occurred after the overall annealing cycle.

Structural analysis reveals that the annealing cycles lead to homogeneous layers of $Ni_xFe_{3-x}O_4$. In the case of sample A consideration of an additional NiO layer on the surface and interface leads to the best agreement between calculated and experimentally observed XRR and SR-XRD results. For sample B SR-XRD indicates a strongly distorted structure

with a vertical lattice constant of $c = 0.8304$ nm, whereas the vertical lattice constant $c = 0.8334$ nm of sample A is close to that of bulk $NiFe_2O_4$ ($a_{NFO}^{bulk} = 0.8339$ nm).

These findings are supported by the soft XPS and HAXPES experiments. First, the formation of Fe^{3+} upon annealing at 600 °C is confirmed by the shape and binding energy positions of the Fe $2p$ core level spectra. Further annealing at 800 °C does not cause any changes in the Fe $2p$ spectra. Second, for sample B the shape and binding energy of the Ni $2p$ spectra indicate the formation of an inverse spinel ferrite, whereas in the case of sample A NiO characteristic features first diminish after annealing at 600 °C and then reappear after the entire annealing cycle at 800 °C. Due to surface sensitivity soft XPS analysis clearly reveals the occurrence of Ni^{2+} in NiO stoichiometry in the near-surface region after the last annealing step. Further, HAXPES analysis shows also an increasing amount of Ni^{2+} ions. This may be associated with the much thicker initial NiO layer of sample A, leading to Ni diffusion to the sample surface. We assume that $NiFe_2O_4$ is formed on top of the residual NiO film after the annealing step of 600 °C, as observed in the soft XPS and HAXPES. However, further annealing at 800 °C results in segregation and formation of NiO on top of a well-ordered stoichiometric $NiFe_2O_4$ of high crystalline quality. Thus, the nickel ferrite is saturated by Ni if the ferrite assumes $NiFe_2O_4$ stoichiometry. The residual Ni attempts to form NiO on top of the nickel ferrite due to its lower surface energy compared to the surface energy of nickel ferrite [53]. This process, however, is not completed in our case, probably due to kinetic effects.

Furthermore, we determined a Ni:Fe ratio of 1:2.6 for sample B and thus a resulting stoichiometry of $Ni_{0.83}Fe_{2.17}O_4$. This is in accordance with the weak crystalline quality of sample B seen in the XRD measurements.

We employed XMCD to study the internal magnetic properties of the thin films resulting from the Ni interdiffusion process. In excellent agreement with complementary charge-transfer multiplet simulations, we found a strong increase of the Fe_{tet}^{3+} coordinated cation fraction (around 50%) compared to stoichiometric Fe_3O_4, resulting in very small Fe net magnetic moments as determined from the experimental XMCD data by applying the sum rules. The magnetic properties after the annealing cycle are in both samples dominated by the contribution of the Ni^{2+} ions, which exhibit magnetic moments of $0.56\mu_B$/f.u. (sample A) and $1.03\mu_B$/f.u. (sample B). The latter value corresponds quite well to the value very recently reported for a stoichiometric $NiFe_2O_4$ thin film [57]. The lower value found for sample A can be explained by the formation of (antiferromagnetic) NiO-rich islands or clusters at the surface of the sample which contribute to the Ni $L_{2,3}$-XAS signal but not to the corresponding XMCD. Finally, element-specific hysteresis loops performed on sample B show a rather small in-plane coercive field. This is a further indication of the formation of a magnetically well ordered $NiFe_2O_4$-like thin film by means of thermal interdiffusion of Ni^{2+} ions into magnetite from Fe_3O_4/NiO bilayers.

In conclusion we presented a comprehensive study of epitaxially grown Fe_3O_4/NiO heterostructures and their structural evolution due to Ni interdiffusion as a consequence of three distinct thermal annealing steps. A multitechnique approach tackling the structural, chemical, electronic, and magnetic properties leads to a rather complete and conclusive picture which is also in good agreement with corresponding model calculations. We have demonstrated that it is possible to synthesize $Ni_xFe_{3-x}O_4$ thin films with compositions close to stoichiometric $NiFe_2O_4$ with high crystalline quality by thermally induced intermixing of distinct Fe_3O_4/NiO bilayers grown on Nb-doped $SrTiO_3(001)$. If the initial Fe_3O_4 and NiO thin-film thicknesses can be controlled precisely, one may obtain $Ni_xFe_{3-x}O_4$ thin films with tunable band gap employing this approach, which might be of interest for several applications, e.g., in the field of spintronics (spin valves) or for experiments concerning the spin Hall magnetoresistance [29] and the spin Seebeck effect [27,28]. Thus, additional transport effects based on either charge or spin currents can be amplified or suppressed depending on the band gap properties of the $NiFe_2O_4$-like material.

ACKNOWLEDGMENTS

Financial support from the Deutsche Forschungsgemeinschaft (DFG; KU2321/2-1 and KU3271/1-1) is gratefully acknowledged. We thank Diamond Light Source for access to beamline I09 (SI10511-1) that contributed to the results presented here. Additionally, parts of this research were carried out at the light source PETRA III at DESY. We would like to thank F. Bertram for assistance using beamline P08. Furthermore, part of this work was performed at the Advanced Light Source, which is supported by the Director, Office of Science, Office of Basic Energy Sciences, of the U.S. Department of Energy under Contract No. DE-AC03-76SF00098.

[1] P. Weiss and R. Forrer, Ann. Phys. (Paris) **12**, 279 (1929).
[2] P.I. Slick, in *Handbook of Ferromagnetic Materials*, Chapter 3: Ferrites for non-microwave applications (Elsevier, Amsterdam, 1980), Vol. 2, pp. 189–241.
[3] M. I. Katsnelson, V. Y. Irkhin, L. Chioncel, A. I. Lichtenstein, and R. A. de Groot, Rev. Mod. Phys. **80**, 315 (2008).
[4] R. Bliem, E. McDermott, P. Ferstl, M. Setvin, O. Gamba, J. Pavelec, M. A. Schneider, M. Schmid, U. Diebold, P. Blaha, L. Hammer, and G. S. Parkinson, Science **346**, 1215 (2014).
[5] J. M. Byrne, N. Klueglein, C. Pearce, K. M. Rosso, E. Appel, and A. Kappler, Science **347**, 1473 (2015).
[6] K. Balakrishnan, S. K. Arora, and I. V. Shvets, J. Phys.: Condens. Matter **16**, 5387 (2004).
[7] G. E. Sterbinsky, J. Cheng, P. T. Chiu, B. W. Wessels, and D. J. Keavney, J. Vac. Sci. Technol. B **25**, 1389 (2007).
[8] F. Bertram, C. Deiter, O. Hoefert, T. Schemme, F. Timmer, M. Suendorf, B. Zimmermann, and J. Wollschläger, J. Phys. D **45**, 395302 (2012).
[9] F. Bertram, C. Deiter, T. Schemme, S. Jentsch, and J. Wollschläger, J. Appl. Phys. **113**, 184103 (2013).
[10] J. A. Moyer, S. Lee, P. Schiffer, and L. W. Martin, Phys. Rev. B **91**, 064413 (2015).

[11] T. Schemme, N. Pathé, G. Niu, F. Bertram, T. Kuschel, K. Kuepper, and J. Wollschläger, Mat. Res. Exp. **2**, 016101 (2015).
[12] N.-T. H. Kim-Ngan, A. G. Balogh, J. D. Meyer, J. Brötz, M. Zając, T. Ślęzak, and J. Korecki, Surf. Sci. **603**, 1175 (2009).
[13] K. A. Shaw, E. Lochner, and D. M. Lind, J. Appl. Phys. **87**, 1727 (2000).
[14] N.-T. H. Kim-Ngan, A. G. Balogh, J. D. Meyer, J. Brötz, S. Hummelt, M. Zając, T. Ślęzak, and J. Korecki, Surf. Sci. **602**, 2358 (2008).
[15] J. F. Anderson, M. Kuhn, U. Diebold, K. Shaw, P. Stoyanov, and D. Lind, Phys. Rev. B **56**, 9902 (1997).
[16] L. A. Kalev, P. Schurer, and L. Niesen, Phys. Rev. B **68**, 165407 (2003).
[17] H. C. Wu, R. Ramos, R. S. G. Sofin, Z. M. Liao, M. Abid, and I. V. Shvets, Appl. Phys. Lett. **101**, 052402 (2012).
[18] L. Marnitz, K. Rott, S. Niehörster, C. Klewe, D. Meier, S. Fabretti, M. Witziok, A. Krampf, O. Kuschel, T. Schemme, K. Kuepper, J. Wollschläger, A. Thomas, G. Reiss, and T. Kuschel, AIP Adv. **5**, 047103 (2015).
[19] T. Schemme, A. Krampf, F. Bertram, T. Kuschel, K. Kuepper, and J. Wollschläger, J. Appl. Phys. **118**, 113904 (2015).
[20] C. Gatel, E. Snoeck, V. Serin, and A. R. Fert, Eur. Phys. J. B **45**, 157 (2005).
[21] J. Keller, P. Miltényi, B. Beschoten, G. Güntherodt, U. Nowak, and K. D. Usadel, Phys. Rev. B **66**, 014431 (2002).
[22] T. Schemme, O. Kuschel, F. Bertram, K. Kuepper, and J. Wollschläger, Thin Solid Films **589**, 526 (2015).
[23] M. Monti, M. Sanz, M. Oujja, E. Rebollar, M. Castillejo, F. J. Pedrosa, A. Bollero, J. Camarero, J. L. F. Cuñado, N. M. Nemes, F. J. Mompean, M. Garcia-Hernández, S. Nie, K. F. McCarty, A. T. N'Diaye, G. Chen, A. K. Schmid, J. F. Marco, and J. de la Figuera, J. Appl. Phys. **114**, 223902 (2013).
[24] J. Rubio-Zuazo, L. Onandia, E. Salas-Colera, A. Munoz-Noval, and G. R. Castro, J. Phys. Chem. C **119**, 1108 (2015).
[25] M. Pilard, O. Ersen, S. Cherifi, B. Carvello, L. Roiban, B. Muller, F. Scheurer, L. Ranno, and C. Boeglin, Phys. Rev. B **76**, 214436 (2007).
[26] J.-B. Moussy, J. Phys. D **46**, 143001 (2013).
[27] D. Meier, T. Kuschel, L. Shen, A. Gupta, T. Kikkawa, K. Uchida, E. Saitoh, J.-M. Schmalhorst, and G. Reiss, Phys. Rev. B **87**, 054421 (2013).
[28] D. Meier, D. Reinhardt, M. van Straaten, C. Klewe, M. Althammer, M. Schreier, S. T. B. Goennenwein, A. Gupta, M. Schmid, C. H. Back, J.-M. Schmalhorst, T. Kuschel, and G. Reiss, Nat. Commun. **6**, 8211 (2015).
[29] M. Althammer *et al.*, Phys. Rev. B **87**, 224401 (2013).
[30] D. Levy, A. Gilberto, and M. Dapiaggi, J. Solid State Chem. **177**, 1713 (2004).
[31] C. J. Powell and A. Jablonski, Nucl. Instrum. Methods Phys. Res., Sect. A **601**, 54 (2009).
[32] S. Tanuma, C. J. Powell, and D. R. Penn, Surf. Interface Anal. **35**, 268 (2003).
[33] L. G. Parratt, Phys. Rev. **95**, 359 (1954).
[34] L. Névot and P. Croce, Rev. Phys. Appl. **15**, 761 (1980).
[35] F. M. F. de Groot, Coord. Chem. Rev. **249**, 31 (2005).
[36] E. Stavitski and F. M. F. de Groot, Micron **41**, 687 (2010).
[37] S. A. Chambers and S. A. Joyce, Surf. Sci. **420**, 111 (1999).
[38] J. Korecki, B. Handke, N. Spiridis, T. Slezak, F. Flis-Kabulska, and J. Haber, Thin Solid Films **412**, 14 (2002).
[39] R. Pentcheva, W. Moritz, J. Rundgren, S. Frank, D. Schrupp, and M. Scheffler, Surf. Sci. **602**, 1299 (2008).
[40] T. Yamashita and P. Hayes, Appl. Surf. Sci. **254**, 2441 (2008).
[41] T. Fujii, F. M. F. de Groot, G. A. Sawatzky, F. C. Voogt, T. Himba, and K. Okada, Phys. Rev. B **59**, 3195 (1999).
[42] P. C. J. Graat and M. A. J. Somers, Appl. Surf. Sci. **100-101**, 36 (1996).
[43] N. S. McIntyre and M. G. Cook, Anal. Chem. **47**, 2208 (1975).
[44] M. Hoppe, S. Döring, M. Gorgoi, S. Cramm, and M. Müller, Phys. Rev. B **91**, 054418 (2015).
[45] L. Soriano, I. Preda, A. Gutiérrez, S. Palacín, M. Abbate, and A. Vollmer, Phys. Rev. B **75**, 233417 (2007).
[46] S. Uhlenbrock, C. Scharfschwerdtt, M. Neumannt, G. Illing, and H.-J. Freund, J. Phys.: Condens. Matter **4**, 7973 (1992).
[47] A. P. Grosvenor, M. C. Biesinger, R. S. C. Smart, and N. S. McIntyre, Surf. Sci. **600**, 1771 (2006).
[48] B. L. Henke, E. M. Gullikson, and J. C. Davis, At. Data. Nucl. Data Tables **54**, 181 (1993).
[49] M. C. Biesinger, B. P. Payne, A. P. Grosvenor, L. W. M. Lau, A. R. Gerson, and R. S. C. Smart, Appl. Surf. Sci. **257**, 2717 (2011).
[50] R. M. Cornell and U. Schwertmann, *The Iron Oxides*, 2nd ed. (Wiley-VCH, Weinheim, 2003).
[51] M. B. Trzhaskovskaya, V. I. Nefedov, and V. G. Yarzhemsky, At. Data Nucl. Data Tables **77**, 97 (2001).
[52] J. T. Newberg, D. E. Starr, S. Yamamoto, S. Kaya, T. Kendelewicz, E. R. Mysak, S. Porsgaard, M. B. Salmeron, G. E. Brown, Jr., A. Nilsson, and H. Bluhm, Surf. Sci. **605**, 89 (2011).
[53] C. J. O'Brien, Z. Rak, and D. W. Brenner, J. Phys.: Condens. Matter **25**, 445008 (2013).
[54] C. T. Chen, Y. U. Idzerda, H.-J. Lin, N. V. Smith, G. Meigs, E. Chaban, G. H. Ho, E. Pellegrin, and F. Sette, Phys. Rev. Lett. **75**, 152 (1995).
[55] Y. Teramura, A. Tanaka, and T. Jo, J. Phys. Soc. Jpn. **65**, 1053 (1996).
[56] C. Piamonteze, P. Miedema, and F. M. F. de Groot, Phys. Rev. B **80**, 184410 (2009).
[57] C. Klewe, M. Meinert, A. Boehnke, K. Kuepper, E. Arenholz, A. Gupta, J.-M. Schmalhorst, T. Kuschel, and G. Reiss, J. Appl. Phys. **115**, 123903 (2014).
[58] R. Pattrick, G. Van der Laan, C. Henderson, P. Kuiper, E. Dudzik, and D. Vaughan, Eur. J. Mineral. **14**, 1095 (2002).
[59] G. F. M. Gomes, T. E. P. Bueno, D. E. Parreiras, G. J. P. Abreu, A. de Siervo, J. C. Cezar, H.-D. Pfannes, and R. Paniago, Phys. Rev. B **90**, 134422 (2014).
[60] G. H. Jaffari, A. K. Rumaiz, J. C. Woicik, and S. I. Shah, J. Appl. Phys. **111**, 093906 (2012).
[61] C. Jin, Q. Zhang, W. B. Mi, E. Y. Jiang, and H. L. Bai, J. Phys. D **43**, 385001 (2010).
[62] A. Shan, X. Wu, J. Lu, C. Chen, and R. Wang, CrystEngComm **17**, 1603 (2015).

Chapter 3

Publication H7

[**H7**] L. Schneider, T. Rinkel, B. Voß, A. Chrobak, J. P. Klare, J. Neethling, J. Olivier, D. Schnaniel, E.-E. Bendeif, F. Bondino, E. Magnano, I. Píš. K. Balinski, J. Wollschläger, H.-J. Steinhoff, M. Haase, and K. Kuepper. *Characterization of multifunctional β-$NaEuF_4$/$NaGdF_4$ core-shell nanoparticles with narrow size distribution*, Nanoscale **8**, 2832 (2016), doi: 10.1039/c5nr06915g.

Nanoscale

PAPER

View Article Online
View Journal | View Issue

Cite this: *Nanoscale*, 2016, **8**, 2832

Characterization of multifunctional β-$NaEuF_4$/$NaGdF_4$ core–shell nanoparticles with narrow size distribution†

Lilli Schneider,*[a] Thorben Rinkel,[b] Benjamin Voß,[b] Artur Chrobak,[c] Johann P. Klare,[a] Jan Neethling,[d] Jaco Olivier,[d] Dominik Schaniel,[e] El-Eulmi Bendeif,[e] Federica Bondino,[f] Elena Magnano,[f] Igor Píš,[f,g] Kamil Balinski,[a] Joachim Wollschläger,[a] Heinz-Jürgen Steinhoff,[a] Markus Haase[b] and Karsten Kuepper*[a]

Received 6th October 2015,
Accepted 27th December 2015

DOI: 10.1039/c5nr06915g

www.rsc.org/nanoscale

The properties of β-$NaEuF_4$/$NaGdF_4$ core–shell nanocrystals have been thoroughly investigated. Nanoparticles with narrow size distribution and an overall diameter of ~22 nm have been produced with either small β-$NaEuF_4$ cores (~3 nm diameter) or large β-$NaEuF_4$ cores (~18 nm diameter). The structural properties and core–shell formation are investigated by X-ray diffraction, transmission electron microscopy and electron paramagnetic resonance, respectively. Optical luminescence measurements and X-ray photoelectron spectroscopy are employed to gain information about the optical emission bands and valence states of the rare earth constituents. Magnetic characterization is performed by SQUID and X-ray magnetic circular dichroism measurements at the rare earth $M_{4,5}$ edges. The characterization of the core–shell nanoparticles by means of these complementary techniques demonstrates that partial intermixing of core and shell materials takes place, and a significant fraction of europium is present in the divalent state which has significant influence on the magnetic properties. Hence, we obtained a combination of red emitting Eu^{3+} ions and paramagnetic Gd^{3+} ions, which may be highly valuable for potential future applications.

1 Introduction

$NaREF_4$ nanoparticles (RE: rare earth) have attracted increasing interest in recent years for applications in biological labeling and imaging,[1–20] photodynamic therapy and drug delivery,[21–26] photovoltaics,[27–30] photonics[31–33] and security labeling.[34–36] Frequently, nanocrystals with core–shell structure are synthesized, since a shell of inert material increases the quantum yield of a luminescent particle core by decreasing energy losses on the particle surface.[37–39] Particles containing one or more shells of the doped material furthermore allow us to spatially separate the dopant ions with different functionalities and to control the migration of energy within such structures.[40–49] For lanthanide ions emitting in the red and near infrared spectral regions, fluoride host materials are of particular interest because the very low phonon frequencies of fluoride lattices decrease the probabilities of multiphonon relaxation processes, resulting in high quantum yields. One example is the Eu^{3+} ion, displaying pure red emission in many host materials, because all transitions except those from the $^5D_0$ level are quenched due to multiphonon relaxation. In the fluoride host, however, also transitions from the higher $^5D_1$, $^5D_2$ and $^5D_3$ levels are observed provided that the concentration of the Eu^{3+} dopant is low. At higher concentrations, however, cross-relaxation between adjacent Eu^{3+} in the lattice leads to quenching of the $^5D_1$, $^5D_2$ and $^5D_3$ transitions in these materials, too. Trivalent gadolinium, on the other hand, is characterized by a relatively large energy gap between the ground state ($^8S_{7/2}$) and the lowest excited level ($^6P_{7/2}$).[21] Importantly, this excited level is situated in the ultraviolet spectral

[a]*Department of Physics, Center of Physics and Chemistry of New Materials, Universität Osnabrück, Barbarastr. 7, 49076 Osnabrück, Germany. E-mail: lischroe@uos.de, kkuepper@uos.de*
[b]*Institute of Chemistry of New Materials, Center of Physics and Chemistry of New Materials, Universität Osnabrück, Barbarastr. 7, 49076 Osnabrück, Germany*
[c]*Institute of Physics, Silesian University, Uniwersytecka 4, 40-007 Katowice, Poland*
[d]*Centre for HRTEM, Nelson Mandela Metropolitan University, P.O. Box 77000, Port Elizabeth, South Africa*
[e]*Université de Lorraine, CRM2, UMR 7036, Vandoeuvre-les-Nancy, F-54506, France*
[f]*IOM CNR, Laboratorio TASC, S.S. 14 km 163.5, 34149 Basovizza, Trieste, Italy*
[g]*Elettra-Sincrotrone Trieste S.C.p.A., S.S. 14 km 163.5, 34149 Basovizza, Trieste, Italy*

†Electronic supplementary information (ESI) available. See DOI: 10.1039/C5NR06915G

region, *i.e.* well above the emitting $^5D_0$, $^5D_1$, $^5D_2$ and $^5D_3$ levels of Eu^{3+}. A $NaGdF_4$ shell around a $NaEuF_4$ core can therefore improve the luminescence efficiency of the core. Moreover, the lattice mismatch between the core and the shell is very low due the very similar lattice constants of $NaGdF_4$ and $NaEuF_4$. In addition to their interesting optical properties, europium and gadolinium have remarkable magnetic properties. Owing to their seven unpaired electrons, Gd^{3+} ions in the ground state can, for instance, efficiently alter the relaxation times of the surrounding water protons and are therefore the basis of the most commonly used contrast agents in magneto resonance imaging.[50] While gadolinium ions usually form the oxidation state III+, europium compounds can contain either Eu^{3+} or Eu^{2+} ions, or both. Trivalent europium in the ground state ($^7F_0$, $S = 3$, $L = 3$, $J = 0$) has no magnetic moment while divalent europium has seven unpaired electrons in the ground state ($^8S_{7/2}$, $S = 8$, $L = 0$, $J = 7/2$). Interestingly in some trivalent compounds formation of divalent europium states on the surface was observed.[51,52] Moreover, Kachkanov *et al.* detected an optically induced magnetic moment of Eu^{3+} ions in GdN.[53]

In this work, we synthesized core–shell systems composed of a β-$NaEuF_4$ core and a β-$NaGdF_4$ shell. This structure has two advantages. Firstly, the influence of different surrounding media on the β-$NaEuF_4$ core can be minimized or entirely removed. Secondly, the combination of red emitting Eu^{3+} ions and paramagnetic Gd^{3+} ions is highly valuable.

The nominal size is the expected size based on the used materials respectively precursor particles. We use a number of complementary methods to evaluate the structure of β-$NaEuF_4$/$NaGdF_4$ core–shell particles and to study their electronic and magnetic properties. Detailed knowledge of these properties is indispensable to compare the results with those of Eu^{3+} doped β-$NaGdF_4$ nanoparticles and to further optimize the core–shell system in question. Structural properties and core–shell formation are determined by means of X-ray powder diffraction (XRD) and high resolution transmission electron microscopy (HR-TEM). Core–shell formation is further investigated by electron paramagnetic resonance (EPR) and optical luminescence spectroscopy. Chemical and electronic properties with special emphasis on the Eu and Gd valence states are determined employing X-ray photoelectron spectroscopy (XPS), whereas magnetic characterization is performed with a superconducting quantum interference device (SQUID) magnetometer. The measured magnetization curves are analyzed by means of Monte Carlo based Heisenberg simulations. Finally we performed element specific X-ray magnetic circular dichroism (XMCD) at the Eu $M_{4,5}$ and Gd $M_{4,5}$ edges to gain a complete picture of the internal magnetic structure of the multifunctional β-$NaEuF_4$/$NaGdF_4$ core–shell nanoparticles.

2 Results and discussion

2.1 Total scattering measurement and PDF analysis

Fig. 1 shows the pair distribution functions (PDFs) for both core–shell samples as well as the 22 nm β-$NaGdF_4$ nanocrystals doped with 1% Eu. The two samples containing low Eu and high Gd concentration (20 nm β-$NaEuF_4$/$NaGdF_4$ core–shell nanoparticles (NPs) with a 3 nm β-$NaEuF_4$ core, 22 nm β-$NaGdF_4$ nanoparticle (NP) doped with 1% Eu) exhibit very similar PDFs that differ significantly from the core–shell sample with the 18 nm β-$NaEuF_4$ core. Comparing the two core–shell samples (20 nm β-$NaEuF_4$/$NaGdF_4$ core–shell nanoparticles with a 3 nm β-$NaEuF_4$ core, 22 nm β-$NaEuF_4$/$NaGdF_4$ core–shell nanoparticles with an 18 nm β-$NaEuF_4$ core) we can clearly identify shifts of the peak positions in the PDF (corresponding to atom–atom distances). Note that the structures of bulk β-$NaEuF_4$ and β-$NaGdF_4$ are quite similar and the differences in bond distances between the different atoms are thus expected to be small. In order to enhance the visibility of the structural differences we calculated the differences between the corresponding PDFs, given as $\Delta G(r)$ in Fig. 1. One can clearly see that the difference between the PDF of the 20 nm β-$NaEuF_4$/$NaGdF_4$ core–shell nanoparticles with a 3 nm β-$NaEuF_4$ core and the 22 nm β-$NaGdF_4$ NP doped with 1% Eu is very small, resulting in very weak features in the $\Delta G(r)$. A core–shell nanoparticle with a small β-$NaEuF_4$ core thus exhibits almost the same structure as a nanoparticle doped with 1% Eu, indicating that the structural relaxation is similar for these two cases. In other words, from the PDF analysis alone it is impossible to distinguish between the structure of the core–shell NP and a homogeneously doped NP. In contrast, the difference of the two PDFs ($\Delta G(r)$) of the two core–shell samples is much more pronounced. Almost all peak positions are affected and the shifts are more pronounced for larger atom–atom distances r. In order to investigate this result in more detail we performed simulations of the PDFs based on pure crystalline, spherical 22 nm β-$NaGdF_4$ and β-$NaEuF_4$ nanocrystals. The results are shown in Fig. 2. The distances are slightly shorter in the β-$NaGdF_4$ nanoparticle as expected from the smaller lattice parameters. We observe a good agreement between the simulated peak positions in the PDF for the

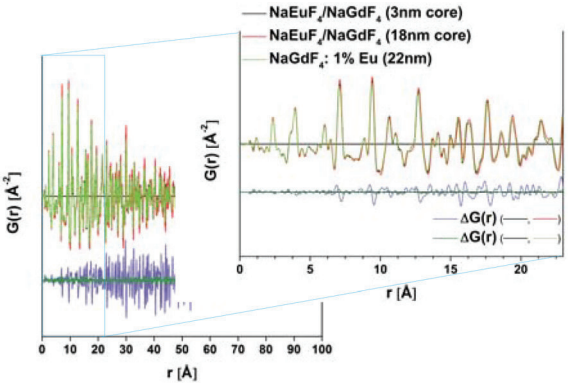

Fig. 1 Comparison of atomic PDFs in real space, $G(r)$ for 20 nm β-$NaEuF_4$/$NaGdF_4$ core–shell nanoparticles with a 3 nm β-$NaEuF_4$ core and ~8.5 nm β-$NaGdF_4$ shell, 22 nm β-$NaEuF_4$/$NaGdF_4$ core–shell nanoparticles (NPs) with an 18 nm β-$NaEuF_4$ core and 22 nm β-$NaGdF_4$ nanoparticle (NP) doped with 1% Eu and their differential PDFs.

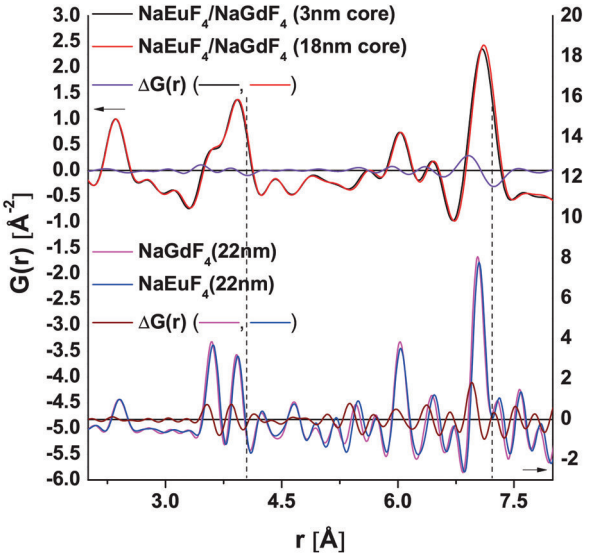

Fig. 2 Comparison of observed PDFs for 20 nm β-$NaEuF_4$/$NaGdF_4$ core–shell nanoparticles with a 3 nm β-$NaEuF_4$ core and ~8.5 nm β-$NaGdF_4$ shell and 22 nm β-$NaEuF_4$/$NaGdF_4$ core–shell NPs with an 18 nm β-$NaEuF_4$ core and calculated PDFs of 22 nm β-$NaGdF_4$ and β-$NaEuF_4$ spheres with the corresponding differential PDFs (spectra are normalized to the first peak).

two pure nanoparticles and the experimentally determined PDF. The peaks are broader in the experimental PDF, which is due to a lower resolution of the experiment, but also due to the fact that in the core–shell nanoparticles we expect some strain and defects as well as a not perfectly spherical shape. We don't expect a significant impact of the particle-size distribution on the PDF since the size distributions are rather narrow, *e.g.*, the β-$NaEuF_4$/$NaGdF_4$ (3 nm core) nanoparticles exhibit a size distribution of 16.8 nm ± 5% (see Table 1), corresponding to particles ranging from 16 nm to 17.7 nm. If the structural difference (*e.g.* distances between first neighbours) between two such nanoparticles is well below the resolution of 0.138 Å, there will be no visible effect on the experimental PDF. For illustration one can compare the two simulated PDFs for the 22 nm β-$NaGdF_4$ and β-$NaEuF_4$ particles given in Fig. 2, where the difference in the first neighbour distances between the pure Gd and the pure Eu sample is of the order of 0.02 Å, which is at the limit of visibility in the $G(r)$. Structural differences between two identical nanoparticles differing only by 5% in size would therefore not be detected in the experiment. As a first conclusion we can state that a β-$NaEuF_4$/$NaGdF_4$ core–shell nanoparticle with a 3 nm β-$NaEuF_4$ core exhibits approximately the same structure as a slightly Eu-doped β-$NaGdF_4$ nanoparticle and its main structural parameters are those of the β-$NaGdF_4$ structure. β-$NaEuF_4$/$NaGdF_4$ core–shell nanoparticles with an 18 nm β-$NaEuF_4$ core on the other hand resemble the corresponding pure β-$NaEuF_4$ structure. Due to the limited resolution of the experiment a more detailed modelling, *e.g.* to investigate the core–shell interface, is currently not possible. High-resolution electron microscopy investigations were carried out for further characterisation of the nanoparticles.

Table 1 Sample label, nominal size and size distribution determined by transmission electron microscopy (TEM) analysis (Fig. S2 and S4)

Samples	Nominal size	Size (from TEM)
$NaEuF_4$/$NaGdF_4$ (3 nm core)	20 nm	16.8 nm ± 5%
$NaEuF_4$/$NaGdF_4$ (18 nm core)	22 nm	23 nm ± 3.8%
$NaGdF_4$:1% Eu	22 nm	25.4 nm ± 4%
$NaEuF_4$ (3 nm)	3 nm	Not evaluable
$NaEuF_4$ (18 nm)	18 nm	19.7 nm ± 4.2%
$NaGdF_4$/$NaEuF_4$ (3 nm core)	20 nm	20.2 nm ± 3.9%
$NaEuF_4$:1% Gd	22 nm	24.5 nm ± 5.4%
$NaGdF_4$ (3 nm)	3 nm	Not evaluable
$NaGdF_4$ (22 nm)	22 nm	25.6 nm ± 5.8%

2.2 TEM-HRTEM

The morphology of the nanoparticles was characterized by transmission electron microscopy (TEM). It can be seen that the particles are nearly spherical or slightly elongated and retain the initial morphology of the precursor core particles (Fig. 3). Inter-planar spacings were measured using fast Fourier transform (FFT) analysis of the HRSTEM images. Inter-planar spacings with distances 0.29 nm, 0.18 nm and 0.16 nm were measured. These match very closely to the theoretical values for the (1,1,0), (0,0,2) and (1,1,2) planes respectively. Because the lattice constants between the core and the shell are similar, no significant differences are observed. Fig. 4(a)

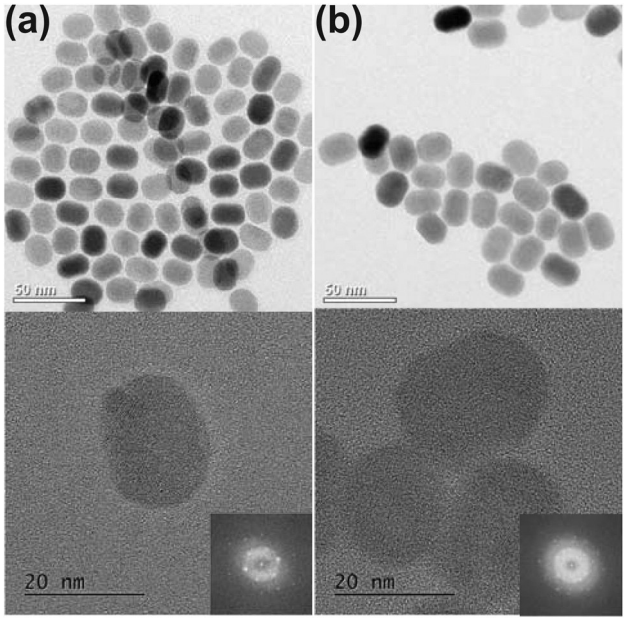

Fig. 3 TEM images showing (top) general morphology and (bottom) high-resolution images of the (a) 18 nm β-$NaEuF_4$ NP and (b) 22 nm β-$NaEuF_4$/$NaGdF_4$ NP with a 2 nm β-$NaGdF_4$ shell around the 18 nm β-$NaEuF_4$ core. The insets show the fast Fourier transforms (FFTs) of HR-TEM images.

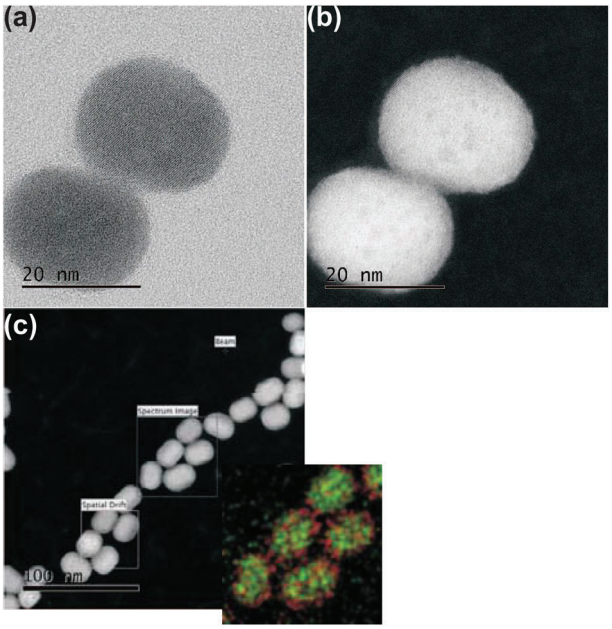

Fig. 4 High resolution scanning transmission electron microscopy bright field (HRSTEM-BF) image of (a) 22 nm β-$NaEuF_4$/$NaGdF_4$ core–shell NPs with an 18 nm β-$NaEuF_4$ core and 2 nm β-$NaGdF_4$ shell and (b) the corresponding high-angle annular dark field (HAADF) high resolution scanning transmission electron microscope (HRSTEM) image. And (c) scanning transmission electron microscope-electron energy loss spectroscopy (STEM-EELS) survey image and colour map of Eu (green) and Gd (red).

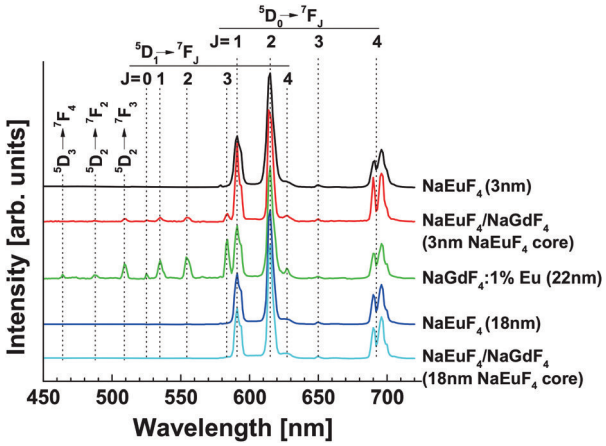

Fig. 5 Normalized emission spectra of 3 nm β-$NaEuF_4$, 20 nm β-$NaEuF_4$/$NaGdF_4$ NPs with a 3 nm core, 22 β-$NaGdF_4$ NP doped with 1% Eu, 18 nm β-$NaEuF_4$ and 22 nm β-$NaEuF_4$/$NaGdF_4$ NPs with an 18 nm β-$NaEuF_4$ core. The spectra were recorded under 394 nm excitation of the Eu^{3+} ions ($^7F_{0,1} \rightarrow {}^5L_6$). All particles consist of hexagonal phase (β-phase).

shows the high-resolution bright field scanning transmission electron microscopy (BF STEM) images of the core–shell nanoparticles with an 18 nm β-$NaEuF_4$ core and a 2 nm β-$NaGdF_4$ shell and (b) the corresponding high-angle annular dark field (HAADF) image.

The HAADF HRSTEM image of the 22 nm β-$NaEuF_4$/$NaGdF_4$ core–shell NPs with an 18 nm β-$NaEuF_4$ core and 2 nm β-$NaGdF_4$ shell in Fig. 4(b) does not show significant variation within the nanoparticle.

The STEM-EELS mapping of the 22 nm β-$NaEuF_4$/$NaGdF_4$ core–shell NPs with an 18 nm β-$NaEuF_4$ core and 2 nm β-$NaGdF_4$ shell (Fig. 4(c)) shows according to the colour map (inset) evidence of a core shell structure with Eu (green) in the center and Gd (red) on the surface.

2.3 Luminescence

The optical properties of the β-$NaEuF_4$ core and β-$NaEuF_4$/$NaGdF_4$ core–shell nanocrystals were studied by photoluminescence spectroscopy. As expected, excitation at the $^7F_{0,1} \rightarrow {}^5L_6$ transition of Eu^{3+} at ~394 nm results in Eu^{3+} emission for all nanoparticles containing Eu^{3+} ions (Fig. 5). In all cases the highest emission intensities are recorded at ~591, 614 and 696 nm corresponding to the $^5D_0 \rightarrow {}^7F_1$, $^5D_0 \rightarrow {}^7F_2$ and $^5D_0 \rightarrow {}^7F_4$ intra-4f shell transitions of Eu^{3+} respectively.[54] These transitions are characteristic for luminescent materials containing Eu^{3+} ions and are, for instance, also observed for the β-$NaGdF_4$ nanocrystals doped with 1 mol% of Eu^{3+}. Fig. 5 shows, however, that the emission spectrum of such weakly doped particles displays additional lines between 450 nm and 580 nm, caused by transitions from the higher excited $^5D_3$, $^5D_2$ and $^5D_1$ levels of Eu^{3+} to its ^7F_J ground state multiplet. These emission lines are very weak in materials containing Eu^{3+} in high concentrations, since cross-relaxation between adjacent Eu^{3+} ions is known to quench the luminescence from these states. The $^5D_3$, $^5D_2$ and $^5D_1$ emission lines are therefore characteristic for Eu^{3+} ions having no Eu^{3+} neighbors in the crystal lattice and display negligible intensity, for instance, in the case of β-$NaEuF_4$ core particles (Fig. 5).[55,56] Fig. 5 shows, however, that after the formation of the $NaGdF_4$ shell, the $^5D_3$, $^5D_2$ and $^5D_1$ emission lines appear in the spectrum of the core–shell particles. This indicates that some Eu^{3+} ions are released from the β-$NaEuF_4$ core and incorporate into $NaGdF_4$ during formation of the shell. The figure also shows that the transitions from the higher ^5D states are much less intense for core–shell particles with 18 nm cores indicating that the number of Eu^{3+} ions released decreases with increasing core size. This observation is in accord with the lower surface-to-bulk ratio of 18 nm core particles compared to 3 nm core particles, since the release of Eu^{3+} ions should be proportional to the total surface area of all core particles. To further substantiate this result, we have investigated the core–shell particles containing Gd^{3+} by EPR spectroscopy.

2.4 Electron paramagnetic resonance spectroscopy

In general, the EPR spectrum of Gd^{3+} ions ($S = 7/2$) is characterized by the Zeeman interaction with a g-value ≈2 and exhibits significant contributions from zero-field splitting. The mean distance between two adjacent Gd^{3+} ions in the crystal lattice is reflected in the broadness of the EPR spectrum that

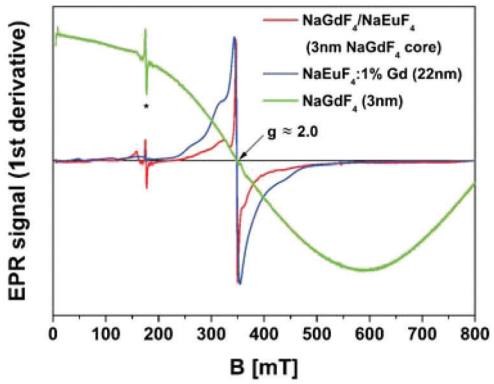

Fig. 6 Normalized EPR spectra of 20 nm core–shell particles composed of a 3 nm β-$NaGdF_4$ core and an ~8.5 nm β-$NaEuF_4$ shell (red), 22 nm β-$NaEuF_4$ NPs doped with 1% Gd (blue) and 3 nm β-$NaGdF_4$ precursor particles (green). Due to the large width of the EPR spectrum of the precursor particles it has a significantly lower intensity compared to the other spectra and consequently displays more noise when the spectra are normalized to the same signal height (scaling factors: blue, ×1; red, ×10; green, ×11). The asterisk denotes an impurity signal of the microwave cavity present in all spectra at 175 mT.

increases with increasing Gd concentration due to dipolar and isotropic exchange interactions between the ions, as observed in Fig. 6 for 3 nm β-$NaGdF_4$ particles (green spectrum).[57] A similar broadening due to Gd^{3+}–Gd^{3+} interactions has been observed for $NaYF_4$/$NaGdF_4$ core–shell nanocrystals, even if the shell of $NaGdF_4$ is as thin as 1 nm.[58] In the study presented here we investigated core–shell particles with significantly thicker shells, consisting of a small 3 nm β-$NaEuF_4$ core and an ~8.5 nm thick β-$NaGdF_4$ shell. Since the EPR signal of such particles would be fully dominated by the broad spectrum of the undiluted Gd^{3+} ions in the shell, we used core–shell nanocrystals with inverted composition in the EPR measurements, *i.e.*, 3 nm β-$NaGdF_4$ core particles with an ~8.5 nm β-$NaEuF_4$ shell. In Fig. 6, the EPR spectrum of these core–shell particles (red line) is compared with the EPR spectrum of β-$NaEuF_4$ nanocrystals doped with 1% Gd^{3+} (blue line) and the EPR spectrum of 3 nm β-$NaGdF_4$ core particles (green line). Note that all spectra are normalized at maximum signal height as indicated by the scaling factors given in the figure. The highest scaling factor was used for the $NaGdF_4$ core particles as the strong interaction of the Gd^{3+} ions in these particles leads to strong broadening of their EPR signal (green line). The lowest scaling factor was used in the spectrum of the weakly doped β-$NaEuF_4$:1% Gd particles. This spectrum exhibits a dominating narrow EPR signal (peak-to-peak width, $\Delta B_{pp} \approx 10$ mT) in the $g = 2$ region and additional contributions at higher g-values (lower magnetic fields), the latter indicating the presence of Gd^{3+} ions at sites with different symmetries and/or crystal fields compared to the bulk sites. Since we used rather large $NaEuF_4$:1% Gd particles with a diameter of 22 nm, the contribution from surface Gd^{3+} sites, however, is almost negligible in this case. The additional contributions therefore indicate that the Gd^{3+} dopant ions are not homogeneously distributed inside the particles as observed before.[58] Finally, the high scaling factor used for the β-$NaGdF_4$/$NaEuF_4$ core–shell nanocrystals shows that their EPR signal is much weaker than the signal of the doped β-$NaEuF_4$:1% Gd particles, although both samples contain europium and gadolinium in the same molar ratio of 99 to 1. The much lower intensity is in accord with the core shell structure, since the signal of the Gd^{3+} ions in the core is expected to be strongly broadened. Similar to the doped β-$NaEuF_4$:1% Gd particles, however, the normalized EPR spectrum of the core–shell particles also displays a narrow signal at $g \approx 2.0$ characteristic for isolated or weakly interacting Gd^{3+} ions. Since this signal is even narrower ($\Delta B_{pp} \approx 3$ mT) and of higher relative intensity compared to the doped β-$NaEuF_4$:1% Gd particles, it indicates the presence of highly diluted ($\ll$1%) Gd^{3+} ions in the β-$NaEuF_4$ shell. Komban *et al.* concluded from the EPR data for $NaYF_4$:Gd core–shell particles that the shell structure grows from dissolved precursor particles and that most likely also Y^{3+} ions are released from the surface of the core-precursors during the reaction.[58] The EPR data for the β-$NaGdF_4$:Eu core–shell particles shown in Fig. 6 indicates that these nanocrystals are formed in a similar way and therefore support the conclusions drawn above from luminescence spectroscopy.

2.5 Chemical properties, core level XPS

We employed core level XPS to investigate the chemical states of the Eu and Gd ions of the nanoparticles and core–shell systems in question. Fig. 7(a) displays the Gd 3d X-ray photoelectron spectra of the core–shell and pure β-$NaGdF_4$ (3 nm diameter) nanoparticles. The corresponding spectrum of a GdF_3 single crystal[52] is also shown for comparison. For all samples the Gd $3d_{5/2}$ and $3d_{3/2}$ core level binding energies are located at 1187.5 eV and 1219.5 eV, respectively. All the spectra show no distinct satellite features between the $3d_{5/2}$ and $3d_{3/2}$ main peaks indicating the absence of any metallic Gd contributions.[59]

Fig. 7(b)–(d) show the Eu 4d (and Gd 4d (Fig. 7(d))) spectra of pure β-$NaEuF_4$ (3 nm and 18 nm (Fig. 7(b) and (c))) and the β-$NaEuF_4$/$NaGdF_4$ core–shell nanoparticles with an 18 nm β-$NaEuF_4$ core (Fig. 7(d)). The Eu 4d XPS of the 3 nm β-$NaEuF_4$ nanoparticles comprises three distinct features located at 129.9 eV (A), 137.4 eV (B), and 143.4 eV (C). Features B and C can be attributed to the Eu^{3+} $4d_{5/2}$ and Eu^{3+} $4d_{3/2}$ states, whereas the lower binding energy peak A represents the Eu^{2+} $4d_{5/2}$ states,[52] whereas the Eu^{2+} $4d_{3/2}$ states are overlapping with the Eu^{3+} $4d_{5/2}$ states and not visible as distinct features in the corresponding Eu 4d spectra. We de-convolute these spectra using Gaussian/Lorentzian line profiles. In the case of the β-$NaEuF_4$/$NaGdF_4$ core–shell nanoparticles (18 nm β-$NaEuF_4$ core) this de-convolution approach is extended to the Gd^{3+} $4d_{5/2}$ and Gd^{3+} $4d_{3/2}$ states, assuming a pure trivalent Gd valence state in accordance with the results presented in Fig. 7(a). With the fitting approach described we are able to determine the Eu cation distribution of the nanoparticles investigated here. One can already see by the naked eye that the 3 nm β-$NaEuF_4$ nanoparticles comprise the highest

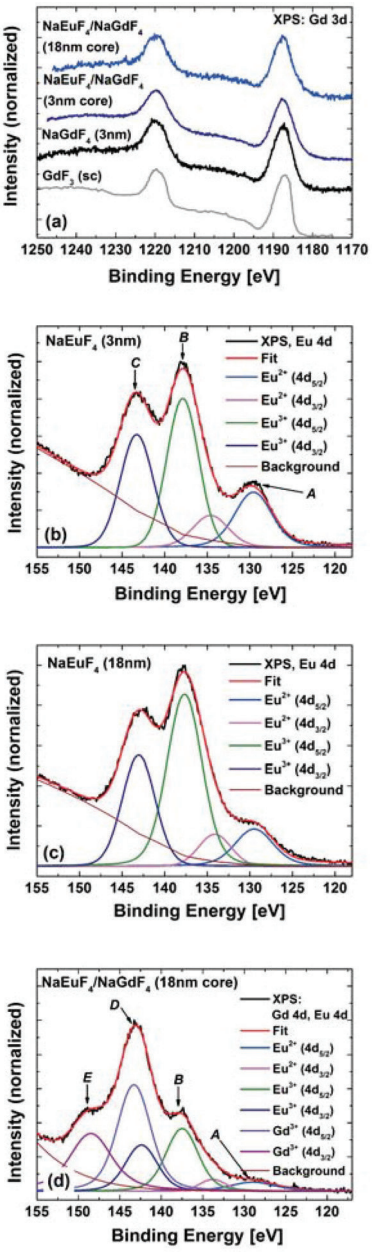

Fig. 7 Normalized XPS spectra of: (a) Gd 3d-core level of β-$NaEuF_4$/$NaGdF_4$ core–shell nanoparticles with 18 nm and 3 nm β-$NaEuF_4$ cores, 3 nm pure β-$NaGdF_4$ nanoparticles, and a GdF_3 single crystal[52] as a reference. (b) Eu 4d-core level of pure 3 nm β-$NaEuF_4$ nanoparticles, de-convoluted into Eu^{2+} and Eu^{3+} fractions. (c) Eu 4d-core level of pure 18 nm β-$NaEuF_4$ nanoparticles, de-convoluted into Eu^{2+} and Eu^{3+} fractions. (d) Eu 4d-core level of β-$NaEuF_4$/$NaGdF_4$ core–shell nanoparticles with an 18 nm β-$NaEuF_4$ core. Eu and Gd spectra are partly overlapping, and are de-convoluted into Eu^{2+}, Eu^{3+} and Gd^{3+} contributions.

amount of Eu^{2+} ions, we find the Eu valence state in this sample to be composed out of 30% Eu^{2+} and 70% Eu^{3+} ions. The Eu^{2+} fraction is significantly reduced for the other two samples, we find fractions of 20% Eu^{2+} for the 18 nm β-$NaEuF_4$ nanoparticles and 18% Eu^{2+} for the β-$NaEuF_4$/$NaGdF_4$ core–shell nanoparticles, respectively. We assume that this result can be likely due to the different surface to bulk ratios of the samples as the formation of divalent Eu should predominantly occur at the surface (interface) of the sample, since a similar effect has been reported by Burian *et al.* on different EuF_3 surfaces and interfaces.[52]

2.6 Electronic and magnetic properties

In order to elucidate further the magnetic properties all over the nanocrystals superconducting quantum interference device (SQUID) magnetometry measurements were performed.

Fig. 8(a) and (b) show thermomagnetic curves $M(T)$ of the precursor particles of pure β-$NaGdF_4$ and β-$NaEuF_4$ respectively. In the case of β-$NaGdF_4$ particles, the $M(T)$ dependences fulfill the Curie law but with small deviation that is clearly demonstrated in the $M \times T(T)$ curves. For pure Curie law (*i.e.* $M \sim 1/T$), the $M \times T(T)$ dependence should be a flat line, while the observed linear deviation indicates temperature independent component of magnetization which, in our case, can be attributed to some blocked magnetic moments of Gd. In the case of β-$NaEuF_4$ particles, the thermomagnetic curves are typical as for Eu^{3+} ions, showing the so-called van Vleck paramagnetism which is relatively weak and temperature independent. At low temperatures, below 20 K, traces of classical paramagnetic behavior are observed, *i.e.* sharp increase in magnetization with decreasing temperature. This effect is caused by an expected contribution of Eu^{2+} ions that pose magnetic moment and follow the Curie law. The possible origin of the Eu^{2+} presence is a surface valence transition, typical for nanoparticles containing Eu.

Fig. 8(c) shows hysteresis loops, determined at 2 K, for (i) pure β-$NaEuF_4$ and β-$NaGdF_4$ precursor particles, (ii) 22 nm β-$NaGdF_4$ nanocrystals doped with 1% of Eu and (iii) β-$NaEuF_4$/$NaGdF_4$ core–shell particles. Generally, the β-$NaEuF_4$ samples (3 nm and 18 nm) are paramagnetic. However, for the β-$NaEuF_4$ 3 nm nanocrystals some saturated component is detected which confirms the presence of magnetic Eu^{2+} ions. This answers the expectation of Eu^{2+} formation on the surface, consequently due to the large bulk to surface ratio in the 18 nm nanocrystals no signal is detectable. The pure β-$NaGdF_4$ precursor particles, β-$NaEuF_4$/$NaGdF_4$ core–shell particles with the 18 nm β-$NaEuF_4$ core and 22 nm β-$NaGdF_4$ nanocrystals doped with 1% Eu are paramagnetic with saturation magnetization as expected from the literature.[60] Surprisingly the β-$NaEuF_4$/$NaGdF_4$ core–shell nanocrystals with the 3 nm core show a butterfly shaped hysteresis loop. A similar behavior was recently found in rare earth based single molecular magnets.[61] The explanation of the hysteresis loop for the β-$NaEuF_4$/$NaGdF_4$ core–shell particles with the 3 nm β-$NaEuF_4$ core can be some magnetic anisotropy. Accounting the fact that for 22 nm β-$NaGdF_4$ and 3 nm β-$NaGdF_4$ samples the effect of hysteresis broadening was not observed one may propose a model in which the anisotropy exists at the interface between a magnetic shell and a non-magnetic core.

In order to confirm this hypothesis Monte Carlo simulations were performed. The simulations are based on the Heisenberg model and the so-called simulated annealing, as

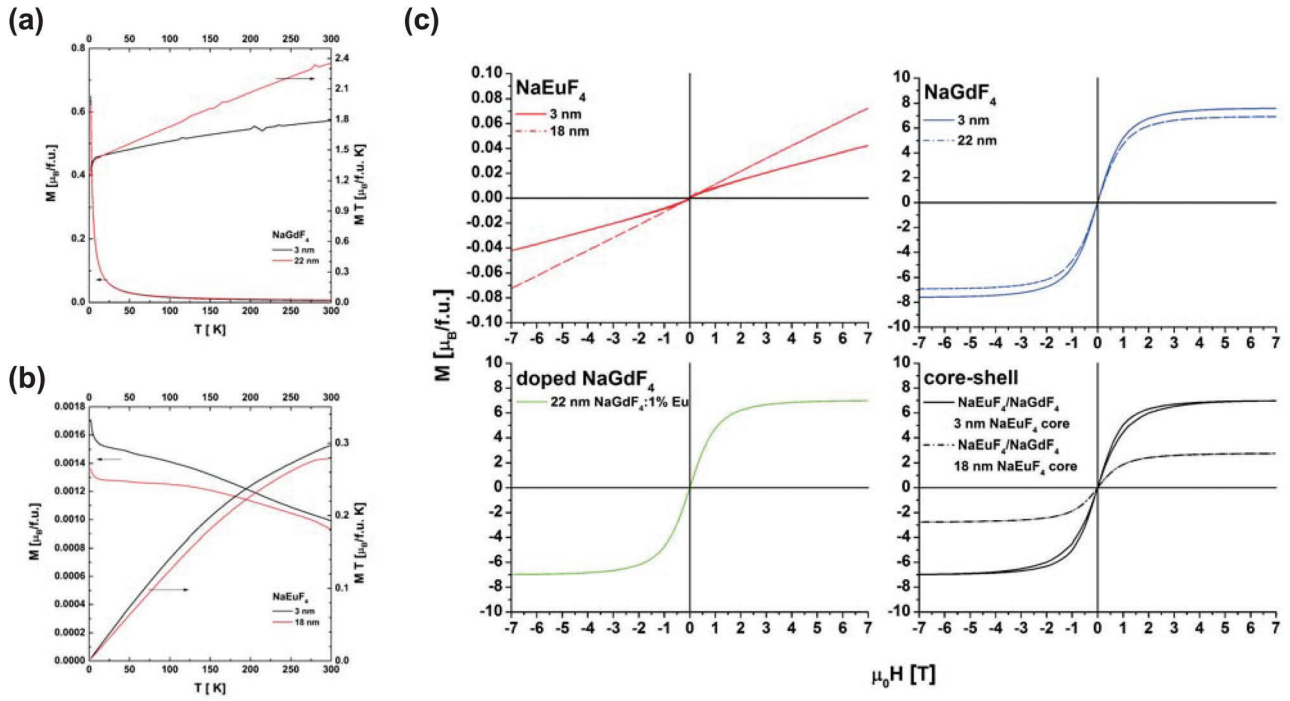

Fig. 8 Thermomagnetic $M(T)$ curves measured in $\mu_0 H$ = 0.1 T of (a) β-$NaGdF_4$ and (b) β-$NaEuF_4$ particles and (c) hysteresis loops of pure β-$NaEuF_4$ and β-$NaGdF_4$ precursor particles, 22 nm β-$NaGdF_4$ nanocrystals doped with 1% Eu and β-$NaEuF_4$/$NaGdF_4$ core–shell particles at 2 K.

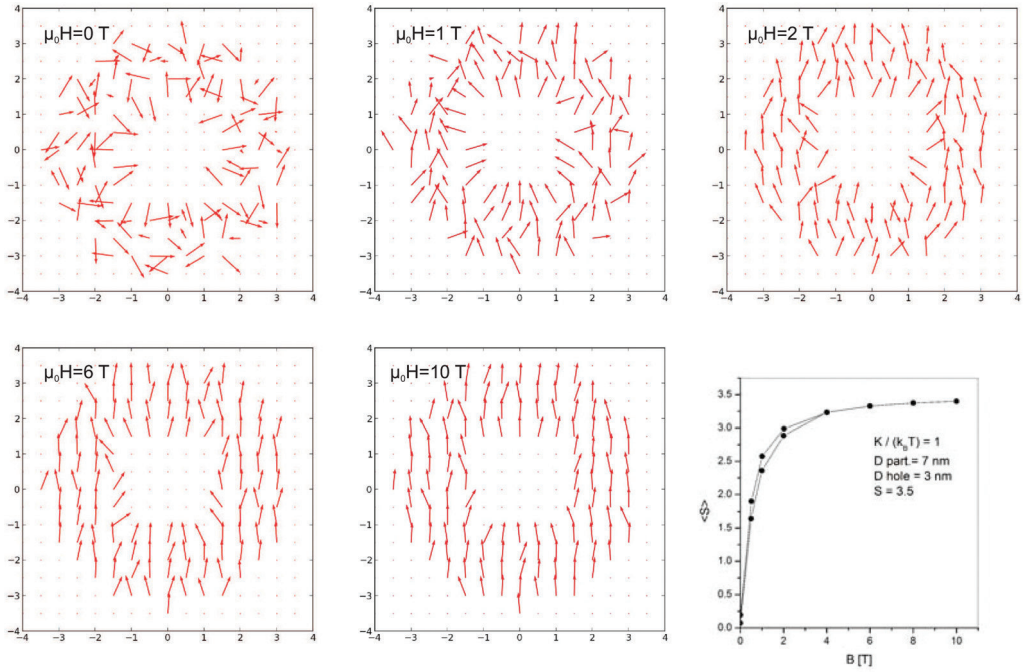

Fig. 9 Spin configurations (central section) for the simulated particles in the fields of 0 T, 1 T, 2 T, 6 T and 10 T (scales in nm) and the simulated hysteresis loops (the first quadrant) for the particle.

described by Ziółkowski and Chrobak.[62] The analyzed particle consists of a spherical magnetic shell (7 nm in diameter) and a nonmagnetic core (3 nm). In the magnetic net, spin S = 3.5, exchange integral parameter J = 0 and radial magnetic anisotropy coefficient $K = k_B T$. Fig. 9 depicts the spin configurations for different applied magnetic fields from 0 T to 10 T.

The resulting average spin in the direction of magnetic field (*i.e.* magnetization of the particle) as a function of increasing and decreasing field is presented in Fig. 9. As shown, this part of simulated hysteresis loop also reveals the butterfly shape. It should be underlined that good qualitative agreement with experimental data could be obtained only with the assumption of the surface anisotropy. The performed simulations including an influence of dipolar interactions, magnetic frustrations, weak ferro and antiferro couplings do not bring satisfactory results. Finally, one can conclude that the magnetization processes of β-$NaGdF_4$ nanoparticles can be affected by anisotropy that leads to the appearing of butterfly shaped hysteresis loops and deviation from the Curie law (see Fig. 8(a)).

In order to tackle the internal magnetic structure of selected β-$NaEuF_4$ and the β-$NaEuF_4$/$NaGdF_4$ core–shell nanocrystals with an 18 nm β-$NaEuF_4$ core in detail we performed X-ray magnetic circular dichroism (XMCD) at the Gd and Eu $M_{4,5}$-edges. XMCD is a very powerful tool to determine the magnetic properties of a compound in question valence and element specific.

Fig. 10 presents the Eu $M_{4,5}$-edge X-ray absorption spectroscopy (XAS) and XMCD spectra of the β-$NaEuF_4$/$NaGdF_4$ core–shell nanocrystals with an 18 nm β-$NaEuF_4$ core along with the Gd M_5-edge of the 2 nm β-$NaGdF_4$ shell. The Gd M_5-edge exhibits a large dichroic signal (~20%) of negative sign and a typical Gd^{3+} multiplet structure.[63]

In contrast the Eu $M_{4,5}$-edge XMCD shows a rather weak negative dichroism of ~2% at the M_5 edge. However, this measured dichroic signal is significantly stronger than expected according to the SQUID data of the pure β-$NaEuF_4$ and β-$NaGdF_4$ nanoparticles. Here the maximum recorded magnetization (see Fig. 8(c)) of the β-$NaEuF_4$ nanocrystals is less than 1% compared to the β-$NaGdF_4$ nanocrystals of same size. Since both, Eu and Gd M_5 exhibit negative signs the net moments are parallelly aligned to each other. Fig. 10(b) displays the Eu $M_{4,5}$-edge XA- and XMCD spectra of the core–shell nanoparticles with those of pure 3 nm β-$NaEuF_4$ nanoparticles. The XPS spectra (see section 2.5) reveal an increased amount of divalent Eu ions which is also reflected in the X-ray absorption- and XMCD spectra of this sample. The M_5 edge XMCD of the 3 nm β-$NaEuF_4$ nanoparticles is dominated by two distinct features located at 1128 eV and 1131 eV, which can be attributed to Eu^{2+} and Eu^{3+} contributions to the XMCD signal.[64] In the case of the core–shell nanocrystals the intensity of the XMCD at 1128 eV is much less pronounced, which is in accordance with the XPS results indicating a significantly lower Eu^{2+} fraction compared to the 3 nm β-$NaEuF_4$ nanoparticles. The XMCD peak at 1132 eV can be presumed as being due to Eu^{3+} ions with a total magnetic quantum number $J \neq 0$, since Eu^{3+} in its magnetic ground state with $J = 0$ would produce no dichroic signal at all. On the other hand, Eu^{2+} ions are in a $J = 7/2$ ground state, leading to a "spin only" moment of $7\mu_B$ per Eu ion. This means that already quite a small fraction of uncompensated moments originating from Eu^{2+} ions may lead to a significant contribution to the overall Eu $M_{4,5}$-edge XCMD signal. As we have already pointed out the

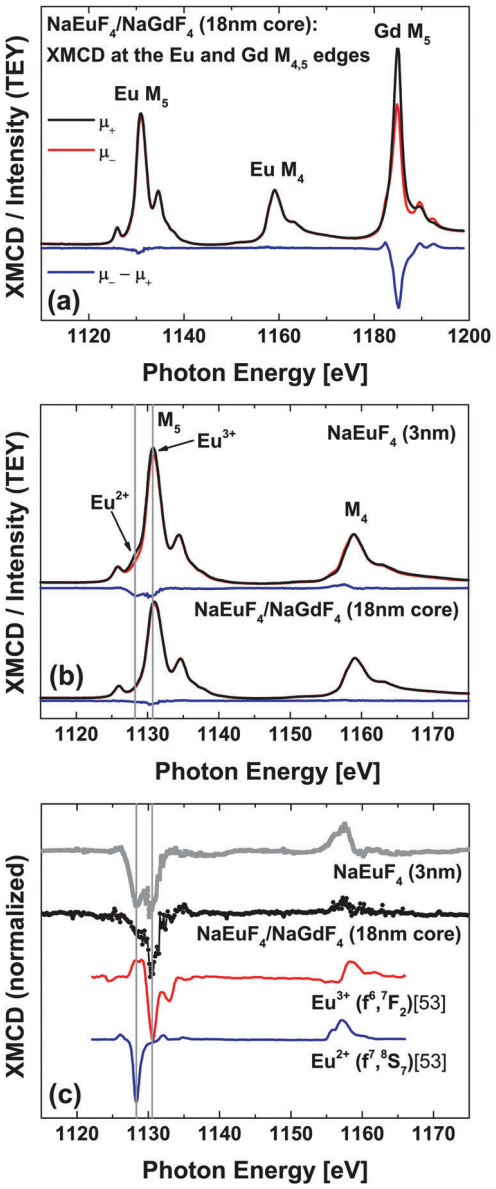

Fig. 10 (a) Gd M_5 and Eu $M_{4,5}$-edge XAS and XMCD of the β-$NaEuF_4$/$NaGdF_4$ core–shell nanocrystals with an 18 nm β-$NaEuF_4$ core. (b) Eu $M_{4,5}$-edge XAS and XMCD of the β-$NaEuF_4$/$NaGdF_4$ core–shell nanocrystals with an 18 nm β-$NaEuF_4$ core and the pure 3 nm β-$NaEuF_4$ nanoparticles. (c) Eu $M_{4,5}$-edge XMCD spectra in comparison with the corresponding atomic multiplet calculations of the $^7F_2$ Eu^{3+} and the $^8S_7$ Eu^{2+} final states. The simulated spectra have been extracted from Kachkanov *et al.*[53] The experiments have been performed under an external magnetic field of $B = 6$ T and with the samples at a temperature of 6 K. Spectra are offset vertically for clarity.

overall dichroic Eu signal is much higher than expected from the SQUID magnetometry data. One potential reason is that the Eu^{3+}-signal stems from ions in the $^7F_2$ ($J = 1$) state. This is likely populated *via* the excitation of the probing X-ray beam during the XMCD measurement. Note that 4f intrashell transitions into the $^7F_2$ also dominate the luminescence spectra presented in Fig. 5. A similar effect has been reported by Kachkanov *et al.*[53] for Eu^{3+} doped GaN layers. It seems that

β-$NaEuF_4$ based nanocrystals and core–shell systems could be another example of a material in which the magnetic state can be altered by light excitation. In order to investigate this highly interesting effect in more detail future experiments by means of magneto optical SQUID and/or XMCD measurements in luminescence yield would be desirable.

3 Conclusions

We synthesized β-$NaEuF_4$/$NaGdF_4$ core–shell nanoparticles with narrow size distribution and an overall size of around 22 nm diameter. The particles contained either a small β-$NaEuF_4$ core with a diameter of only ~3 nm or a large β-$NaEuF_4$ core with a diameter of ~18 nm. Structural PDF analysis of the XRD measurements shows differences in peak positions between the both core–shell samples, although the differences in bond distance between the different atoms of bulk β-$NaEuF_4$ and β-$NaGdF_4$ are small. Comparison with simulation based on pure crystalline, spherical β-$NaEuF_4$ and β-$NaGdF_4$ nanoparticles point out that the β-$NaEuF_4$/$NaGdF_4$ core–shell nanoparticle with a 3 nm β-$NaEuF_4$ core exhibits structural parameters of β-$NaGdF_4$ structure, whereas β-$NaEuF_4$/$NaGdF_4$ core–shell nanoparticles with an 18 nm β-$NaEuF_4$ core resemble the β-$NaEuF_4$ structure. HR-TEM images reveal core–shell formation for the β-$NaEuF_4$/$NaGdF_4$ core–shell nanoparticles with an 18 nm β-$NaEuF_4$ core. The Eu^{3+} photoluminescence and Gd^{3+} ESR spectra both indicate that rare earth ions of the small 3 nm particle cores were released during shell growth and incorporate into the shell material. In contrast the system with the large β-$NaEuF_4$ core does not exhibit additional peaks in the Eu^{3+} luminescence spectra indicating that only a small number of Eu^{3+} ions are present in the $NaGdF_4$ shell. As to the Eu and Gd valance states, X-ray photoelectron-core level spectroscopy reveals significant fractions of Eu^{2+} ions in the β-$NaEuF_4$ precursors as well as the β-$NaEuF_4$/$NaGdF_4$ core–shell nanoparticles with an 18 nm β-$NaEuF_4$ core. Larger β-$NaEuF_4$ nanoparticles and surrounded by the β-$NaGdF_4$ shell reduce the Eu^{2+} fraction in agreement with results reported for EuF_3 thin film surfaces and interfaces.[52] The presence of Eu^{2+} in the β-$NaEuF_4$ nanoparticles as well as in the core–shell systems is confirmed by SQUID magnetometry. $M(T)$ curves of the β-$NaEuF_4$ precursors exhibit a sharp increase in magnetization below 20 K stemming from Eu^{2+} ions since only the Eu^{3+} ions contribute a weak van Vleck paramagnetism. In the case of the core–shell system with 3 nm β-$NaEuF_4$ core we find a butterfly-shaped hysteresis loop which is known for single molecular magnets, for instance. This result could be reproduced by Heisenberg model simulations of a magnetic sphere comprising a non-magnetic core. XMCD at the Eu and $M_{4,5}$ edges demonstrates the parallel alignment of Gd and Eu moments in the core–shell nanoparticles with a large β-$NaEuF_4$ core. The magnetic properties are dictated by the paramagnetic Gd^{3+} ions in the surrounding β-$NaGdF_4$ shell. However, both the Eu^{2+} and Eu^{3+} ions contribute to the overall magnetic properties of the system. In particular the Eu^{3+} contribution is much higher than expected from the weak van Vleck paramagnetism. This might be due to the fact that the exciting X-rays populate the $J = 1$ state of Eu^{3+} *via* 4f transitions which can be also seen in the optical spectra. In future studies the core–shell formation with small β-$NaEuF_4$ cores will be further optimized, also to investigate the interesting butterfly shaped magnetic hysteresis in more detail. The fact that the magnetic state of Eu^{3+} might be altered by external light excitation is another interesting aspect which may be investigated by SQUID experiments under optical light excitation or XMCD using luminescence yield as the detection mode. Finally the multifunctionality of the β-$NaEuF_4$/$NaGdF_4$ core–shell nanoparticles could be further improved, *e.g.* by transition metal doping into the β-$NaEuF_4$ core and/or the β-$NaGdF_4$ shell. In summary we have successfully synthesized and carefully characterized multifunctional β-$NaEuF_4$/$NaGdF_4$ core–shell nanoparticles combining intense red optical emission from the Eu^{3+} ions with the paramagnetic properties stemming mainly from the Gd^{3+} ions.

4 Experimental

4.1 Materials

Sodium oleate (82%, Sigma-Aldrich), sodium fluoride (99%, Sigma-Aldrich), ammonium fluoride (98%, Sigma-Aldrich), oleic acid (90%, Alfa Aesar), 1-octadecene (90%, Alfa Aesar) and hydrated rare-earth chlorides of $EuCl_3$ and $GdCl_3$ (99.9%, Treibacher Industrie AG) were used as received.

Rare-earth oleates. The rare-earth oleates were prepared as given in the literature.[65] In a typical synthesis of europium oleate 60 mmol europium chloride and 180 mmol sodium oleate were dispersed in 120 ml ethanol, 80 ml water and 210 ml hexane. The resulting turbid solution was heated for 14 h under reflux (at about 60 °C). The resulting transparent organic phase containing the europium oleate was separated at room temperature and the hexane was removed with a rotary evaporator, yielding europium oleate. Gadolinium oleate was prepared analogously.

Synthesis of cubic phase precursor nanocrystals. The synthesis of the sub-10 nm particles of α-$NaREF_4$ (RE = Eu, Gd) is based on the reaction of rare-earth oleates and NaF in a mixture of oleic acid and 1-octadecene, similar to the procedure given by Liu *et al.*[66] In our case, rare-earth oleate and sodium fluoride were used in a molar ratio of 1 to 8. Oleic acid and 1-octadecene were added to the 1 to 8 mixture of rare-earth oleate and NaF (10 ml of each solvent per 1 mmol of rare-earth oleate) and the mixture was degassed in a vacuum Schlenk-line 100 Pa) for 1 h at 100 °C under stirring. The setup was three times subjected to vacuum and then refilled with nitrogen before the reaction mixture was heated at 200 °C. After 60 min at 200 °C and slow nitrogen flow the stirred solution was allowed to cool to room temperature. The excess of sodium fluoride was removed by centrifugation. The clear supernatant was mixed with an equal volume of ethanol leading to precipitation of the nanoparticles, which were

separated by centrifugation. The particles were purified by redispersing the precipitate in hexane (3 ml hexane per 1 mmol of rare-earth oleate), followed by precipitation with ethanol and separation of the particles by centrifugation.

Synthesis of hexagonal phase precursor nanocrystals. Hexagonal phase precursor particles of $NaREF_4$ were prepared by dispersing the corresponding rare-earth oleate and sodium oleate in a molar ratio of 1 : 2.5 in oleic acid and 1-octadecene (10 ml of each solvent per 1 mmol of rare-earth oleate) followed by degassing at 100 °C for 1 h under vacuum (100 Pa) in a Schlenk-line. Subsequently, 4 mmol ammonium fluoride per 1 mmol of rare-earth oleate was added at 100 °C to the clear yellowish solution under nitrogen flow. The vessel was three times subjected to vacuum and then refilled with nitrogen (vacuum applied for 5 seconds only) and the stirred solution was subsequently heated at 200 °C for 60 min under slow nitrogen flow. After cooling to room temperature an equal volume of ethanol was added to the solution, resulting in precipitation of the precursor particles. The particles were separated by centrifugation and purified as given above for the cubic phase precursor nanocrystals.

Growth of the final product particles. We used a method published earlier by the group of one of the present authors.[67] Product particles with different final sizes were obtained by varying the molar ratio of hexagonal and cubic phase precursor particles. In a typical synthesis, 3.76 mg β-$NaEuF_4$ and 1.28 g α-$NaGdF_4$ precursor particles were re-dispersed in a solvent mixture consisting of 10 ml of oleic acid and 10 ml of 1-octadecene. The mixture was then heated at 100 °C for 60 min under vacuum and stirring. After the vessel was three times subjected to vacuum and then refilled with nitrogen, the solution was heated to 320 °C under nitrogen flow. After the desired reaction time, in this case 40 min, the reaction was stopped and the solution was cooled down to room temperature. After adding 60 ml of a 1 : 2 mixture of hexane and ethanol, the precipitate was separated from the solution by centrifugation. The precipitate was purified two times as given above for the precursor particles. The synthesis procedure for all $NaREF_4$ product particles was the same.

4.2 Experimental methods

The total scattering X-ray measurements were performed on the high energy scattering beamline P02.1 at PETRA III (DESY, Hamburg, Germany). The data sets were collected using a high energy monochromatic beam (59.875 keV, λ = 0.20707 Å) and a Perkin Elmer flat panel detector placed at 303 mm from the samples. The wavelength and the sample to detector distance have been determined by using a LaB_6 NIST standard. The used experimental setup allows to collect total scattering data over a sufficiently high momentum transfer ($Q \sim 22.72$ Å^{-1}) corresponding to a d spacing of 0.138 Å. We note here that the total scattering measurements have been conducted under the same experimental conditions for all the studied samples. The collected data were then corrected for experimental effects (absorption, multiple scattering, polarization, Compton scattering and Laue diffuse scattering) and the scattering signals from the air and the experimental set up were measured independently under exactly the same conditions as the samples and subtracted as a background in the data reduction procedure. For obtaining the experimental atomic pair distribution function $G(r)$ by a direct sine Fourier transformation of the resulting total scattering structure function $S(Q)$, the data were truncated at a finite maximum value of Q_{max} = 18.13 Å^{-1} beyond which the signal-to-noise ratio became unfavourable. All data processing was done using Fit-2D[68] and PDFgetX3[69] software.

A double Cs corrected JEOL ARM 200F transmission electron microscope operated at 200 kV was used for the analysis in the study. High angle annular dark field (HAADF) scanning transmission electron microscopy (STEM) was used along with electron energy loss spectroscopy (EELS) Spectrum Imaging (SI) using the DualEELS™ mode on the Gatan GIF Quantum 965 ERS™ spectrometer fitted on the microscope as well as EDS using an Oxford XMax 80 SDD.

Fluorescence spectra of the nanocrystals were recorded with a Fluorolog 3-22 spectrometer (Jobin Yvon) equipped with double monochromators for both channels.

The EPR spectra of the sample were recorded with a home made X-band EPR spectrometer (9 GHz) equipped with a dielectric resonator (DM5) (Bruker Biospin, Rheinstetten, Germany). The microwave power was set to 1.0 mW, the B-field modulation amplitude was 0.3 mT.

The XPS measurements were performed using a PHI 5600CI multitechnique spectrometer with monochromatic Al Kα = 1486.6 eV radiation of 0.3 eV at full width at half-maximum. The overall resolution of the spectrometer is 1.5% of the pass energy of the analyzer, 0.88 eV in the present case. The XPS measurements were performed at room temperature.

The XAS and XMCD measurements were performed at the Beamline for Advanced Dichroism (BACH) at the Elettra Synchrotron Facility.[70] The samples were mounted into a cryostat equipped with a 6.5 T superconducting magnet, the sample stage was connected to a pumped helium cryostat, reaching a base temperature of around 6.0 K during the experiments presented here. The measurements at the Gd and Eu $M_{4,5}$ edges have been recorded under external magnetic fields of 6 T in the total electron yield mode.

The FC–ZFC and hysteresis loop measurements were performed at the A. Chełkowski Institute of Physics, University of Silesia, Katowice, Poland, with the use of SQUID magnetometer (MPMS XL7 Quantum Design). All measurements have been performed in the 2 K–300 K temperature range up to 7 T magnetic field.

Acknowledgements

Parts of this research were carried out at the light source PETRA III at DESY, a member of the Helmholtz Association (HGF). We would like to thank J. Gamcová for assistance in using beamline P02.1. We thank all Beamline scientists for their excellent and generous technical support.

References

1 S. Gai, C. Li, P. Yang and J. Lin, *Chem. Rev.*, 2014, **114**, 2343–2389.
2 C. Liu, Y. Hou and M. Gao, *Adv. Mater.*, 2014, **26**, 6922–6932.
3 D. K. Chatterjee, M. K. Gnanasammandhan and Y. Zhang, *Small*, 2010, **6**, 2781–2795.
4 F. Wang, D. Banerjee, Y. Liu, X. Chen and X. Liu, *Analyst*, 2010, **135**, 1839–1854.
5 D. Vennerberg and Z. Lin, *Sci. Adv. Mater.*, 2011, **3**, 26–40.
6 O. S. Wolfbeis, *Chem. Soc. Rev.*, 2015, **44**, 4743–4768.
7 Z. Li, Y. Zhang and S. Jiang, *Adv. Mater.*, 2008, **20**, 4765–4769.
8 G. Chen, T. Y. Ohulchanskyy, S. Liu, W.-C. Law, F. Wu, M. T. Swihart, H. Hans Ågren and P. N. Prasad, *ACS Nano*, 2012, **6**, 2969–2977.
9 Q. Liu, Y. Sun, T. Yang, W. Feng, C. Li and F. Li, *J. Am. Chem. Soc.*, 2011, **133**, 17122–17125.
10 J. Liu, Y. Liu, W. Bu, J. Bu, Y. Sun, J. Du and J. Shi, *J. Am. Chem. Soc.*, 2014, **136**, 9701–9709.
11 Y. Sun, X. Zhu, J. Peng and F. Li, *ACS Nano*, 2013, **7**, 11290–11300.
12 Y.-F. Wang, G.-Y. Liu, L.-D. Sun, J.-W. Xiao, J.-C. Zhou and C.-H. Yan, *ACS Nano*, 2013, **7**, 7200–7206.
13 R. Naccache, P. Chevallier, J. Lagueux, Y. Gossuin, S. Laurent, L. Vander Elst, C. Chilian, J. A. Capobianco and M.-A. Fortin, *Adv. Healthcare Mater.*, 2013, **2**, 1478–1488.
14 R. Qiao, C. Liu, M. Liu, H. Hu, C. Liu, Y. Hou, K. Wu, Y. Lin, J. Liang and M. Gao, *ACS Nano*, 2015, **9**, 2120–2129.
15 Y. Deng, H. Wang, W. Gu, S. Li, N. Xiao, C. Shao, Q. Xu and L. Ye, *J. Mater. Chem. B*, 2014, **2**, 1521–1529.
16 H. Groult, J. Ruiz-Cabello, J. Pellico, A. V. Lechuga-Vieco, R. Bhavesh, M. Zamai, E. Almarza, I. Martin-Padura, E. Cantelar, M. P. Martinez-Alcazar and F. Herranz, *Bioconjugate Chem.*, 2015, **26**, 153–160.
17 C. Liu, W. Ma, Z. Gao, J. Huang, Y. Hou, C. Xu, W. Yang and M. Gao, *J. Mater. Chem. C*, 2014, **2**, 9637–9642.
18 R. Wang, X. Li, L. Zhou and F. Zhang, *Angew. Chem., Int. Ed.*, 2014, **126**, 12282–12286.
19 H. Xing, S. Zhang, W. Bu, X. Zheng, L. Wang, Q. Xiao, D. Ni, J. Zhang, L. Zhou, W. Peng, K. Zhao, Y. Hua and J. Shi, *Adv. Mater.*, 2014, **26**, 3867–3872.
20 Q. Zhan, J. Qian, H. Liang, G. Somesfalean, D. Wang, S. He, Z. Zhang and S. Andersson-Engels, *ACS Nano*, 2011, **5**, 3744–3757.
21 D. Yang, P. Ma, Z. Hou, Z. Cheng, C. Li and J. Lin, *Chem. Soc. Rev.*, 2015, **44**, 1416–1448.
22 Y. Dai, H. Xiao, J. Liu, Q. Yuan, P. Ma, D. Yang, C. Li, Z. Cheng, Z. Hou, P. Yang and J. Lin, *J. Am. Chem. Soc.*, 2013, **135**, 18920–18929.
23 Y. I. Park, H. M. Kim, J. H. Kim, K. C. Moon, B. Yoo, K. T. Lee, N. Lee, Y. Choi, W. Park, D. Ling, K. Na, W. K. Moon, S. H. Choi, H. S. Park, S.-Y. Yoon, Y. D. Suh, S. H. Lee and T. Hyeon, *Adv. Mater.*, 2012, **24**, 5755–5761.
24 G. Tian, Z. Gu, L. Zhou, W. Yin, X. Liu, L. Yan, S. Jin, W. Ren, G. Xing, S. Li and Y. Zhao, *Adv. Mater.*, 2012, **24**, 1226–1231.
25 D. Yang, X. Kang, P. Ma, Y. Dai, Z. Hou, Z. Cheng, C. Li and J. Lin, *Biomaterials*, 2013, **34**, 1601–1612.
26 L. Wang, J. Liu, Y. Dai, Q. Yang, Y. Zhang, P. Yang, Z. Cheng, H. Lian, C. Li, Z. Hou, P. Ma and J. Lin, *Langmuir*, 2014, **30**, 13042–13051.
27 R. Naccache, F. Vetrone and J. A. Capobianco, *ChemSusChem*, 2013, **6**, 1308–1311.
28 H. Lian, Z. Hou, M. Shang, D. Geng, Y. Zhang and J. Lin, *Energy*, 2013, **57**, 270–283.
29 J. Shen, Z. Li, R. Cheng, Q. Luo, Y. Luo, Y. Chen, X. Chen, Z. Sun and S. Huang, *ACS Appl. Mater. Interfaces*, 2014, **6**, 17454–17462.
30 G.-B. Shan, H. Assaaoudi and G. P. Demopoulos, *ACS Appl. Mater. Interfaces*, 2011, **3**, 3239–3243.
31 H. Zhu, X. Chen, L. M. Jin, Q. J. Wang, F. Wang and S. F. Yu, *ACS Nano*, 2013, **7**, 11420–11426.
32 Y. Zhou, S.-T. Han, X. Chen, F. Wang, Y.-B. Tang and V. Roy, *Nat. Commun.*, 2014, **5**, 1–8.
33 D. Peng, Q. Ju, X. Chen, R. Ma, B. Chen, G. Bai, J. Hao, X. Qiao, X. Fan and F. Wang, *Chem. Mater.*, 2015, **27**, 3115–3120.
34 W. J. Kim, M. Nyk and P. N. Prasad, *Nanotechnology*, 2009, **20**, 185301.
35 Y. Lu, J. Zhao, R. Zhang, Y. Liu, D. Liu, E. M. Goldys, X. Yang, P. Xi, A. Sunna, J. Lu, Y. Shi, R. C. Leif, Y. Huo, J. Shen, J. A. Piper, J. P. Robinson and D. Jin, *Nat. Photonics*, 2014, **8**, 32–36.
36 J. M. Meruga, A. Baride, W. Cross, J. J. Kellar and P. S. May, *J. Mater. Chem. C*, 2014, **2**, 2221–2227.
37 G.-S. Yi and G.-M. Chow, *Chem. Mater.*, 2007, **19**, 341–343.
38 Y.-F. Wang, L.-D. Sun, J.-W. Xiao, W. Feng, J.-C. Zhou, J. Shen and C.-H. Yan, *Chemistry*, 2012, **18**, 5558–5564.
39 D. Chen and P. Huang, *Dalton Trans.*, 2014, **43**, 11299–11304.
40 G. Chen, H. Agren, T. Y. Ohulchanskyy and P. N. Prasad, *Chem. Soc. Rev.*, 2015, **44**, 1680–1713.
41 M.-K. Tsang, G. Bai and J. Hao, *Chem. Soc. Rev.*, 2015, **44**, 1585–1607.
42 F. Vetrone, R. Naccache, V. Mahalingam, C. G. Morgan and J. A. Capobianco, *Adv. Funct. Mater.*, 2009, **19**, 2924–2929.
43 Y. Liu, D. Tu, H. Zhu, R. Li, W. Luo and X. Chen, *Adv. Mater.*, 2010, **22**, 3266–3271.
44 F. Wang, R. Deng, J. Wang, Q. Wang, Y. Han, H. Zhu, X. Chen and X. Liu, *Nat. Mater.*, 2011, **10**, 968–973.
45 M. Quintanilla, F. Ren, D. Ma and F. Vetrone, *ACS Photonics*, 2014, **1**, 662–669.
46 C. Dong, A. Korinek, B. Blasiak, B. Tomanek and F. C. J. M. van Veggel, *Chem. Mater.*, 2012, **24**, 1297–1305.
47 Q. Su, S. Han, X. Xie, H. Zhu, H. Chen, C.-K. Chen, R.-S. Liu, X. Chen, F. Wang and X. Liu, *J. Am. Chem. Soc.*, 2012, **134**, 20849–20857.

48 H. Wen, H. Zhu, X. Chen, T. F. Hung, B. Wang, G. Zhu, S. F. Yu and F. Wang, *Angew. Chem., Int. Ed.*, 2013, **125**, 13661–13665.
49 X. Li, R. Wang, F. Zhang and D. Zhao, *Nano Lett.*, 2014, **14**, 3634–3639.
50 M. Bottrill, L. Kwok and N. J. Long, *Chem. Soc. Rev.*, 2006, **35**, 557–571.
51 E.-J. Cho and S.-J. Oh, *Phys. Rev. B: Condens. Matter*, 1999, **59**, R15613–R15616.
52 W. Burian, J. Szade, T. O'Keevan and Z. Celinski, *Phys. Status Solidi B*, 2004, **241**, R15–R18.
53 V. Kachkanov, M. J. Wallace, G. van der Laan, S. S. Dhesi, S. A. Cavill, Y. Fujiwara and K. P. O'Donnell, *Sci. Rep.*, 2012, **2**, 1–5.
54 G. H. Dieke, *Spectra and energy levels of rare-earth ions in crystals*, Interscience Publishers, New York, 1968.
55 P. Ptacek, H. Schaefer, K. Koempe and M. Haase, *Adv. Funct. Mater.*, 2007, **17**, 3843–3848.
56 C. Li, Z. Quan, J. Yang, P. Yang and J. Lin, *Inorg. Chem.*, 2007, **46**, 6329–6337.
57 C. M. Brodbeck and L. E. Iton, *J. Chem. Phys.*, 1985, **83**, 4285–4299.
58 R. Komban, J. P. Klare, B. Voss, J. Nordmann, H.-J. Steinhoff and M. Haase, *Angew. Chem., Int. Ed.*, 2012, **51**, 6506–6510.
59 J. Szade and M. Neumann, *J. Phys.: Condens. Matter*, 2001, **13**, 2717.
60 F. Li, C. Li, X. Liu, Y. Chen, T. Bai, L. Wang, Z. Shi and S. Feng, *Chem. – Eur. J.*, 2012, **18**, 11641–11646.
61 L. Margheriti, D. Chiappe, M. Mannini, P.-E. Car, P. Sainctavit, M.-A. Arrio, F. B. de Mongeot, J. C. Cezar, F. M. Piras, A. Magnani, E. Otero, A. Caneschi and R. Sessoli, *Adv. Mater.*, 2010, **22**, 5488–5493.
62 G. Ziółkowski and A. Chrobak, *Acta Phys. Pol., A*, 2015, **127**, 597–598.
63 G. Champion, N. Lalioti, V. Tangoulis, M.-A. Arrio, P. Sainctavit, F. Villain, A. Caneschi, D. Gatteschi, C. Giorgetti, F. Baudelet, M. Verdaguer and C. Cartier dit Moulin, *J. Am. Chem. Soc.*, 2003, **125**, 8371–8376.
64 B. J. Ruck, H. J. Trodahl, J. H. Richter, J. C. Cezar, F. Wilhelm, A. Rogalev, V. N. Antonov, B. D. Le and C. Meyer, *Phys. Rev. B: Condens. Matter*, 2011, **83**, 174404.
65 J. Park, K. An, Y. Hwang, J.-G. Park, H.-J. Noh, J.-Y. Kim, J.-H. Park, N.-M. Hwang and T. Hyeon, *Nat. Mater.*, 2004, **3**, 891–895.
66 C. Liu, H. Wang, X. Zhang and D. Chen, *J. Mater. Chem.*, 2009, **19**, 489–496.
67 B. Voss and M. Haase, *ACS Nano*, 2013, **7**, 11242–11254.
68 A. P. Hammersley, S. O. Svensson, M. Hanfland, A. N. Fitch and D. Hausermann, *High Pressure Res.*, 1996, **14**, 235–248.
69 P. Juhas, T. Davis, C. Farrow and S. Billinge, *J. Appl. Crystallogr.*, 2013, **46**, 560–566.
70 M. Zangrando, M. Finazzi, G. Paolucci, G. Comelli, B. Diviacco, R. P. Walker, D. Cocco and F. Parmigiani, *Rev. Sci. Instrum.*, 2001, **72**, 1313–1319.

Publication H8

[**H8**] K. Kuepper, C. Derks, C. Taubitz, M. Prinz, L. Joly and J. P. Kappler, A. Postnikov, W. L. Yang, T. V. Kuznetsova, and P. Ziemann. *Electronic structure nd soft-X-ray-induced photoreduction studies of iron-based magnetic polyoxometalates of type*$\{(M)M_5\}_{12}Fe_{30}^{III}$ *(M=*Mo^{VI}*,* W^{VI}*)*, Dalton Transactions **42**, 7924 (2013), doi: 10.1039/c3dt32759k.

Dalton Transactions

RSC Publishing

PAPER

Electronic structure and soft-X-ray-induced photoreduction studies of iron-based magnetic polyoxometalates of type $\{(M)M_5\}_{12}Fe^{III}_{30}$ ($M = Mo^{VI}$, W^{VI})

Cite this: *Dalton Trans.*, 2013, **42**, 7924

Karsten Kuepper,*[a,b] Christine Derks,[b] Christian Taubitz,[b] Manuel Prinz,[b] Loïc Joly,[c] Jean-Paul Kappler,[c] Andrei Postnikov,[d,e] Wanli Yang,[f] Tatyana V. Kuznetsova,[g] Ulf Wiedwald,[a] Paul Ziemann[a] and Manfred Neumann[b]

Giant Keplerate-type molecules with a $\{Mo_{72}Fe_{30}\}$ core show a number of very interesting properties, making them particularly promising for various applications. So far, only limited data on the electronic structure of these molecules from X-ray spectra and electronic structure calculations have been available. Here we present a combined electronic and magnetic structure study of three Keplerate-type nanospheres—two with a $\{Mo_{72}Fe_{30}\}$ core and one with a $\{W_{72}Fe_{30}\}$ core by means of X-ray absorption spectroscopy, X-ray magnetic circular dichroism (XMCD), SQUID magnetometry, and complementary theoretical approaches. Furthermore, we present detailed studies of the Fe^{3+}-to-Fe^{2+} photoreduction process, which is induced under soft X-ray radiation in these molecules. We observe that the photoreduction rate greatly depends on the ligand structure surrounding the Fe ions, with negatively charged ligands leading to a dramatically reduced photoreduction rate. This opens the possibility of tailoring such polyoxometalates by X-ray spectroscopic studies and also for potential applications in the field of X-ray induced photochemistry.

Received 19th November 2012,
Accepted 22nd January 2013

DOI: 10.1039/c3dt32759k

www.rsc.org/dalton

1. Introduction

Polyoxometalates (POM) make a fascinating class of inorganic compounds which, in a sense, closes a gap between "conventional" transition-metal (TM) oxides and molecular magnets. They link, by mediation of oxygen, the TM atoms together into structures in which quite strict rules govern the emerging short-range order. Other than imposing a crystal-type periodicity, these rules of chemical bonding may give rise to huge molecules of fancy shapes and beautiful sophistication.[1] Such entities may further be connected into a molecular crystal, allowing variations depending on the particularly used "glue" of solvent molecules. The measurable electronic, magnetic or vibrational properties of polyoxometalates are, however, primarily shaped by the physics within individual molecular units, weakly coupled between themselves.

Possible "use" of POMs, beyond the chemist's professional satisfaction and the general aesthetical reward, leaves space to fantasy, *e.g.* in the sense of confinement/transport of smaller molecules or in staging/tuning magnetic interactions. The latter aspect underlines the closeness of POMs to metallo-organic molecules, or molecular magnets, in view of similar mechanisms (and strength) of interatomic magnetic coupling, and, generally, of the chemical bonding involved. Even if the bare POM carcase is typically free of "conventionally organic" carbon or nitrogen, they are frequent members of auxiliary details keeping the POM molecule together.

Although POMs have been a subject of study for some time by a number of groups worldwide, *e.g.*, [2–7] we emphasize the long-term efforts by the group of Achim Müller in Bielefeld, to which we owe the introduction into the subject and the synthesis of systems used in our present study.

In particular, the giant neutral Keplerate-type molecules, $\{Mo_{72}M_{30}\}$ (M = Fe^{III}, Cr^{III}, V^{IV}, and Ln^{III}), show a number of intriguing properties making them extremely promising,

[a]*Institute of Solid State Physics, Ulm University, Albert-Einstein-Allee 11, 89069 Ulm, Germany. E-mail: kkuepper@uos.de*
[b]*Department of Physics, University of Osnabrück, Barbarastr. 7, 49069 Osnabrück, Germany*
[c]*IPCMS UCMS 7504 CNRS—Université de Strasbourg, 23 rue du Loess, BP 43, 67034 Strasbourg Cedex 2, France*
[d]*University of Lorraine, LCP-A2MC 1 Bd Arago, F-57078 Metz, France*
[e]*Faculty of Physics, University of Bielefeld, P.O. Box 100131, D-33501 Bielefeld, Germany*
[f]*Advanced Light Source, Lawrence Berkeley National Laboratory, Berkeley, CA 94720, USA*
[g]*Institute of Metal Physics, Russian Academy of Sciences, Ural Div., S. Kovalevskaya str. 18, 620990 Ekaterinburg, Russia*

potential candidates for various applications and models, *i.e.* quasicrystals[8] and water exchange in minerals.[9] Recently, a remarkable self-recognition phenomenon, leading to separate blackberry-type structures of the $\{Mo_{72}Fe_{30}\}$ and $\{Mo_{72}Cr_{30}\}$ molecules in dilute solutions, has been reported.[10] Moreover, such types of Keplerates with 30 transition-metal ions (*e.g.*, Fe^{III} or Cr^{III}), symmetrically placed on an icosidodecahedral surface, are model compounds for a mesoscopic magnetic kagomé lattice at low temperatures.[11–13] In particular, the magnetic properties of the neutral $\{Mo_{72}Fe_{30}\}$ molecule (formula of the compound: $[Mo_{72}Fe_{30}O_{252}(CH_3COO)_{10}\{Mo_2O_7(H_2O)\}\{H_2Mo_2O_8(H_2O)\}_3(H_2O)_{91}]\cdot ca.\ 150H_2O \equiv$ **1** $\equiv$ **1a**$\cdot ca.\ 150H_2O$) have been investigated in a number of experimental and theoretical studies, including notably magnetic ones.[12–17] Also, recently, a $\{W_{72}Fe_{30}\}$-type cluster (formula of the compound $Na_6(NH_4)_{20}[Fe^{III}(H_2O)_6]_2[\{(W^{VI})W^{VI}_5O_{21}(SO_4)\}_{12}\{(Fe(H_2O))_{30}\}(SO_4)_{13}(H_2O)_{34}]$ *ca.* $200H_2O \equiv$ **2** $\equiv Na_6(NH_4)_{20}[Fe^{III}(H_2O)_6]_2\cdot$**2a**$\cdot ca.\ 200H_2O$), where molybdenum atoms of the pentagonal units are replaced by tungsten ones, has been reported.[18] While the 30 Fe^{III} ions in this anion form a spherical network based on corner-shared triangles as in the $\{Mo_{72}Fe_{30}\}$ molecule, there are differences in detail. First, the electron delocalization of the 3d electrons of the Fe^{III} ions is somewhat weaker than those in **1**, resulting in a weakened antiferromagnetic Fe–Fe interaction in **2** in comparison with that in **1**. Second, there are significant differences in the chemistry of the ligands. The $\{W_{72}Fe_{30}\}$ cluster **2** contains 25 SO_4^{2-} instead of the 10 acetate ligands in **1**, with the consequence that **2** is negatively charged (**1** is neutral). A $\{Mo_{72}Fe_{30}\}$ cluster with SO_4^{2-} ligands has also been synthesized (formula of the compound $Na_9K_3[K_{20}\subset Mo^{VI}_{70}Fe^{III}_{30}O_{252}(SO_4)_{24}(H_2O)_{75}]\cdot ca.\ 140H_2O \equiv$ **3** $\equiv Na_9K_3$**3a**$\cdot ca.\ 140H_2O$).[19]

The magnetic properties of metallo-organic complexes are of common interest due to the ongoing miniaturization of future memory devices. So-called single molecular magnets and related metallo-organic compounds are one potential vision for active functionals in future devices.

In the present study, we probe two of POM systems by different tools of X-ray spectroscopy. Such tools, especially when applied in combination and supported by first-principle calculations, are powerful in revealing information about distribution of electronic states and chemical bonding. Regarding the Fe_{30}-based Keplerate-type compounds described above, no X-ray spectroscopic study of the electronic and chemical structures is available to date. Furthermore, X-ray magnetic circular dichroism (XMCD) at transition metal L edges is an advanced technique since it enables one to determine spin and orbital magnetic moments separately.[20]

One important issue which arises in this relation is potential "radiation damage". X-ray-induced photochemistry, investigated by means of soft XAS, has been reported for two Fe-based metallo-organic complexes.[21–24] These studies addressed potential mechanisms for the photo-oxidation/photoreduction/ligand-photolysis effects, which could also have been induced by the cleavage of chemical bonds between the transition metal and ligands for different reasons.

Soft XAS in the total electron yield (TEY) mode has a probing depth of a few nanometers only, suggesting that many secondary electrons are generated, which may play an important role in explaining the radiation-damage effects. Furthermore, it has been demonstrated that the damage effects can be retarded by the presence of "electron reservoirs" *via* molecule–substrate interactions.[23] George *et al.*[22] have reported that the observed X-ray induced photochemistry depends not only on the Fe valence but also on the ligand structure. This leads to the question of whether, and how, the X-ray induced "damage" effects in metallo-organic complexes can be "tailored" by means of their coordination chemistry. This offers an interesting alternative view onto X-ray-induced photochemistry as an opportunity to learn more about hitherto uncharacterized metal sites, rather than a cause of undesirable potential damage. However, a detailed spectroscopic study of chemical and electronic structures of metallo-organic compounds requires care, and one always has to consider potential soft-X-ray-induced modifications at both the transition metal and the ligand sites.

This paper aims to address two gaps in knowledge. First, because we wanted to investigate the topic of soft-X-ray-induced photoreduction in Fe-based metallo-organic complexes, we performed a detailed XAS study (in dependence of the overall photon flux) at the Fe $L_{2,3}$ edges and the OK edge of **1**, **2**, and **3**. We report a tendency toward Fe^{3+} to Fe^{2+} photoreduction in all three molecules, although this process was significantly slower for molecules **2** and **3**. This observation might be related to the presence of negatively charged SO_4^{2-} ligands. These results also demonstrate the possibility that (soft) X-rays can be used as an active, rather than passive, probe of metallo-organic complexes.

Second, we performed a detailed study of the electronic and magnetic properties by means of soft XAS and XMCD in combination with first-principles electronic-structure calculations and charge-transfer multiple simulations.

2. Experimental and theoretical procedures

We probed the Fe^{3+}-to-Fe^{2+}photoreduction of the two $Mo_{72}Fe_{30}$ molecules (**1** and **3**) by means of Fe $L_{2,3}$ edge XAS, using the total electron yield (TEY), at the Russian–German Beamline (RGBL) at BESSY II. We used the full flux of the dipole beamline and recorded a series of Fe $L_{2,3}$ edge XAS on different spots on both molecules, with the samples being at room temperature. Each scan was completed in approximately 14 min.

A comparable XAS study (also using TEY as detection mode) of the $W_{72}Fe_{30}(SO^{4-})$ (**2**) and $Mo_{72}Fe_{30}(Ac)$ (**1**) was carried out at room temperature at the Advanced Light Source, beamline 8.0.1, using the X-ray fluorescence end station of the University of Tennessee at Knoxville.[25] Photons with energies of 500–750 eV were provided to the end station *via* a spherical 925-lines per mm-grating monochromator. The undulator-based beamline delivers a flux on the order of 10^{12} photons s^{-1}

at Fe L edge photon energies around 700 eV. In order to minimize radiation damage effects, we used the high energy flank of the undulator gap to reduce the incoming photon flux to around 5–10% of the maximum photon flux for the first scan on each fresh sample spot. Each scan was completed in approximately 8 min.

The XMCD experiments were performed at the surface and interface microscopy (SIM) beamline of the Swiss Light Source (SLS). We used the 7 T cryomagnetic TBT-XMCD end station, working with a ^{3}He–^{4}He dilution setup in order to reach base temperatures of around 0.7 K.[26] The sample with $W_{72}Fe_{30}$ core (**2**) was pasted on carbon tape before connecting the sample holder to the cryostat coldfinger. The spectra were recorded using the total electron yield (TEY). The undulator-based beamline delivers a flux on the order of 10^{12} photons s^{-1} at Fe L edge photon energies of around 700 eV. In order to minimize radiation damage effects, we tuned the beamline optics in order to reduce the incoming photon flux to around 1–2% of the maximum photon flux.

Magnetization measurements were performed with a Quantum Design MPMS SQUID magnetometer.

First-principles density-functional calculations were performed by the SIESTA method,[27,28] which uses norm-conserving pseudopotentials in combination with numerical atom-centered strictly confined basis functions. Exchange-correlation potential was taken after the generalized gradient approximation (GGA) in the formulation of Perdew–Burke–Ernzerhof.[29]

The molecule (neutral $Fe_{30}Mo_{72}$-acetate, or (6-)-charged $Fe_{30}W_{72}$-sulfate) was placed in a cubic simulation cell having a 36 Å edge, preventing an overlap of basis functions across the cell boundary with the molecule's spurious replicas. Basis functions were generated by the split-norm technique, the standard one in SIESTA. Typically, the quality of the basis set was "double-zeta with polarization orbitals",[30] except for the Fe 3d status, which was of triple-zeta quality. An earlier calculation by the same method on another (Ni-based) oxovanadate system is described by Postnikov *et al.*[31]

Fe $L_{2,3}$ edge XAS spectra were simulated within the charge-transfer multiplet model using the TT-multiplet program.[32–34] After the atomic energy levels of the initial ($2p^n3d^m$) and final ($2p^{n-1}3d^{m+1}$) states were calculated and reduced to 80% of their Hartree–Fock values (see Table 1), an octahedral crystal field was considered. Finally, we accounted for charge transfer by introducing $3d^{m+1}\underline{L}$ states and broadened the simulated spectra, considering lifetime broadening and spectrometer resolution.

3. Results and discussion

3.1 Soft-X-ray-radiation-induced Fe photoreduction

To gain more knowledge of the exact nature of the underlying mechanism of the soft-X-ray-induced photoreduction process for Fe ions in **1**, **2**, and **3**, we measured a series of Fe $L_{2,3}$ edge XAS for both **1** and **2** systems (Fig. 1). These measurements were performed at an undulator-based beamline (see Experimental and theoretical procedures section), whereby we first reduced the photon flux to approximately 10% of its maximal intensity for the first Fe $L_{2,3}$ edge scans of molecules **1** and **2**. Next, we doubled the flux with each completed set of XAS performed at the Fe $L_{2,3}$ edges untill maximum photon flux was reached. We observed a significant Fe^{3+} to Fe^{2+} reduction in both molecules. It is noteworthy that the Fe^{3+} ions in the (charge neutral) acetate-containing molecule **1** were significantly faster at reducing to Fe^{2+} than those in the sulfate-containing molecule **2** (see also Fig. 1). After a total of four XAS scans at the Fe $L_{2,3}$ edges from fitting the measured spectra to charge-transfer multiplet calculations (more details can be found in the Experimental and theoretical procedures section), it can be estimated that only 12.5% of Fe^{3+} ions were left in molecule **1**, but 37.5% remained in **2**. The observed difference in the Fe photoreduction rates may be due to the fact that for molecule **1** the coordination is acetate and for **2** it is SO_4^{2-}.

In Fig. 2, we present Fe $L_{2,3}$ edge XAS series for molecules **1** and **3**, taken at the Russian–German Beamline at BESSY II. All scans were acquired with the full intensity of the dipole beamline. The charge-neutral molecule **1** undergoes a relatively rapid Fe^{3+} to Fe^{2+} photoreduction (Fig. 2c). After only three scans across the Fe $L_{2,3}$ edges, we found a 75% fraction of Fe^{2+} ions, as concluded from a comparison with the corresponding superimposed multiplet simulations. It is notable that much faster Fe^{3+} to Fe^{2+} photoreduction processes (within one single Fe $L_{2,3}$ edge XAS scan) have been observed for a star-shaped

Table 1 Slater integrals (in eV) used for the Fe^{2+} and Fe^{3+} charge-transfer multiplet simulations of the Fe $L_{2,3}$ edge XAS. The spin–orbit parameters were not reduced, whereas the d–d and p–d integrals were reduced to 80% of the Hartree–Fock values for the subsequent simulation of the spectra

	Fe^{2+} $2p^63d^6$ initial	Fe^{2+} $2p^53d^7$ final	Fe^{2+} $2p^63d^7\underline{L}$ initial	Fe^{2+} $2p^53d^8\underline{L}$ final	Fe^{3+} $2p^63d^5$ initial	Fe^{3+} $2p^53d^6$ final	Fe^{3+} $2p^63d^6\underline{L}$ initial	Fe^{3+} $2p^53d^7\underline{L}$ final
Slater integrals								
F^2_{3d3d}	10.966	11.779	9.762	10.623	12.043	12.818	10.966	11.779
F^4_{3d3d}	6.815	7.327	6.018	6.560	7.535	8.023	6.815	7.327
F^2_{2p3d}		6.793		6.143		7.446		6.793
G^1_{2p3d}		5.004		4.467		5.566		5.004
G^3_{2p3d}		2.844		2.538		3.166		2.844
Spin–orbit coupling								
LS_{2p}		8.200		8.202		8.199		8.200
LS_{3d}	0.000	0.000	0.000	0.000	0.059	0.074	0.052	0.067

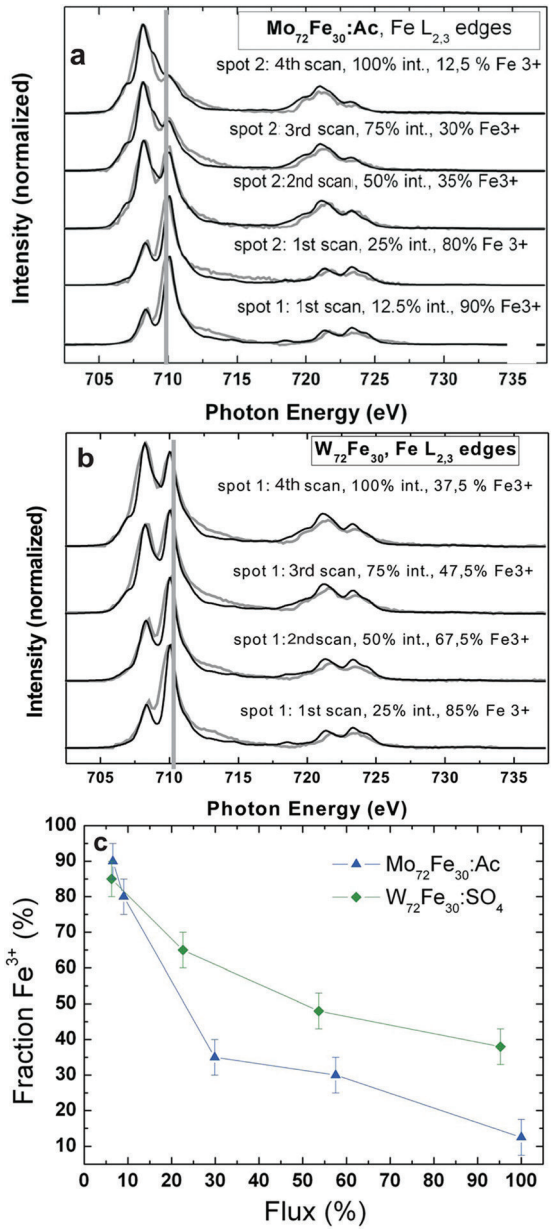

Fig. 1 (a) Fe $L_{2,3}$ edge XAS series of **1**, and (b) **2**; grey lines represent the experimental data; black lines represent the corresponding simulated spectra, which were obtained by superimposing corresponding fractions of the simulated Fe^{3+} and Fe^{2+} spectra. (c) Fraction of Fe^{3+} (derived from the corresponding multiplet simulations) *versus* the percentage X-ray photon flux time for the XAS series shown in the top panel.

Fe_4 single magnetic molecule,[24] where the Fe^{3+} ions are coordinated within an octahedral environment comprising four oxygen atoms and two nitrogen ligands. Also, for molecule **3** (Fig. 2a and 2b), a Fe^{3+} to Fe^{2+} photoreduction can be observed. The difference is that in **3** with its SO_4^{2-} ligands, the soft X-ray induced photoreduction rate at the Fe site is noticeably lower than that in **1**. Two different spots of **3** have been probed with different storage-ring currents (spot 1: 294–260 mA, spot 2: 188–173 mA). After approximately seven scans on spot 1 (scans 6 and 7 were taken only across the Fe L_3

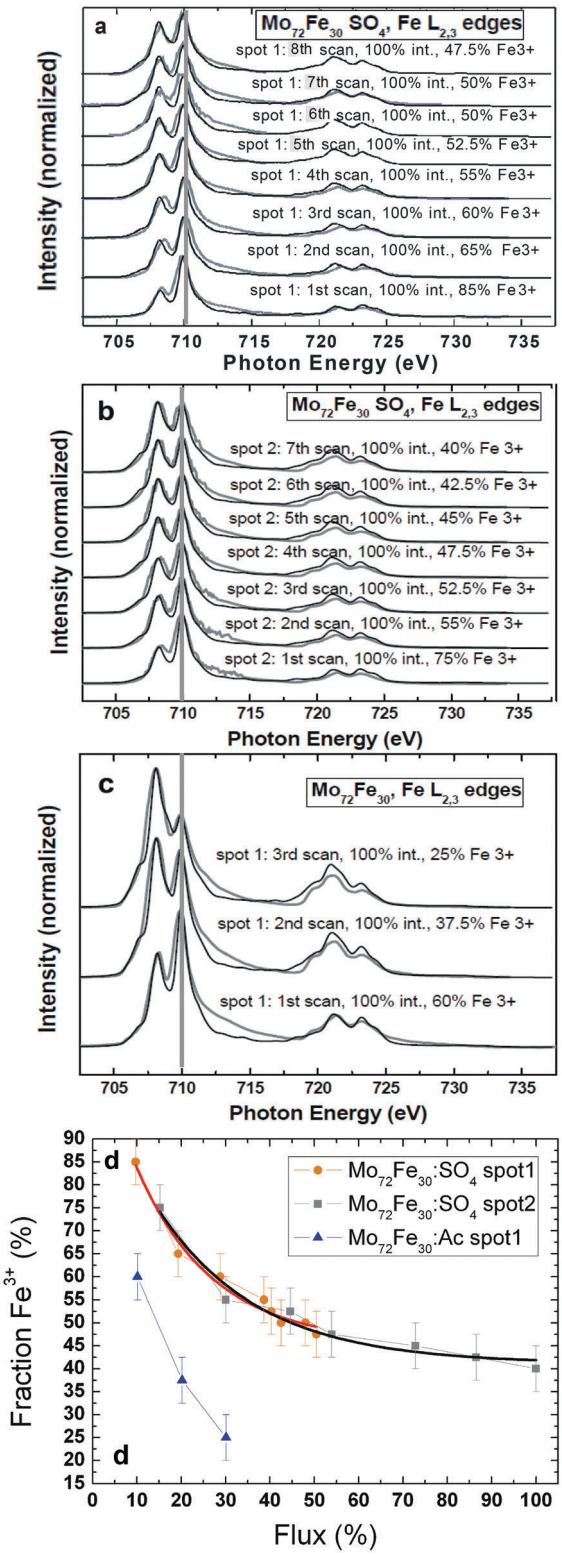

Fig. 2 (a) First series of Fe $L_{2,3}$ edge XAS of molecule **3** (spot 1); grey lines represent the experimental data; black lines represent the corresponding simulated spectra that were obtained by superimposing corresponding fractions of the simulated Fe^{3+} and Fe^{2+} spectra. (b) Second series of Fe $L_{2,3}$ edge XAS of molecule **3** (spot 2). (c) Series of Fe $L_{2,3}$ edge XAS of molecule **1**. (d) Fraction of Fe^{3+} (derived from the corresponding multiplet simulations) *versus* the percentage of overall X-ray-photon flux for the three XAS series, including exponential fits (solid lines) for the two series taken on **3**.

edge), there was still a 47.5% fraction of Fe^{3+} ions, and on spot 2, we observed a 40% Fe^{3+} fraction. We present a more quantitative analysis in Fig. 2d. The two series taken on **3** almost perfectly match when calibrated to the overall percentage photon flux, whereas a much more rapid photoreduction of **1** leads to a much steeper curve in this plot. Moreover, it is possible to fit the observed Fe^{3+} to Fe^{2+} photoreduction process observed for **3** by considering a simple exponential decay (solid black and orange fits in Fig. 2d). This may be an indication that the soft X-ray induced Fe photoreduction process, at least in these molecules, likely occurs within a single step, ruling out the possibility that two or more parallel processes occur on different slopes and timescales. We conclude that the different coordination chemistry seems to have a significant influence on the timescale of the soft X-ray induced Fe^{3+} to Fe^{2+} photoreduction process. The observed soft X-ray induced photoreduction may have several potential reasons.[22,23,35,36] Whereas photo-oxidation under soft X-ray exposure dominates in Fe(0) and Fe(I) coordination complexes, photoreduction is found for Fe(III) and Fe(IV) based metallo-organic complexes.[22] Also potential related phenomena such as ligand photolysis and/or ligand to metal charge transfer might be of importance.[35] Very recently a counterion dependence of an observed Mn^{3+} to Mn^{2+} photoreduction reduction rate in $(Mn_6^{III}Cr^{III})^{3+}$ complexes has been reported.[36] In these complexes the soft X-ray induced photoreduction rate was supposed to be lower in the presence of oxidizing counterions since these might release fewer electrons under soft X-ray exposure which may mediate the photoreduction process. Whereas we cannot exclude any of the above mentioned potential reasons for the photoreduction studies in this work, a plausible qualitative interpretation of this is that the observed photoreduction likely occurs because of the electrons liberated by the soft-X-ray excitation from the (ligand) atoms surrounding the transition-metal center.[22] As these are then transferred from the ligand to the metal centers, one can quantitatively understand why molecules with the negatively charged SO_4^{2-} ligands exhibit a lower photoreduction rate independent of the overall X-ray flux. The negative ligands "screen" the electrons of the surrounding matrix, leading to a repulsive potential. As previously described, the presence of "electron reservoirs" *via* metallic substrates can also lead to weaker radiation-damage effects.[23] We also want to mention that, as to the charge transfer multiplet simulations, the crystal-field strength of the Fe^{2+} ions is noticeably lower (0.2 eV) than that of the original Fe^{3+} ions (0.8 eV), indicating major changes in the local crystal-field environment (and subsequently the Fe–O bonding length) around the Fe ions during the photoreduction process.

3.2 Electronic and magnetic structure

3.2.1 Density-functional theory calculations. As demonstrated earlier on a number of occasions,[37] first-principles calculations performed at the accuracy level of the density-functional theory (DFT) provide a realistic description of ground-state charge density and magnetic configurations, even if it is not as accurate as quantum chemistry schemes in the treatment of electron-correlation effects. This technique even provides some insight into spectral characteristics, regarding

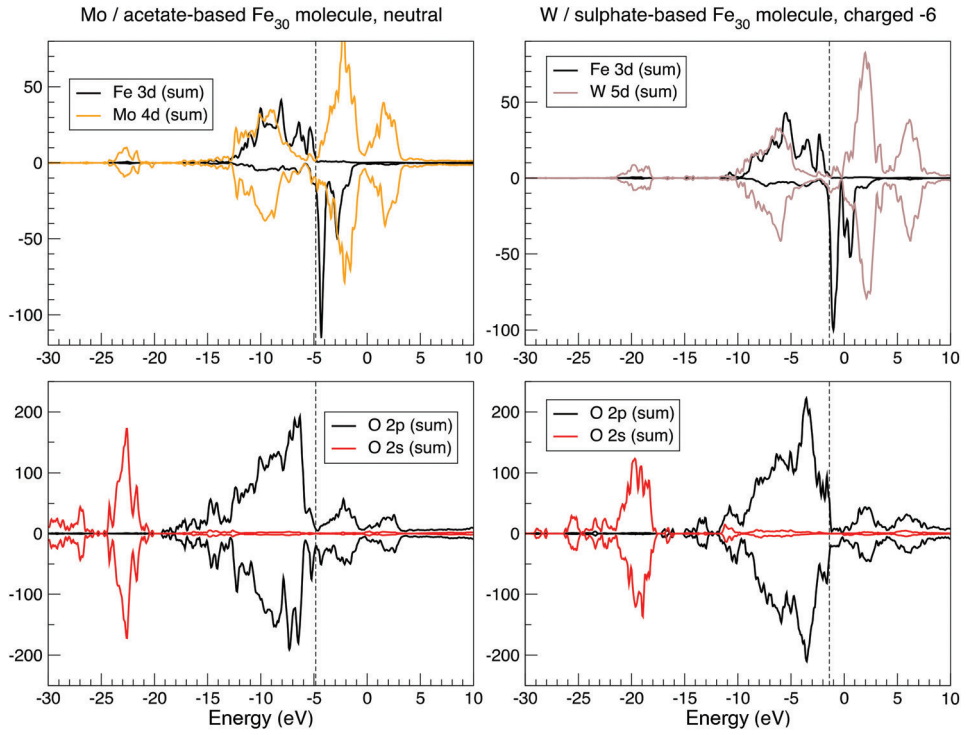

Fig. 3 Selected local densities of states in $Fe_{30}Mo_{72}$-acetate (left panel) and $Fe_{30}W_{72}$-sulfate (right panel), summed up over all atoms of a given type, as calculated by the SIESTA method. See text for details.

the interpretation of valence-band XPS, ligand XAS, or X-ray emission. DFT is advantageous because it considers the actual crystal or molecular structure, without the need to adopt simplifying structural suggestions. For the system under study, this becomes particularly important because the structural "soccer ball" pattern of Fe_{30} systems surpasses the "typical" size of molecular magnets, while remaining short of developing periodicity-related (solid-like) features.

To start a DFT calculation, one needs to specify a realistic structural model. Although the crystal structure, including solvent molecules, is known, we preferred to organize calculations for isolated molecular units, stripping them of solvent and defining, if needed, their net charge. Specifically, two systems have been selected for the present calculation:

1. $Mo_{72}Fe_{30}O_{252}(CH_3COO)_{10}\{Mo_2O_7(H_2O)\}\{H_2Mo_2O_8(H_2O)\}_3(H_2O)_{91}$ (**1a**) or $Fe_{30}Mo_{80}O_{398}C_{20}H_{226}$ (754 atoms), denoted henceforth as $Fe_{30}Mo_{72}$-acetate, whose structure is described in the literature.[38] The $Fe_{30}(Mo_6O_{15})_{12}$ ball, supplemented inwards and outwards with oxygen atoms and water molecules, is interwoven internally by 10 CH_3COO^- ions, one $Mo_2O_7(H_2O)^{2-}$, and three $H_2Mo_2O_8(H_2O)^{2-}$ groups, as described in the literature,[38] and has a zero nominal charge.

2. $[Na_6(NH_4)_{20}\{(W^{VI})W^{VI}_5O_{21}(SO_4)\}_{12}\{Fe(H_2O)\}_{30}(SO_4)_{13}(H_2O)_{34}]^{6-}$ ($Na_6(NH_4)_{20}$·**2a**) or $Fe_{30}W_{72}O_{416}N_{20}H_{208}S_{25}Na_6$ (777 atoms), denoted henceforth as $Fe_{30}W_{72}$-sulfate, is structurally characterized in the literature.[18] This structure is identical to the previous one with regard to the "soccer ball" composition (the Mo atoms now being replaced by W); however, the inner interweaving is executed by SO_4^{2-} ions, which can dock in three different positions, as previously published.[18] Furthermore, 20 ammonium cations are placed in the middle of, and slightly above, the hexagon faces of the "soccer ball," and six sodium ions form an octahedral cage around the molecule, helping to further compensate for the excess negative charge. Two $Fe^{III}(H_2O)_6$ units, which according to Todea *et al.*[18] co-crystallize with the molecular ball, were not included in the calculation. Consequently, the nominal charge assigned to the remaining molecular unit was 6−.

A practical detail in setting up the calculation was the selection of a valid docking formation of the inner groups (acetate, Mo–O, or sulfate) inside the ball, from the many equivalent possibilities that were averaged in the crystallographic analysis. Although we assumed that the exact choice would not have a noticeable effect on the electronic structure, such a decision still had to be made. Obviously, the two systems, while being structurally similar, are quite different from the chemistry viewpoint and with respect to the technical details of calculation. Therefore, it could be instructive to compare the two systems, with the expected primary effect being due to the difference between Mo and W, and the secondary effect being due to different linkers inside the ball.

The question of the magnetic structure of Fe_{30} systems is not simple and deserves, in principle, a detailed discussion. Namely, in view of the system being apparently magnetically frustrated, an option of the non-collinear setting of local magnetic moments has been addressed.[12] In the present study, we are predominantly interested in chemical bonding and spectral features, for which accessing a particular magnetic order is expected to have a less significant effect. Therefore, the results presented below correspond to the ferromagnetic setting of Fe magnetic moments. The calculation readily converges to a high-spin magnetic solution of 150 μ_B per molecule. This corresponds to the formal Fe^{III} valence, consistent with chemical intuition. The spatial distribution of spin density can be characterized in two ways—by local partial (basis-function-projected) densities of states (DOS) and by spatially resolved charge/spin density. Local charge and magnetic states of different atoms can be further characterized by the respective (basis-dependent, and hence ambiguous) Mulliken populations. The valence-states Mulliken charge at the Fe sites corresponds to approximately 7.5, with a slight variation over different centers, instead of 8 for a free atom. This value is less than that observed for the nominally expected Fe^{3+} situation, in which local magnetic moments correspond to approximately 4 μ_B. However, this value is close to that obtained by the DFT characterization of other similar (octahedrally O-coordinated) Fe-based molecular magnets.[39,40] As in the latter case, the local DOS at the Fe sites, shown in Fig. 3,

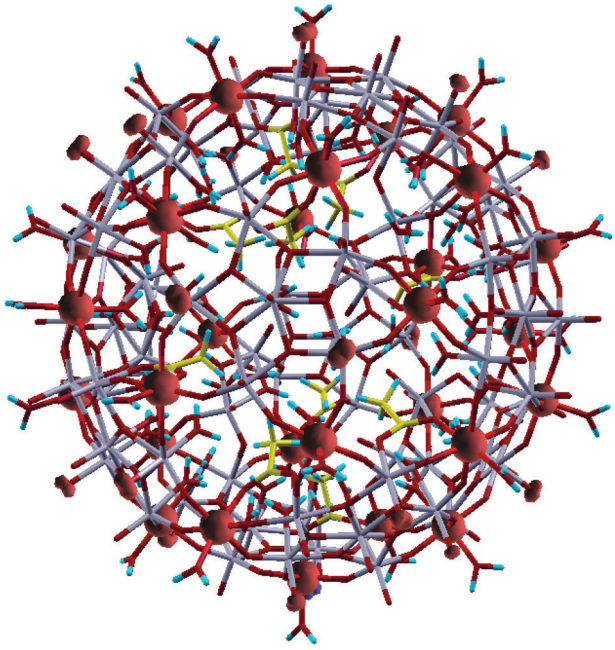

Fig. 4 Spin-density isosurfaces of a conveniently chosen value in $Fe_{30}Mo_{72}$-acetate. The molecule is shown in wireframe representation. Fe atoms (on the ball surface) carry spin moments and are hidden within the (nearly spherical) spin-density isosurface bulbs. Mo atoms (grey-colored bunches) are also situated on the ball surface, interconnected by oxygen (red/dark) atoms. Further oxygen atoms are flanking Fe and Mo roughly along the ball radius, outwards and inwards. Most of these oxygen atoms, notably all outward ones from Fe and many inward ones from Fe and Mo, are parts of water molecules (where protons are shown as blue dashes); other inward oxygen atoms from Fe and Mo are connected *via* acetate or Mo–O linkers inside the ball. (The C atoms of acetate groups are shown in yellow). Outward O atoms from Mo atoms are standalone; some of them carry substantial spin moment (witnessed by "clouds" of spin-density isosurfaces).

reveal fully occupied majority-spin bands and empty minority-spin bands. Therefore, the local moment associated with a Fe atom must be approximately 5 μ_B, of which 1 μ_B is obviously delocalized over the neighboring oxygen centers. The $Fe3d^5\uparrow 3d^0\downarrow$ configuration, when stripped of all 4s electrons, corresponds to the formal Fe^{III} valence, thus resolving an apparent controversy. In terms of spatial spin-density distribution, this situation corresponds to the spherical shape of the half-filled 3d shell of Fe atoms, as seen in Fig. 4.

By comparing the DOS for both systems in Fig. 3, their hybridization structure seems to be quite similar, as revealed by the similarity of the Mo 4d and W 5d contributions, along with those of Fe and O between the two systems. Minor differences are only in part related to different chemistry, and otherwise reveal a slightly different structure (a more perfect ball, with less disturbing internal linkers, in the $Fe_{30}W_{72}$-sulfate system). The large size of the system marks a difference from "conventional" molecular magnets such as "ferric wheels",[39] for example, while the high density of the energy levels and the near disappearance of the band gap make the system behave like a semi-metal. Additional charging (as different values of nominal charge of the molecule from those stated above were also tested) does not lead to a dramatically different magnetic state.

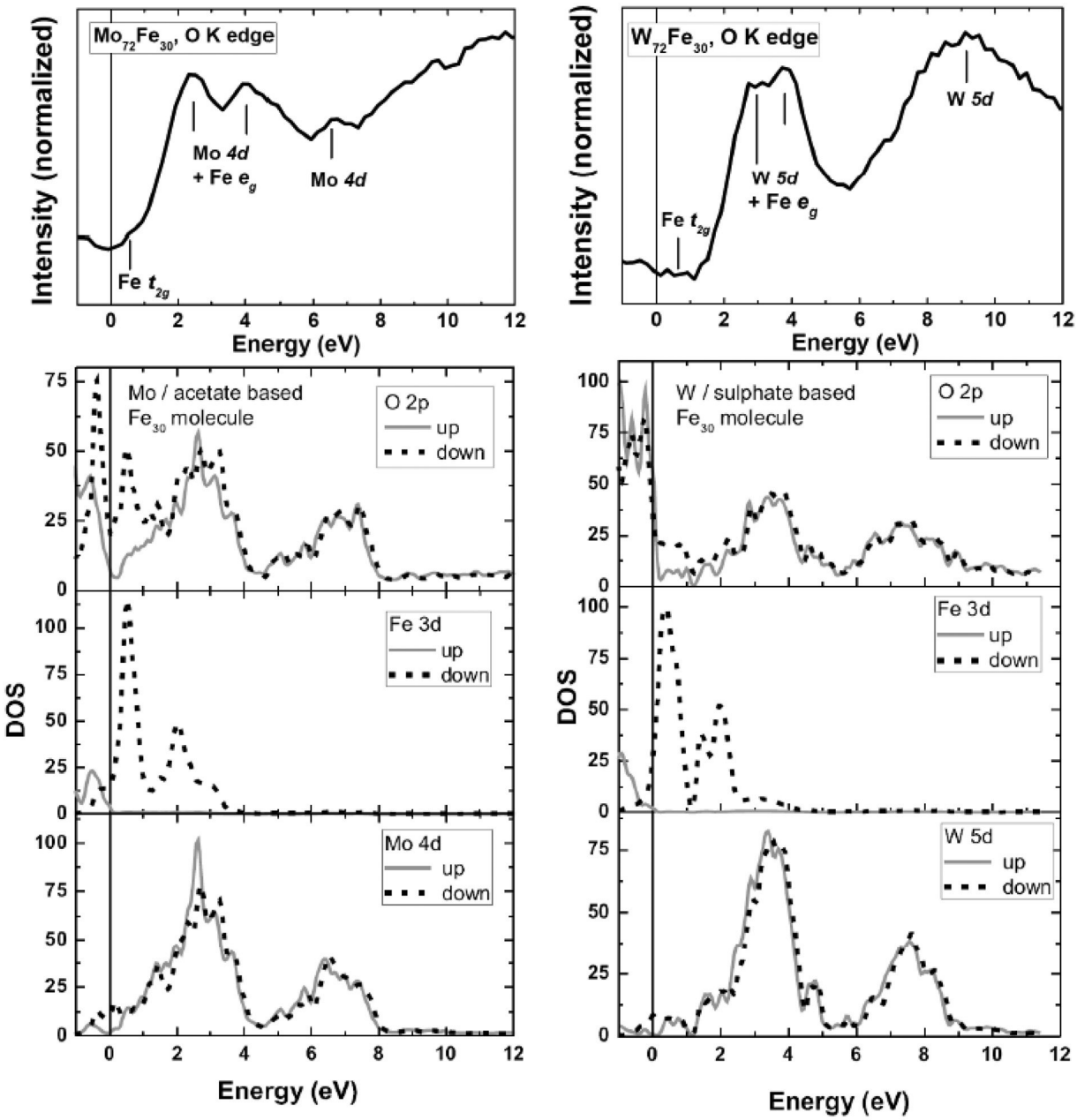

Fig. 5 Top: O K edge XAS series of **1** (left) and **2** (right). The thick lines represent spectra taken at a low photon flux and a fresh spot of the corresponding sample. Bottom: Calculated unoccupied densities of states for **1** (left) and **2** (right).

3.2.2 XAS at the O K edges. Fig. 5 presents the oxygen XAS of molecules **1** and **2** along with the projected calculated DOS. We discuss the spectra taken at a low photon flux on a fresh spot to obtain as much information as possible from the "original" electronic ground state (upper panel of Fig. 5). Hence, these spectra are not, or only minimally, influenced by potential changes induced by soft X-ray radiation. These O K edge XAS spectra considerably represent the hybridization between the Fe 3d, Mo 4d (W 5d) states and the unoccupied O 2p states, and thus the conduction band of molecules **1** and **2**. The spectra have been brought to a common energy scale with the Fermi energy set to zero. Both O K edge XAS spectra comprise three distinct main features. The O K edge XAS of **1** consist of two maxima located around 2 and 4.5 eV, respectively, and a somewhat less intense peak at approximately 7 eV. These regions can be attributed to hybridized O 2p/Mo 4d bands with the help of electronic structure calculations. However, some detailed differences are observed. The theoretical results suggest a minimum intensity at 4.5 eV (Fig. 5, bottom-left panel), whereas we observe an intense absorption peak at approximately 4 eV.

For molecule **2**, we find an overall similar situation. Here the two main peaks representing hybridized O 2p/W 5d bands are located at 2 and 3 eV, respectively, followed by a rather broad feature spanning the range from ~7 to 11 eV. Similar to the theoretical results of **1**, the calculated unoccupied DOS of **2** is again somewhat shifted toward the Fermi level in comparison with that observed in the experimental O K XAS features. It is noteworthy that the theoretical results reproduce the overall features and shape of the experimental O K XAS, since there is no significant interaction of the oxygen core hole with the oxygen or metal valence electrons. Therefore the O K edge spectra can be described to large extent within a single-particle scheme. However, the observed differences might be related to the fact that the DFT calculations do not include core hole potentials.

Since the strength of hybridization between Mo 4d (W 5d) and the unoccupied O 2p states is significantly stronger than that of the Fe 3d states, the O K edge XAS spectra are dominated mostly by the hybridized Mo 4d (W 5d)/O 2p states, as discussed above. Apart from this, small features are located at 0.75 eV (**1**) and 0.5 eV (**2**), which can be associated with hybridized Fe 3d t_{2g} states, based on comparison with the theoretical results (see Fig. 5). On the other side, the Fe 3d e_g states are overlapped by the contributions from Mo 4d and W 5d, respectively.

Next, to discuss the Fe 3d states, we plotted the local density of the 3d states, summed up over all Fe sites of molecule **1** in the ferromagnetic configuration (Fig. 6). According to DFT calculations, the Fe-3d-related states responsible for magnetism are not strongly localized and flow onto neighboring atoms. At the same time, their "on-site" (Fe-centered) part clearly reveals the spatial organization of these states as either e_g-like or t_{2g}-like type (in corresponding energy intervals) in both occupied and unoccupied parts of the spectrum. We present a corresponding illustration of the Mo 4d states in Fig. 7.

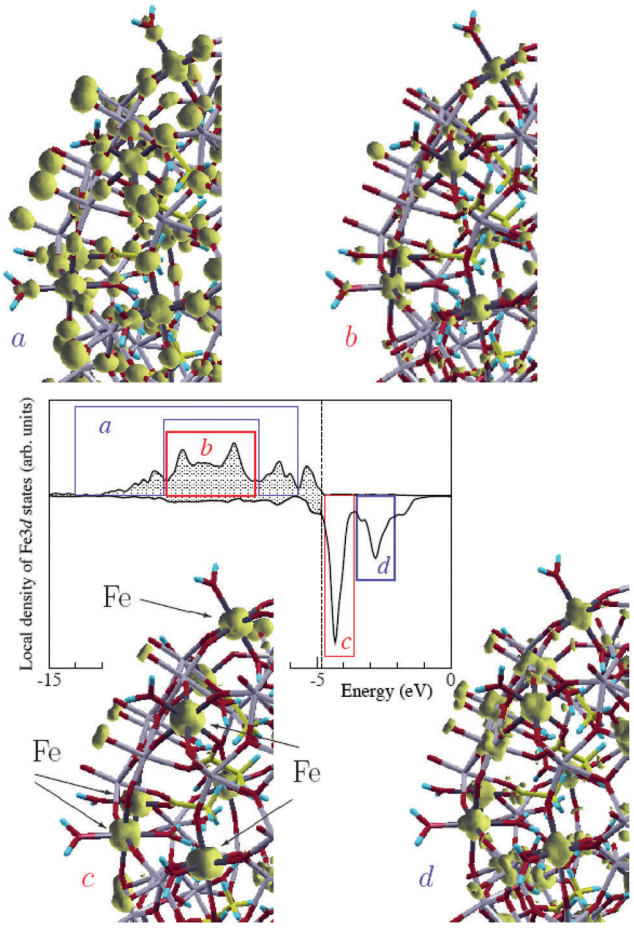

Fig. 6 Central panel: local density of 3d states, summed up over all Fe sites of molecule **1** in the ferromagnetic configuration. The vertical dashed line separates occupied (shaded) and vacant states. The energy windows over which the Fe 3d states noticeably have an e_g or t_{2g} character are indicated by blue and red blocks, respectively. Four peripheral figures: charge densities integrated over energies within each of the indicated energy windows, namely in occupied majority-spin states (a, b) and unoccupied minority-spin states (c, d), shown by an isosurface for a conveniently chosen value in each case, to underline the symmetry of the charge density in the vicinity of the Fe centers. Only a fragment of the full Fe_{30} ball is shown in each case. Positions of the Fe atoms are indicated by arrows in the "c" panel. Note that the "a" panel comprises the result of integration over two intervals, separated by the "b" region.

The Fe $L_{2,3}$ edges XAS of all three molecules (**1**, **2**, and **3**) are quite similar (Fig. 1 and 2). Like the O K edge XAS discussed above, these spectra were also recorded with a noticeable reduced photon flux (see Experimental and theoretical procedures section) and at a new position for each scan. The shape of the spectrum clearly reflects a predominant Fe^{3+} character in an octahedral coordination. We obtained the best-fit solution from charge-transfer multiplet simulations by considering an octahedral crystal field of 0.2 eV for the Fe^{2+} simulation (10% spectral weight in Fig. 6) and 10 Dq = 0.8 eV for the Fe^{3+} simulation (90% spectral weight in Fig. 6). The Slater spin–orbit integrals are summarized in Table 1. The energy difference between configurations $E(2p^63d^m)$ and $E(2p^53d^{m+1}L)$ was set to 4.5 eV for Fe^{2+} and Fe^{3+}. This resulted in a simulated 77.5% $3d^6$ and 22.5% $3d^7L$ ground-state charge-transfer

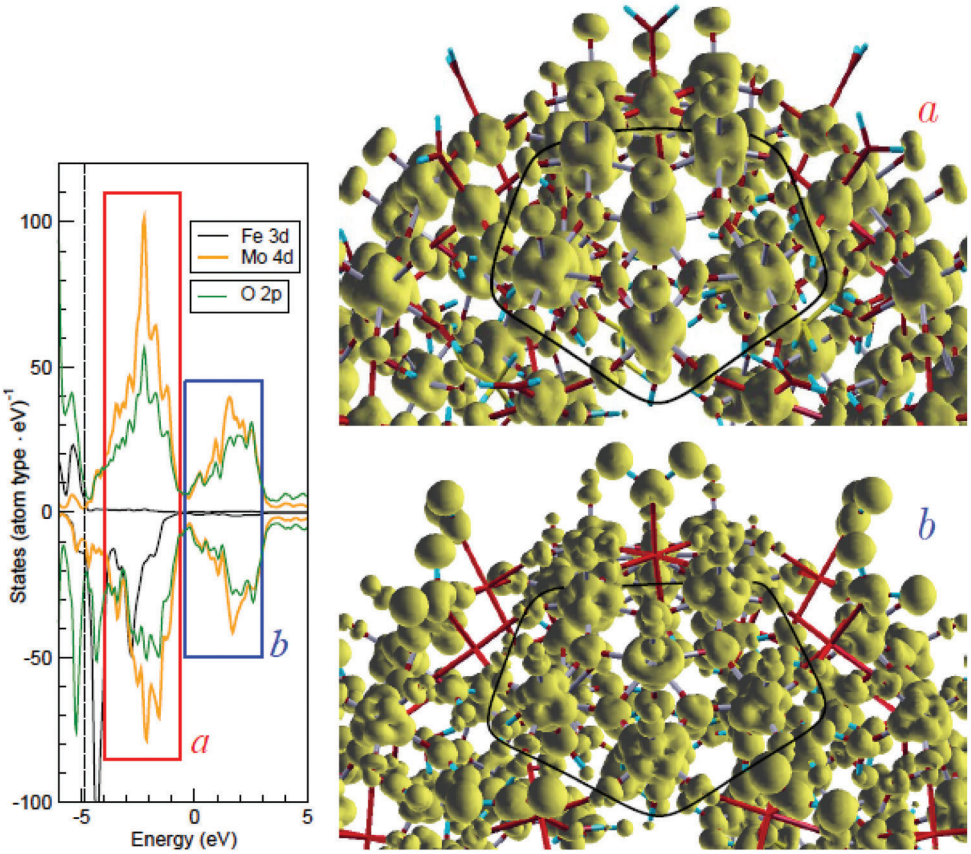

Fig. 7 Isosurfaces of the (unoccupied) charge density summed up over two energy windows, indicated as "a" and "b" in the density of state shown on the left, where the dashed line at ~−4 eV separates the occupied and vacant states. Only a part of molecule **1** is shown; $MoMo_5O_5$ pentagons are marked in both figures by a thick black line, which passes through oxygen atoms connecting the $MoMo_5O_5$ blocks with their neighboring Fe atoms (immediately outwards from each pentagon side). In the radial sense, every Mo atom is connected to an oxygen atom outwards and to a water molecule inwards; Fe atoms are connected to water molecules both outwards and inwards. Note a quasi-t_{2g} character of the Mo 4d states in the "a" window (where the Fe 3d states are e_g-like) and the quasi-e_g character in the "b" window (where the states are missing).

configuration for the Fe^{2+} ions, and an 80.8% $3d^5$ and 19.2% $3d^6L$ configuration for Fe^{3+}.

3.2.3 Magnetic properties of 2 ({$W_{72}Fe_{30}$} core). Powder of **2** was examined by means of SQUID magnetometry to tackle the integral magnetization as a function of external field and temperature (Fig. 8a). The largest magnetic moment per molecule μ_M = 58 μ_B is observed in an external field of 5.5 T at 2 K. There is almost no temperature dependence between 2 K and 5 K, whereas at 15 K (still at 5.5 T), a significantly lower magnetization of approx. 43 μ_B is found. The overall shape of the magnetization curve is qualitatively similar to that of the $Mo_{72}Fe_{30}$ molecule **1** (at an effective temperature of the spins of 4 K).[12,14] Also, as for **1**, a nearest-neighbor antiferromagnetic Fe–Fe interaction has been reported for **2** very recently.[18] Fig. 8b displays the Fe $L_{2,3}$ edge spectra recorded with left and right circularly polarized light, at a sample temperature of 0.7 K and an external field of 6.5 T. The corresponding XMCD signal (blue) and its integral (orange) are also shown. Both the (isotropic) XAS and the XMCD can be reproduced with charge-transfer multiplet simulations comprising 85% Fe^{3+} and 15% Fe^{2+}, respectively. This corresponds to the initial Fe L edge XAS taken on a fresh spot of **2** in Fig. 1. Therefore, a potential radiation damage or soft X-ray induced photoreduction can be considered as minimal. Sum rule analysis[20] yields a magnetic spin moment of μ_s = 51.8 μ_B per molecule and an almost quenched orbital contribution to the magnetic moment. Since the "conventional" spin sum rule leads to underestimated moments for ionic systems due to core–hole Coulomb interactions,[41,42] the spin sum rule correction factors after Teramura *et al.*,[41] *i.e.* 1/0.685 for Fe^{2+} and 1/0.875 for Fe^{3+} ions have been used. The derived moment of approximately 52 μ_B per molecule is somewhat lower than that obtained by SQUID magnetometry. This deviation may be due to the following possible reasons:

(i) Weak initial Fe^{3+} to Fe^{2+} photoreduction processes cannot be entirely excluded.

(ii) The spin sum rule correction factor used has been derived for a perfectly octahedral and homogenous crystal field, whereas already small deviations formed, as in case of our systems, may lead to a somewhat different correction factor.[42]

(iii) Weak antiferromagnetic intermolecular interactions might be present in particular at low temperatures (T = 0.7 K).

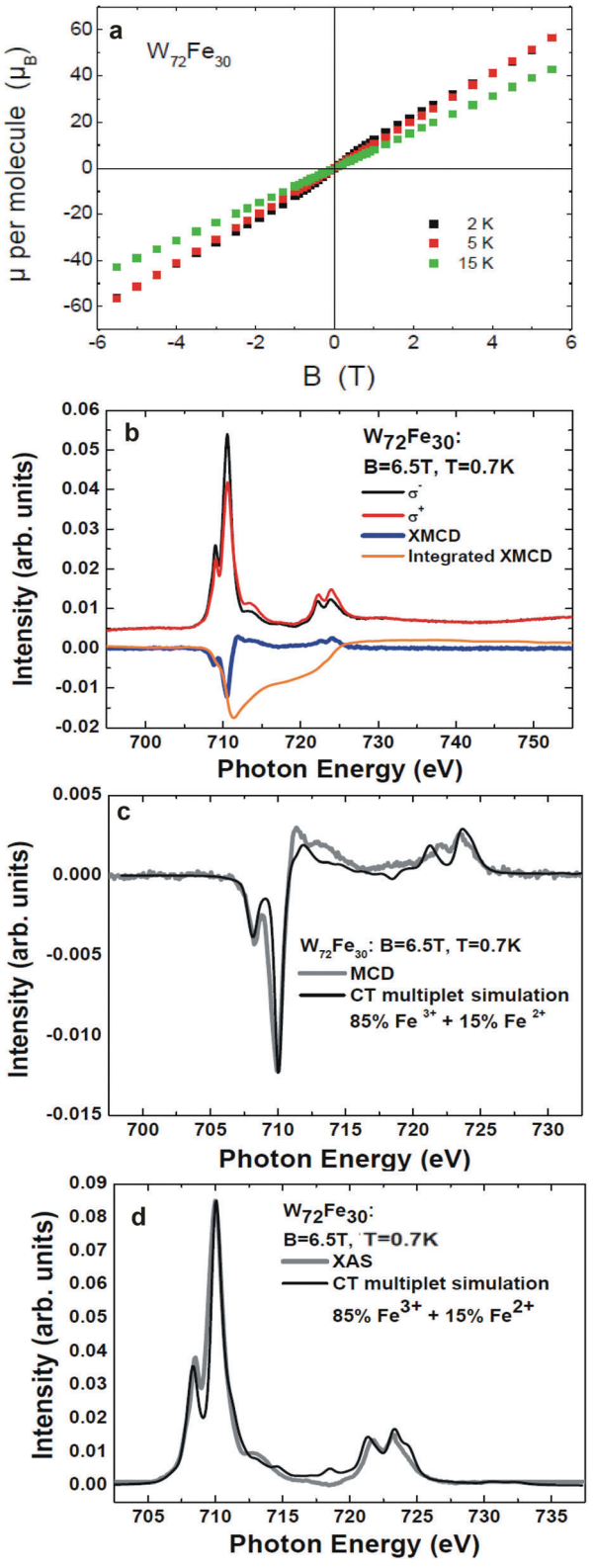

Fig. 8 (a) Magnetization of $W_{72}Fe_{30}$ (**2**) at 2 K, 5 K, and 15 K as a function of field. (b) Fe $L_{2,3}$ edges of **2** recorded with left and right circularly polarized X-rays, the corresponding XMCD signal, and its integral. These measurements were performed with a significantly reduced X-ray exposure (1–2% of the full beamline intensity) at a temperature of 0.7 K in an external field of 6.5 T. (c) and (d) Isotropic XMCD and isotropic XAS signals in comparison with charge-transfer multiplet simulations.

(iv) As hinted by the first-principles calculations, some of the Fe-3d-related states responsible for magnetism are not strongly localized. Since XAS at transition metal L edges on ionic compounds is a probe of the localized electronic structure and coordination of the transition metal ion in question, possible "interstitial or hybridized spin states" may not be entirely included into the element specific XMCD signal.

However, it can be concluded that most of the Fe 3d spin states responsible for the magnetic moment (≥85%) are localized at the "on-site" (Fe-centered) part of the Fe 3d states of **2**.

4. Summary

We investigated the electronic structure of three giant Keplerate-structural-type molecules with $Mo_{72}Fe_{30}$ and $W_{72}Fe_{30}$ cores by means of soft XAS and complementary theoretical approaches. For all three molecules, an Fe^{3+} to Fe^{2+} photoreduction process can be observed by means of Fe $L_{2,3}$ edge XAS. The crystal-field strength of the Fe^{2+} ions is noticeably lower (0.2 eV) than that of the original Fe^{3+} ions, indicating major changes in the local crystal-field environment (and subsequently the Fe–O bonding length) around the Fe ions during the photoreduction process. Hence, the photoreduction process might be explained by breaking up ligand bonds from the surrounding matrix of the Fe ions due to the soft X-ray radiation, initiating an electron transfer and a subsequent change in the crystal-field environment. The presence of negatively charged SO_4^{2-} ligands appears to slow down the Fe photoreduction process, whereas its potential influence on changes in the Mo and W ions still has to be investigated in more detail. The negative charge of the ligands likely builds a kind of repulsive "screening potential," slowing down the electron-transfer process toward Fe.

According to the first-principles calculations, the electronic structure of molecules **1** and **2** is quite similar. The high density of the energy levels and the near disappearance of the band gap make the system behave like a semi-metal. The conduction band comprises the Fe 3d states of t_{2g} nature located close to the Fermi energy, followed by Mo 4d (**1**) or W 5d (**2**) states, which are strongly hybridized with the empty O 2p states. An overall good agreement is observed between the first-principles electronic structure calculations and the O K edge XAS. The comparison of the Fe $L_{2,3}$ edges XAS spectra of the three molecules (**1**, **2** and **3**) reveals that the Fe ions behave similarly in these complexes. In combination with charge-transfer multiplet simulations, we find a relatively ionic Fe^{3+} ground state for all complexes. However, some admixtures of Fe^{2+} ions cannot be excluded completely, and here we cannot dismiss the beginning of a Fe photoreduction process due to "radiation damage." Considering these findings we probed the magnetic properties of the molecule with $W_{72}Fe_{30}$ core (**2**) by means of SQUID magnetometry and XMCD. Comparison between these two approaches reveals that most of the magnetic moment is dominated by "on-site" (Fe-centered) part of the Fe 3d states of **2**.

Acknowledgements

We are indebted to A. Müller and co-workers for generously providing samples. We thank J. Schnack for carefully reading our manuscript and suggesting very valuable improvements. This work was performed at the Advanced Light Source, Lawrence Berkeley National Laboratory, Berkeley, USA; which is operated under contract No. DE-AC02-05CH11231, BESSY II (Helmholtz – Zentrum Berlin), Germany, and the Swiss Light Source (Paul Scherrer Institute), Switzerland. Financial and travel support from the SFB 569, the PhD programme of the Federal State of Lower Saxony, Germany, the DFG GRK 965, the DFG FOR 945, and the EU's Seventh Framework Programme are gratefully acknowledged. We thank all beamline scientists for their excellent and generous technical support. T.V.K thanks the RFBR (Project Nos. 11-02-01221 and 11-02-00379) and bilateral Program "Russian–German Laboratory at BESSY" for financial support.

References

1 A. Müller and P. Gouzerh, *Chem. Soc. Rev.*, 2012, **41**, 7431–7463, DOI: 10.1039/c2cs35169b.
2 M. T. Pope and A. Müller, *Angew. Chem., Int. Ed. Engl.*, 1991, **30**, 34–48, DOI: 10.1002/anie.199100341.
3 D. Gatteschi, R. Sessoli, W. Plass, A. Müller, E. Krickemeyer, J. Meyer, D. Sölter and P. Adler, *Inorg. Chem.*, 1996, **35**, 1926–1934, DOI: 10.1021/ic951085l.
4 A. Müller, F. Peters, M. T. Pope and D. Gatteschi, *Chem. Rev.*, 1998, **98**, 239–271, DOI: 10.1021/cr9603946.
5 J. M. Clemente-Juan, E. Coronado, A. Gaita-Ariño, C. Giménez-Saiz, H. U. Gudel, A. Sieber, R. Bircher and H. Mutka, *Inorg. Chem.*, 2005, **44**, 3389–3395, DOI: 10.1021/ic048552w.
6 S. K. Pati and C. N. R. Rao, *Chem. Commun.*, 2008, 4683–4693, DOI: 10.1039/b807207h.
7 U. Kortz, A. Müller, J. van Slageren, J. Schnack, N. S. Dalal and M. Dressel, *Coord. Chem. Rev.*, 2009, **253**, 2315–2327, DOI: 10.1016/j.ccr.2009.01.014.
8 A. Müller, *Nat. Chem.*, 2009, **1**, 13–14, DOI: 10.1038/nchem.140.
9 E. Balogh, A. M. Todea, A. Müller and W. H. Casey, *Inorg. Chem.*, 2007, **46**, 7087–7092, DOI: 10.1021/ic7009308.
10 T. Liu, M. L. K. Langston, D. Li, J. M. Pigga, C. Pichon, A. M. Todea and A. Mueller, *Science*, 2011, **331**, 1590–1592, DOI: 10.1126/science.1201121.
11 A. Müller, S. K. Das, P. Kögerler, H. Bögge, M. Schmidtmann, A. X. Trautwein, V. Schunemann, E. Krickemeyer and W. Preetz, *Angew. Chem., Int. Ed.*, 2000, **39**, 1612–1614.
12 A. Müller, M. Luban, C. Schröder, R. Modler, P. Kögerler, M. Axenovich, J. Schnack, P. C. Canfield, S. Bud'ko and N. Harrison, *ChemPhysChem*, 2001, **2**, 517–521, DOI: 10.1002/1439-7641(20010917)2:8/9<517::AID-CPHC517>3.0.CO;2-1.
13 C. Schröder, H. Nojiri, J. Schnack, P. Hage, M. Luban and P. Kögerler, *Phys. Rev. Lett.*, 2005, **94**, 017205–017209, DOI: 10.1103/PhysRevLett.94.017205.
14 J. Schnack, M. Luban and R. Modler, *Europhys. Lett.*, 2001, **56**, 863–869, DOI: 10.1209/epl/i2001-00599-0.
15 A. Müller, A. M. Todea, J. van Slageren, M. Dressel, H. Bögge, M. Schmidtmann, M. Luban, L. Engelhardt and M. Rusu, *Angew. Chem., Int. Ed.*, 2005, **44**, 3857–3861, DOI: 10.1002/anie.200500697.
16 O. Waldmann, *Phys. Rev. B: Condens. Matter Mater. Phys.*, 2007, **75**, 012415–012419, DOI: 10.1103/PhysRevB.75.012415.
17 C. Schröder, R. Prozorov, P. Kögerler, M. D. Vannette, X. Fang, M. Luban, A. Matsuo, K. Kindo, A. Müller and A. M. Todea, *Phys. Rev. B: Condens. Matter Mater. Phys.*, 2008, **77**, 224409-1–224409-8, DOI: 10.1103/PhysRevB.77.224409.
18 A. M. Todea, A. Merca, H. Bögge, T. Glaser, J. M. Pigga, M. L. K. Langston, T. Liu, R. Prozorov, M. Luban, C. Schröder, W. H. Casey and A. Müller, *Angew. Chem., Int. Ed.*, 2010, **49**, 514–519, DOI: 10.1002/anie.200905460.
19 A. M. Todea, J. Szakács, S. Konar, H. Bögge, D. C. Crans, T. Glaser, H. Rousselière, R. Thouvenot, P. Gouzerh and A. Müller, *Chem.–Eur. J.*, 2011, **17**, 6635, DOI: 10.1002/chem.201003260.
20 C. T. Chen, Y. U. Idzerda, H. J. Lin, N. V. Smith, G. Meigs, E. Chaban, G. H. Ho, E. Pellegrin and F. Sette, *Phys. Rev. Lett.*, 1995, **75**, 152–155, DOI: 10.1103/PhysRevLett.75.152.
21 D. Collison, C. D. Garner, C. M. McGrath, J. F. W. Mosselmans, M. D. Roper, J. M. W. Seddon, E. Sinn and N. A. Young, *J. Synchrotron Radiat.*, 1999, **6**, 585–587, DOI: 10.1107/S0909049598014964.
22 S. J. George, J. Fu, Y. Guo, O. B. Drury, S. Friedrich, T. Rauchfuss, P. I. Volkers, J. C. Peters, V. Scott, S. D. Brown, C. M. Thomas and S. P. Cramer, *Inorg. Chim. Acta*, 2008, **361**, 1157–1165, DOI: 10.1016/j.ica.2007.10.039.
23 N. Schmidt, A. Scheurer, S. Sperner and R. H. Fink, *Z. Naturforsch. Sect. B-a J. Chem. Sci.*, 2010, **65**, 390–398.
24 K. Kuepper, C. Taubitz, D. Taubitz, U. Wiedwald, A. Scheurer, S. Sperner, R. W. Saafrank, J. Kappler, L. Joly, P. Ziemann and M. Neumann, *J. Phys. Chem. Lett.*, 2011, **2**, 1491–1496, DOI: 10.1021/jz2005013.
25 J. J. Jia, T. A. Callcott, J. Yurkas, A. W. Ellis, F. J. Himpsel, M. G. Samant, J. Stöhr, D. L. Ederer, J. A. Carlisle, E. A. Hudson, L. J. Terminello, D. K. Shuh and R. C. C. Perera, *Rev. Sci. Instrum.*, 1995, **66**, 1394–1397, DOI: 10.1063/1.1145985.
26 I. Letard, P. Sainctavit, C. Cartier Dit Moulin, J. Kappler, P. Ghigna, D. Gatteschi and B. Doddi, *J. Appl. Phys.*, 2007, **101**, 113920, DOI: 10.1063/1.2745318.
27 J. M. Soler, E. Artacho, J. D. Gale, A. García, J. Junquera, P. Ordejón and D. Sánchez-Portal, *J. Phys.: Condens. Matter*, 2002, **14**, 2745–2779, DOI: 10.1088/0953-8984/14/11/302.
28 SIESTA homepage, http://www.icmab.es/siesta/
29 J. P. Perdew, K. Burke and M. Ernzerhof, *Phys. Rev. Lett.*, 1996, **77**, 3865, DOI: 10.1103/PhysRevLett.77.3865.

30 J. Junquera, Ó. Paz, D. Sánchez-Portal and E. Artacho, *Phys. Rev. B: Condens. Matter*, 2001, **64**, 235111, DOI: 10.1103/PhysRevB.64.235111.
31 A. V. Postnikov, M. Brüger and J. Schnack, *Phase Transitions*, 2005, **78**, 47–59, DOI: 10.1080/01411590412331316744.
32 F. M. F. de Groot, *J. Electron Spectrosc. Relat. Phenom.*, 1994, **67**, 529–622, DOI: 10.1016/0368-2048(93)02041-J.
33 F. M. F. de Groot, *Coord. Chem. Rev.*, 2005, **249**, 31–63, DOI: 10.1016/j.ccr.2004.03.018.
34 F. M. F. de Groot and A. Kotani, *Core Level Spectroscopy of Solids*, Francis & Taylor, 2008.
35 S. Bonhommeau, N. Pontius, S. Cobo, L. Salmon, F. M. F. de Groot, G. Molnár, A. Bousseksou, H. A. Dürr and W. Eberhardt, *Phys. Chem. Chem. Phys.*, 2008, **10**, 5882–5889, DOI: 10.1039/b806783j.
36 A. Helmstedt, M. D. Sacher, A. Gryzia, A. Harder, A. Brechling, N. Mueller, U. Heinzmann, V. Hoeke, E. Krickemeyer, T. Glaser, S. Bouvron and M. Fonin, *J. Electron Spectrosc. Relat. Phenom.*, 2012, **184**, 583–588, DOI: 10.1016/j.elspec.2011.11.002.
37 A. V. Postnikov, J. Kortus and M. R. Pederson, *Phys. Status Solidi B*, 2006, **243**, 2533–2572, DOI: 10.1002/pssb.200541490.
38 A. Müller, S. K. Das, E. Krickemeyer, P. Kögerler, H. Bögge and M. Schmidtmann, *Solid State Sci.*, 2000, **2**, 847–854, DOI: 10.1016/S1293-2558(00)01082-7.
39 A. V. Postnikov, S. G. Chiuzbăian, M. Neumann and S. Blügel, *J. Phys. Chem. Solids*, 2004, **65**, 813–817, DOI: 10.1016/j.jpcs.2003.11.025.
40 A. F. Takács, M. Neumann, A. V. Postnikov, K. Kuepper, A. Scheurer, S. Sperner, R. W. Saalfrank and K. C. Prince, *J. Chem. Phys.*, 2006, **124**, 044503, DOI: 10.1063/1.2155340.
41 Y. Teramura, A. Tanaka and T. Jo, *J. Phys. Soc. Jpn.*, 1996, **65**, 1053–1055, DOI: 10.1143/JPSJ.65.1053.
42 C. Piamonteze, P. Miedema and F. M. F. de Groot, *Phys. Rev. B: Condens. Matter Mater. Phys.*, 2009, **80**, 184410, DOI: 10.1103/PhysRevB.80.184410.

Publication H9

[**H9**] S. Khanra, K. Kuepper, T. Weyermüller, M. Prinz, M. Raekers, S. Voget, A. V. Postnikov, F. M. F. De Groot, S. J. George, M. Coldea, M. Neumann, and P. Chaudhuri. *Star-Shaped molecule of Mn(II)$_4$O$_6$ Core with an St=10 High-Spin State: A Theoretical and Experimental Study with XPS, XMCD, and Other Magnetic Methods*, Inorg. Chem. **47**, 4605 (2008), doi: 10.1021/ic7023007.

Inorganic Chemistry
including bioinorganic chemistry

Article

Star-Shaped Molecule of Mn^{II}_4O Core with an $S = 10$ High-Spin State. A Theoretical and Experimental Study with XPS, XMCD, and Other Magnetic Methods

Sumit Khanra, Karsten Kuepper, Thomas Weyhermu#ller, Manuel Prinz, Michael Raekers, Sebastian Voget, Andrei V. Postnikov, Frank M. F. de Groot, Simon J. George, Marin Coldea, Manfred Neumann, and Phalguni Chaudhuri

Inorg. Chem., **2008**, 47 (11), 4605-4617 • DOI: 10.1021/ic7023007 • Publication Date (Web): 06 May 2008

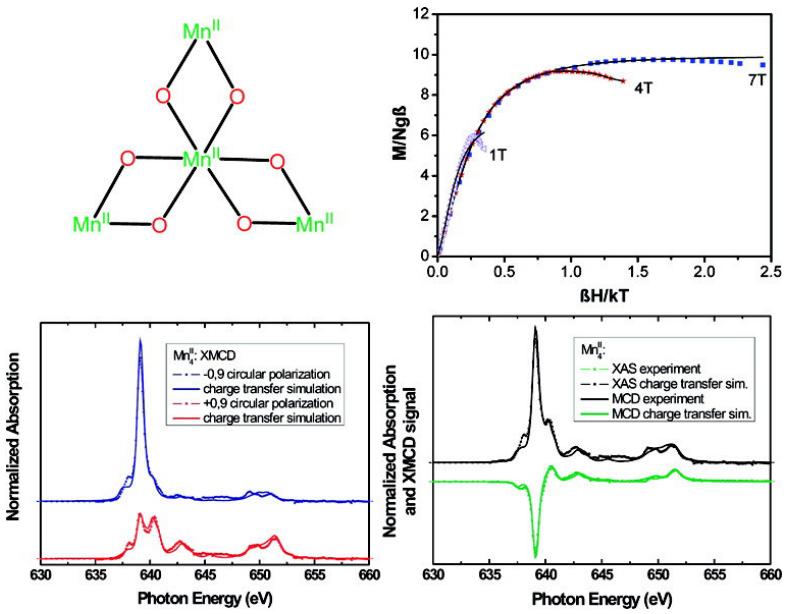

More About This Article

Additional resources and features associated with this article are available within the HTML version:

- Supporting Information
- Links to the 1 articles that cite this article, as of the time of this article download
- Access to high resolution figures
- Links to articles and content related to this article
- Copyright permission to reproduce figures and/or text from this article

Inorg. Chem. **2008**, *47*, 4605−4617

Star-Shaped Molecule of $Mn^{II}_4O_6$ Core with an $S_t = 10$ High-Spin State. A Theoretical and Experimental Study with XPS, XMCD, and Other Magnetic Methods

Sumit Khanra,[†] Karsten Kuepper,[‡] Thomas Weyhermüller,[†] Manuel Prinz,[§] Michael Raekers,[§] Sebastian Voget,[§] Andrei V. Postnikov,[||] Frank M. F. de Groot,[⊥] Simon J. George,[#] Marin Coldea,[▽] Manfred Neumann,*[,§] and Phalguni Chaudhuri*[,†]

Max-Planck-Institut für Bioanorganische Chemie, Stiftstrasse 34−36, D-45470 Mülheim an der Ruhr, Germany, Forschungszentrum Dresden-Rossendorf, Institute of Ion Beam Physics and Materials Research, P.O. Box 510119, D-01314 Dresden, Germany, Department of Physics, University of Osnabrück, Barbarastrasse 7, D-49069 Osnabrück, Germany, Laboratoire de Physique des Milieux Denses, Institute de Physique Electronique et Chimie, Paul Verlaine University, 1 Bd Arago, F-57078 Metz, France, Department of Inorganic Chemistry and Catalysis, Utrecht University, Sorbonnelaan 16, 3584 CA Utrecht, The Netherlands, Advanced Biological and Environmental X-ray Facility, Lawrence Berkeley National Laboratory, 1 Cyclotron Road, Berkeley, California 94720, and Faculty of Physics, University Babes—Bolyai, R-3400 Cluj—Napoca, Romania

Received November 22, 2007

We report a comprehensive study of the electronic and magnetic properties of a star-shaped molecule comprising a $Mn^{II}_4O_6$ core. One feature of this compound is weak magnetic coupling constants compared to other similar polyoxo compounds. This leads to complicated low-lying magnetic states in which the ground state is not well separated from the upper-lying states, yielding a high-spin molecule with a giant magnetic moment of up to 20 μ_B/formula unit. We apply X-ray diffraction and magnetometry as well as other X-ray spectroscopic techniques, namely, X-ray photoelectron spectroscopy, X-ray magnetic circular dichroism, and X-ray emission spectroscopy. We compare our experimental results with ab initio electronic band structure calculations as well as the localized electronic structure around the Mn^{2+} ions with charge-transfer multiplet calculations.

1. Introduction

Exchange-coupled polymetallic complexes, in which spin coupling between paramagnetic metal ions is propagated via bridging atoms, are of special interest to researchers who seek new molecule-based magnetic materials[1,2] displaying interesting electronic properties and to bioinorganic chemists who investigate the structure and function of polynuclear metal centers in proteins.[3]There is an impressive diversity of spin-coupled structures in biology, e.g., ascorbate oxidase, cytochrome oxidase, ribonucleotide reductase, water-oxidizing complex of photosystem II, etc. The intimate relationship between spin coupling and molecular structure has fostered, on the other hand, the emergence of molecular magnetism as a multidisciplinary field.[4]The fundamental understanding regarding the factors that determine the spin states of polynuclear transition-metal complexes owes much to the study of model compounds where magnetostructural correlations can be established in a systematic way. To achieve this goal, the influence of parameters such as the symmetry of magnetic orbitals,

* To whom correspondence should be addressed. E-mail: mneumann@uos.de (M.N.), chaudh@mpi-muelheim.mpg.de (P.C.).
[†] Max-Planck-Institut für Bioanorganische Chemie.
[‡] Institute of Ion Beam Physics and Materials Research.
[§] University of Osnabrück.
[||] Paul Verlaine University.
[⊥] Utrecht University.
[#] Lawrence Berkeley National Laboratory.
[▽] University Babes—Bolyai.

(1) (a) *Magnetic Molecular Materials*; Gatteschi, D., Kahn, O., Miller, J. S., Palacio, F., Eds.; Kluwer Academic Publishers: Dordrecht, The Netherlands, 1991. (b) *Research Frontiers in Magnetochemistry*; O'Connor, C. J., Ed.; World Scientific: Singapore, 1993. (c) A tribute to Oliver Kahn: *J. Solid State Chem.* **2001**, *159* No. 2 (July). (d) *Magnetism: Molecules to Materials*; Miller, J. S., Brillon, M., Eds.; Wiley-VCH: Weinheim, Germany, 2002.

10.1021/ic7023007 CCC: $40.75
Published on Web 05/06/2008

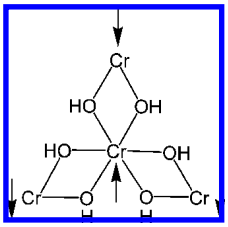

Figure 1. Chromium(III) analogue of Werner's hexol.

the nature of bridging and terminal ligands, and changes in coordination geometry is being studied. Surprisingly, few studies of the influence of the molecular topology on the magnetic properties of coordination complexes have been performed.[5] For example, the chromium(III) analogue of the Werner's hexol, $[Cr^{III}\{(OH)_2Cr^{III}en_2\}_3](ClO_4)_6$ exhibits a high-spin $S_t = 3$ ground state[6] owing to its topology, as shown in Figure 1.

A ferromagnetic-like behavior is obtained with a ground state characterized by a large spin, although the interaction between the nearest-neighbor Cr^{III} ions ($S_{Cr} = {}^3/_2$) is antiferromagnetic. This effective ferromagnetic coupling between the outer ions is very interesting in the context of synthesizing "high-spin" molecules. The best result would be obtained in a topology where a maximum number of spins align in the same direction, as shown in Figure 1. The other two topological possibilities for tetranuclear complexes, namely, the square and the linear arrangements, led in the case of identical metal ions to a diamagnetic ground state because of the equal number of spins in each direction. Thus, it is possible to tune the magnetic properties of polynuclear complexes by controlling the topology and the nature of the ions in the interaction. This approach is particularly promising for the synthesis of "high-spin" molecules. Of particular concern in this context is the development of synthetic routes that can provide high nuclear metal complexes with high spins in a controlled fashion. Among the variety of methodologies applied to synthesize polymetallic coordination compounds, the use of "metalloligands", i.e., metal complexes as ligands,[7] in which the ligands already bound to one metal have a free lone pair of electrons for coordination to a second metal of the same or different kind, has proven to be very successful; this route offers many potential advantages over the self-assembled route in which no control upon the products that are formed is possible, whereas the approach of using metalloligands proceeds step by step and

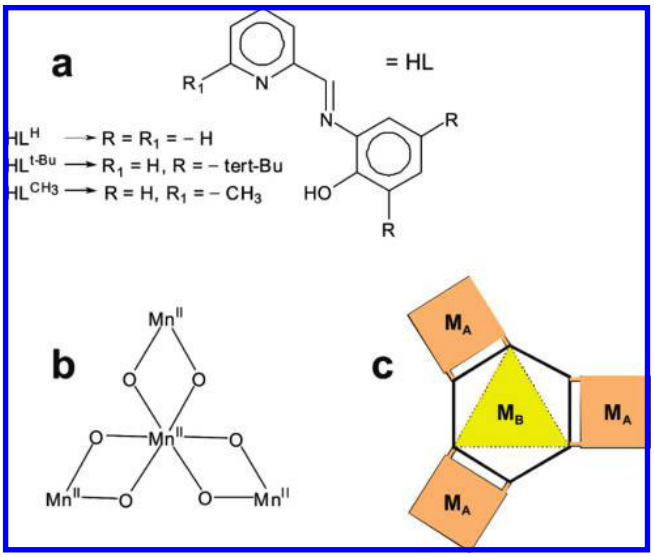

Figure 2. (a) Formula and abbreviations of the ligands used. (b) Core structure of compound **2** illustrating the topology of the high-spin d^5 Mn^{II} ions. (c) Concept of "metal complexes as ligands" depicted in modular form.

provides a route to gaining control of the nuclearity in addition to the preparation of species containing different metal ions, i.e., heterometallic complexes. We have been favoring the strategy of using "complexes as ligands" for a few years and have already reported star-shaped tetranuclear molecules like $Ni^{II}(Ni^{II}L)_3$[8] and $Cr^{III}(Mn^{II}\text{-oxime})_3$,[9] as depicted in the modular form (Figure 2). As a continuation of our interest in phenol-containing ligands,[10] we report here the use of a mononuclear, neutral manganese(II) complex $Mn^{II}L_2$ (**1**), in which the phenoxo oxygen atoms of the tridentate ligand $[L]^-$ occupy the cis position, as a building block to generate the star-shaped Mn_4O_6 motif (Figure 2).

In this paper, we explore the electronic and magnetic properties of the star-shaped molecule of the Mn_4O_6 core. Similar to the iron star molecule,[11,12] it is expected that the spins of the outer three manganese ions will couple antiparallel to that of the central ion, leading to an overall

(2) Kahn, O. *Molecular Magnetism*; VCH: New York, 1993.
(3) (a); Holm, R. H.; Solomon, E. I., Guest Eds. *Chem. Rev.* **1996**, *96* (7); **2004**, *104* (2). (b) *Bioinorganic Chemistry of Copper*; Karlin, K. D., Tyeklár, Z., Eds.; Chapman & Hall: New York, 1993. (c) *Mechanistic Bioinorganic Chemistry*; Holden, H. T., Pecoraro, V. L., Eds.; American Chemical Society: Washington, DC, 1995. (d) *Handbook of Metalloproteins*; Messerschmidt A., Huber, R., Poulos, T., Wieghardt, K., Eds.; John Wiley & Sons: Chichester, U.K., 2001.
(4) (a) Christou, G.; Gatteschi, D.; Hendnrickson, D. N.; Sessoli, R. *MRS Bull.* **2000**, *25*, 66. (b) Gatteschi, D.; Sessoli, R. *Angew. Chem., Int. Ed.* **2003**, *42*, 268. (c) Bircher, R.; Chaboussard, G.; Dobe, C.; Güdel, H. U.; Ochsenbein, S. T.; Sieber, A.; Waldmann, O. *Adv. Funct. Mater.* **2006**, *16*, 209.
(5) (a) Lloret, F.; Journaux, Y.; Julve, M. *Inorg. Chem.* **1990**, *29*, 3967. (b) Hodgson, D. J.; Michelsen, K.; Pedersen, E.; Towle, D. K. *Inorg. Chem.* **1991**, *30*, 815.
(6) (a) Andersen, P.; Berg, T. *Acta Chem. Scand., Ser. A* **1978**, *32*, 989. (b) Güdel, H.; Hauser, U. *Inorg. Chem.* **1980**, *19*, 1325.
(7) (a) Kahn, O. *Adv. Inorg. Chem.* **1995**, *43*, 179. (b) Gruber, S. J.; Harris, C. M.; Sinn, E. *J. Inorg. Nucl. Chem.* **1968**, *30*, 1805. (c) Selbin, J.; Ganguly, L. *J. Inorg. Nucl. Chem. Lett.* **1969**, *5*, 715. (d) Singh, C. B.; Sahoo, B. *J. Inorg. Nucl. Chem.* **1974**, *36*, 1259. (e) Linkvedt, R. L.; Kramer, L. S.; Ranger, G.; Corfield, P. W.; Glick, M. D. *Inorg. Chem.* **1983**, *22*, 3580. (f) Luneau, D.; Oshio, H.; Okawa, H.; Kida, S. *J. Chem. Soc., Dalton Trans.* **1990**, 2283. (g) Chaudhuri, P.; Winter, M.; Fleischhauer, P.; Haase, W.; Flörke, U.; Haupt, H.-J. *J. Chem. Soc., Chem. Commun.* **1990**, 1728.
(8) Pavlishchuk, V.; Birkelbach, F.; Weyhermüller, T.; Wieghardt, K.; Chaudhuri, P. *Inorg. Chem.* **2002**, *41*, 4405.
(9) Khanra, S.; Biswas, B.; Golze, C.; Büchner, B.; Kataev, V.; Weyhermuller, T.; Chaudhuri, P. *Dalton Trans.* **2007**, *4*, 481.
(10) (a) Mukherjee, S.; Weyhermüller, T.; Bill, E.; Chaudhuri, P. *Eur. J. Inorg. Chem.* **2004**, 4209. (b) Paine, T. K.; Weyhermüller, T.; Slep, L. D.; Neese, F.; Bill, E.; Bothe, E.; Wieghardt, K.; Chaudhuri, P. *Inorg. Chem.* **2004**, *43*, 7324. (c) Paine, T. K.; Rentschler, E.; Weyhermüller, T.; Chaudhuri, P. *Eur. J. Inorg. Chem.* **2003**, 3167. (d) Görner, H.; Khanra, S.; Weyhermüller, T.; Chaudhuri, P. *J. Phys. Chem. A* **2006**, *110*, 2587. (e) Khanra, S.; Weyhermüller, T.; Bill, E.; Chaudhuri, P. *Inorg. Chem.* **2006**, *45*, 5911.
(11) Saalfrank, R. W.; Scheurer, A.; Bernt, I.; Heinemann, F. W.; Postnikov, A. V.; Schünemann, V.; Trautwein, A. X.; Alam, M.; Rupp, H.; Müller, P. *Dalton Trans.* **2006**, *23*, 2865.
(12) Takács, A. F.; Neumann, M.; Postnikov, A. V.; Kuepper, K.; Scheurer, A.; Sperner, S.; Saalfrank, R. W.; Prince, K. C. *J. Chem. Phys.* **2006**, *124*, 4503-+

ferromagnetic coupling between the outer manganese ions. Because the manganese star molecule comprises four Mn^{2+} ions ($S = {}^5/_2$ spin state), one expects a giant magnetic net moment of 10 μ_B/formula unit (fu). Although far from trivial by means of chemical manipulation (crystallization with different ligands and/or central ions) or deposition on surfaces, this relatively simple model system allows an exact study of its chemical, electronic, and magnetic properties. To achieve a complete characterization of the manganese star molecule, we apply a number of complementary experimental and theoretical approaches. One appealing finding of our work is a weak ferromagnetic coupling in moderate external fields of a few tesla due to the very weak nature of the intramolecular coupling constants. This leads to a "high-spin" molecule with an overall magnetic moment of 20 μ_B/fu in an ideal case.

This Article is structured as follows. The experimental and theoretical procedures are described in the following section. Later on, the synthesis is described and a structural characterization given. We present a detailed analysis of the magnetic properties by means of SQUID and X-ray magnetic circular dichroism (XMCD) techniques. Whereas the first method tackles the overall magnetic properties of the compound in question, XMCD is well-known for its unique capabilities not only to be an element-specific probe of the magnetization but also to enable the separation into orbital and spin moment.[13,14] The underlying mechanism of X-ray absorption spectroscopy (XAS), furthermore, gains deep insight into the local electronic structure of the Mn^{2+} ions. Besides XAS, the techniques of X-ray photoelectron spectroscopy (XPS) and X-ray emission spectroscopy (XES) are tools of unique precision concerning the analysis of the spatial distribution of the electron and chemical bonding of transition-metal compounds, including molecular magnets.[12,15–17] The latter probes are especially useful in combination with first principles electronic structure calculations, and we will present a detailed analysis of the electronic valence band structure of the manganese star molecule by comparing experimental and theoretical results. Finally, we sum up our main conclusions.

2. Experimental and Theoretical Procedures

2.1. Experimental Methods. 2.1.1. Materials and Physical Measurements. Reagent- or analytical-grade materials were obtained from commercial suppliers and used without further purification. Elemental analyses (C, H, N, and metal) were performed by the Microanalytical Laboratory, Mülheim, Germany. Fourier transform IR spectra of the samples in KBr disks were recorded with a Perkin-Elmer 2000 FT-IR instrument. Magnetic susceptibilities of powdered samples were recorded with a SQUID magnetometer in the temperature range 2−290 K with an applied field of 1 T. Experimental susceptibility data were corrected for their underlying diamagnetism using Pascal's constants. Mass spectra were recorded with either a Finnigan MAT 8200 (electron ionization, EIMS) or a MAT 95 (electrospray, ESI-MS) instrument.

2.1.2. Preparations. The substituted and unsubstituted derivatives of 2-hydroxyphenyl(2-pyridylmethaneimine), HL, were prepared by the Schiff base condensation of 2-pyridylaldehyde (or its derivatives) and 2-aminophenol (or its 2,6-di-*tert*-butyl derivative) using the same protocol. As an example, the protocol for the di-*tert*-butyl derivative is given below.

A solution of 3,5-di-*tert*-butyl-2-aminophenol (5.75 g, 26 mmol) and pyridine-2-aldehyde (2.83 g, 26 mmol) in distilled methanol (400 mL) was stirred at room temperature under argon for 12 h, after which the precipitated yellow solid was separated by filtration and dried in air. Yield: 7.5 g (92%). Purity was checked by gas chromatography (GC; Hewlett-Packard 6890): retention time 23.1 min; column Rtx-5 amine 15m, S-77, detector, FID, temp program 60−310 °C (8 °C/min) ∼95%. EI-MS: *m*/*z* 310 (61%), 295 (33%), 232 (100%). IR (KBr, cm^{-1}): 3335s, 2992−2865s, 1623s, 1590s, 1577s, 1481s, 1468s, 1438s, 1413s, 1389m, 1363s, 1295m, 1251s, 1190s, 1146s, 1125s, 959s, 881m, 863m, 806m, 780m, 761m, 742m, 683m, 648m. ^{1}H NMR (400 MHz, $CDCl_3$): 1.313−1.443 (18H, m), 7.290−7.310 (3H, m), 7.742 (2H, m), 8.188−8.208 (1H, d), 8.684 (1H, d), 8.848 (1H, s).

Mononuclear $[Mn^{II}L_2]$ and Their Derivatives. The mononuclear complexes were also prepared very similarly by the reaction of a solution of HL (2 mmol) in acetone (20 mL) with manganese(II) acetylacetonate (0.25 g, 1 mmol) in acetone (30 mL), whereupon the yellow slurry changed its color to deep red. After stirring for 1 h, the red solid was isolated by filtration and washed thoroughly with acetone to yield $[Mn^{II}L_2]$. Yield: ∼50%.

$[Mn^{II}L^H_2]$. Anal. Calcd for $C_{24}H_{18}N_4O_2Mn$ (449.37): C, 64.15; H, 4.04; N, 12.47; Mn, 12.23. Found: C, 64.3; H, 4.1; N, 12.5; Mn, 12.4. EI-MS: *m*/*z* 449 (81.7%) $[M]^+$, 371 (49.2%) $[M - C_5H_4N]^+$, 252 (100%) $[M - L]^+$, 196 (68.9%) $[L]^+$. X-ray-quality crystals of $[Mn^{II}L^{CH_3}_2]\cdot CH_3OH$ (**1**) were grown from a solution of $[Mn^{II}L^{CH_3}_2]$ in methanol.

$[Mn^{II}_4L^H_6](BF_4)_2\cdot 2CH_3CN\cdot H_2O$ (2). A solution of mononuclear $[Mn^{II}L^H_2]$ (0.45 g, 1 mmol) and $Mn(CH_3COO)_2\cdot 4H_2O$ (0.09 g, 0.33 mmol) in a solvent mixture of acetonitrile/methanol (1:1, 30 mL) was stirred in the presence of air for 0.5 h, and Bu_4NBF_4 (0.96 g/3 mmol) was then added to the deep-colored, nearly black solution. The precipitated red solid was separated by filtration, washed with diethyl ether, and air dried. X-ray-quality crystals were grown by diffusion of diethyl ether into an acetonitrile solution of red $[Mn^{II}_4L^H_6](BF_4)_2$. Yield: 0.22 g (40%). Anal. Calcd for $C_{76}H_{62}B_2F_8Mn_4N_{14}O_7$ (1676.78): C, 54.44; H, 3.73; N, 11.70; Mn, 13.11. Found: C, 54.4; H, 3.6; N, 11.6; Mn, 13.2. IR (KBr, cm^{-1}): 3053, 1585, 1479, 1457, 1298, 1280, 1146, 1083, 1061, 865, 750. ESI-MS: *m*/*z* 701 (100%) $[M - 2(BF_4)]^{2+}$, 1489 (10%) $[M\text{-}BF_4]^+$.

2.1.3. X-ray Crystallographic Data Collection and Refinement of the Structures. The crystallographic data for $HL^{t\text{-}Bu}$, the mononuclear **1**, and the tetranuclear **2** are summarized in Table 1. A perspective view and selected bond lengths of the $HL^{t\text{-}Bu}$ ligand are presented in Figure 3 and Table 2. Graphite-monochromated Mo Kα radiation (λ = 0.710 73 Å) was used for all three compounds. The crystals of $HL^{t\text{-}Bu}$, **1**, and **2** were fixed with perfluoropolyether onto glass fibers and mounted on a Nonius-

(13) Chen, C. T.; Idzerda, Y. U.; Lin, H.-J.; Smith, N. V.; Meigs, G.; Chaban, E.; Ho, G. H.; Pellegrin, E.; Sette, F. *Phys. Rev. Lett.* **1995**, *75*, 152–155.
(14) Funk, T.; Deb, A.; George, S. J.; Wang, H. X.; Cramer, S. P. *Coord. Chem. Rev.* **2005**, *249*, 3.
(15) Kuepper, K.; Bondino, F.; Prince, K.; Zangrando, M.; Zacchigna, M.; Takacs, A.; Crainic, T.; Matteucci, M.; Parmigiani, F.; Winiarski, A.; Galakhov, V.; Mukovskii, Y.; Neumann, M. *J. Phys. Chem. B* **2005**, *109*, 15667–15670.
(16) Kuepper, K.; Falub, M.; Prince, K.; Galakhov, V.; Troyanchuk, I.; Chiuzbaian, S.; Matteucci, M.; Wett, D.; Szargan, R.; Ovechkina, N.; Mukovskii, Y.; Neumann, M. *J. Phys. Chem. B* **2005**, *109*, 9354–9361.
(17) Kuepper, K.; Kadiroglu, M.; Postnikov, A. V.; Prince, K. C.; Matteucci, M.; Galakhov, V. R.; Hesse, H.; Borstel, G.; Neumann, M. *J. Phys.: Condens. Matter* **2005**, *17*, 4309–4317.

Table 1. Crystal Data and Structure Refinement for $HL^{t\text{-}Bu}$, Complex **1**·CH_3OH, and Complex **2**·$2CH_3CN$·H_2O

	$HL^{t\text{-}Bu}$	complex **1**·CH_3OH	complex **2**·$2CH_3CN$·H_2O
empirical formula	$C_{20}H_{26}N_2O$	$C_{27}H_{26}MnN_4O_3$	$C_{76}H_{62}B_2F_8Mn_4N_{14}O_7$
fw	310.43	509.46	1676.78
temperature (K)	100(2)	100(2)	100(2)
wavelength (Å)	0.71073	0.71073	0.71073
cryst syst	monoclinic	monoclinic	tetragonal
space group	$P2_1/c$	$P2_1/c$	$I4_1/a$
unit cell dimens	a = 16.6521(7) Å	a = 9.1261(4) Å	a = 17.0154(9) Å
	b = 11.1917(5) Å	b = 26.6124(12) Å	b = 17.0154(9) Å
	c = 9.7074(4) Å	c = 10.6470(6) Å	c = 53.619(4) Å
	β = 95.486(5)°	β = 110.09(1)°	$\alpha = \beta = \gamma = 90°$
vol (Å^3), Z	1800.84(13), 4	2428.5(2), 4	15524.0(16), 8
calcd density (Mg/m^3)	1.145	1.393	1.435
abs coeff (mm^{-1})	0.071	0.580	0.717
F(000)	672	1060	6832
cryst size (mm)	0.11 × 0.10 × 0.02	0.10 × 0.05 × 0.04	0.23 × 0.17 × 0.13
θ range for data collection (deg)	4.44−27.50	7.07−30.97	2.24−26.35
reflns collcd/unique	28 118/4117 [R(int) = 0.0895]	61 457/7593 [R(int) = 0.0520]	53 622/7932 [R(int) = 0.0338]
abs corrn	semiempirical from equiv	not measd	Gaussian, face-indexed
refinement method	full-matrix least squares on F^2	full-matrix least squares on F^2	full matrix least squares on F^2
data/restraints/param	4117/0/215	7593/0/320	7843/0/507
GOF on F^2	1.013	1.035	1.028
final R indices [$I > 2\sigma(I)$]	R1 = 0.0513, wR2 = 0.0957	R1 = 0.0327, wR2 = 0.0758	R1 = 0.0353, wR2 = 0.0930
R indices (all data)	R1 = 0.0865, wR2 = 0.1084	R1 = 0.0445, wR2 = 0.0815	R1 = 0.0571, wR2 = 0.1742
largest diff peak and hole (e/Å^3)	+0.272 and −0.200	+0.373 and −0.222	+0.649 and −0.413

Kappa CCD diffractometer equipped with a cryogenic nitrogen cold stream operating at 100(2) K. Final cell constants were obtained from a least-squares fit of all measured reflections. Intensity data were corrected for Lorentz and polarization effects. The intensity data set of $HL^{t\text{-}Bu}$ and of **2** were corrected for absorption with the use of either the semiempirical method for $HL^{t\text{-}Bu}$ or the Gaussian, face-indexed program for **2**, whereas the data set for **1** was not corrected for absorption. The Siemens *SHELXTL* software package (Sheldrick, G. M. *SHELXTL*; Universität Göttingen: Göttingen, Germany) was used for solution, refinement, and artwork of the structures; the neutral atom scattering factors of the program were used. The structures were solved and refined by direct methods and difference Fourier techniques. Non-hydrogen atoms were refined anisotropically, and hydrogen atoms were placed at calculated positions and refined as riding atoms with isotropic displacement parameters. Split atom models were used to account for disorder of the solvent molecules.

2.1.4. X-ray Spectroscopic Techniques. The soft XAS and XMCD spectroscopy were performed at the elliptically polarizing undulator Beamline 4.0.2 of the Advanced Light Source (ALS), Berkeley, CA.[18] The samples have been mounted into a cryostat equipped with a 6 T superconducting magnet,[19] the sample stage was connected to a pumped helium cryostat, reaching a base temperature of around 5.0 K during the experiments presented here. The measurements at the Mn L edge have been recorded under external magnetic fields of different strength in the total electron yield mode.

The X-ray emission spectra were recorded at the soft X-ray fluorescence end station at the undulator-based Beamline 8.0.1 of the ALS.[20] The excitation energies were set to about 543.9 eV for

Table 2. Selected Bond Lengths (Å) and Angles (deg) for $HL^{t\text{-}Bu}$

O(1)−C(2)	1.3701(18)	N(8)−C(9)	1.273(2)
C(2)−C(3)	1.401(2)	C(9)−C(10)	1.473(2)
C(2)−C(7)	1.404(2)	C(10)−N(11)	1.349(2)
C(3)−C(4)	1.399(2)	C(10)−C(15)	1.388(2)
C(4)−C(5)	1.394(2)	N(11)−C(12)	1.340(2)
C(5)−C(6)	1.388(2)	C(12)−C(13)	1.384(2)
C(6)−C(7)	1.395(2)	C(13)−C(14)	1.389(2)
C(7)−N(8)	1.418(2)	C(14)−C(15)	1.378(2)
O(1)−C(2)−C(3)	119.64(14)	C(6)−C(7)−N(8)	123.92(14)
O(1)−C(2)−C(7)	119.83(14)	C(2)−C(7)−N(8)	115.86(13)
C(3)−C(2)−C(7)	120.53(14)	C(9)−N(8)−C(7)	118.73(13)
C(4)−C(3)−C(2)	116.86(14)	N(8)−C(9)−C(10)	122.50(14)
C(4)−C(3)−C(16)	121.37(14)	N(11)−C(10)−C(15)	123.35(15)
C(2)−C(3)−C(16)	121.77(14)	N811)-C(10)−C(9)	113.80(13)
C(5)−C(4)−C(3)	124.06(15)	C(15)−C(10)−C(9)	122.84(14)
C(6)−C(5)−C(4)	117.41(14)	C(12)−N(11)−C(10)	116.93(14)
C(6)−C(5)−C(20)	120.23(14)	N(11)−C(12)−C(13)	123.46(16)
C(4)−C(5)−C(20)	122.33(14)	C(12)−C(13)−C(14)	118.69(16)
C(5)−C(6)−C(7)	120.94(15)	C(15)−C(14)−C(13)	118.91(15)
C(6)−C(7)−C(2)	120.18(14)	C(14)−C(15)−C(10)	118.64(15)
O(1)···N(11a) (intermol.)	2.90	O(1)···N(8) (intramol.)	2.71

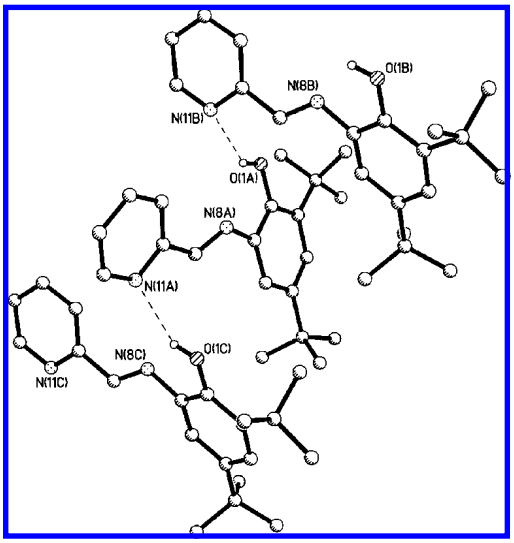

Figure 3. Molecular structure of the 2,6-di-*tert*-butyl-substituted ligand $HL^{t\text{-}Bu}$.

(18) Young, A. T.; Martynov, V.; Padmore, H. A. *J. Electron Spectrosc. Relat. Phenom.* **1999**, *103*, 885.
(19) Funk, T.; Friedrich, S.; Young, A.; Arenholz, E.; Cramer, S. P. *Rev. Sci. Instrum.* **2002**, *73*, 1649.
(20) Jia, J. J.; Callcott, T. A.; Yurkas, J.; Ellis, A. W.; Himpsel, F. J.; Samant, M. G.; Stöhr, G.; Ederer, D. L.; Carlisle, J. A.; Hudson, E. A.; Terminello, L. J.; Shuh, D. K.; Perera, R. C. C. *Rev. Sci. Instrum.* **1995**, *66*, 1394–1397.

the O K edge and 639.1 eV for the Mn L_3 edge, with an overall resolution (beamline plus spectrometer) set to around 1 eV for the XES measurements.

The complementary XPS measurements were performed at the Department of Physics, University of Osnabrück, Osnabrück, Germany, using a PHI 5600CI multitechnique spectrometer with monochromatic Al Kα = 1486.6 eV radiation of 0.3 eV at full-width at half-maximum. The overall resolution of the spectrometer is 1.5% of the pass energy of the analyzer, 0.35 eV in the present case. The XES and XPS measurements were performed at room temperature.

2.2. Theoretical Section. 2.2.1. DFT Calculations. The electronic structure calculations have been done within the density functional theory (DFT) paradigm, technically using the Siesta calculation method[21] and band structure code.[22] This implementation uses norm-conserving pseudopotentials, which were in our case generated within the Troullier−Martins scheme.[23] The pseudopotential for manganese has been constructed in the $4s^13p^63d^54f^0$ configuration of the valence states, with corresponding pseudoionization radii 2.00, 1.90, 1.90, and 1.50 Bohr in s through f channels. The parameters of other pseudopotentials were as follows (charge configuration followed by the corresponding radius in Bohr): H $1s^1(1.25)2p^0(1.25)3d^0(1.25)4f^0(1.25)$; C $2s^2(1.25)2p^2(1.25)3d^0(1.25)$-$4f^0(1.25)$; N $2s^2(1.25)2p^3(1.25)3d^0(1.25)4f^0(1.25)$; O $2s^2(1.15)2p^4$-$(1.15)3d^0(1.15)4f^0(1.15)$.

As for (atom-centered and strictly confined) basis functions, they were constructed as pseudoatomic orbitals for given pseudopotentials, see, e.g., refs 24 and 25. They have been taken in (at least) double-ζ quality, adding polarization orbitals for O and N (which are responsible for the chemical bonding with Mn) and extending up to triple-ζ in the Mn 3d channel (and adding polarization orbitals to Mn 4s). The spin-density isosurface plots were prepared with the *XCrySDen* software.[26]

2.2.2. Multiplet Calculations. The XAS and MCD line shapes of the Mn $L_{2,3}$ edges were simulated using the TT multiplet simulation program.[27,28] First, the energy levels of the initial ($2p^63d^5$) and final ($2p^53d^6$) states were calculated in spherical (O_3) symmetry. The parameters include the spin−orbit coupling of the 2p core and 3d valence band electrons, the 3d3d as well as the 2p3d Slater integrals in the initial and final states, which are summarized in Table 3. The d−d and p−d integrals were reduced to 90% of the values[29] shown in the table, whereas the spin−orbit parameters were not reduced. Then a cubic crystal field (O_h symmetry) of 0.6 eV strength and an internal exchange field of 0.05 eV were considered in the crystal-field approach. Finally admixtures of other configurations, namely, a charge-transfer configuration $3d^6\underline{L}$, were considered by performing additional monopole calculations for the initial (between $2p^63d^5$ and $2p^63d^6\underline{L}$) and final (between $2p^53d^6$ and $2p^53d^7\underline{L}$) states. The energy difference between the two configurations $E(2p^63d^5) - E(2p^63d^6\underline{L})$ = Δ was set to 9.0 eV, which corresponds to the value found for MnO.[30] For a comparison with the experiment, the lifetime broadening of the 2p core hole and the resolution of the spectrometer were taken into account.

Table 3. Slater Integrals Used for the Multiplet Simulations of the Mn $L_{2,3}$ XA and MCD Spectra[a]

	$2p^63d^5$ initial state	$2p^53d^6$ final state	$2p^63d^6\underline{L}$ initial state	$2p^53d^7\underline{L}$ final state
Slater Integrals				
F^2_{3d3d}	10.316	11.155	9.073	9.972
F^4_{3d3d}	6.414	6.943	5.591	6.157
F^2_{2p3d}		6.321		5.653
G^1_{2p3d}		4.606		4.059
G^3_{2p3d}		2.618		2.305
Spin−Orbit Coupling				
LS_{2p}		6.846		6.847
LS_{3d}	0.040	0.053	0.035	0.046

[a] For the calculations, the d−d and p−d integrals were reduced to 90% of the values shown in the table, whereas the spin−orbit parameters were not reduced.

3. Results and Discussion

3.1. Molecular Structures of $HL^{t\text{-}Bu}$ and $[MnL^{CH_3}_2]$. The ligand 2-hydroxyphenyl(2-pyridylmethaneimine), HL^R, was prepared according to a modified procedure reported in the literature by the Schiff base condensation of 2-pyridylaldehyde (or its 2-methyl derivative) and 2-aminophenol (or its 2,6-di-*tert*-butyl derivative). The purity of the ligand was checked by liquid chromatography to be ca. 99.0%. The IR, ^{1}H NMR, and MS results are in agreement with the literature data, and hence no further discussion is necessary. To gain insight into the metrical parameters of the ligand, we have determined the structure of the ligand in its di-*tert*-butyl form by X-ray diffractometry. The structure of the ligand $HL^{t\text{-}Bu}$ in the solid state is shown in Figure 3.

The X-ray analysis of single crystals of $HL^{t\text{-}Bu}$, performed at 100 K, reveals a strong intramolecular hydrogen bonding between the phenolic hydroxyl group O(1) and the imine nitrogen N(8) with O(1)H···N(8) at 2.71 Å, whereas an intermolecular hydrogen bonding between the O(1) and the pyridine nitrogen N(11a) of the neighboring molecule at O(1)···N(11a) 2.90 Å can be envisaged. It is noteworthy that the C(7)−N(8) distance with 1.418(2) Å is of double-bond character, as expected. The bond lengths and angles for $HL^{t\text{-}Bu}$, listed in Table 2, seem reasonable and do not warrant any special discussion. Methanolic solutions of HL^R were treated with manganous(II) salts, in a 2:1 ratio under argon in the presence of a base, and the solution was heated to reflux to yield the mononuclear precursor **1**. In the IR spectrum of the complex, the OH stretching vibrations of the free ligand are missing, indicating the coordinated phenoxide groups. EI-MS spectrometry was helpful in detecting the mononuclear nature for $[MnL^H_2]^0$. The molecular ion peak at *m*/*z* 449 (81.7%), together with the fragments at *m*/*z* 371 (49.2%), 252 (100%), 196 (68.9%), 173 (24.2%), 120 (35%), and 109 (26.3%), clearly indicates the identity of the precursor $[MnL^H_2]^0$. Because the manganese precursor,

(21) Soler, J. M.; Artacho, E.; Gale, J. D.; García, A.; Junquera, J.; Ordejón, P.; Sánchez-Portal, D. *J. Phys.: Condens. Matter* **2002**, *14*, 2745–2779.
(22) URL: http://www.uam.es/siesta.
(23) Troullier, N.; Martins, J. L. *Phys. Rev. B* **1991**, *43*, 1993–2006.
(24) Junquera, J.; Paz, Ó.; Sánchez-Portal, D.; Artacho, E. *Phys. Rev. B* **2001**, *64*, 235111.
(25) Sánchez-Portal, D.; Artacho, E.; Soler, J. M. *J. Phys.: Condens. Matter* **1996**, *8*, 3859–380.
(26) Kokalj, A. *Comput. Mater. Sci.* **2003**, *28*, 155.
(27) de Groot, F. M. F. *J. Electron Spectrosc. Relat. Phenom.* **1994**, *67*, 529.
(28) de Groot, F. M. F. *Coord. Chem. Rev.* **2005**, *249*, 31.
(29) Uozumi, T.; Okada, K.; Kotani, A.; Zimmermann, R.; Steiner, P.; Hüfner, S.; Tezuka, Y.; Shin, S. *J. Electron Spectrosc. Relat. Phenom.* **1997**, *83*, 9.
(30) Okada, K.; Kotani, A. *J. Phys. Soc. Jpn.* **1992**, *61*, 4619.

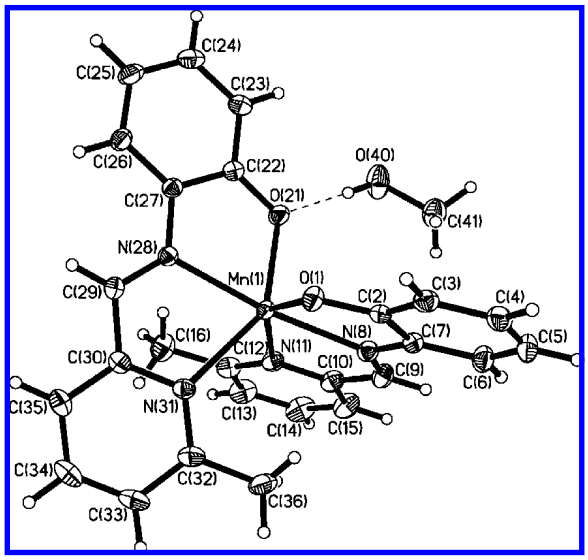

Figure 4. ORTEP diagram of the mononuclear **1**.

Table 4. Selected Bond Lengths (Å) and Angles (deg) for **1**

Mn(1)−O(1)	2.1197(9)	N(8)−C(9)	1.2837(15)
Mn(1)−O(21)	2.1485(8)	N(28)−C(29)	1.2860(15)
Mn(1)−N(8)	2.2249(10)		
Mn81)−N(28)	2.2287(10)		
Mn(1)−N(31)	2.3283(10)		
Mn(1)−N(11)	2.4012(10)		
O(1)−Mn(1)−O(21)	101.43(4)	N(8)−Mn(1)−N(31)	114.39(4)
O(1)−Mn(1)−N(8)	75.55(4)	N(28)−Mn(1)−N(31)	71.61(4)
O(21)−Mn(1)−N(8)	100.38(3)	O(1)−Mn(1)−N(11)	145.06(3)
O(1)−Mn(1)−N(28)	99.80(3)	O(21)−Mn(1)−N(11)	93.71(3)
O(21)−Mn(1)−N(28)	74.56(3)	N(8)−Mn(1)−N(11)	70.82(4)
N(8)−Mn(1)−N(28)	172.51(4)	N(28)−Mn(1)−N(11)	114.60(4)
O(1)−Mn(1)−N(31)	96.02(3)	N(31)−Mn(1)−N(11)	89.47(4)
O(21)−Mn(1)−N(31)	144.04(3)		

prepared in a different way, has been reported[31] without any structural parameters, we grew single crystals of the compound with the 2-methyl derivative (Figure 2) of the ligand (HL^{CH_3}) for the structure determination. Figure 4 shows the ORTEP diagram for the structure of compound $[Mn_2L^{CH_3}]$. Selected bond lengths and angles are summarized in Table 4.

The overall geometry around the manganese atom Mn(1) is best described as a distorted octahedron with two cis-positioned oxygens O(1) and O(21) of the phenolate groups arising from two different ligands; the two tridentate ligands are found to be almost planar and perpendicular to one another. A methanol molecule of crystallization is hydrogen bonded to O(21) with O(21)···HO(40) at 2.702 Å. The pyridine and the phenyl rings of the ligands are not strictly parallel, with an average separation of 4.3 Å. There are no other remarkable features in the structure of $[Mn_2L^{CH_3}]^0$. The bond lengths with average Mn(1)−O at 2.134(1) and Mn(1)−N at 2.296 Å are consistent with those typical for high-spin manganese(II) compounds.[32] This assignment is also complemented by the magnetic susceptibility measurements (20−290 K), which exhibit a temperature-independent

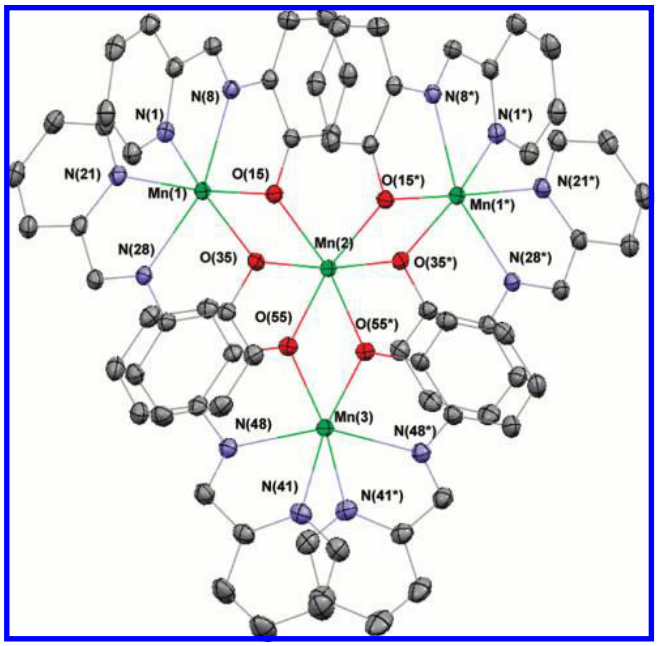

Figure 5. Molecular structure of the cation in complex **2**.

Table 5. Selected Bond Lengths (Å) and Angles (deg) for **2**

Mn(1)···Mn(2)	3.286	Mn(3)···Mn(2)	3.322
Mn(1)−O(15)	2.139(14)	Mn(2)−O(55)	2.17(14)
Mn(1)−O(35)	2.144(14)	Mn(2)−O(55)	2.17(14)
Mn(1)−N(28)	2.214(2)	Mn(2)−O(15)	2.181(14)
Mn(1)−N(8)	2.223(2)	Mn(2)−O(15)	2.181(14)
Mn(1)−N(1)	2.288(2)	Mn(2)−O(35)	2.186(14)
Mn(1)−N(21)	2.313(2)	Mn(2)−O(35)	2.186(14)
Mn(3)−O(55)	2.141(14)	N(50)−Mn(3)−N(42)	143.56(11)
Mn(3)−O(55)	2.247(14)	N(10)−Mn(1)−N(2)	141.7(12)
Mn(3)−N(48)	2.226(2)	O(15)−Mn(1)−O(35)	82.00(5)
Mn(3)−N(48)	2.226(2)	O(55)−Mn(3)−O(55)	79.81(8)
Mn(3)−N(41)	2.337(2)	O(55)−Mn(2)−O(55)	78.55(7)
Mn(3)−N(41)	2.337(2)	O(15)−Mn(2)−O(15)	93.68(8)
		O(55)−Mn(2)−O(15)	168.54(5)
		Mn(1)−O(15)−Mn(2)	99.07(6)

magnetic moment μ_{eff} of 5.90 ± 0.02 μ_B, resulting from a high-spin d^5 electron configuration. The structure is comparable to the reported[33] $[Fe^{III}L^{H}_2]ClO_4 \cdot H_2O$ and $[Fe^{III}L^{H}_2]PF_6 \cdot CH_3OH$.

3.2. Molecular Structure of 2. The structure consists of discrete tetranuclear dications $[Mn_4L_6]^{2+}$, tetrafluoroborate anions, acetonitrile, and water as solvent molecules of crystallization. A view of the entire complex cation is given in Figure 5.

Relevant bond distances and angles are listed in Table 5. The complex cation in **2** can be described as three neutral $[MnL^{H}_2]^0$ units acting as bidentate ligands through the cis-disposed phenolate oxygens for the central Mn(2), yielding the central $Mn(2)O_6$ core. The three peripheral manganese atoms Mn(1), Mn(1*), and Mn(3) form an isosceles triangular arrangement with the centrally situated Mn(2) atom, as schematically shown in the left panel of Figure 10, with corresponding Mn−Mn distances. The labeling of corresponding interaction parameters (to be discussed below) is introduced in the right panel of Figure 10. The bridging plane

(31) Reddig, N.; Triller, M. U.; Pursche, D.; Rompel, A.; Krebs, B. *Z. Anorg. Allg. Chem.* **2002**, *628*, 2458.
(32) *Comprehensive Coordination Chemistry*; Wilkinson, G., Ed.; Pergamon: Oxford, U.K., 1987; Vol. *4*.
(33) (a) Hayami, S.; Gu, Z.; Shiro, M.; Einaga, Y.; Fujishima, A.; Sato, O. *J. Am. Chem. Soc.* **2000**, *122*, 7126. (b) Juhsz, G.; Hayami, S.; Sato, O.; Maeda, Y. *Chem. Phys. Lett.* **2002**, *364*, 164.

comprising the Mn_2O_2 atoms is strictly planar for Mn(3) due to the imposed 2-fold symmetry, whereas the mean deviation for the atoms involving Mn(1)O(35)Mn(2)O(15) is only 0.019 Å from the mean plane, thus lending the tetranuclear cation a propeller shape, as is also evidenced by the dihedral angles of 93.5° and 84.7° between the planes involving $Mn(2)Mn(3)O_2/Mn(2)Mn(1)O_2$ and $Mn(2)Mn(1)O_2/Mn(2)$-$Mn(1*)O_2$, respectively.

All apical manganese atoms, Mn(1), Mn(3), and Mn(1*), are coordinated to four nitrogen atoms [pyridine nitrogens N(1) and N(21) and azomethine nitrogens N(8) and N(28) for Mn(1)] and two phenolate oxygens, O(15) and O(35), resulting in a six-coordinated MnN_4O_2 core, which is attained by ligation of two deprotonated ligands to each of the manganese atoms Mn(1), Mn(3), and Mn(1*). Although Mn(1) and Mn(3) are crystallographically independent, their structural parameters are comparable. The Mn−N bond lengths, as expected, are longer than the corresponding Mn−O distances; on the other hand, Mn−N(pyridine) distances are longer than the Mn−N(azomethine) bond lengths. The Mn−O(phenoxide) at average 2.141 Å and the Mn−N at average 2.267 Å fall well within the ranges that are considered as normal covalent bonds for high-spin d^5 Mn^{II} ions and are very similar to those for the mononuclear **1**. All cis angles at the apical manganese centers deviate from the ideal 90°, with the smallest for Mn(1) and Mn(2) being 72.14(6) and 71.65(6)° for the cis angles N(8)−Mn(1)−N(1) and N(48)−Mn(3)−N(41), respectively, indicating large angular distortions of the coordination environments. The central manganese atom Mn(2) is surrounded by an almost perfect octahedron (maximum deviation of the twist angles between the octahedral faces being 6°) of six phenolato oxygen atoms O(15), O(35), and O(55) and their equivalents. The angle at the bridging phenolate oxygen, Mn−O(phenolate)−Mn, varies only between 98.75(6)° and 100.82(6)°. The Mn(2)−O distance of average 2.179 Å is significantly longer than the trivalent Mn−O distances, ca. 2.00 Å, indicating that Mn(2) is in a lower oxidation state than III+. That the central Mn(2) ion must be ascribed to a II+ (high-spin d^5) oxidation is borne out by the facts that (i) two tetrafluoroborate anions are present for maintaining the electroneutrality of the dicationic $[Mn_4L_6]^{2+}$ complex and (ii) the magnetic data can only be simulated by considering an $S_{Mn} = {}^5/_2$ for the central Mn(2) center. The molecules in the crystal are well-separated from each other, with the shortest Mn···Mn distance between neighboring complexes being 10.34 Å. The structural parameters are very similar to those reported[31,34] recently for $[Mn_4L_6](BPh_4)_2$ and $[Mn_4L_6]$-$(ClO_4)_2$ complexes.

3.3. Magnetic Susceptibility Measurements. Magnetic susceptibility data for the polycrystalline sample of the tetranuclear complex **2** were collected in the temperature range 2−290 K in an applied magnetic field of 1 T. The magnetic moment μ_{eff}/molecule for **2** of 11.75 μ_B ($\chi_M T$ = 17.257 cm^3 K mol^{-1}) at 290 K increases monotonically with decreasing temperature until the value of μ_{eff} = 12.428 μ_B ($\chi_M T$ = 19.31 cm^3 K mol^{-1}) is attained at 10 K, below which μ_{eff} decreases, reaching a value of 7.99 μ_B ($\chi_M T$ = 7.98 cm^3 K mol^{-1}) at 2 K. This temperature dependence indicates an overall ferromagnetic coupling. We use the Heisenberg spin Hamiltonian in the form

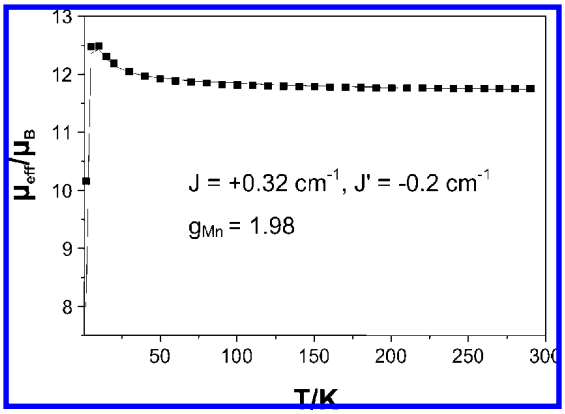

Figure 6. Plot of μ_{eff} vs temperature (T) for complex **2**.

$$H = -2J(S_2 \cdot S_1 + S_1^* \cdot S_2) - 2J' S_2 \cdot S_3 \qquad (1)$$

for an isotropic exchange coupling with $S_1 = S_2 = S_3 = S_1^* = {}^5/_2$ for **2**. The experimental data as the effective magnetic moments μ_{eff} vs temperature (T) are displayed in Figure 6. The experimental magnetic data were simulated using a least-squares computer program[35] with a full-matrix diagonalization approach, and the solid line in Figure 6 represents the simulation.

The magnetic analysis was carried out using a "two-J" model corroborating with two different prevailing bridging angles, Mn(1)−O−Mn(2) at 98.9° and Mn(2)−O−Mn(3) at 100.8°, depicted in Figure 10. In order to avoid overparametrization, we have set the single ion axial zero-field splitting, D, to zero and considered a unique isotropic g factor to evaluate the magnitude for the main parameters J and J' (see Figure 10).

The best-fit parameters are $J = +0.32$ cm^{-1} and $J' = -0.2$ cm^{-1} with $g_{Mn} = 1.98$. It is worth mentioning that the experimental data can also be simulated with a "one-J" model, leading to the fit parameters $J = J' = +0.2$ cm^{-1}, $g_{Mn} = 1.98$, and $\Theta = -0.2$ K. Because the nature of the signs of the exchange parameters corroborates with the Mn−O−Mn angle correlation and the Mn(2)···Mn(1) and Mn(2)···Mn(3) separations, we prefer the two-J model. To verify further the weak ferromagnetic interactions, variable-temperature variable-field (VTVH) measurements have been performed with 1, 4, and 7 T in the temperature range of 1.95−290 K, depicted in Figure 7.

The magnetization increases more rapidly than that of the uncoupled system with the saturation magnetization at 10 N$g\beta$, confirming the ferromagnetic interaction. At very low temperatures (2−3 K), there are small drops in the magnetization curves. That the saturation occurs much more slowly indicates the weakness and the presence of additional antiferromagnetic interactions, supporting further our "two-

(34) Gao, E.-Q.; Bai, S.-Q.; Zheng, H.; Yan, C.-H. *Inorg. Chem.* **2005**, *44*, 677.

(35) Bill, E. Max-Planck-Institut für Bioanorganische Chemie, Mülheim an der Ruhr, Germany, 2005.

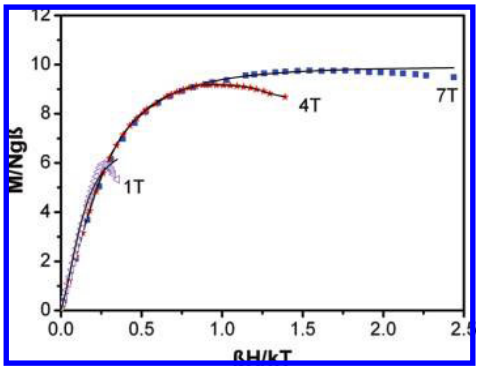

Figure 7. VTVH plots for complex **2** at 1, 4, and 7 T in the temperature range 2−290 K.

J' model. The parameters evaluated from the VTVH measurements are $J = +0.47$ cm^{-1}, $J' = -0.19$ cm^{-1}, and $g_{Mn} = 1.98$, which are very similar to those from the isofield measurements. So, the high-spin Mn^{II} centers with $S = {}^5/_2$ in **2** exhibit weak dominant ferromagnetic coupling, yielding a "high-spin" molecule with an $S_t = 10$ ground state. Because of the weak nature of the couplings, the molecule shows a complicated low-lying magnetic structure with the ground state not well-separated from the upper-lying states. Accordingly, the measured magnetization has more contributions from excited states of lower spins than from the ground-state spin. The above discussion is qualitatively valid, although we have ignored the zero-field-splitting effects. The magnetic behavior of **2** is similar to that reported for the analogous perchlorate salt, for which the authors used a "one-*J*" model together with the Weiss constant Θ (see above).[34] Because of negligible zero-field-splitting and intermolecular effects, magnetic moments extracted from XMCD measurements, to be discussed in the next section, can nicely be fitted by a Brillouin magnetization curve.

Exchange coupling constants in bis(μ-phenoxo)-bridged dimanganese(II) complexes published,[36] the number of which is much smaller than that of the diferric(III) analogues, have been found to be very small, lying in a small range of +0.2 to −1.88 cm^{-1}. The angle at the bridging phenoxide oxygen is expected to be important because this affects the nature of σ and π overlap between the manganese magnetic orbitals and the oxygen p_x, p_y, and p_z orbitals that mediate the exchange interaction. Such correlations between the exchange integral *J* and the M−O−M bridging angle[37,38] have been tried to be established for nickel(II) and copper(II), and the exchange interaction changes from antiferromagnetic to ferromagnetic at an angle, in most cases, below 98°. However, such magnetostructural analyses for the coupled manganese(II) and iron(III) complexes are far more intrinsically difficult because of the larger number of magnetic orbitals and exchange pathways involved for high-spin d^5 ions. Nevertheless, some semiempirical correlations between *J* and the bridging parameters have been attempted to be established for diiron(III) complexes[39] with phenoxo, alkoxo, and hydroxo bridges. It is notable that all diiron(III) complexes display antiferromagnetic interactions except one whose ferromagnetic coupling[40] has been attributed to the distortion of the coordination geometry, based on extended Hückel molecular orbital calculations. That the exchange interactions for the ferric complexes are much stronger than those for the isoelectronic manganese(II) complexes reflects the stronger covalency of the iron(III)−ligand bonds in comparison to that for the manganese(II)−ligand bonds. All reported six-coordinated bis(μ-phenoxo)-bridged dimanganese(II)[36] complexes exhibit weak antiferromagnetic interactions. However, only one five-coordinated bis(μ-phenoxo)-dimanganese(II) compound has been found to be very weakly ferromagnetically coupled ($J = +0.24$ cm^{-1}).[36a] Overall, the exchange parameter *J*, both ferro- and antiferromagnetic exchange, is found to be very low for all reported manganese(II) complexes including the present complex **2** because ineffective $t_{2g}-t_{2g}$ π pathways dominate the exchange; this weak nature is further augmented by the deviation of the metal geometry toward a trigonal prism (D_{3h}). Similar star-shaped $Fe^{III}{}_4O_6$ motifs[11,12,41] have been found to be antiferromagnetically coupled, yielding a ground state of $S_t = {}^{10}/_2$.

3.4. XMCD. The top panel of Figure 8 displays the X-ray absorption spectra (dotted lines) excited with 90% left and right circularly polarized light in an external magnetic field of 5 T.

The thinner solid lines represent the corresponding Mn^{2+} charge-transfer multiplet calculations. The spectra have been calculated at $T = 5$ K using the multiplet program developed by Thole, which is based upon the codes of Cowan and

(36) (a) Chang, H.-R.; Larsen, S. C.; Boyd, P. D. W.; Pierpont, C. G.; Hendrickson, D. N. *J. Am. Chem. Soc.* **1988**, *110*, 4565. (b) Yu, S.-B.; Wang, C.-P.; Day, E. P.; Holm, R. H. *Inorg. Chem.* **1991**, *30*, 4067. (c) Gallo, E.; Solari, E.; Re, N.; Floriani, C.; Chiesi-Villa, A.; Rizzoli, C. *J. Am. Chem. Soc.* **1997**, *119*, 5144. (d) Blanchard, S.; Blondin, G.; Riviére, E.; Nierlich, M.; Girerd, J.-J. *Inorg. Chem.* **2003**, *42*, 4568. (e) Alexiou, M.; Dendrinou-Samara, C.; Karagianni, A.; Biswas, S.; Zaleski, C. M.; Kampf, J.; Yoder, D.; Penner-Hahn, J. E.; Pecoraro, V. L.; Kessisoglou, D. P. *Inorg. Chem.* **2003**, *42*, 2185. (f) Coucouvanis, D.; Greiwe, K.; Salifoglou, A.; Challen, P.; Simolpoulos, A.; Kostikas, A. *Inorg. Chem.* **1988**, *27*, 593. (g) Qian, M.; Gou, S.; Chantrapromma, S.; Raj, S. S. S.; Fun, H.-K.; Zeng, Q.; Yu, Z.; You, X. *Inorg. Chim. Acta* **2000**, *305*, 83.

(37) (a) Crawford, V. H.; Richardson, H. W.; Wasson, J. R.; Hodgson, D. J.; Hatfield, W. E. *Inorg. Chem.* **1976**, *15*, 2107. (b) Hodgson, D. J. *Prog. Inorg. Chem.* **1975**, *19*, 173.

(38) (a) Nanda, K. K.; Thompson, L. K.; Bridson, J. N.; Nag, K. *J. Chem. Soc., Chem. Commun.* **1994**, 1337. (b) Halcrow, M. A.; Sun, J.-S.; Huffman, J. C.; Christou, G. *Inorg. Chem.* **1995**, *34*, 4167. (c) Clemente-Juan, J. M.; Chansou, B.; Donnadieu, B.; Tuchagues, J. P. *Inorg. Chem.* **2000**, *39*, 5515. (d) Mukherjee, S.; Weyhermüller, T.; Bothe, E.; Wieghardt, K.; Chaudhuri, P. *Eur. J. Inorg. Chem.* **2003**, 863. (e) Paine, T. K.; Rentschler, E.; Weyhermüller, T.; Chaudhuri, P. *Eur. J. Inorg. Chem.* **2003**, 3167. (f) Fondo, M.; Garca-Deibe, A. M.; Ocampo, N.; Sanmartin, J.; Bermejo, M. R.; Llamas-Saiz, A. L. *Dalton Trans.* **2006**, 4260. (g) Chaudhuri, P.; Wagner, R.; Weyhermüller, T. *Inorg. Chem.* **2007**, *46*, 5134.

(39) (a) Gorun, S. M.; Lippard, S. *J. Inorg. Chem.* **1991**, *30*, 1625. (b) Weihe, H.; Güdel, H. U. *J. Am. Chem. Soc.* **1997**, *119*, 6539. (c) Werner, R.; Ostrovsky, S.; Griesar, K.; Haase, W. *Inorg. Chim. Acta* **2001**, *326*, 78.

(40) Snyder, B. S.; Patterson, G. S.; Abrahamson, A. J.; Holm, R. H. *J. Am. Chem. Soc.* **1986**, *111*, 5214.

(41) (a) Barra, A. L.; Caneschi, A.; Cornia, A.; Fabrizi de Biani, F.; Gatteschi, D.; Sangregorio, C.; Sessoli, R.; Sorace, L. *J. Am. Chem. Soc.* **1999**, *121*, 5302. (b) Saalfrank, R. W.; Scheurer, A.; Bernt, I.; Heinamann, F. W.; Postnikov, A. V.; Schünemann, V.; Trautwein, A. X.; Alam, M. S.; Rupp, H.; Müller, P. *Dalton Trans.* **2006**, 2865. and references cited therein.

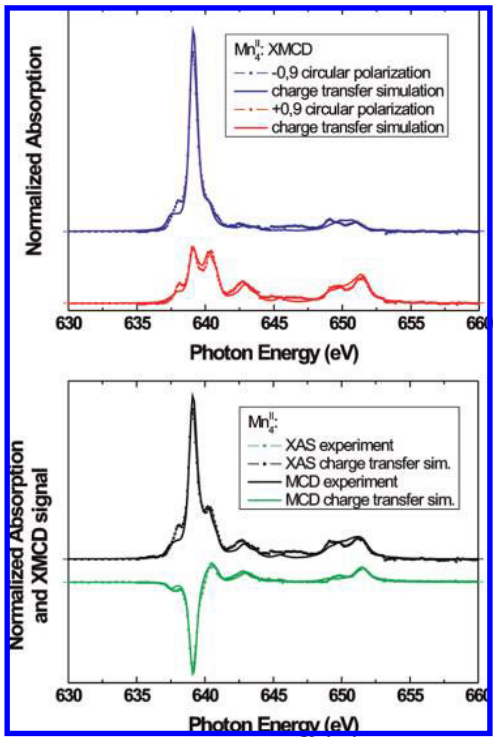

Figure 8. Left and right polarized X-ray absorption spectra recorded in an external magnetic field of 5 T at a temperature of 5 K (top panel) and the corresponding XAS and XMCD signals (bottom panel). The XMCD signal has been normalized to 100% circular polarization. The experimental results are compared with corresponding charge-transfer mulitiplet calculations; we used an octahedral crystal field of 0.6 eV strength.

Butler.[27,28,42,43] In a first step, the Slater integrals and the spin−orbit couplings were calculated in spherical symmetry, these are summarized in Table 3. Then a cubic crystal field (10 Dq) and an external magnetic field of $\mu_B H = 0.05$ eV along the z direction were applied. Finally, the mixing of the $3d^5$ with $3d^6$ charge-transfer states was considered by introducing the energy difference between the two configurations, $\Delta = E(3d^6\underline{L}) - E(3d^5)$. Scanning through the parameter room of 10 Dq and Δ, we find an almost perfect agreement between the experimental and theoretical spectra with 10 Dq = 0.6 eV and Δ = 9.0 eV (Figure 8). In order to enable a direct comparison between experiment and simulation, the calculated spectra have been normalized to 90% circular polarization plus 10% z-polarized absorption ($q = 0$ transitions), for both left and right circularly polarized light. Furthermore, the calculated spectra have been convoluted with the overall experimental resolution (lifetime broadening + spectrometer resolution).

The bottom panel of Figure 8 shows the sum (XAS) and the difference (MCD) of the dichroic XAS spectra displayed in the top panel of Figure 8. The Mn $L_{2,3}$ XAS consists of a shoulder at about 638.0 eV, a main peak at 639.0 eV, and two further shoulders located around 640 and 642.5 eV, respectively. These features represent the excitations originating from the Mn $2p_{3/2}$ core level, followed by the excitations from the Mn $2p_{1/2}$ core level around 649.0 and 651.5 eV. The XAS, sensitive to the chemical environment of the absorbing atom, clearly reflects a pretty ionic Mn^{2+} valence state. From the charge-transfer multiplet simulations, we can extract a 93.8% $3d^5$ and 6.2% $3d^6\underline{L}$ configuration. It is noted that, although only ~6% charge-transfer states are involved, the charge-transfer multiplet simulation leads to a significant improvement as compared to a simple ligand-field simulation. This especially accounts for the intensity and energetic position of the shoulders between the Mn L_2 and Mn L_3 main peaks.

Moreover, XAS is a direct probe of the local crystal-field environment (strength) around the absorbing manganese atom; with the help of our charge-transfer multiplet calculations, we determine an octahedral crystal field of 0.6 eV strength. In spite of the structural characterization revealing the octahedral environment to be somewhat distorted, this is a good estimation of the average crystal-field strength, present around the manganese atoms. In order to extract the spin and orbital magnetic moments, we applied the sum rules as developed by Chen et al.[13] From the experimental data, we evaluate a spin moment $m_{spin} = 12.35\ \mu_B$/fu (3.09 μ_B/manganese atom) and an orbital moment of $m_{orb} = 0.36\ \mu_B$/fu (0.09 μ_B/atom). From the ground state of the charge-transfer multiplet calculations, we calculate $m_{spin} = 5.00\ \mu_B$/atom and $m_{orb} = 0.00\ \mu_B$/atom. If we apply the sum rules to the theoretical spectra, we extract $m_{spin} = 3.59\ \mu_B$/atom and $m_{orb} = 0.02\ \mu_B$/atom. This implies an error in the spin sum rule due to the effect of the core hole Coulombic interactions that mix the character of the L_3 and L_2 edges. This error is estimated from the calculations to be 3.59/5.00 = 0.72. This value is close to that obtained for a crystal-field calculation of a Mn^{2+} ion with 10 Dq = 1.5 eV.[44] It is noted that the variations of these values (as well as the error) with 10 Dq are small and that in the case of a high-spin $3d^5$ ground state also the spin−orbit coupling has no influence on the sum rule.[45]

This correction factor is only valid if the L_3 to L_2 splitting is sufficiently large so that no considerable L_3−L_2 mixing is present[44] as in the present case. Considering the sum rules and the correction factor for the spin sum rule, we yield a spin moment of $m_{spin} = 17.65\ \mu_B$/fu and a small orbital moment of $m_{orb} = 0.36\ \mu_B$/fu for the "manganese star" molecule under an external field of 5 T and at a temperature of 5 K.

Moreover, we analyzed the magnetization behavior by performing XMCD measurements at a number of different external fields (Figure 9). Table 6 lists the results. Because we have found in section 3.3 that effects from zero-field splitting or intramolecular interactions are negligible, one can nicely extract the (theoretical) magnetization curve by fitting the experimental data with the help of a Brillouin function using an uncoupled $S = {}^5/_2$ as the spin ground state for the "manganese star" molecule (Figure 9).[34,46] The experimental data are in good agreement with a Brillouin

(42) Butler, P. H. *Point Group Symmetry, Applications, Methods and Tables*; Plenum: New York, 1981.
(43) Cowan, R. D. *The Theory of Atomic Structure and Spectra*; University of California Press: Berkeley, CA, 1981.
(44) Termamura, Y.; Tanaka, A.; Jo, T. *J. Phys. Soc. Jpn.* **1996**, *65*, 1053.
(45) de Groot, F.; Kotani, A. *Core Level Spectroscopy of Solid*; Taylor & Francis: London, 2008.
(46) Neese, F.; Solomon, E. I. *Inorg. Chem.* **1999**, *38*, 1847.

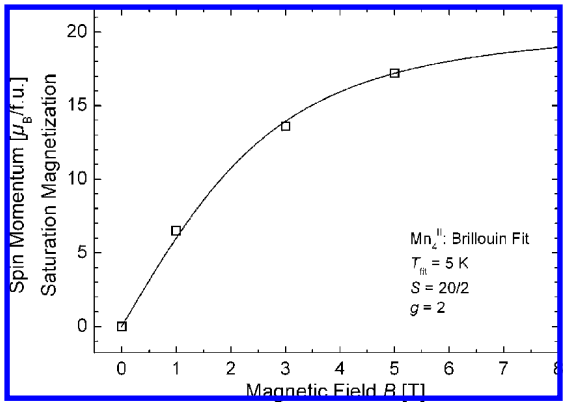

Figure 9. Experimental data of the spin magnetic moment determined at external fields of 0, 1, 3, and 5 T (squares) and the fit of the magnetization by the Brillouin function (solid line). We fitted the magnetization curve by means of a Brillouin function.

Table 6. Spin and Orbital Moments As Obtained from the Experimental XMCD Data at External Magnetic Field Strength

1 T	3 T	5 T
$m_{spin} = 6.51\ \mu_B$/fu $m_{orb} = 0.10\ \mu_B$/fu	$m_{spin} = 13.62\ \mu_B$/fu $m_{orb} = 0.17\ \mu_B$/fu	$m_{spin} = 17.15\ \mu_B$/fu $m_{orb} = 0.36\ \mu_B$/fu

function considering a simple ionic state for the Mn^{2+} ions and a sample temperature of 5 K during the XMCD experiments. Thus, this result is also a nice manifestation of the weak coupling constants between the central ion and the three outer ions, leading to an overall weak ferromagnetic coupling in quite moderate external magnetic fields. See also sections 3.3 and 3.4 (magnetic measurements and ab initio theory).

3.5. Electronic Structure Calculations of the $Mn^{II}_4O_6$ Core. In setting up our calculations, we allowed different orientations of the spin moments at manganese atoms; all magnetic solutions turned out to be stable, with nearly identical values of local magnetic moments and charges (according to the Mulliken population analysis). Moreover, the local densities of states (LDOSs) calculated for different magnetic configurations are almost indistinguishable. This reveals a high enough localization of the electronic states that are responsible for magnetic behavior (mostly Mn 3d, with a slight admixture of O or N 2p) on manganese centers. Obviously, there is a difference in LDOSs at the central and peripheral manganese atoms, which are in different chemical environments. Moreover, among the peripheral manganese atoms, which are structurally (topologically) identical, one differs from two others because of the specific packing of molecular units in the crystal and a slight difference in the bond lengths resulting from that. This means that each star-shaped molecule does not quite have a 3-fold symmetry axis but rather a variation of a mirror-plane symmetry. Correspondingly, for the sake of fitting the results to the Heisenberg (or any other) model, one should allow two distinct center−peripheric (strong) couplings and, in principle, two peripheric−peripheric (weak) ones.

Table 7 gives the data for the total (overall orbitals) Mulliken occupation numbers and HOMO−LUMO energies in both spin channels, for all magnetic configurations considered, in the nominal (experimental determined) structure. The total energies are also given, relative to the lowest one (that for the situation with the central spin opposite to three others). The configurations are numbered by combinations of U and D letters, according to up or down spin setting on four manganese atoms 1, 2, 3, and 1* (see Figure 10). We consider only eight nonequivalent configurations; the other eight can be obtained by inverting the spins on all atoms.

Table 7. Local Magnetic Moments (in μ_B) on Manganese Atoms (1, 2, 3, and 1*), Total Magnetic Moment per Molecule M, HOMO−LUMO Energy Difference, and Total Energies (Relative to the Ground-State Configuration) for Different Magnetic Configurations of the "Manganese-Star" Molecule

config	1	2	3	1*	M (μ_B)	HOMO−LUMO (eV)	ΔE_{tot} (meV)
UUUU	4.68	4.71	4.69	4.68	20	0.404	12.20
DUUU	−4.68	4.70	4.69	4.68	10	0.439	7.38
UDUU	4.68	−4.70	4.69	4.68	10	0.523	0.00
UUDU	4.68	4.70	−4.69	4.68	10	0.424	8.90
UUUD	4.68	4.70	4.69	−4.68	10	0.440	7.33
DDUU	−4.68	−4.70	4.69	4.68	0	0.453	4.36
DUDU	−4.68	4.70	−4.69	4.68	0	0.459	4.42
DUUD	−4.68	4.70	4.69	−4.68	0	0.519	2.64

The fact that the local magnetic moments are almost insensitive to the orientation is an argument in favor of the validity of the Heisenberg model, even if a priori we cannot be sure that the correction terms to it are not important. As a spin value to use in the Heisenberg fit, we took the nominal value $S = {}^5/_2$ because this is exactly a change by 10 μ_B/molecule accompanying an inversion of a single manganese spin. All magnetic configurations studied have a pronounced band gap and are therefore easily identifiable as corresponding to an inversion of $S = {}^5/_2$ spins. The difference from the nominal number ($m_{Mn} \sim 4\ \mu_B$), following from the Mulliken populations, merely indicated that this "rigid" moment is not fully localized at the manganese site but involves some admixture from the ligand states. For the $S = {}^5/_2$ spin, one can be relatively sure about the unimportance of orbital moment and anisotropic exchange terms, even if this would, in principle, need to be checked.

The least-squares fit to the Heisenberg Hamiltonan (eq 1) with four Heisenberg exchange parameters as marked in the right panel of Figure 10, from seven energy differences of Table 7 yields the following values: $J = -2.26$ K, $J' = -1.38$ K, $J_1 = -0.08$ K, and $J'_1 = -0.03$ K (-1.57, -0.96, -0.06, and -0.02 cm^{-1}, respectively). Whereas all interaction parameters are antiferromagnetic, the J_1 and J'_1, which account for "second-neighbor" manganese interaction, are, in fact, negligible. Of the remaining two, the J that couples the central manganese to its nearest peripheric counterpart is dominant.

Comparing these results with the above parameters from the magnetization fit (+0.32 and −0.2 cm^{-1} for J and J',

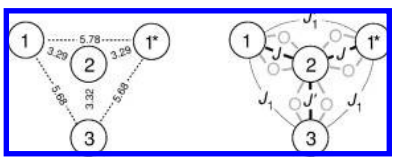

Figure 10. Left panel: distances (in Å) between manganese atoms in the "manganese star" molecule. Right panel: labeling of corresponding different exchange parameters.

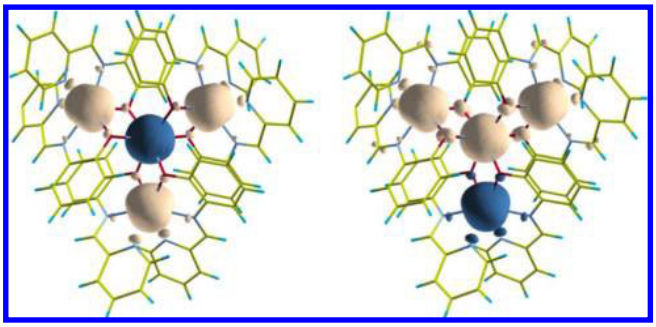

Figure 11. Isosurfaces of spin density corresponding to ±0.05 e/Å^3 for UDUU (left panel) and UUDU (right panel) configurations. Positive and negative magnetic density is shown by two colors.

respectively), one marks opposite signs of the dominant interaction, as they follow from the experiment and theory. This is unusual because typically the DFT (in whatever practical scheme) is accurate enough to yield not only the sign but also the order of magnitude of exchange parameters, overestimating their value, however, by a factor of 3−5 (due to an underestimation of correlation effects within strongly localized d shells). This "consistency" in the order of magnitude between experiment and theory holds also in the present case: the interaction parameters calculated for the "manganese star" molecule are by a factor of ∼50 smaller than those estimated for the "ferric star",[11,12] a $Fe^{III}[Fe^{III}L_2]_3$ star-type molecule with similar 3d ion topology and bridging as the present one but different types of ligands L.

The experimental situation (J positive and of larger absolute value than the negative J') would favor, among the configurations listed in Table 7, the UUDU one. According to the DFT, this configuration is almost degenerate with the other two, in which one or another of the peripheric spins is set antiparallel to three others, ferromagnetically coupled. The energy separation from the DFT ground state (with the central spin inverted) is merely ∼8 meV. A possible explanation of the experiment vs DFT controversy could be that strong interaction of DUUU, UUDU, and UUUD states yields a mixed ground state, whose energy is lower than that of the pure UDUU state.

Figure 11 shows spin-density isosurfaces in the UDUU (nominal DFT ground state) and UUDU (its apparent competitor, according to experiment) configurations. The spin-density level is chosen in the figure to be very low in order to show the spilling of magnetic density from manganese over neighboring oxygen and nitrogen atoms. Isosurfaces for a slightly higher spin-density level would have been nearly spherical, centered at the manganese atoms. One sees that the spilling of the local magnetic moment from manganese onto its nitrogen neighbors is not affected by the magnetic configuration. This visual impression from Figure 11 is confirmed by the Mulliken population analysis for nitrogen magnetic moments, which are on the order of 0.015−0.030 μ_B and stable (changing from one configuration to the other) within 20%. The Mn(2)−Mn(3) bridging oxygens also maintain their induced local moment (of ∼0.02 μ_B, parallel to that of the peripheric manganese). On the contrary, the magetic moments induced on Mn(1)−Mn(2) oxygen bridge atoms within the "ferromagnetic" Mn(1)−Mn(2)−Mn(1*) fragment of UUDU are 2 times larger (∼0.04 μ_B) than those in the corresponding "ferrimagnetic" block of the UDUU configuration. An intriguing question arises of whether this apparently different magnetization of bridge oxygen atoms could ever be probed by experimental techniques. The "differently itinerant" character of the magnetic density in two compared configurations, UDUU vs UUDU, may also play a role in determining their relative stability. An argumentation here may be that the DFT generally underestimates the tendency toward charge localization in similar systems; therefore, the level of the "DFT error" can be different in slightly more localized and slightly less localized situations. This can be important here, in view of very small energy differences between competing configurations.

Another point to consider, in view of rather small values of exchange parameters J, is their possible dependence on the details of the crystal structure, in both experiment and theory. In order to further analyze a competition between UDUU and UUDU configurations, we allowed independent structural relaxation in these two magnetic states. This led to an overall energy lowering by ∼30 eV/molecule, maintaining, however, the energy difference between two separately relaxed cases within 15 meV. On the average, we found good agreement with experimentally measured structures: the "long" Mn(1,1*)−Mn(2) distances are 3.285 Å (UUDU-relaxed) and 3.281 Å (UDUU-relaxed), to be compared to the measured 3.286 Å; the "short" Mn(3)−Mn(2) distances are 3.351, 3.350 and 3.322 Å, correspondingly, and the Mn−O−Mn angles (≈99° for the short bridges and ≈101° for the long bridges) agree within 1.5° throughout the three structures. Still, the minute structural differences produce markedly different exchange constants: $J \sim -0.6$ K and $J' \sim -0.1$ K, as estimated from the energy differences (similar to those in Table 7) in the UUDU-relaxed structure.

The obtained "scattering" of calculation data ($J \sim -2.2/-0.6$ K) can serve to estimate the "empirical" accuracy of the DFT treatment in our case, in addition to possible basic limitations of DFT, in the extraction of exchange interaction parameters. Our results show that, because magnetic interactions in the manganese star are quite weak, small variations of the crystal structure with temperature or in the magnetic field may have a non-negligible effect on the *definition* and *extraction* of the J parameters.

The LDOS (Figures 12 and 13) and spin density plots (Figure 11) discussed in the following are as obtained for the nominal DFT ground state (UDUU configuration).

Both figures reveal a fair amount of localization of the Mn 3d states, with weak but appreciable admixture to O 2p and N 2p states (that is responsible for binding the manganese atoms into a molecule). LDOS at two manganese sites have similarities, but the differences cannot be overlooked. The splitting into t_{2g} and e_g bands, particularly pronounced in the region of vacant states, is more net for (the central) Mn(2), which is in a more perfect octahedral environment, whereas that around Mn(1) is considerably distorted.

Figure 12 displays the calculated partial densities of states (pDOS) of Mn 3d, O 1s, and N 1s. These states are largely

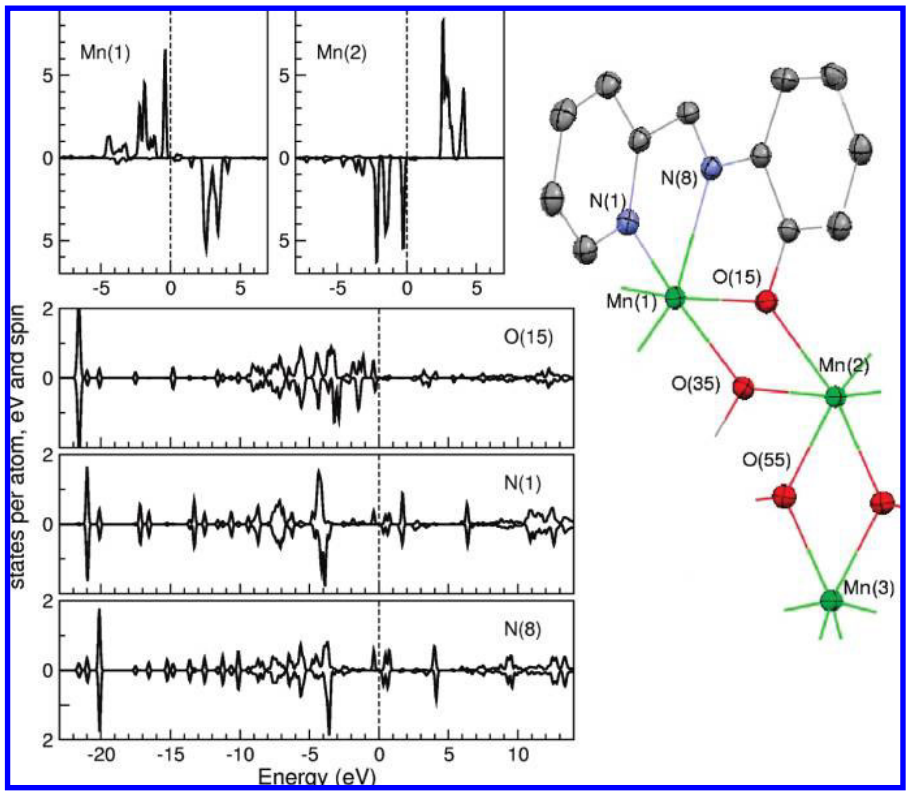

Figure 12. LDOSs of two manganese atoms and their 2p-type neighbors, calculated for the "manganese star" molecule in magnetic ground-state configuration UDUU. The numbering of atoms is shown in the inset.

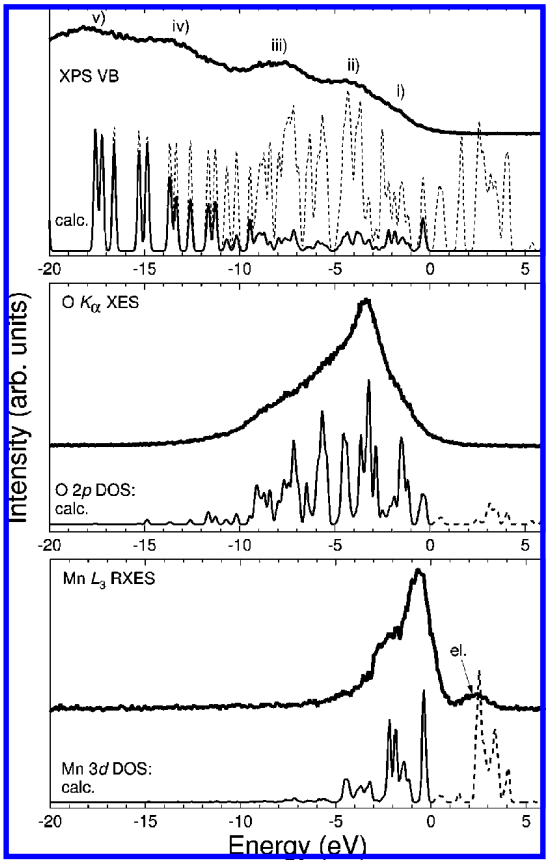

Figure 13. XPS valence band region (tDOS) compared to corresponding DFT calculations. The photoionization cross sections were taken into account for the solid line. Lower panels: XES spectra of the Mn L edge and O K edge in comparison with the calculated pDOSs.

energetically overlapping and form a common valence band going down to ∼−20 eV below the Fermi level. The calculated densities of states can be used to understand the XPS valence band and the Mn and O K XES results (Figure 13). The XES spectra have been brought to a common energy loss scale with the XPS valence band and the calculated densities of states. Thus, in Figure 13, the XES spectra reflect the element-specific partial densities of states. The XPS valence band comprises five distinct features labeled (i)−(v). A broad shoulder spans the range from the Fermi level to about −4 eV, followed by two local intensity maxima at around −5 and −9 eV. Finally bands (iv) and (v) are located between (−13) and (−16) eV and between (−18) and (−22) eV, respectively. With the help of the XES and the calculated pDOS, we can assign band (i) to Mn 3d states, namely, the spin-up states of the outer manganese ions and the spin-down states of the central manganese ion (see the top panel of Figure 12). Feature (ii) comprises also a considerable amount of Mn 3d states, which are likely hybridized with N 2p and O 2p states via charge transfer. However, the relatively weak overlap between the Mn L and O K XES indicates that charge-transfer effects are relatively weak in this compound. Finally, bands (iv) and (v) can be attributed to overlapping of O 2p and C 2s states and to N 2s states, respectively. This is in agreement with other observations pointing toward a weak covalency in the Mn−O bonds: the peaks in the Mn-DOS (of the central atom) are quite narrow and sparse, in contrast to more extended t_{2g}- and e_g-like subbands visible in the density of state of the central atom in the iron star.[12] Moreover, much smaller values of (super)exchange param-

eters in the manganese star, as compared to the iron star, also reveal a lower covalency in the former system.

4. Conclusions

We have studied an $S_t = 10$ high-spin molecule, namely, a star-shaped molecule with the $Mn^{II}_4O_6$ core, leading to a number of interesting results. A detailed X-ray structural analysis has been performed. Magnetic susceptibility measurements exhibit weak exchange coupling constants between the four Mn^{2+} ions. Thus, the magnetization measurements indicate complicated low-lying states in which the ground state is not well-separated, resulting from a dominant weak ferromagnetic coupling and a giant moment of up to 20 μ_B/fu. XMCD measurements reveal that almost the complete magnetic moment is located around the Mn^{2+} ions. Furthermore, we can conclude that a few charge-transfer states are present; charge-transfer multiplet calculations reveal 93.8% $3d^5$ and 6.2% $3d^6\underline{L}$ configurations. Finally, electronic structure calculations confirm that the interaction parameters are much smaller (by a factor of ~50) than those for related compounds like the "ferric star" molecule.[12] The "manganese star" is a very interesting prototype for polymetallic complexes with weak exchange coupling constants.

Acknowledgment. E. Arenholz and J. D. Denlinger are acknowledged for excellent technical support. We thank J. Schnack and M. Brüger for helpful discussions. Financial support by the Graduate College 695, Deutsche Forschungsgemeinschaft (Priority Program "Molecular Magnetism"), and the Ph.D. program (Lower Saxony) is gratefully acknowledged. Part of the work was performed at the ALS, which is supported by the U.S. Department of Energy under Contract DE-AC03-76SF00098.

IC7023007

Publication H10

[**H10**] M. Prinz, K. Kuepper, C. Taubitz, M. Raekers, B. Biswas, T. Weyhermüller, M. Uhlarz, J. Wosnitza, J. Schnack, A. V. Postnikov, C. Schröder, S. J. George, M. Neumann, and P. Chaudhuri. *A star-shaped heteronuclear $Cr^{III}Mn_3^{II}$ species and its electronic and magnetic structure: Spin frustration studied by XMCD, high field magnetic measurements and theoretical simulations*, Inorg. Chem. **49**, 2093 (2010), doi: 10.1021/ic9012119.

Inorganic Chemistry
Article

Inorg. Chem. **XXXX**, *XXX*, 000–000 **A**
DOI: 10.1021/ic9012119

A Star-Shaped Heteronuclear $Cr^{III}Mn^{II}_3$ Species and Its Precise Electronic and Magnetic Structure: Spin Frustration Studied by X-Ray Spectroscopic, Magnetic, and Theoretical Methods

Manuel Prinz,[†] Karsten Kuepper,[‡,♦] Christian Taubitz,[†] Michael Raekers,[†] Sumit Khanra,[§] Biplab Biswas,[§] Thomas Weyhermüller,[§] Marc Uhlarz,[∥] Joachim Wosnitza,[∥] Jürgen Schnack,[⊥] Andrei V. Postnikov,[#] Christian Schröder,[▽] Simon J. George,[○] Manfred Neumann,*[,†] and Phalguni Chaudhuri*[,§]

[†]*University of Osnabrück, Department of Physics, Barbarastrasse 7, D-49069 Osnabrück, Germany,* [‡]*Forschungszentrum Dresden-Rossendorf, Institut für Ionenstrahlphysik und Materialforschung, D-01314 Dresden, Germany,* [§]*Max-Planck-Institut für Bioanorganische Chemie, Stiftstrasse 34-36, D-45470 Mülheim an der Ruhr, Germany,* [∥]*Hochfeld-Magnetlabor Dresden, Forschungszentrum Dresden-Rossendorf, D-01314 Dresden, Germany,* [⊥]*Fakultät für Physik, Universität Bielefeld, Postfach 100131, D-33501 Bielefeld, Germany,* [#]*Laboratoire de Physique des Milieux Denses, Institut Jean Barriol, Paul Verlaine University, 1 Bd. Arago, 57078 Metz, France,* [▽]*University of Applied Sciences Bielefeld, Department of Engineering Sciences and Mathematics Wilhelm-Bertelsmann-Str. 10, D-33602 Bielefeld, Germany, and* [○]*Advanced Biological and Environmental X-ray Facility, Lawrence Berkeley National Laboratory, 1 Cyclotron Road, Berkeley, California 94720.* [♦] *Present address: University of Ulm, Department of Solid State Physics, Albert Einstein-Allee 11, 89069 Ulm, Germany.*

Received June 24, 2009

Molecular magnets incorporate transition-metal ions with organic groups providing a bridge to mediate magnetic exchange interactions between the ions. Among them are star-shaped molecules in which antiferromagnetic couplings between the central and peripheral atoms are predominantly present. Those configurations lead to an appreciable spin moment in the nonfrustrated ground state. In spite of its topologically simple magnetic structure, the $[Cr^{III}Mn^{II}_3(PyA)_6Cl_3]$ (**$CrMn_3$**) molecule, in which PyA represents the monoanion of *syn*-pyridine-2-aldoxime, exhibits nontrivial magnetic properties, which emerge from the combined action of single-ion anisotropy and frustration. In the present work, we elucidate the underlying electronic and magnetic properties of the heteronuclear, spin-frustrated **$CrMn_3$** molecule by applying X-ray magnetic circular dichroism (XMCD), as well as magnetization measurements in high magnetic fields, density functional theory, and ligand-field multiplet calculations. Quantum-model calculations based on a Heisenberg Hamiltonian augmented with local anisotropic terms enable us not only to improve the accuracy of the exchange interactions but also to determine the dominant local anisotropies. A discussion of the various spin Hamiltonian parameters not only leads to a validation of our element selective transition metal L edge XMCD spin moments at a magnetic field of 5 T and a temperature of 5 K but also allows us to monitor an interesting effect of anisotropy and frustration of the manganese and chromium ions.

1. Introduction

Magnetic materials comprising nanosized molecular building blocks have attracted large interest from several scientific disciplines. Chemically stable free radicals incorporated in purely organic compounds reveal long-range magnetic interactions at low temperatures. The flexibility available in carbon chemistry is exploited to synthesize such compounds. The most promising molecular magnets are polymetallic clusters, containing transition-metal ions bridged by molecular groups to mediate exchange interactions between the paramagnetic centers. Such interactions may result in ground states with a relatively large total spin (S).[1]

Compared to other transition metals, complexes containing manganese ions are especially often characterized by ground states with large magnetic moments, and this in

*To whom correspondence should be addressed. E-mail: chaudh@mpi-muelheim.mpg.de (P.C.), mneumann@uos.de (M.N.).

(1) (a) Blundell, S. J. *Contemp. Phys.* **2007**, *48*(5), 275–290. (b) Sessoli, R.; Gatteschi, D.; Caneschi, A.; Novak, M. *Nature* **1993**, *365*, 141–143. (c) Kahn, O. *Molecular Magnetism*; Wiley: Singapore, 1993.

conjunction with the presence of highly Jahn−Teller distorted Mn ions makes manganese clusters ideal candidates for high-spin molecules.[2] Due to the combined action of intramolecular exchange and large negative (easy-axis-type) magnetoanisotropy (D), the phenomenon of single-molecule magnetism (SMM) arises for such compounds, for which a significant barrier to thermally activated magnetization relaxation is characteristic.[3]

Very intensively investigated molecular magnets are the dodecanuclear complexes $[Mn_{12}O_{12}(O_2CR)_{16}(H_2O)_x]^{n-}$ ($n = 0, 1, 2$; $x = 3, 4$), but also manganese-containing polymetallic clusters with nuclearity ranging from 2 to 84 have been synthesized and reveal a large spin ground state and magnetoanisotropy.[4] The up to date highest blocking temperature is reached in hexanuclear manganese compounds.[5,6] Because these molecules display not only a magnetization hysteresis but also quantum tunneling of magnetization (QTM)[7,8] and quantum interference,[9] they are promising new materials for practical applications like ultradense magnetic data storage, quantum computing, or other interesting devices.[10−12] These properties are governed by the already mentioned magnetic anisotropy barrier of the magnetic core, which originates from the spin−orbit coupling in the paramagnetic ions in a high-spin state.[13] For a better understanding especially of the microscopic mechanisms, experimental and theoretical investigations in high-spin molecules are required.

Regarding the interplay of topology and exchange interactions in polynuclear high-spin clusters, another interesting effect can be observed: magnetic frustration which appears due to, e.g., triangular arrangements of antiferromagnetic exchange pathways.[14] Geometric frustration of interacting spins leads to a variety of fascinating phenomena[14−16] in low-dimensional and molecular magnetism: (1) a nontrivially, i.e., orbitally, degenerate ground state;[17,18] (2) many low-lying nonmagnetic excitations below the first triplet excitation;[19] (3) magnetization plateaus of the magnetization curve $M(B)$ at $T = 0$;[24] (4) large magnetization jumps at $T = 0$;[24] (5) (quantum) phase transitions at $T = 0$.[16] These phenomena do not occur in so-called bipartite spin systems, i.e., spin systems that can be divided into two sublattices.[20−22] Very prominent examples of geometrically frustrated spin systems exhibiting a rich spectrum of frustration phenomena are the giant Keplerate molecules.[23−25]

The present publication is devoted to the study of the electronic and revisited magnetic properties of an amazing manganese-containing high-spin molecule: the spin-frustrated star-shaped heterotetranuclear $Cr^{III}Mn^{II}_3$ complex.[26] The investigations of topologically similar, but chemically different, ferric and manganese star-shaped molecules show that there are star-shaped molecules in which predominately antiferromagnetic couplings of the central ion with its peripheral neighbors lead to an appreciable spin moment in the nonfrustrated ground state.[27−29] In spite of its topologically simple magnetic system, the $[Cr^{III}Mn^{II}_3(PyA)_6Cl_3]$ molecule (**$CrMn_3$**) exhibits the above-mentioned nontrivial magnetic properties, *single-ion anisotropy and frustration*, bearing interesting consequences for the chromium ion.

The tetranuclear complex contains three Mn^{2+} ions ($3d^5$, high-spin, $S = 5/2$) and a single Cr^{3+} ion ($3d^3$, high-spin, $S = 3/2$). The expected saturation magnetization is actually reached at a magnetic field of about 12 T at 1.8 K. The special form of the magnetization curve gives rise to the assumption that anisotropy and frustration effects are of great importance.

Here, we show that X-ray magnetic circular dichroism (XMCD) is a very powerful technique to study heteronuclear molecule-based magnets because of its generally high sensitivity to the local electronic structure, and moreover by the force of element and shell selectivity of the Mn^{2+} and Cr^{3+} ions in our case. Furthermore, XMCD is one of the rare experimental methods to determine element-selective

(2) Hendrickson, D. N.; Christou, G.; Ishimoto, H.; Yoo, J.; Brechin, E. K.; Yamaguchi, A.; Rumberger, E. M.; Aubin, S. M. J.; Sun, Z.; Aromi, G. *Mol. Cryst. Liq. Cryst.* **2002**, *376*, 301–313.
(3) Sessoli, R.; Gatteschi, D.; Hendrickson, D. N.; Christou, G. *MRS Bull.* **2000**, *25*, 66–71.
(4) See, for example: (a) Tasiopoulos, A. J.; Vinslava, A.; Wernsdorfer, W.; Abboud, K. A.; Christou, G. *Angew. Chem., Int. Ed.* **2004**, *43*, 2117–2121. (b) Miyasaka, H.; Clérac, R.; Wernsdorfer, W.; Lecren, L.; Bonhomme, C.; Sugiura, K.; Yamashita, M. *Angew. Chem., Int. Ed.* **2004**, *43*, 2801–2805. (c) Murugesu, M.; Wernsdorfer, W.; Raftery, J.; Christou, G.; Brechin, E. K. *Inorg. Chem.* **2004**, *43*, 4203–4209. (d) Milios, C. J.; Raptopoulou, C. P.; Terzis, A.; Lloret, F.; Vicente, R.; Perlepes, S. P.; Escuer, A. *Angew. Chem., Int. Ed.* **2003**, *43*, 210–212. (e) Wittick, L. M.; Murray, K. S.; Moubaraki, B.; Batten, S. R.; Spiccia, L.; Berry, K. J. *Dalton Trans.* **2004**, 1003–1011.
(5) Milios, C. J.; Vinslava, A.; Wernsdorfer, W.; Moggach, S.; Parsons, S.; Perlepes, S. P.; Christou, G.; Brechin, E. K. *J. Am. Chem. Soc.* **2007**, *129*, 2754.
(6) Carretta, S.; Guidi, T.; Santini, P.; Amoretti, G.; Pieper, O.; Lake, B.; van Slageren, J.; El Hallak, F.; Wernsdorfer, W.; Mutka, H.; Russina, M.; Milios, C. J.; Brechin, E. K. *Phys. Rev. Lett.* **2008**, *100*, 157203.
(7) Friedman, J. R.; Sarachik, M. P.; Tejada, J.; Ziolo, R. *Phys. Rev. Lett.* **1996**, *76*, 3830–3833.
(8) Thomas, L.; Lionti, F.; Ballou, R.; Gatteschi, D.; Sessoli, R.; Barbara, B. *Nature* (*London*) **1996**, *383*, 145.
(9) Wernsdorfer, W.; Sessoli, R. *Nature* **1999**, *284*(5411), 133–135.
(10) Verdaguer, M.; Bleuzen, A.; Train, C.; Garde, R.; Fabrizi de Biani, F.; Desplanches, C. *Philos. Trans. R. Soc. A* (*London*) **1999**, *357*, 2959.
(11) Leuenberger, M. N.; Loss, D. *Nature* (*London*) **2001**, *410*, 789.
(12) Ohkoshi, S.-I.; Hashimoto, K. *Electrochem. Soc. Interface* **2002**, *11*, 34.
(13) van Vleck, J. *Phys. Rev.* **1937**, *52*, 1178.
(14) Greedan, J. *J. Mater. Chem.* **2001**, *11*, 37.
(15) Schnack, J Molecular Magnetism. In *Lecture Notes in Physics 645*; Springer: Berlin, 2004; pp 155−194.
(16) Schröder, C.; Schmidt, H.-J.; Schnack, J.; Luban, M. *Phys. Rev. Lett.* **2005**, *94*, 207203.
(17) Dai, D; Whangbo, M.-H. *J. Chem. Phys.* **2004**, *121*(2), 672.
(18) Kahn, O. *Chem. Phys. Lett.* **1997**, *265*, 109–114.
(19) (a) Schmidt, R.; Richter, J.; Schnack, J. *J. Magn. Magn. Mater.* **2005**, *295*(2), 164–167. (b) Waldtmann, C.; Everts, H. U.; Bernu, B.; Lhuillier, C.; Sindzingre, P.; Lecheminant, P.; Pierre, L. *Eur. Phys. J. B* **1998**, *2*, 501. (c) Moessner, R. *Can. J. Phys.* **2001**, *79*, 128.
(20) Lieb, E. H.; Schultz, D. T.; Mattis, D. C. *Ann. Phys.* (*N.Y.*) **1961**, *16*, 407.
(21) Lieb, E. H.; Mattis, D. C. *J. Math. Phys.* **1962**, *3*, 749.
(22) Schnack, J. *J. Low Temp. Phys.* **2006**, *142*(3−4), 279–284.
(23) Müller, A. *Chem. Phys. Chem.* **2001**, *2*, 517.
(24) (a) Schröder, C.; Nojiri, H.; Schnack, J.; Hage, P.; Luban, M.; Kögerler, P. *Phys. Rev. Lett.* **2005**, *94*, 017205. (b) Rousochatzakis, I.; Läuchli, A. M.; Mila, F. *Phys. Rev. B* **2008**, *77*, 094420. (c) Schulenburg, J.; Honecker, A.; Schnack, J.; Richter, J.; Schmidt, H.-J. *Phys. Rev. Lett.* **2002**, *88*, 167207.
(25) Schröder, C.; Prozorov, R.; Kögerler, P.; Vannette, M. D.; Fang, X.; Luban, M.; Matsuo, A.; Kindo, K.; Müller, A.; Todea, A. M. *Phys. Rev. B* **2008**, *77*, 224409.
(26) Khanra, S.; Biswas, B.; Golze, C.; Büchner, B.; Kataev, V.; Weyhermüller, T.; Chaudhuri, P. *Dalton Trans.* **2007**, 481–487.
(27) Saalfrank, R. W.; Scheurer, A.; Bernt, I.; Heinemann, F. W.; Postnikov, A. V.; Schünemann, V.; Trautwein, A. X.; Alam, M.; Rupp, H.; Müller, P. *Dalton Trans.* **2006**, *23*, 2865.
(28) Takács, A. F.; Neumann, M.; Postnikov, A. V.; Kuepper, K.; Scheurer, A.; Sperner, S.; Saalfrank, R. W.; Prince, K. C. *J. Chem. Phys.* **2006**, *124*, 4503.
(29) (a) Khanra, S.; Kuepper, K.; Weyhermüller, T.; Prinz, M.; Raekers, M.; Voget, S.; Postnikov, A. V.; de Groot, F. M. F.; George, S. J.; Coldea, M.; Neumann, M.; Chaudhuri, P. *Inorg. Chem.* **2008**, *47*. (b) Arroi, M.-A.; Scuiller, A.; Cartier dit Moulin, Ch.; Sainctavit, Ph.; Mallah, T.; Verdaguer, M. *J. Am. Chem. Soc.* **1999**, *121*, 6414.

spin and orbital moments separately in heteronuclear systems.[30,31]

This article is arranged as follows. In section 2, we give a brief overview of the molecular structure and basic magnetic properties. Later on, the experimental and theoretical procedures are described in section 3. We present a detailed analysis of the advanced magnetic properties by means of magnetization measurements using a high-magnetic-field extraction technique (up to $B = 14$ T). On the basis of the high-field measurements, theoretical simulations using an anisotropic spin Hamiltonian are presented. These simulations enable us not only to supply accurate values of the exchange interactions but also to determine the dominant local anisotropies. A discussion of the various spin-Hamiltonian parameters leads to a validation of our element-selective transition-metal L-edge XMCD spin-moment contribution presented in section 4. Here, we also provide charge-transfer multiplet model calculations for the chromium L edge to discuss the valence and crystal-field excitations, along with the results of calculations, within the density functional theory, of spatial spin density. Finally, we end up with our main conclusions in section 5.

2. Structure and Magnetic Properties of $[Cr^{III}Mn^{II}{}_3(PyA)_6Cl_3]$

The synthesis and structure refinement of the present heterotetranuclear complex have been carried out at the Max-Planck-Institute for Bioinorganic Chemistry at Mülheim a. d. Ruhr, Germany. Khanra et al. reported earlier magnetic and HF-EPR measurements of this spin-frustrated compound.[26] The tetranuclear star-shaped complex $[Cr^{III}Mn^{II}{}_3(PyA)_6Cl_3]$ (**$CrMn_3$**) molecule contains a $Cr^{III}Mn^{II}{}_3$ trigonal core with a Cr(1) atom surrounded by three Mn(1) centers at the apexes of an equilateral triangle (Figure 1), so that the cluster comprises the C_3 symmetry. The three Mn(II) ions form an equilateral triangle with the Cr(III) ion placed above the Mn−Mn−Mn plane (chlorine atoms below). The peripheral manganese centers, 6-fold coordinated in highly distorted $MnOClN_4$ cores, are linked through the oximate (μ_2-O−N) group. Each Mn(II) ion is linked to the central Cr(1) atom through two oximate (N−O) and one μ_2-O_{ox} donor. The central chromium atom Cr(1) is in almost perfect octahedral coordination. The six oximato oxygen ligands (deviation from 90° being less than 1.8°), O(1), and O(11) and their equivalents are pendant from the three peripheral $Mn(PyA)_2$ fragments. It was concluded that the **$CrMn_3$** complex contains a $Cr^{III}Mn^{II}{}_3$ (high spin) core.[26]

The magnetization of a polycrystalline **$CrMn_3$** sample has been measured between 2 and 290 K in magnetic fields of 1, 4, and 7 T. EPR spectra have been collected at a temperature of 10 K in magnetic fields up to 15 T and in a frequency range between 19 and 388 GHz. The investigations revealed the following conclusions:

The exchange interactions $J_{CrMn} = -0.29$ cm^{-1} and $J_{MnMn} = -0.07$ cm^{-1}, defined by eq 1 and shown as

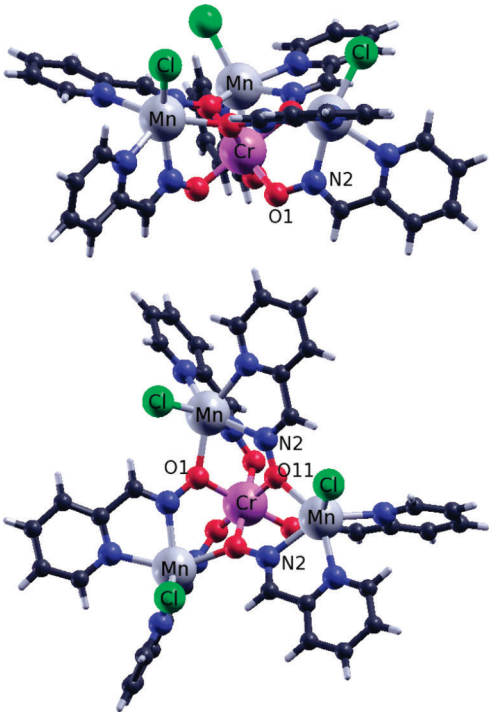

Figure 1. Two perspective views of the $[Cr^{III}Mn^{II}{}_3(PyA)_6Cl_3]$ molecule. The labeling O1, O11, and N2 is after ref 26. The figure was created with the XCrySDen software.[57]

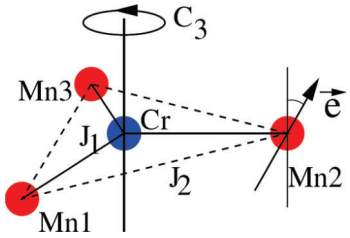

Figure 2. Schematic structure of the **$CrMn_3$** molecule. The central chromium spin is antiferromagnetically coupled by $J_1 = J_{Cr-Mn}$ to the three surrounding manganese ions (solid lines). The manganese ions are coupled antiferromagnetically with each other by the exchange interaction $J_2 = J_{Mn-Mn}$ (dashed lines). The dominant local anisotropy axes are given by the unit vectors $\vec{e}_k$.

J_1 and J_2 in Figure 2, are weakly antiferromagnetic. This is not common among Cr(III) and Mn(II) ions in triply oximato-bridged complexes.[32]

The experimental magnetization data could not be simulated without taking into account exchange interactions between the Mn(II) spins connected through an oximate bridge, although the peripheral Mn···Mn distances are long at 5.49 Å. A zero-field spitting parameter D of -1 cm^{-1} was found from the magnetic measurements in agreement with the HF-EPR measurements.[26] For a more detailed structural and magnetochemical characterization, see ref 26.

(30) Chen, C. T.; Idzerda, Y. U.; Lin, H.-J.; Smith, N. V.; Meigs, G.; Chaban, E.; Ho, G. H.; Pellegrin, E.; Sette, F. *Phys. Rev. Lett.* **1995**, *75*, 152–155.

(31) Funk, T.; Deb, A.; George, S. J.; Wang, H. X.; Cramer, S. P. *Coord. Chem. Rev.* **2005**, *249*, 3.

(32) (a) Ross, S.; Weyhermüller, T.; Bill, E.; Wieghardt, K.; Chaudhuri, P. *Inorg. Chem.* **2001**, *40*, 6656. (b) Ross, S.; Weyhermüller, T.; Bill, E.; Bothe, E.; Flörke, U.; Wieghardt, K.; Chaudhuri, P. *Eur. J. Inorg. Chem.* **2004**, 984. (c) Weyhermüller, T.; Wagner, R.; Khanra, S.; Chaudhuri, P. *Dalton Trans.* **2003**, 2539. (d) Khanra, S.; Weyhermüller, T.; Rentschler, E.; Chaudhuri, P. *Inorg. Chem.* **2005**, *44*, 8176.

3. Experimental and Theoretical Procedures

3.1. Experimental Methods. 3.1.1. X-Ray Spectroscopic Techniques. The XMCD spectroscopy was performed at the elliptically polarizing undulator beamline 4.0.2 of the Advanced Light Source (ALS), Berkeley, California.[33] The samples were mounted into a cryostat equipped with a 6-T superconducting magnet;[34] the sample stage was connected to a pumped helium cryostat reaching base temperatures of around 20.0 and 5.0 K during the experiments presented here. The measurements at the Mn *L* edge have been recorded under external magnetic fields of different strengths in the total electron yield (TEY) mode.

3.1.2. Magnetization Measurements. The magnetization measurements were performed in a commercial PPMS magnetometer (Quantum Design, 6325 Lusk Boulevard, San Diego, CA 92121-3733) equipped with a superconducting 14-T magnet. The magnetic moment of the samples was determined by use of a DC extraction-mode technique after careful temperature and field stabilization. For each measurement, the sample was moved at a high, uniform speed through a detection coil set. The sample moment was then derived from the recorded profile of induction voltage versus sample position. Each measurement at fixed temperature and magnetic field was performed five times in rapid succession, in order to obtain an averaged value for better resolution.

3.2. Theory. 3.2.1. Density-Functional Theory. The electronic structure was calculated by use of the generalized gradient approximation of the density functional theory,[35,36] using the SIESTA (Spanish Initiative for Electronic Simulations with Thousands of Atoms) calculation method.[37,38] More details and results will be published elsewhere along with X-ray electron and emission spectroscopic data.[39]

3.2.2. Ligand-Field Multiplet Model. The XAS lineshapes of the chromium $L_{2,3}$ edge were simulated within charge transfer multiplet-model calculations (CTM) using the TTmultiplet program.[40] First, the energy levels of the initial state ($2p^63d^3$) and final state ($2p^53d^4$) were calculated in spherical (O_3) symmetry. The parameters include the spin−orbit coupling of the 2p core and 3d valence-band electrons, the 3d3d as well as the 2p3d Slater integrals in the initial and final states. The d−d and p−d integrals were reduced to 80% of their atomic Hartree−Fock values, whereas the spin−orbit parameters were not reduced. Then, a cubic crystal field (O_h symmetry) of 10 Dq = 2.2 eV strength was considered in the crystal-field approach. Finally, a charge transfer configuration $3d^4\underline{L}$ was considerd. The energy difference between the two configurations $E(2p^63d^3) - E(2p^63d^4\underline{L}) = \Delta$ was set to 4.0 eV. For comparison with experimental results, the lifetime broadening of the 2p core hole and the resolution of the spectrometer were taken properly into account.

3.2.3. Simulations with Anisotropic Spin Hamiltonians. In order to model the spin system of **$CrMn_3$**, the following microscopic spin Hamiltonian has been used[6,41,42]

$$H = -2\sum_{k<l} J_{kl}\vec{s}_k\cdot\vec{s}_l + \sum_k d_k(\vec{e}_k\cdot\vec{s}_k)^2 + \mu_B\sum_k \vec{B}\cdot g_k\cdot\vec{s}_k \quad (1)$$

The first term accounts for the superexchange coupling between the paramagnetic centers (Heisenberg term). For **$CrMn_3$**, we employ two couplings: J_{Cr-Mn} for the interaction of the central chromium spin with the three surrounding manganese ions (solid lines in Figure 2) and J_{Mn-Mn} for the interaction between the manganese ions (dashed lines in Figure 2).

The second term in eq 1 models the single-ion anisotropy of Mn and Cr, respectively, by means of the dominant axis of the local anisotropy tensor (so-called *D* term). The unit vectors $\vec{e}_k$ set the directions of the local anisotropy axes. The prefactors d_k denote the strength of the local anisotropy; a negative value corresponds to an easy axis, a positive one to a hard axis. The last term in eq 1 reflects the interaction with the applied magnetic field (Zeeman term). In this work, we assume an isotropic **g** tensor. Since we investigated a powder sample, an orientational average is applied using discrete Lebedev−Laikov grids.[43]

We have also performed classical spin-dynamic simulations in order to investigate the field-dependent classical ground state and low-temperature properties, in particular to study the role of the exchange couplings and anisotropies for certain temperatures and external magnetic fields. We write the Hamiltonian of the classical system as

$$H_c = -2\sum_{k<l} J^c_{kl}\vec{m}_k\cdot\vec{m}_l + \sum_k d^c_k(\vec{e}_k\cdot\vec{m}_k)^2 + \mu_c\sum_k \vec{B}\cdot\vec{m}_k \quad (2)$$

The spins $\vec{m}_k$ are classical unit vectors whose orientations are specified by the polar and azimuthal angles, θ_i and φ_i, all extending from 0 to π and 0 to 2π, respectively. The Hamiltonian of eq 2 provides the classical counterpart to the quantum Heisenberg model eq 1. This correspondence is achieved by replacing in eq 1 all quantum spin operators by $\vec{s}_k = \sqrt{s_k(s_k+1)}\cdot\vec{m}_k$, with s_k describing the spin quantum number of a given ion.[44] It thus follows that $J^c_{kl} = \sqrt{s_k(s_k+1)s_l(s_l+1)}\cdot J_{kl}$ and $d^c_k = s_k(s_k+1)d_k$; moreover, the quantity μ_c in eq 1 is given by $\mu_c = (g_k\mu_B)\sqrt{s_k(s_k+1)}$ where g_k is the Landé *g* factor for a given ion and μ_B is the Bohr magneton. We have checked the applicability of our classical treatment by comparing the results of classical Monte Carlo calculations with the above-described exact quantum model calculations.

Furthermore, we have studied the low-temperature field-dependent spin dynamics. An effective method for investigating this property is to use the numerical solution of the stochastic Landau−Lifshitz equation which simulates the time evolution of the spin system coupled to the heat bath. Fluctuating fields with white noise characteristics are used to account for the effects of the interaction of the spin system with the heat bath. Those environmental degrees of freedom are also responsible for the damped precession of the magnetization parametrized by a phenomenological damping factor.

(33) Young, A. T.; Martynov, V.; Padmore, H. A. *J. Electron. Spectrosc. Relat. Phenom.* **1999**, *103*, 885.
(34) Funk, T.; Friedrich, S.; Young, A.; Arenholz, E.; Cramer, S. P. *Rev. Sci. Instrum.* **2002**, *73*, 1649.
(35) Perdew, J. P.; Burke, K.; Ernzerhof, M. *Phys. Rev. Lett.* **1996**, *77*(18), 3865–3868.
(36) Perdew, J. P.; Burke, K.; Ernzerhof, M. *Phys. Rev. Lett.* **1997**, *78*(7), 1396.
(37) Soler, J. M.; Artacho, E.; Gale, J. D.; García, A.; Junquera, J.; Ordejón, P.; Sánchez-Portal, D. *J. Phys.: Condens. Matter* **2002**, *14*(11), 2745–2779.
(38) Siesta - Home. http://www.uam.es/siesta (accessed Jan 2010).
(39) Postnikov, A. V. Manuscript in preparation.
(40) (a) de Groot, F. M. F. *J. Electron. Spectrosc. Relat. Phenom.* **1994**, *67*, 529. (b) de Groot, F. M. F. *Coord. Chem. Rev.* **2005**, *249*, 31. (c) Butler, P. H. *Point Group Symmetry, Applications, Methods and Tables*; Plenum: New York, 1981. (d) Cowan, R. D. *The Theory of Atomic Structure and Spectra*; University of California Press: Berkeley, 1981.
(41) Schnack, J.; Brüger, M.; Luban, M.; Kögerler, P.; Morosan, E.; Fuchs, R.; Modler, R.; Nojiri, H.; Rai, R. C.; Cao, J.; Musfeldt, J. L.; Wei, X. *Phys. Rev. B* **2006**, *73*, 094401.
(42) (a) Glaser, T.; Heidemeier, M.; Krickemeyer, E.; Bögge, H.; Stammler, A.; Fröhlich, R.; Bill, E.; Schnack, J. *Inorg. Chem.* **2009**, *48*(2), 607–620. (b) Schnack, J. *Magn. Condens. Matter Phys.* **2009**, *12*, 323–330.
(43) Lebedev, V. I.; Laikov, D. N. *Dokl. Math.* **1999**, *59*(3), 477–481.
(44) Ciftja, O.; Luban, M.; Auslender, M.; Luscombe, J. H. *Phys. Rev. B* **1999**, *60*, 10122.

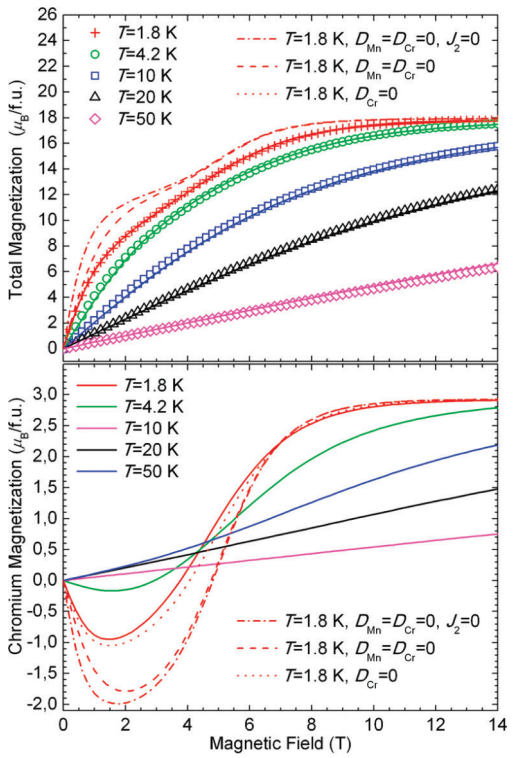

Figure 3. Top panel: Magnetic-field dependence of the magnetization per $[Cr^{III}Mn^{II}_3(PyA)_6Cl_3]$ molecule. The experimental data for various temperatures are given by symbols. The lines represent theoretical estimates using the parameters given in the text. Bottom panel: Theoretical estimates of the local magnetization of the center Cr ion in the **$CrMn_3$** magnetic core for various temperatures. See text for more details.

4. Results and Discussion

4.1. Magnetization Measurements and Anisotropic Spin-Hamiltonian Simulations. Some gross properties of the magnetic heterotetranuclear complex $[Cr^{III}Mn^{II}_3(PyA)_6Cl_3]$ have been investigated previously. It has been found that, besides a dominant antiferromagnetic exchange interaction between the central chromium spin ($s_{Cr} = 3/2$) and its surrounding manganese spins ($s_{Mn} = 5/2$), a frustrating antiferromagnetic coupling between the manganese ions exists.[26] A sizable zero-field splitting was also inferred from EPR measurements. In this section, we report on detailed investigations of the microscopic parameters of **$CrMn_3$**.

For a more detailed study of the magnetic properties of **$CrMn_3$**, the magnetization of a polycrystalline sample has been measured at high magnetic fields by using a standard inductive method. Magnetic fields from 0 to 14 T at temperatures of 1.8, 4.2, 10, 20, and 50 K have been applied. The results are shown by symbols in the upper panel of Figure 3. The observed magnetic-field dependence of the magnetization as well as the field needed to reach saturation at $18\,\mu_B$ ($s_{Cr} = 3/2$, $3s_{Mn} = 5/2$) reflects a nontrivial magnetic interaction between the magnetic ions. Near $B = 0$, a detailed analysis revealed no magnetic hysteresis.

The high-field magnetization measurements enable us not only to determine accurately the exchange interactions but also to determine the dominant local anisotropies. To this end, Hamiltonian 1 is used. Following ref 26, we assume that **$CrMn_3$** possesses C_3 symmetry; i.e., the exchange coupling J_{Cr-Mn} of the central chromium is the same for all three surrounding manganese ions, and J_{Mn-Mn} is equal between the latter. For the local anisotropies, this symmetry implies that the anisotropy axes of the manganese ions share a common angle ϑ with respect to the C_3 axis of the molecule. The azimuthal angles ϕ_κ differ by 120° between adjacent spins. Their exact orientation relative to the molecular skeleton cannot be specified since neither the two other principal axes of the **d** tensor (so-called E-terms) nor the coupling of spins to orbital/structural parameters have been included in the spin-Hamiltonian. For chromium, the C_3 symmetry implies that its anisotropy axis coincides with the rotational one of the molecule. Using these assumptions, we arrive at a fit describing best the magnetization data shown in Figure 3 (top panel) for $J_{Cr-Mn} = -0.29\ cm^{-1}$, $J_{Mn-Mn} = -0.07\ cm^{-1}$, $d_{Mn} = -1.05\ cm^{-1}$, $\vartheta_{Mn} = 15°$, and $d_{Cr} = 0.40\ cm^{-1}$. We used $g_{Mn} = 2.0$ and $g_{Cr} = 1.95$ as in ref 26. The exchange couplings differ somewhat from those found in ref 26, since we now have incorporated the local anisotropies in the spin Hamiltonian, eq 1. On first glance, it is astonishing that Mn(II) with a half-filled d shell should have an anisotropy as large as $d_{Mn} = -1.05\ cm^{-1}$. However, the 6-fold coordination of the manganese ions in **$CrMn_3$** results in a highly distorted $MnOClN_4$ core. In such a distorted local environment, Mn(II) can reach anisotropies of up to $1.5\ cm^{-1}$, as has been shown in recent investigations.[45,46] Concerning ϑ_{Mn}, we would like to mention that there are Mn−Cl bonds pointing out of the Mn_3 plane, and it is well conceivable that the directions of the Mn anisotropy axes are fixed by the Cl ions. The accuracy of the fit depends differently on the various parameters. Variations of the exchange parameters as well as of the manganese anisotropy strength have drastic consequences, whereas variations of ϑ_{Mn} and of the chromium anisotropy do influence the fit only mildly. We assumed isotropic **g** tensors for simplicity. An inclusion of an improved **g** tensor, reasonably deviating from 2.0, might modify the obtained values, but not much.

The theoretical results with the above parameters (solid lines) are compared to the experimental data (symbols) in the upper panel of Figure 3. We would like to discuss the influence of the various spin-Hamiltonian parameters on the magnetization. To this end, we show for $T = 1.8$ K, as a dashed-dotted curve, the result corresponding to the case where only the coupling between the manganese and chromium ions is considered, and all other terms are set to zero. Such a system would be bipartite, i.e., nonfrustrated. An inclusion of the manganese−manganese coupling results in a weak frustration. The result is depicted by the dashed curve; the deviation from the bipartite system is largest at low fields. The dotted curve, which is hardly visible on top of the solid line, presents the result for the case of manganese anisotropies included as well. The chromium anisotropy then contributes only a minor improvement to the final fit.

(45) Duboc, C.; Collomb, M. N.; Pécaut, J.; Deronzier, A.; Neese, F. *Chem.—Eur. J.* **2008**, *14*, 6498–6509.
(46) Pichon, C.; Mialane, P; Rivière, E.; Blain, G.; Dolbecq, A.; Marrot, J.; Sécheresse, F.; Duboc, C. *Inorg. Chem.* **2007**, *46*, 7710–7712.

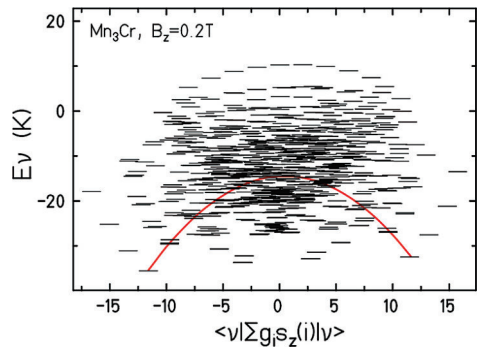

Figure 4. Energy spectrum of the **$CrMn_3$** magnetic core evaluated at a magnetic field of $B_z = 0.2$ T to separate degenerate states. The solid line shows a fictitious anisotropy barrier derived from the two lowest-energy eigenvalues on either side. The corresponding zero-field splitting parameter of these curves is $D = -0.575$ K.

Referring to the lower panel of Figure 3, we discuss the theoretical behavior of the chromium moment as a function of field for the same temperatures as in the top panel. At a low temperature ($T = 1.8$ K) and fields below 3 T, the chromium moment points predominantly opposite of the field direction. This can be understood from the fact that the three dominating manganese moments align themselves along the field direction, whereas the Cr moment, that is antiferromagnetically coupled to each of latter, points in the opposite direction. Thus, the Cr moment is largely reduced by frustration and anisotropy. For $T = 1.8$ K, indeed, the bipartite case (only $J_{Cr-Mn} \neq 0$) shows the largest antiparallel alignment. The frustration due to J_{Mn-Mn} reduces the Cr moment somewhat. The largest impact arises from the manganese anisotropy, which reduces the chromium moment at $B = 2$ T by about a factor of 2. Counterintuitively, the chromium anisotropy has little influence on the chromium moment (dotted curve). Due to the given functional dependence of the chromium moment, its expectation value virtually vanishes in certain temperature and field regions, i.e., around 5 K and in fields of up to about 4.

To discuss the uniaxial anisotropy, we refer to Figure 4, which shows the energy eigenvalue spectrum of the **$CrMn_3$** magnetic core. Since the Hamiltonian is anisotropic, these eigenvalues do not belong to multiplets of the total spin. Nevertheless, they can be correlated with the total magnetization of the respective eigenstate, which depends on field. In order to split possible degeneracies, we present the eigenvalues at a rather small field of $B_z = 0.2$ T along the molecular C_3 axis. As can be derived from the data and qualitatively seen in the figure, the total ground state at $B = 0$ is 2-fold degenerate with a magnetization of approximately $\pm 12\,\mu_B$.

One can also see that these states do not belong to a well-separated ground-state multiplet, which is only split by anisotropy terms. On the contrary, the spectrum is rather dense. If one would try to attach an anisotropy barrier to the two ground states ($M \approx \pm 6$) and the next higher-lying states with $M \approx \pm 5$, one would arrive at an anisotropy barrier as given by the solid line in Figure 5. The corresponding zero-field splitting parameter is $D = -0.575$ K. Nevertheless, this discussion is purely fictitious. What would be needed to constitute a single molecule magnet is that the local Mn anisotropy axes would be aligned parallelly.

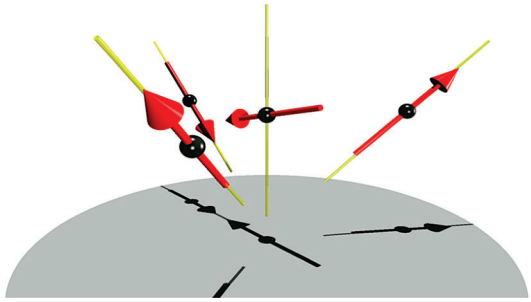

Figure 5. Classical ground-state configuration of **$CrMn_3$** as obtained by spin dynamics simulations at $T = 0$ and $B = 0$.

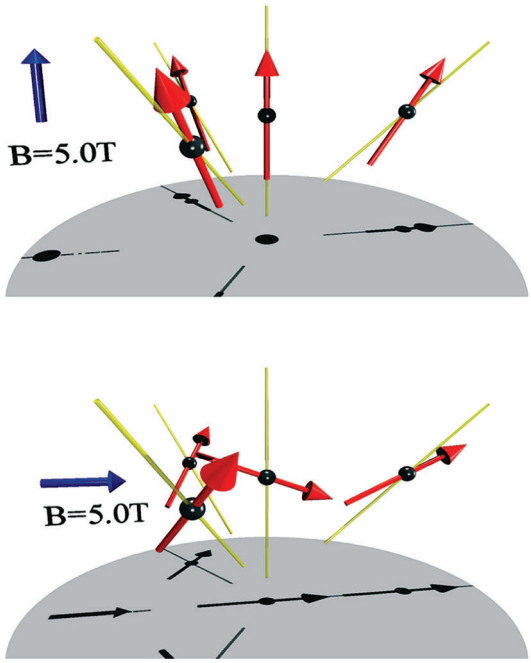

Figure 6. Classical ground-state configuration of **$CrMn_3$** as obtained by spin-dynamic simulations at $T = 0$ and an external field $B = 5$ T applied in different directions.

In Figure 5, we show the classical ground-state configuration of **$CrMn_3$** as obtained by classical spin-dynamics simulations at $T = 0$ and $B = 0$. The local anisotropy axes are depicted as yellow sticks. According to the model parameters, the strong easy-axis anisotropy dominates the orientation of the manganese spins in an up−up−down fashion, almost independent of the rather weak exchange interactions in the system. Only a very small canting with respect to the anisotropy axes is visible. The easy-plane anisotropy of the central chromium spin becomes apparent, with a small canting in the direction of the downward pointing manganese spin. This situation changes when an external field is applied. In Figure 6, we show simulation results for the spin orientations in an external field of 5 T applied along two different directions. Compared to the ground state at 0 T, one manganese spin is flipped, so that the up−up−down configuration is replaced by an up−up−up configuration in both cases. At 5 T, the Zeeman energy is much larger than the exchange interactions between all spins. However, the system is not yet fully saturated due to the fact that the anisotropy is still important.

We performed as well finite-temperature Monte Carlo and spin-dynamic simulations. For temperatures not too low ($T \approx 5$ K), our classical Monte Carlo simulations show qualitatively the same results as the "exact" quantum calculations. In particular, the element-specific magnetization curves show a vanishing local moment at the central chromium site at around 5 T. By using our stochastic Landau−Lifshitz method, we can directly study the time evolution of the classical spin system coupled to a heat bath at this field value. Here, we find a rather large and "stiff" local magnetic moment at the manganese sites; i.e., thermal fluctuations have little influence on the spin-vector motion due to the large local anisotropies. In contrast to this, the central chromium spin-vector motion is heavily influenced by thermal fluctuations.[47] We have found that its net moment is only nonzero for the component in the external field direction. Therefore, an orientational average would lead to a vanishing moment as derived from our magnetization data and as observed in our XMCD measurements (see below).

4.2. X-Ray Magnetic Circular Dichroism. In this section, we report on our detailed study of the XMCD transition-metal $L_{2,3}$ spectra of the paramagnetic centers, manganese and chromium, in the **$CrMn_3$** complex. The Cr XAS spectrum of **$CrMn_3$** is compared to ligand-field multiplet model calculations, whereas the Mn XMCD spectra are matched to the spectra and corresponding CTM calculations of our earlier investigations of a star-shaped $S_t = 10$ high-spin molecule with a $Mn^{II}{}_4O_6$ core (MnStar).[29] For this polymetallic complex with very weak exchange coupling, it was possible to probe almost the complete magnetic moment at the manganese ions by XMCD, yielding a giant total magnetic moment of 20 μ_B per molecule.

The **$CrMn_3$** and MnStar Mn $L_{2,3}$ X-ray absorption spectra excited by soft X-rays with 90% left and right circularly polarized light measured at 5 T and 5 K are presented in the top panel of Figure 7. The bottom panel displays the corresponding XAS spectra and the dichroic signals. The experimental spectra are given by circles and squares for **$CrMn_3$** and MnStar, respectively. The Mn^{2+} CTM calculations have been taken from Khanra et al.[29] In contrast to these calculations, it was not possible to reproduce the Mn L-edge XAS spectra of **$CrMn_3$** assuming neither O_h nor even the C_{4h} symmetry. A highly distorted 6-fold $OClN_4$ coordination of the Mn^{II} ions leads to a strongly anisotropic exchange field, and the **$CrMn_3$** CTM calculations become challenging. In the lower panel of Figure 8, we compare the sum (XAS) over the two helicities shown in the top panel and the dichroic (MCD) signals of **$CrMn_3$** (circles) and MnStar (squares).

The characteristic two Mn L edges visible at about 640 and 652 eV originate from the spin−orbit coupling of the 2p shell representing the $2p_{3/2}$ and $2p_{1/2}$ to 3d transitions. In detail, the Mn $L_{3,2}$ XAS comprises six main features: a shoulder at approximately 639.0 eV, the Mn L_3 main peak at 640.0 eV, two additional L_3 shoulders at higher energies of 641.0 and 643.5 eV, and two peaks at the L_2 edge at 650.0 and 652.5 eV. This sequence holds for both the **$CrMn_3$** and MnStar XAS spectra, clearly revealing the Mn^{2+} ($3d^5$) valence state by force of the fact that the XAS is sensitive to the local electronic structure and chemical environment.

(47) We invite the reader to study our animations on http://spin.fh-bielefeld.de (accessed Jan 2010).

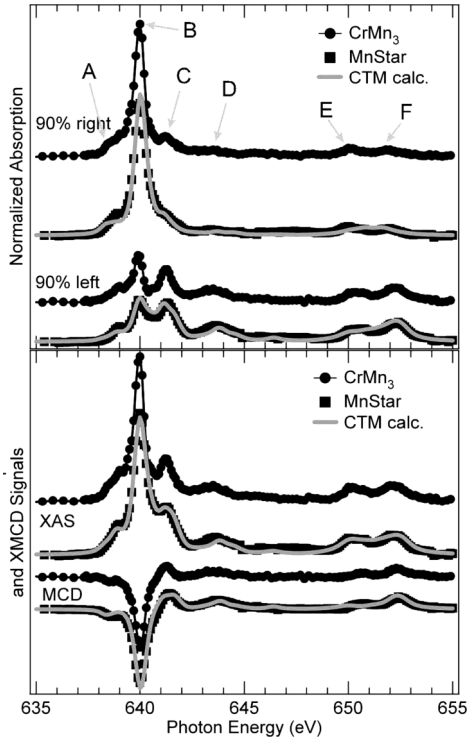

Figure 7. Dichroic Mn $L_{2,3}$ spectra of **$CrMn_3$** (circles) and the MnStar (squares) taken at a temperature of 5 K and an applied magnetic field of 5 T (top panel) and corresponding XAS and MCD signals (bottom panel). The solid lines represent the appropriate Mn^{2+}Star CTM calculations.

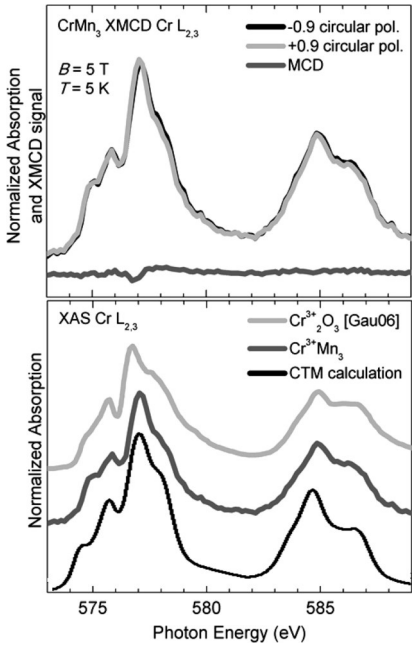

Figure 8. Dichroic Cr $L_{2,3}$ spectra and MCD signal of **$CrMn_3$** taken at a temperature of 5 K and an applied magnetic field of 5 T (top viewgraph). Comparison of the **$CrMn_3$** and Cr_2O_3.[49] Cr L edge XA spectra plotted along with CTM calculations for a Cr^{3+} ion in O_h symmetry ($10Dq = 2.2$ eV; bottom viewgraph).

To better understand the ionic Mn^{2+} behavior, it is necessary to mention that we extracted a 93.8% $3d^5$ and a 6.2% $3d^6\underline{L}$ configuration from the MnStar CTM calculations.[29] This is noteworthy, because charge transfer can result in a deformation of the multiplet structure and an appearance of satellite structures.[48] Furthermore, the local crystal-field strength around the absorbing manganese atom can be probed directly by XAS. The close resemblance of the **$CrMn_3$** and MnStar Mn XAS spectra suggests that the crystal-field splitting in **$CrMn_3$** is equally as large as in MnStar, namely, 10 Dq = 0.6 eV. Compared to values found for manganese oxides, this magnitude is rather low. However, for similar molecules like Mn_4 or $CrMn_6$, similar values of 10 Dq have been found.[29]

The upper panel of Figure 8 presents the dichroic XAS and MCD spectra of the chromium ion in the magnetic core of **$CrMn_3$** at 5 T and 5 K. Compared to the Mn^{2+} X-ray absorption spectra, the Cr^{3+} ones comprise rather broad peaks. Two main peaks are located at 577.0 and 585.0 eV for the L_3 and L_2 edges, respectively. Clear multiplet structures around the main peaks are visible. The spectrum allows to identify eight features, which are unique signatures for the Cr^{3+} ion being in an octahedral environment.[49] Looking at the XMCD signal of chromium is at first glance astonishing: no significant signal was recorded.

To get a deeper insight into the local symmetry and multiplet structure of the Cr ion, we also performed ligand-field (LF) multiplet calculations (using the TTmultiplet program) for trivalent chromium in the O_h symmetry. The result is given as the black solid line in the lower panel of Figure 8 together with the corresponding XAS Cr $L_{2,3}$ edge of Cr_2O_3 (see ref 49) and the isotropic XAS of **$CrMn_3$**. All spectra have a very similar shape. The **$CrMn_3$** XAS spectrum (dark gray) agrees nearly perfectly with the Cr_2O_3 spectrum (light gray). There is one particular feature shifting: the main peak of the Cr L_3 edge of **$CrMn_3$** is located at 577.0 eV photon energy, compared to 576.6 eV in the XAS spectrum of Cr_2O_3. Also, the relative intensities of the peaks at the L_3 and L_2 edges differ slightly. With the charge transfer multiplet calculation, we were able to reproduce the characteristic features of the **$CrMn_3$** absorption spectrum, and we find a 75.2% $3d^3$ and 24.8% $3d^4\underline{L}$ configuration.

We applied the XMCD sum rules developed by Thole and Carra, that later were confirmed experimentally by Chen et al.[30,50,51] in order to extract the element selective spin and orbital moments of the Mn^{2+} and Cr^{3+} ions in **$CrMn_3$**. From our experimental data recorded at 5.0 K, we extracted a local manganese spin moment of m_{Spin} = 7.24 μ_B per molecule (2.41 μ_B per manganese atom) and an orbital moment of m_{Orb} = 1.56 μ_B per molecule (0.52 μ_B per manganese atom).

Sum rule analysis of the experiment performed at 20.0 K yielded m_{Spin} = 3.88 μ_B and m_{Orb} = 0.015 μ_B per molecule. Because the sum rules can only be applied properly when the separation of the $2p_{3/2}$ and $2p_{1/2}$ levels is large enough to clearly distinguish the $j_{3/2}$ and $j_{1/2}$ excitations, a spin-correction factor of 1/0.680 is necessary if the spectral features of the L_2 and L_3 edges do overlap. In this case, a quantum-mechanical superposition of the $j_{3/2}$ and $j_{1/2}$ excitations appears during the absorption process. In our earlier work, we already discussed and validated this correction factor, which was first proposed and calculated by Teramura et al.[29,52,53] Using this spin-correction factor, we obtain a local manganese spin moment of m_{Spin} = 10.65 μ_B per molecule and a rather large orbital moment of m_{Orb} = 1.56 μ_B per molecule at 5 T and 5 K, whereas at a temperature of 20 K we obtain m_{Spin} = 5.71 μ_B and m_{Orb} = 0.05 μ_B. Although we find a quite good agreement between the magnetic moment obtained from the MCD and the magnetometry, we want to point out that very recently it has been found that the correction factor depends on the crystal field strength, also the nonzero orbital moment can influence the spin sum rule correction factor.[54]

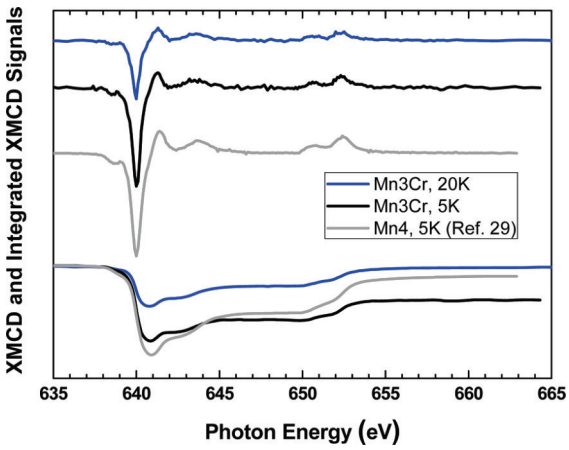

Figure 9. Experimental Mn $L_{2,3}$ MCD signals of **$CrMn_3$** recorded at 5 K (black) and 20 K (blue) and MnStar[29] (gray) plotted along with the corresponding MCD integrated intensities.

Next, we compare the above-mentioned results with those obtained on the **Mn_4** (MnStar).[29] Although the manganese $L_{2,3}$ edge MCD signals of MnStar and **$CrMn_3$** look very similar at first glance, the orbital angular-momentum distribution for these two compounds is very different. Figure 9 shows a comparison of the **$CrMn_3$** and MnStar manganese $L_{2,3}$ edge MCD signals and their integrated intensities at 5 K. The integrated intensity of the overall MCD (L_2 and L_3 edges) indicates the presence of an unquenched orbital angular Mn momentum in **$CrMn_3$** at 5 K. In contrast, for the MnStar, an almost completely quenched orbital moment is found at 5 K.[29] The result for **$CrMn_3$** is surprising because it is inconsistent with a half filled $3d^5$ state, where all d orbitals are perfectly balanced within the $\pm m$ contributions. On the one side, potential errors in the sum rule analysis, such as offset corrections or a too short integration range,

(48) van der Laan, G.; Kirkman, I. W. *J. Phys. Condens. Mater*. **1992**, *4*, 4189.
(49) Gaudry, E.; Sainctavit, P.; Juillot, F.; Bondioli, F.; Ohresser, P.; Letard, I. *Phys. Chem. Miner*. **2006**, *32*, 710.
(50) Thole, B. T.; Carra, P.; Sette, F.; van der Laan, G. *Phys. Rev. Lett*. **1992**, *68*, 1943.
(51) Carra, P.; Thole, B. T.; Altarelli, M.; Wang, X. D. *Phys. Rev. Lett*. **1993**, *70*, 694.
(52) de Groot, F.; Kotani, A. *Core Level Spectroscopy of Solid*; Taylor & Francis: London, 2008.
(53) Termamura, Y.; Tanaka, A.; Jo, T. *J. Phys. Soc. Jpn*. **1996**, *65*, 1053.
(54) Piamonteze, C.; Miedema, P.; de Groot, F. M. F. *Phys. Rev. B* **2009**, 184410.

can cause the overestimation of orbital momentums.[55a] However, we want note that the Mn ions in **$CrMn_3$** are in a strongly distorted and inhomogenous crystal field, which may lift the electronic degeneracy. A similar effect has been very recently reported for ε-Fe_2O_3.[55b] In contrast, we do not find a significant Mn orbital momentum at the temperature of 20 K (external field still 5 T). Furthermore, high-field EPR measurements performed at 10 K on **$CrMn_3$** yielded a g factor of 2.05 for the Mn ions.[26] That also indicates a positive Mn orbital angular momentum. One can speculate about reasons for this surprising result. It might be due to changes in the local Mn electronic structure, e.g., the Mn−ligand bond length as a consequence of structural changes taking place between 5 and 20 K. Such an effect has been observed in ε-Fe_2O_3 very recently;[55b] however, more experimental studies on the electronic and structural properties on the **$CrMn_3$** compound in this temperature range are necessary to draw any conclusion about this result.

An appropriate determination of the local chromium moment is not possible. In order to employ the spin-correction factor, a sufficiently large L_3/L_2 splitting is required to avoid problems due to the L_3-L_2 mixing.[53] In the case of chromium, this is not the case. Qualitatively, one can assume a very small local magnetic spin moment of chromium, ordered ferromagnetically with respect to the manganese spins, in **$CrMn_3$**.

Comparing the magnetization data at 5 T and 4.2 K—especially the local chromium magnetization extracted by use of the anisotropic Heisenberg model calculations (Figure 3)—with the local magnetic moments of manganese and chromium obtained from our XMCD experiments at 5 T and 5 K, we find perfect agreement. The total magnetization is about 12.5 μ_B per molecule, whereas the local chromium magnetic moment does almost completely disappear but remains ferromagnetically ordered with respect to the manganese spins (Figure 3). Also, the large local anisotropy parameter for manganese ($d_{Mn} = -1.05$ cm^{-1}) obtained from our Heisenberg simulations can be understood qualitatively. The XMCD measurements give direct experimental evidence that the orbital moments of the manganese ions are only partially quenched. *These results can be regarded as a first example of strong anisotropy and frustration effects probed by X-ray magnetic circular dichroism.*

4.3. Electronic-Structure Calculations. For density-functional calculations, the molecule was prepared in different magnetic configurations, referred to in the following according to how the spin moments of individual atoms (Cr, Mn, Mn, Mn) are set in the U (up) or D (down) direction with respect to the global quantization axis. The total energies of such configurations were compared. We calculated as well the energies for some noncollinear spin configurations but did not reach conclusive results due to convergence problems. Restricting our discussion to collinear cases only, we can emphasize the following:

1. The individual spins on the Cr and Mn positions tend to remain quite stable at values of 3/2 and 5/2, respectively, but can be inverted at relatively low energy cost.
2. The saturation value of the total spin, 18/2 as in the UUUU configuration, agrees with the results of the magnetization measurements.
3. At variance with what could have been expected, i.e., a preferential antiparallel coupling between Cr and Mn, the DUUU configuration is energetically, by 39 meV, higher compared to the UUUU configuration. However, the inversion of two spins, such as in the DDUU and other degenerate configurations, is by merely 13 meV higher in energy than the fully magnetized situation. Hence, it can be expected that a mixture of several such "two spins up, two spins down" configurations might ultimately emerge as the ground state. Apparently, this is a manifestation of strong frustration, as also evidenced by Heisenberg and classical spin dynamic simulations done in our work.
4. Obviously (for reasons typical for DFT calculations in molecular magnets where the intra-atomic correlation effects are underestimated, see, e.g., ref 56), the magnetic splitting within the 3d shells of Cr and Mn comes out too small, and consequently the HOMO−LUMO gap is strongly underestimated. However, it does not fully disappear, at least in the most "competitive" spin configurations, amounting to 0.51 eV in UUUU, 0.63 eV in DUUU, and 0.70 eV in DDUU. The latter supports the above argument that the mixing of several DDUU-like states might result in a stable and energetically favorable (frustrated) configuration.

For discussing the spatial distribution of spin density, we use the DUUU configuration, because it shows a reasonable "spin contrast" in the Cr−Mn coupling (see Figure 10).

It should be noted that each individual spin is not fully localized on a 3d center, so that the coresponding magnetic density somehow spills onto the neighboring atoms. However, the spins remain quite "rigid", in the sense that, in a different spin configuration, the spatial spin density around a given center in first approximation would be inverted (i.e., spin up becomes spin down).

The on-site magnetic spin density is quite spherical around the Mn atoms, with their half-filled and hence symmetric d shells, and pronouncedly "cube-like" at the Cr site, where in a simplified view "only" the t_{2g} orbitals are occupied. This different shape is even more pronounced in higher spin-density isosurfaces (not shown) which are more closely confined to the atom cores.

Observing the spin density spilled onto the neighbors of a 3d center, we find it octahedrally symmetric, according to the placement of oxygen atoms around the Cr site, whereas that of the Mn atoms is strongly anisotropic (Figure 10). For one thing, the Mn's are already structurally placed in low-symmetry positions; moreover, one

(55) (a) Goering, E.; Lafkioti, F; Gold, S. *Phys. Rev. Lett.* **2006**, *96*, 039701. (b) Tseng, J.-C.; Souza-Neto, N. M.; Haskel, D.; Gich, M.; Frontera, C.; Roig, A.; van Veenendaal, M.; Nogués, J. *Phys. Rev. B* **2009**, *79*, 094404.

(56) Postnikov, A. V.; Kortus, J.; Pederson, M. R. *Phys. Stat. Sol. B* **2006**, *243*(11), 2533–2572.

(57) Kokalj, A. *J. Mol. Graphics Modell.* **1999**, *17*, 176. The code is available from http://www.xcrysden.org (accessed Jan 2010).

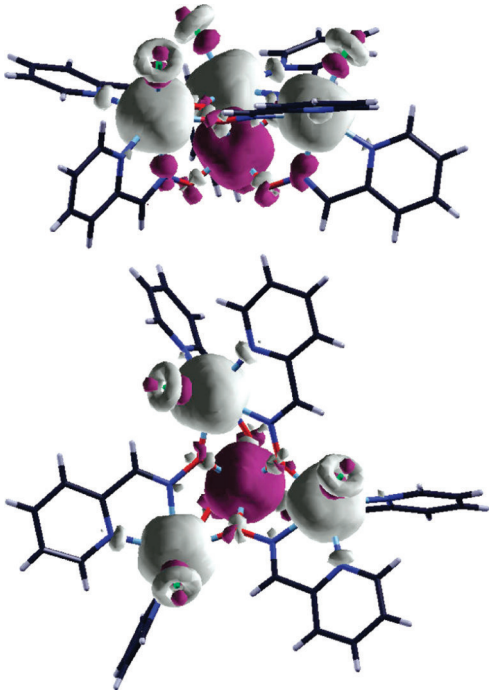

Figure 10. Two views of the spin-density isosurfaces, corresponding to $\pm 0.0025\ e/Å^3$, in the DUUU configuration of **$CrMn_3$**. Positive/negative values are indicated by light gray/dark violet color. The molecular structure is shown as a framework, with orientation and color code as in Figure 1.

can see that the Cl 3p shell, although almost fully occupied, exhibits an interesting break of symmetry in its related spin (Figure 10). This might be an important source of anisotropy found for the Cr atoms in the spin-Hamiltonian simulations, as was already mentioned in section 4.1.

5. Conclusions

In summary, we presented a comprehensive investigation of the electronic structure and the magnetic properties of the star-shaped heteronuclear $Cr^{III}Mn^{II}_3$ complex. Various X-ray spectroscopic methods were used to investigate the internal chemical, electronic, and magnetic structure of **$CrMn_3$**. The XAS spectra of the manganese and chromium L edges were measured and compared to Mn^{2+} Star spectra investigated earlier[29] or modeled within the ligand-field multiplet model, respectively, in order to investigate the valence and local symmetry. Crystal-field and charge-transfer parameters were extracted from the calculations and are in good agreement with earlier data.

Using magnetization measurements, element-selective XMCD at the Mn and Cr L edges, and quantum model calculations based on an anisotropic Heisenberg Hamiltonian, we were able to understand the complete magnetic structure of the **$CrMn_3$** magnetic core, including the manganese single-ion anisotropy and frustration. The experimental data fit perfectly to the quantum calculations, allowing an accurate determination of the exchange interactions and of the dominant local anisotropies. The extracted parameters were used to perform classical spin-dynamic simulations. The field-dependent classical ground state and low-temperature properties were studied in our extensive work on the **$CrMn_3$** complex.

Acknowledgment. E. Arenholz and J. D. Denlinger are acknowledged for excellent technical support. We would like to thank Joris van Slageren for discussing anisotropy issues with us and for drawing our attention to recent publications on Mn(II) anisotropies. Financial support by the Graduate College and the PhD program (Lower Saxony) is gratefully acknowledged. A.V.P. acknowledges the use of computing resources of the PMMS of the Paul Verlaine University. Part of the work was performed at the Advanced Light Source (A.L.S.), which is supported by the U.S. Department of Energy under Contract No. DE-AC03-76SF00098.

Financial support from the German Research Council (DFG) in the priority program "Molecular Magnetism" as well as through the research group FOR 945 is also thankfully acknowledged.

Publication H11

[**H11**] K. Kuepper, C. Taubitz, D. Taubitz, U. Wiedwald, A. Scheurer, S. Sperner, R. W. Saalfrank, J. P. Kappler, L. Joly, and P. Ziemann. *Magnetic Ground State and Systematic X-ray Photoreduction Studies of an Iron-based Star-Shaped Complex*, J. Phys. Chem. Lett. **2**, 1491 (2011), doi: 10.1021/jz2005013.

THE JOURNAL OF PHYSICAL CHEMISTRY Letters

LETTER

pubs.acs.org/JPCL

Magnetic Ground-State and Systematic X-ray Photoreduction Studies of an Iron-Based Star-Shaped Complex

Karsten Kuepper,*[,†] Christian Taubitz,[‡] Daniel Taubitz,[‡] Ulf Wiedwald,[†] Andreas Scheurer,[§] Stefan Sperner,[§] Rolf W. Saalfrank,[§] Jean-Paul Kappler,[⊥] Loïc Joly,[⊥] Paul Ziemann,[†] and Manfred Neumann[‡]

[†]Institute of Solid State Physics, University of Ulm, Albert-Einstein-Allee 11, 89069 Ulm, Germany

[‡]Department of Physics, University of Osnabrück, Barbarastrasse 7, 49069 Osnabrück, Germany

[§]Department Chemie und Pharmazie, Lehrstuhl für Anorganische und Allgemeine Chemie, Universität Erlangen-Nürnberg, 91058 Erlangen, Germany

[⊥]IPCMS UCMS 7504 CNRS, Université de Strasbourg, 23 rue du Loess, BP 43, 67034, France

ABSTRACT: We revisit the star-shaped iron-based single-molecule magnet $[Fe^{III}\{Fe^{III}(L)_2\}_3]$ (**2**) (exact chemical formula $C_{30}H_{66}Fe_4N_6O_{12}$, H_2L = *N*-methyldiethanolamine) in order to clarify some open questions concerning the exact electronic and magnetic properties arising from earlier studies on this specific compound. Namely, we address the internal magnetic structure by applying X-ray magnetic circular dichroism to the Fe $L_{2,3}$ edges and carefully investigate radiation photochemistry. We observe an Fe^{3+} to Fe^{2+} photoreduction process, taking place under soft X-ray radiation.

SECTION: Molecular Structure, Quantum Chemistry, General Theory

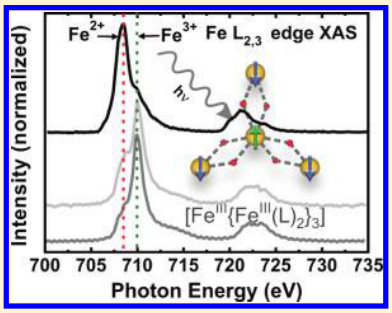

In the quest for new materials for ultrahigh density storage devices or for quantum computing, researchers seek among others for new molecule-based magnets. In such magnetic molecules, spin coupling between paramagnetic transition-metal ions is mediated via bridging ligand atoms, leading to a variety of interesting fundamental properties such as intramolecular exchange interactions or magnetic anisotropy.[1−5] Besides the famous Mn12−Ac cluster,[6] so-called star-shaped molecules, which are comprised of four transition-metal ions in the form of a central ion and three peripheral ions, belong to the most promising and simplest inorganic systems showing single-molecule magnet (SMM) behavior.[7] A couple of star-shaped molecules with intriguing magnetic properties have been reported; among them are those with a Cr^{III}_4 core with a high spin state $S = 3$,[8] a Mn^{II}_4 core with $S = 10$,[9] a Ni^{II}_4 core,[10] or the spin frustrated $Cr^{III}Mn^{II}_3$ complex.[11] The star-shaped trigonal, metal-centered Fe_4 complex is of special interest due to some remarkable progress concerning substrate deposition and tunneling experiments,[12] which are prerequisites for potential applications as a magnetic memory or a molecular nanojunction. In particular, Mannini et al. demonstrated that an Fe_4 molecule can be wired to a gold surface, which then shows single magnetic molecule behavior, that is, an open magnetic hysteresis loop at low temperature.[13] Tailoring of the molecule orientation by ligand chemistry even led to quantum tunneling of the magnetization.[14] In those recent works, X-ray magnetic circular dichroism (XMCD) played a very crucial role in order to verify that the SMM behavior stems from the Fe^{III} centers on the surface of "bulk-like" films of some hundred nm thickness,[15] as well as for thin, single-monolayer films deposited on gold.[13] Orientation control could also be demonstrated at sub-Kelvin temperatures even by means of angular-dependent XMCD.[14] There are two types of the star-shaped Fe_4 molecule known. The experiments described above have been performed on $[Fe^{III}_4(OCH_3)_6(dpm)_6]$ (**1**) (exact chemical formula $C_{72}H_{132}Fe_4O_{18}$, Hdpm = dipivaloylmethane; Figure 1, left)[16] and its derivatives.[17] Furthermore, another molecule with an Fe_4 core has been reported by Saalfrank et al.,[7] the SMM $[Fe^{III}\{Fe^{III}(L)_2\}_3]$ (**2**) (exact chemical formula $C_{30}H_{66}Fe_4N_6O_{12}$, H_2L = *N*-methyldiethanolamine; Figure 1, center). There are some differences in detail concerning the coordinating ligands of the Fe^{III} ions. Whereas in both complexes the central ion is attached to six μ_2-oxygen donors, building up bridges to the peripheral Fe ions, the three outer Fe ions in **1** are coordinated as well with six surrounding oxygen donors (Figure 1, left). In contrast, the three peripheral ferric ions in **2** are in a nearly octahedral O_4N_2 environment (see Figure 1, center).

There are also somewhat different reports about the Fe valency state in **1** and **2**. Whereas for **1** the predominantly or nearly completely Fe^{3+} is found[13−15,18] in thick films and also single-layered samples, for a powder sample **2** divalent iron, probing by X-ray photoelectron spectroscopy (XPS) and Fe L edge X-ray absorption spectroscopy (XAS) has been reported.[19,20] Very recently, it has been suggested that this discrepancy might be related to soft X-ray radiation induced photoreduction effects of the iron. Such an effect has been

Received: April 13, 2011
Accepted: May 26, 2011

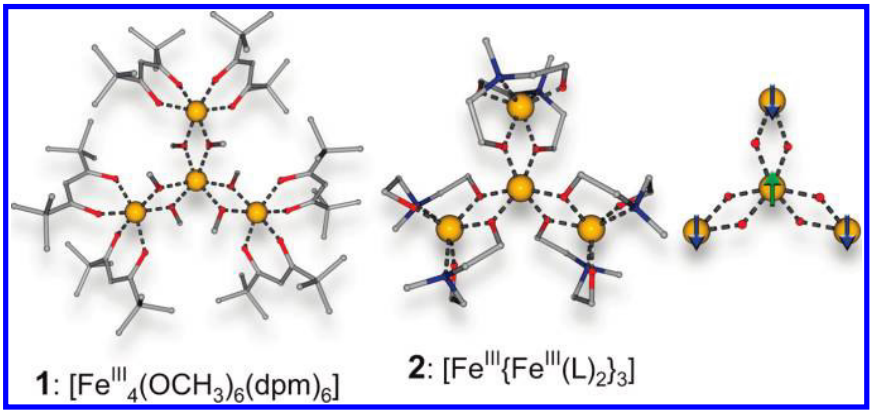

Figure 1. (Left and Center) Molecular structures of the ferric stars [Fe$^{III}_4$(OCH$_3$)$_6$(dpm)$_6$] (**1**) and [Fe^{III}{Fe^{III}(L)$_2$}$_3$] (**2**), respectively, with Fe: gold; O: red; N: blue; and C: gray. Solvate molecules and hydrogen atoms are omitted for clarity. The coordinating bonds from the donor atoms to iron are highlighted as dashed lines. (Right) Illustration of the ferrimagnetic ground state for **1** and **2**.

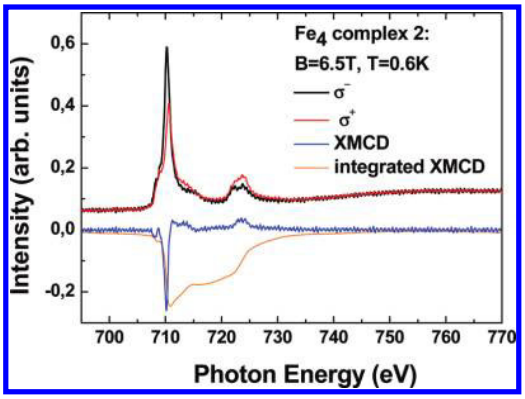

Figure 2. Fe L$_{2,3}$ edges of Fe$_4$ complex **2** recorded with left and right circularly polarized X-rays, the corresponding XMCD signal, and its integral. These measurements were performed with a reduced X-ray exposure (around 1% of the full beamline intensity) at a temperature of 0.6 K and in an external field of 6.5 T.

qualitatively demonstrated by means of Fe L edge XAS and scanning transmission X-ray microscopy for **2**.[21] Whereas an X-ray-induced reduction process from Fe^{3+} to Fe^{2+} was qualitatively demonstrated, some questions about the nature of this phenomenon remain to be clarified. X-ray-induced photochemistry, investigated by means of soft XAS, has been reported on a couple of Fe-based metallo-organic complexes[22,23] and discussed along possible photoreduction (photooxidation) or ligand photolysis mechanisms.[23] Also, charge-transfer effects from the ligand to the metal center or vice versa have been reported recently.[24,25]

In this paper, we address two different aspects concerning the magnetic and chemical properties of the complex [Fe^{III}{Fe^{III}(L)$_2$}$_3$] (**2**). First, we report XMCD measurements on the Fe L$_{2,3}$ edges, identifying the magnetic ground state unambiguously, and compare the local electronic structure around the Fe^{3+} ions with the result obtained on the [Fe$^{III}_4$(OCH$_3$)$_6$(dpm)$_6$] (**1**).[15] Second, we apply XPS in order to characterize and to quantify the photoreduction from Fe^{3+} to Fe^{2+} in **2** in more detail.

Figure 2 displays the Fe L$_{2,3}$ XAS spectra edges of **2** recorded with left and right circularly polarized light. The sample temperature was around 0.6 K, and an external field of 6.5 T was applied. The corresponding XMCD signal (blue) and its integral (orange) are also shown. We find a ferrimagnetic ground state with $S = 5$ for **2** from magnetic sum rule analysis. Using the result of our charge-transfer multiplet simulations as the basis for the assumptions of $n_h = 4.8$ and the spin sum rule correction factor of Teramura et al.,[26] considering mixing effects of the L_2 and L_3 edges via core hole Coulombic interactions, for Fe^{3+} (1/0.685), we obtain a spin moment of m_{spin} = 10.08 μ_b/molecule and an orbital moment of 0.1 μ_b/molecule. The almost quenched orbital moment can be explained by the half-filled $3d^5$ configuration; the overall magnetic moment obtained from the sum rules is in almost perfect agreement with results measured by magnetometry on **2**,[7] confirming its ferrimagnetic ground state of **2** (see Figure 1, right).

In the top panel of Figure 3, the Fe L$_{2,3}$ XAS is shown with charge-transfer multiplet simulations in different crystal field environments. Although the oxygen and nitrogen ligands do not span a perfect octahedral environment around the Fe ions, we find very good agreement of the experimental XAS and an Fe^{3+} charge-transfer simulation in an octahedral (O_h) simulation. This also accounts for the corresponding MCD spectrum (Figure 3, bottom panel). We considered a crystal field strength of $10Dq$ = 0.8 eV and a charge-transfer potential of Δ = 2.5 eV, resulting in a 82% $3d^5$ and 18% $3d^6\underline{L}$ charge-transfer configuration of the ground state. In comparison with experiments performed under almost the same experimental conditions on complex **1**,[15] we find some differences in detail. Whereas both spectra represent a pure Fe^{3+} multiplet structure, we find a significant lower crystal field strength (0.8 eV for **2** compared to 1.5 eV for **1**[15] obtained by ligand field multiplet simulations). This might be due to the different ligand structure around the Fe^{3+} ions, leading to a different local electronic structure of the complex [Fe^{III}{Fe^{III}(L)$_2$}$_3$] (**2**). The unequal coordination environment of **2** compared to that of **1** definitely leads to some deviations in the local electronic structure around the Fe ions. However, different magnetic ground-state properties are not observed.

Concerning the Fe valency, this result contradicts an earlier X-ray spectroscopic study of **2**.[19,20] Because this Fe^{3+}-based metallo-organic complex is obviously sensitive to soft X-ray-induced radiation damage or photoreduction,[21] we reduced the photon flux of the beamline to around 1% of the normal intensity for this experiment. After 6 h of exposure with this strongly reduced photon flux, a shoulder at the low-energy side of the L_3 edge became clearly visible (Figure 3, bottom panel), indicating the presence of some Fe^{2+} ions. In order to confirm the potential Fe^{3+} to Fe^{2+} photoreduction we then set the beamline photon flux back to 100%. Already, the first XAS spectrum measured with full beamline intensity (Figure 3,

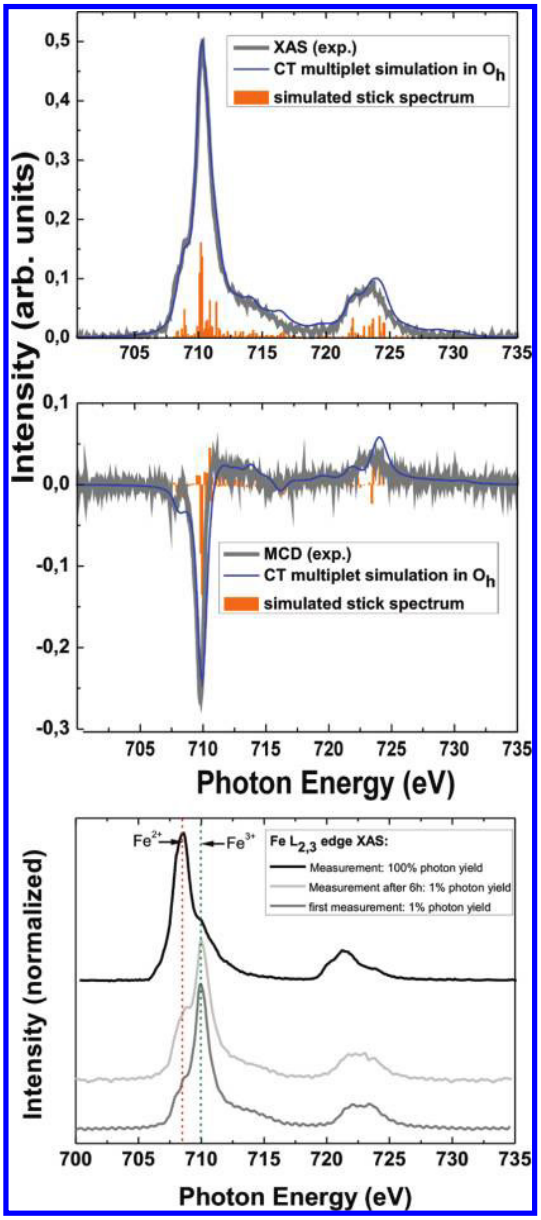

Figure 3. (Upper panel) Fe $L_{2,3}$ isotropic XAS in comparison with charge-transfer multiplet simulations in an octahedral (O_h) crystal field. (Lower panel) Three different XAS spectra (from bottom to top), XAS taken on a fresh sample spot with 1% beamline flux, after 6 h of exposure with 1% beamline flux on the same spot, and with 100% beamline flux on the same spot.

bottom panel, top spectrum) showed a pure Fe^{2+} multiplet structure. Thus, the Fe^{3+} to Fe^{2+} photoreduction process appears to be completed already after only one scan, demonstrating the high sensitivity of **2** to photoreduction. This fact may explain the results reported earlier.[19,20] The Fe_4 SMM of type $[Fe^{III}\{Fe^{III}(L)_2\}_3]$ (**2**) might well be much more sensitive to soft X-ray photoreduction than $[Fe^{III}{}_4(OCH_3)_6(dpm)_6]$ (**1**) because such a strong Fe^{3+} to Fe^{2+} reduction process, already finished after a single XAS scan across the Fe $L_{2,3}$ edge, under standard photon flux conditions of an undulator-based soft X-ray beamline has explicitly not been reported for **1**, neither in bulk form nor bonded to a gold surface.[13−15,18] This might be considered as an indication that the nature of the donor atoms around the iron centers is an important ingredient for the strength of soft X-ray-induced photoreduction in such metallo-organic complexes.

In order to shed more light on the nature of soft X-ray radiation induced photoreduction of the Fe^{3+} ions in this particular interesting Fe_4 SMM, we performed a systematic XPS study of this process. Figure 4 (upper panel) shows Fe 2p XPS of $[Fe^{III}\{Fe^{III}(L)_2\}_3]$ (**2**); a temporal evolution of the Fe valency from Fe^{3+} to Fe^{2+} is clearly visible by comparing the binding energy of the $2p_{3/2}$ peaks of the spectra (chemical shift), which have been saved every 10 cycles (labeled 1−10, 11−20, and so forth in Figure 4) recorded with a strongly reduced X-ray anode intensity (∼10% of the standard intensity). Hence, already, a monochromized standard Al Kα anode induces considerable photoreduction of the Fe^{III} ions in **2**. Because XPS is much more sensitive to chemical bonding and net charges than to crystal field splitting due to screening effects, we can use the reference spectra of FeO (Fe^{2+}) and $LiFeO_2$ (Fe^{3+}) (Figure 4) as a basis for a somewhat more quantitative analysis of the photoreduction process in **2**. We derived superpositions involving different percentages of the FeO and $LiFeO_2$ reference spectra, for instance, 10% of the FeO and 90% of the $LiFeO_2$ Fe 2p XPS, hence representing a reference for the XPS spectrum of a compound containing 10% Fe^{2+} and 90% Fe^{3+} ions. Then, we subtracted each Fe 2p XP spectrum of **2** (Figure 4, top panel) from each of the superimposed spectra representing merged Fe^{2+}/Fe^{3+} reference spectra and derived the mean-square error of each difference. Using this method, we can find the Fe^{3+} to Fe^{2+} ratio of each spectrum of **2** shown in the upper panel of Figure 4 at an accuracy of ∼10%. We present the quantitative temporal development of the Fe^{3+} to Fe^{2+} photoreduction in the lower panel of Figure 4. After 90 cycles with only 10% of the standard power (represented by the black squares), we recorded some more spectra at the same sample spot using full power of the X-ray source (blue dots in Figure 4, lower panel), saved either after each spectrum or after a couple of cycles. The spectra recorded with full power of the X-ray anode were scaled on the total power when comparing with the number of recorded cycles with 10% X-ray source power. One can fit the observed Fe^{3+} to Fe^{2+} photoreduction process by considering a simple exponential decay (red line). In both representations of the obtained photoreduction, one can see that all experimentally obtained Fe^{3+} to Fe^{2+} ratios only deviate 10% or less from the fit. Hence, we find an indication that the soft X-ray-induced Fe photoreduction process in the Fe_4 star-shaped SMM $[Fe^{III}\{Fe^{III}(L)_2\}_3]$ (**2**) likely takes place within a single process, at least ruling out the possibility of two or more parallel processes taking place on different slopes and time scales, whereas the exact nature of the underlying mechanism remains to be explored in more detail. In particular, it would be interesting to study whether this photoreduction process arises due to direct X-ray damage or secondary electrons excited by the incoming photons.

This study demonstrates that performing X-ray spectroscopic studies on coordination complexes like the Fe_4-based SMM needs a very careful consideration and investigation of potential X-ray-induced "damage" effects such as photooxidation or photoreduction. Although the amount of radiation and the number of subsequently excited secondary electrons are specifically high in the soft X-ray regime in the surface near the region of the sample, this basically accounts also for hard X-ray techniques, for example, during crystallographic studies.

On the other hand, this study might also motivate further studies on the exact mechanism of the observed photoreduction

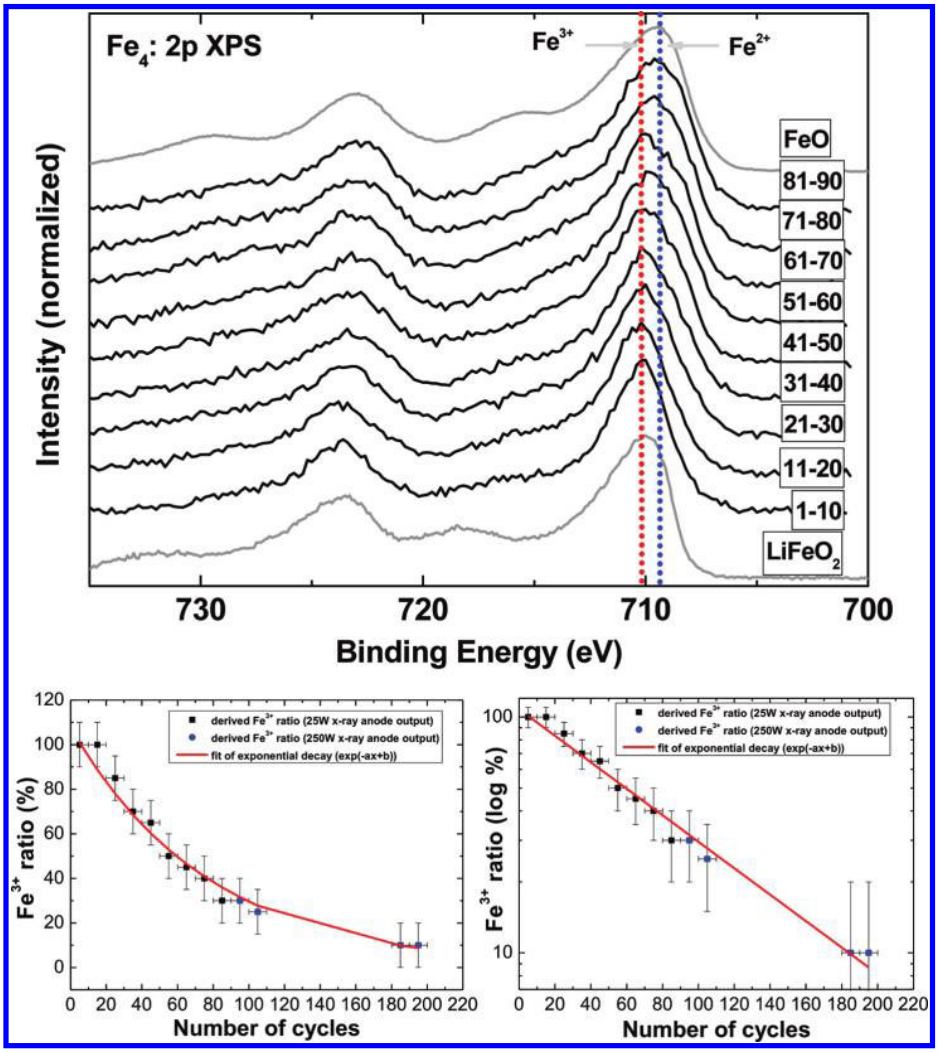

Figure 4. (Upper panel) Fe 2p core-level XPS of Fe_4 complex **2**. Spectra were saved and are plotted for each 10 cycles on the same sample spot (from bottom to top); reference spectra of FeO (Fe^{2+}) and $LiFeO_2$ (Fe^{3+}) are also shown. (Lower panel) Evolution of the Fe^{3+} to Fe^{2+} photoreduction over the number of recorded cycles along with an exponential fit of the Fe^{3+} decay (left) and the corresponding plot brought to a logarithmic scale (right).

process observed in **2**, maybe including a systematic investigation of the influence of different ligand coordination environments.

Finally, the fact that this specific photoreduction process takes place on a single time scale might also serve as useful information to motivate further work in complementary scientific fields such as X-ray radiation induced catalysis or photolysis processes in other similar Fe-based metallo-organic complexes and metalloproteins.[25,27,28]

In summary, we probed the magnetic ground state and addressed the soft X-ray-induced Fe^{3+} to Fe^{2+} photoreduction process in the star-shaped Fe_4 SMM $[Fe^{III}\{Fe^{III}(L)_2\}_3]$ (**2**) comprised of a different ligand environment compared to a similar molecule reported in the literature. We address the following findings: (i) the magnetic ground state of **2** is $S = 5$ as in **1**, whereas the local electronic structure around the iron centers is markedly different, manifesting itself in a reduced crystal field splitting and charge-transfer behavior; (ii) the Fe_4 complex **2** is highly sensitive to Fe^{3+} to Fe^{2+} photoreduction under soft X-ray radiation. In Fe $L_{2,3}$ edge XAS, performed under standard photon flux conditions at an undulator-based beamline, the reduction process may be finished already after one XAS scan; and (iii) with the help of a systematic Fe 2p XPS study, we could quantify the photoreduction process.

EXPERIMENTAL AND THEORETICAL DETAILS

XPS measurements were performed using a PHI 5600CI multitechnique spectrometer with monochromatic Al Kα, that is, 1486.6 eV radiation of 0.3 eV at full width at half-maximum. The intensity of the X-ray source was reduced to around 10% in these experiments. The overall resolution of the spectrometer was 1.5% of the pass energy of the analyzer, 0.45 eV in the present case. The XPS measurements were performed at room temperature. The spectra were calibrated using the C 1s states evolving from adsorbed hydrocarbon (285.0 eV).

XMCD experiments were performed at the Surface and Interface Microscopy (SIM) beamline of the Swiss Light Source (SLS). We used the 7 T cryomagnetic TBT-XMCD endstation, working with a $^3He-^4He$ dilution setup, characterized by base temperatures down to 0.3 K.[29] The samples of $[Fe^{III}\{Fe^{III}(L)_2\}_3]$ (**2**) (see also Figure 2) were pasted on carbon tape before connecting the sample holder to the dilution setup. Each single scan took 5 min.

The undulator-based beamline delivers a photon flux on the order of 10^{12} photons/sec at Fe $L_{2,3}$ edge photon energies of around 700 eV. In order to control potential radiation damage

Table 1. Slater Integrals (in eV) Used for the Fe^{2+} and Fe^{3+} Charge-Transfer Multiplet Simulations of the Fe $L_{2,3}$ XAS and XMCD[a]

	$2p^63d^5$ initial	$2p^53d^6$ final	$2p^63d^6\underline{L}$ initial	$2p^53d^7\underline{L}$ final
Slater Integrals				
F^2_{3d3d}	12.043	12.818	10.966	11.779
F^4_{3d3d}	7.535	8.023	6.815	7.327
F^2_{2p3d}		7.446		6.793
G^1_{2p3d}		5.566		5.004
G^3_{2p3d}		3.166		2.844
Spin−Orbit Coupling				
LS_{2p}		8.199		8.200
LS_{3d}	0.059	0.074	0.052	0.067

[a] Whereas the d−d and p−d integrals were reduced to 80% of the Hartree−Fock values for the subsequent simulation of the spectra, the spin−orbit parameters were not reduced.

effects, we tuned the beamline optics to reduce the flux of the incoming photons to around 1% of the maximum photon flux, and we measured several spots on each sample.

XAS and XMCD spectra were simulated within the charge-transfer multiplet model using the TT-multiplet program.[30−32] After calculating the atomic energy levels of the initial ($2p^n3d^m$) and final ($2p^{n-1}3d^{m+1}$) states and reducing them to 80% of their Hartree−Fock values (see Table 1), an octahedral crystal field was considered. Finally we considered an external magnetic field of $\mu_B B$ = 0.01 eV and charge transfer by introducing $3d^{m+1}\underline{L}$ states and broadened the simulated spectra considering lifetime broadening and spectrometer resolution.

AUTHOR INFORMATION

Corresponding Author

*E-mail: karsten.kuepper@uni-ulm.de.

ACKNOWLEDGMENT

Part of this work has been performed at the Swiss Light Source, Paul Scherrer Institut, Villigen, Switzerland. Financial and travel support from the SFB 569 and 583, the DFG priority programme SPP 1137 *Molecular Magnetism*, SA 276/29-1, and the EU's Seventh Framework Programme are gratefully acknowledged.

REFERENCES

(1) Verdaguer, M.; Bleuzen, A.; Train, C.; Garde, R.; Fabrizi de Biani, F.; Desplanches, C. Room-Temperature Molecule-Based Magnets. *Philos. Trans. R. Soc. London, Ser. A* **1999**, *357*, 2959–2976.

(2) Leuenberger, M. N.; Loss, D. Quantum Computing in Molecular Magnets. *Nature* **2001**, *410*, 789–793.

(3) Kahn, O. *Molecular Magnetism*; VCH: New York, 1993.

(4) Wende, H.; Bernien, M.; Luo, J.; Sorg, C.; Ponpandian, N.; Kurde, J.; Miguel, J.; Piantek, M.; Xu, X.; Eckhold, P.; Kuch, W.; Baberschke, K.; Panchmatia, P. M.; Sanyal, B.; Oppeneer, P. M.; Eriksson, O. Substrate-Induced Magnetic Ordering and Switching of Iron Porphyrin Molecules. *Nat. Mater.* **2007**, *6*, 516–520.

(5) Mögele, F.; Fantauzzi, D.; Wiedwald, U.; Ziemann, P.; Rieger, B. Two-Dimensional Assembly of Magnetic Binuclear Complexes: a Scanning Tunneling Microscopy Study. *Langmuir* **2009**, *25*, 13606–13613.

(6) Sessoli, R.; Gatteschi, D.; Caneschi, A.; Novak, M. A. Magnetic bistability in a metal-ion cluster. *Nature* **1993**, *365*, 141–143.

(7) Saalfrank, R. W.; Scheurer, A.; Bernt, B.; Heinemann, F. W.; Postnikov, A. V.; Schünemann, V.; Trautwein, A. X.; Alam, M. S.; Rupp, H.; Müller, P. The $\{Fe^{III}[Fe^{III}(L^1)_2]_3\}$ Star-Type Single-Molecule Magnet. *Dalton Trans.* **2006**, 2865–2874.

(8) Güdel, H. U.; Hauser, U. Exchange Interactions in Tris[*cis*-di-μ-hydroxo-bis(ethylenediamine)chromium(III)]chromium(III) Tris-(dithionate) Octahydrate. *Inorg. Chem.* **1980**, *19*, 1325–1328.

(9) Khanra, S.; Kuepper, K.; Weyhermüller, T.; Prinz, M.; Raekers, M.; Voget, S.; Postnikov, A. V.; de Groot, F. M. F.; George, S. J.; Coldea, M.; et al. Star-Shaped Molecule of $Mn^{II}_4O_6$ Core with an S_t = 10 High-Spin State. A Theoretical and Experimental Study with XPS, XMCD, and Other Magnetic Methods. *Inorg. Chem.* **2008**, *47*, 4605–4617.

(10) Pavlishchuk, V.; Birkelbach, F.; Weyhermüller, T.; Wieghardt, K.; Chaudhuri, P. Polynuclear Complexes of the Pendent-Arm Ligand 1,4,7-Tris(acetophenoneoxime)-1,4,7-triazacyclononane. *Inorg. Chem.* **2002**, *41*, 4405–4416.

(11) Prinz, M.; Kuepper, K.; Taubitz, C.; Raekers, M.; Khanra, S.; Biswas, B.; Weyhermüller, T.; Uhlarz, M.; Wosnitza, J.; Schnack, J.; et al. A Star-Shaped Heteronuclear $Cr^{III}Mn^{II}_3$ Species and Its Precise Electronic and Magnetic Structure: Spin Frustration Studied by X-ray Spectroscopic, Magnetic, and Theoretical Methods. *Inorg. Chem.* **2010**, *49*, 2093–2102.

(12) Petukhov, K.; Alam, M. S.; Rupp, H.; Strömsdörfer, S.; Müller, P.; Scheurer, A.; Saalfrank, R. W.; Kortus, J.; Postnikov, A.; Ruben, M.; et al. STM Spectroscopy of Magnetic Molecules. *Coord. Chem. Rev.* **2009**, *253*, 2387–2398.

(13) Mannini, M.; Pineider, F.; Sainctavit, P.; Danieli, C.; Otero, E.; Sciancalepore, C.; Talarico, A. M.; Arrio, M.-A.; Cornia, A.; Gatteschi, D.; et al. Magnetic Memory of a Single-Molecule Quantum Magnet Wired to a Gold Surface. *Nat. Mater.* **2009**, *8*, 194–197.

(14) Mannini, M.; Pineider, F.; Danieli, C.; Totti, F.; Sorace, L.; Sainctavit, P.; Arrio, M.-A.; Otero, E.; Joly, L.; Cezar, J. C.; et al. Quantum Tunnelling of the Magnetization in a Monolayer of Oriented Single-Molecule Magnets. *Nature* **2010**, *468*, 417–421.

(15) Mannini, M.; Pineider, F.; Sainctavit, P.; Joly, L.; Fraile-Rodríguez, A.; Arrio, M.-A.; Cartier dit Moulin, C.; Wernsdorfer, W.; Cornia, A.; Gatteschi, D.; et al. X-ray Magnetic Circular Dichroism Picks out Single-Molecule Magnets Suitable for Nanodevices. *Adv. Mater.* **2009**, *21*, 167–171.

(16) Barra, A. L.; Caneschi, A.; Cornia, A.; Fabrizi de Biani, F.; Gatteschi, D.; Sangregorio, C.; Sessoli, R.; Sorace, L. Single-Molecule Magnet Behavior of a Tetranuclear Iron(III) Complex. The Origin of Slow Magnetic Relaxation in Iron(III) Clusters. *J. Am. Chem. Soc.* **1999**, *121*, 5302–5310.

(17) Accorsi, S.; Barra, A.-L.; Caneschi, A.; Chastanet, G.; Cornia, A.; Fabretti, A. C.; Gatteschi, D.; Mortalò, C.; Olivieri, E.; Parenti, F.; et al. Tuning Anisotropy Barriers in a Family of Tetrairon(III) Single-Molecule Magnets with an S = 5 Ground State. *J. Am. Chem. Soc.* **2006**, *128*, 4742–4755.

(18) Rodriguez-Douton, M. J.; Mannini, M.; Armelao, L.; Barra, A.-L.; Tancini, E.; Sessoli, R.; Cornia, A. One-Step Covalent Grafting of Fe_4 Single-Molecule Magnet Monolayers on Gold. *Chem. Commun.* **2011**, *47*, 1467–1469.

(19) Takács, A. F.; Neumann, M.; Postnikov, A. V.; Kuepper, K.; Scheurer, A.; Sperner, S.; Saalfrank, R. W.; Prince, K. C. Electronic Structure Study by Means of X-ray Spectroscopy and Theoretical Calculations of the "Ferric Star" Single Molecule Magnet. *J. Chem. Phys.* **2006**, *124*, 044503.

(20) Some of the authors (K.K., A.S., S.S., R.W.S., and M.N.) also co-authored the work by Takács et al.[19] The X-ray spectroscopic experiments presented in that paper have been not recorded with lowered photon flux, thus resulting in spectra suggesting divalent iron. With these new results presented here, the authors involved in the mentioned earlier work[19] correct those results concerning the Fe valency in complex **2**.

(21) Schmidt, N.; Scheurer, A.; Sperner, S.; Fink, R. H. Microspectroscopic Analysis of the X-ray-Induced Photoreduction in Fe- and Mn-Containing SMMs. *Z. Naturforsch. B* **2010**, *65*, 390–398.

(22) Collison, D.; Garner, C. D.; McGrath, C. M.; Mosselmans, J. F. W.; Roper, M. D.; Seddon, J. M. W.; Sinn, E.; Young, N. A. Soft

X-ray Photochemistry at the $L_{2,3}$-Edges in $K_3[Fe(CN)_6]$, $[Co(acac)_3]$ and $[Cp_2Fe][BF_4]$. *J. Synchrotron Rad.* **1999**, *6*, 585–587.

(23) George, S. J.; Fu, J.; Guo, Y.; Drury, O. B.; Friedrich, S.; Rauchfuss, T.; Volkers, P. I.; Peters, J. C.; Scott, V.; Brown, S. D. et al. X-ray Photochemistry in Iron Complexes from Fe(0) to Fe(IV) — Can a Bug Become a Feature? *Inorg. Chim. Acta* **2008**, *361*, 1157–1165.

(24) Bonhommeau, S.; Pontius, N.; Cobo, S.; Salmon, L.; de Groot, F. M. F.; Molnár, G.; Bousseksou, A.; Dürr, H. A.; Eberhardt, W. Metal-to-Ligand and Ligand-to-Metal Charge Transfer in Thin Films of Prussian Blue Analogues Investigated by X-ray Absorption Spectroscopy. *Phys. Chem. Chem. Phys.* **2008**, *10*, 5882–5889.

(25) Aziz, E. F.; Rittmann-Frank, M. H.; Lange, K. M.; Bonhommeau, S.; Chergui, M. Charge Transfer to Solvent Identified Using Dark Channel Fluorescence-Yield L-Edge Spectroscopy. *Nat. Chem.* **2010**, *2*, 853–857.

(26) Teramura, Y.; Tanaka, A.; Takeo, J. Effect of Coulomb Interaction on the X-ray Magnetic Circular Dichroism Spin Sum Rule in 3d Transition Elements. *J. Phys. Soc. Jpn.* **1999**, *65*, 1053–1055.

(27) Wang, H.; Peng, G.; Miller, L. M.; Scheuring, E. M.; George, S. J.; Chance, M. R.; Cramer, S. P. Iron L-Edge X-ray Absorption Spectroscopy of Myoglobin Complexes and Photolysis Products. *J. Am. Chem. Soc.* **1997**, *119*, 4921–4928.

(28) Cook, P. L.; Johnson, P. S.; Liu, X.; Chin, A.-L.; Himpsel, F. J. Radiation Damage in Biomimetic Dye Molecules for Solar Cells. *J. Chem. Phys.* **2009**, *131*, 214702.

(29) Letard, I.; Sainctavit, P.; Cartier dit Moulin, C.; Kappler, J.-P.; Ghigna, P.; Gatteschi, D.; Doddi, B. Remnant Magnetization of Fe8 High-Spin Molecules: X-ray Magnetic Circular Dichroism at 300 mK. *J. Appl. Phys.* **2007**, *101*, 113920.

(30) de Groot, F. M. F. X-ray Absorption and Dichroism of Transition Metals and Their Compounds. *J. Electron Spectrosc. Relat. Phenom.* **1994**, *67*, 529–622.

(31) de Groot, F. Multiplet Effects in X-ray Spectroscopy. *Coord. Chem. Rev.* **2005**, *249*, 31–63.

(32) de Groot, F.; Kotani, A. Core Level Spectroscopy of Solids. *Advances in Condensed Matter Science*; CRC Press: Boca Raton, FL, 2008; Vol. 6.

Publication H12

[**H12**] K. Balinski, L. Schneider, J. Wöllermann, A. Buling, L Joly, C. Piamonteze, H. L. C. Feltham, S. Brooker, A. K. Powell, B. Delley, and K. Kuepper. *Element specific determination of the magnetic properties of two macrocyclic tetranuclear 3d-4f complexes with Cu_3Tb core by means of X-ray magnetic circular dichroism (XMCD)* , Phys. Chem. Chem. Phys. **20**, 21286-21293 (2018), doi: 10.1039/C7CP08689J.

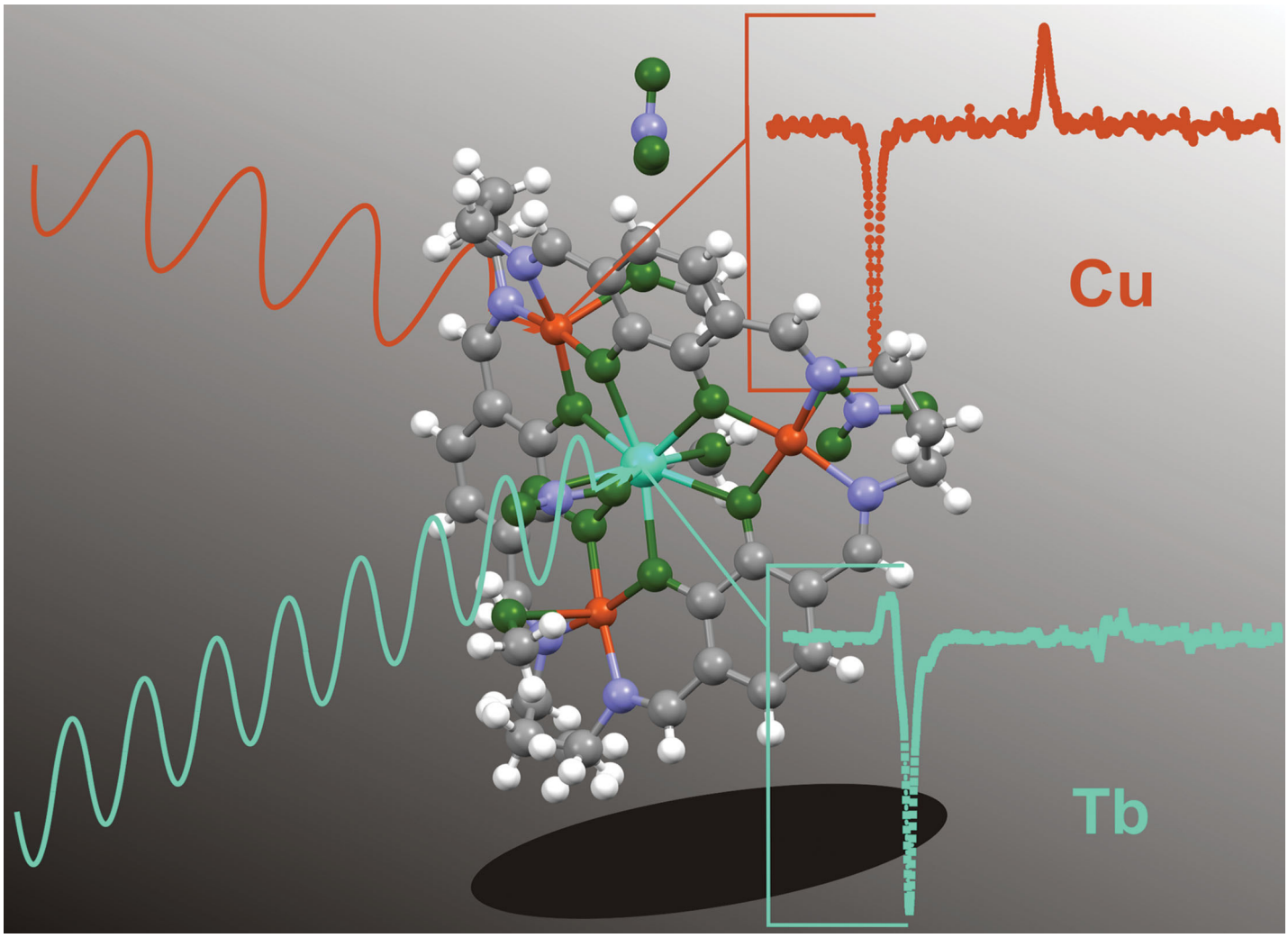

Showcasing collaborative research from the Electronic Structure group, Department of Physics, University of Osnabrück; the Université of Strasbourg; the Paul Scherrer Institute; the Department of Chemistry, University of Otago; and the Institute for Inorganic Chemistry, Karlsruhe Institute of Technology.

Element specific determination of the magnetic properties of two macrocyclic tetranuclear 3d–4f complexes with a Cu_3Tb core by means of X-ray magnetic circular dichroism (XMCD)

In this paper, we investigate two macrocyclic single molecule magnets (SMMs) with 3d–4f Cu_3Tb core by means of X-ray magnetic circular dichroism (XMCD), a useful technique which is not only element specific but also an inherently fast spectroscopic technique.

As featured in:

See K. Kuepper *et al.*, *Phys. Chem. Chem. Phys.*, 2018, **20**, 21286.

ROYAL SOCIETY OF CHEMISTRY

rsc.li/pccp

Registered charity number: 207890

PCCP

PAPER

View Article Online
View Journal | View Issue

Cite this: *Phys. Chem. Chem. Phys.*, 2018, **20**, 21286

Element specific determination of the magnetic properties of two macrocyclic tetranuclear 3d–4f complexes with a Cu_3Tb core by means of X-ray magnetic circular dichroism (XMCD)

K. Balinski,[a] L. Schneider,[a] J. Wöllermann,[a] A. Buling,[a] L. Joly,[b] C. Piamonteze,[c] H. L. C. Feltham,[d] S. Brooker,[d] A. K. Powell,[ef] B. Delley[c] and K. Kuepper*[a]

Received 29th December 2017,
Accepted 29th May 2018

DOI: 10.1039/c7cp08689j

rsc.li/pccp

We apply X-ray magnetic circular dichroism to study the internal magnetic structure of two very promising star shaped macrocyclic complexes with a $Cu^{II}_3Tb^{III}$ core. These complexes are rare examples prepared with a macrocyclic ligand that show indications of SMM (Single Molecule Magnet) behavior, and they differ only in ring size: one has a propylene linked macrocycle, $[Cu^{II}_3Tb^{III}(\mathbf{L^{Pr}})(NO_3)_2(MeOH)(H_2O)_2](NO_3)\cdot 3H_2O$ (nickname: $Cu_3Tb(\mathbf{L^{Pr}})$), and the other has the butylene linked analogue, $[Cu^{II}_3Tb^{III}(\mathbf{L^{Bu}})(NO_3)_2(MeOH)(H_2O)](NO_3)\cdot 3H_2O$ (nickname: $Cu_3Tb(\mathbf{L^{Bu}})$). We analyze the orbital and spin contributions to the Cu and Tb ions quantitatively by applying the spin and orbital sum rules concerning the L_2 (M_4)/L_3 (M_5) edges. In combination with appropriate ligand field simulations, we demonstrate that the Tb(III) ions contribute with high orbital magnetic moments to the magnetic anisotropy, whereas the ligand field determines the easy axis of magnetization. Furthermore, we confirm that the Cu(II) ions in both molecules are in a divalent valence state, the magnetic moments of the three Cu ions appear to be canted due to 3d–3d intramolecular magnetic interactions. For $Cu_3Tb(\mathbf{L^{Pr}})$, the corresponding element specific magnetization loops reflect that the Cu(II) contribution to the overall magnetic picture becomes more important as the temperature is lowered. This implies a low value for the 3d–4f coupling.

Introduction

In magnetic molecules, spin coupling between paramagnetic transition-metal ions is mediated *via* bridging ligand atoms, leading to a variety of interesting fundamental properties such as intramolecular exchange interactions or magnetic anisotropy.[1–5] Besides hundreds of known single molecule magnets (SMMs) and the famous Mn_{12}–Ac cluster,[6] so called star-shaped molecules, which comprise four transition metal ions in the form of a central ion and three peripheral ions, belong to the most promising and simplest inorganic systems showing SMM behavior.[7] A number of star-shaped molecules with intriguing magnetic properties have been reported, including those with a Cr^{III}_4 core with a high spin state $S = 3$,[8] a Mn^{II}_4 core with $S = 10$,[9] a Ni^{II}_4 core,[10] or the spin frustrated $Cr^{III}(Mn^{II})_3$ complex.[11] The star-shaped trigonal, metal-centered Fe_4 complex[12] is of special interest due to some remarkable progress concerning substrate deposition and tunneling experiments.[13,14] In addition to a rich variety of 3d transition metal based SMMs,[15–18] recently, lanthanides (4f ions) have attracted significant interest.[17,19–21,33] For the last few years, complexes comprising both 3d and 4f ions have been under intense discussion as some of them exhibit interesting magnetic properties such as slow relaxation of magnetization making them potentially good candidates for SMMs.[17,22–26] In particular, Tb^{III} and Dy^{III} exhibit high single ion anisotropies,[27] and ferromagnetic coupling between Tb^{III} (Dy^{III}) and 3d transition metal Cu^{II} ions has been reported.[22,28–32]

Feltham *et al.* prepared a family of 3d–4f macrocyclic complexes $[M^{II}_3Ln^{III}(\mathbf{L^n})(NO_3)_{3-m}(solvent)_x](NO_3)_m$ (m = 0 or 1), all of which feature a star shaped $M^{II}_3Ln^{III}$ core, using organic macrocyclic ligands that are large enough to contain several metal ions and provide two types of binding pockets, three N_2O_2 pockets for the three 3d metal ions and one O_6 pocket for the 4f ion (Fig. 1).[31,33]

[a] *Fachbereich Physik and Institut für Physik und Chemie neuer Materialien, Universität Osnabrück, Barbarastr. 7, Osnabrück D-49069, Germany. E-mail: kkuepper@uos.de*
[b] *Université de Strasbourg, CNRS, IPCMS, UMR 7504, Strasbourg F-67000, France*
[c] *Paul Scherrer Institute, Villigen CH-5232, Switzerland*
[d] *Department of Chemistry and the MacDiarmid Institute, University of Otago, P.O. Box 56, Dunedin 9054, New Zealand*
[e] *Institut für Anorganische Chemie, Karlsruhe Institute of Technology, Engesserstrasse 15, Karlsruhe D-76131, Germany*
[f] *Institute of Nanotechnology, Karlsruhe Institute of Technology, Hermann-von-Helmholtz-Platz 1, Eggenstein-Leopoldshafen D-76344, Germany*

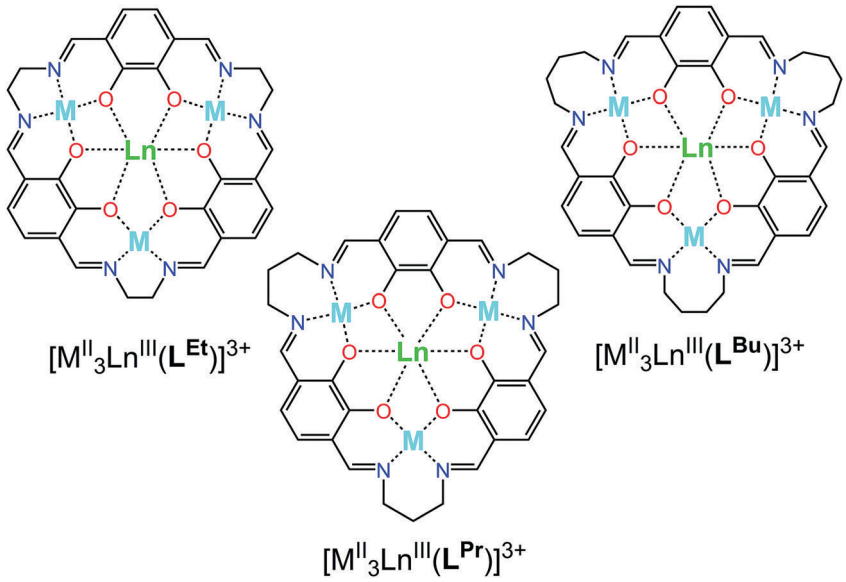

Fig. 1 A star shaped tetrametallic $M^{II}_3Ln^{III}$ core is a feature of all of the members of the large family of 3d–4f macrocyclic complexes $[M^{II}_3Ln^{III}(\mathbf{L^n})(NO_3)_{3-m}(solvent)_x](NO_3)_m$ (m = 0 or 1).

The $[Cu^{II}_3Tb^{III}(\mathbf{L^{Pr}})(NO_3)_2(MeOH)(H_2O)_2](NO_3)\cdot 3H_2O$ cluster (nickname: $Cu_3Tb(\mathbf{L^{Pr}})$, Fig. 2) exhibits slow relaxation of magnetization, and hence SMM behavior.[29] By tuning the ligand field, by encapsulating the $Cu^{II}_3Tb^{III}$ core into a larger, butylene linked, macrocycle, the analogue $[Cu^{II}_3Tb^{III}(\mathbf{L^{Bu}})(NO_3)_2(MeOH)(H_2O)](NO_3)\cdot 3H_2O$ (nickname: $Cu_3Tb(\mathbf{L^{Bu}})$, Fig. 2) was obtained. $Cu_3Tb(\mathbf{L^{Bu}})$ features apical binding of two rather than one nitrate ion to the oblate Tb^{III} ion, and also, a quantifiable relaxation in zero dc field could be measured.[32] 3d–4f complexes exhibit complex magnetic properties as they are dominated by strong spin–orbit coupling and crystal field interactions of the lanthanide ions and exchange interactions between the lanthanide and the transition metal ions.[17,32–35] In X-ray magnetic circular dichroism (XMCD), one uses X-rays (in this case, soft X-rays) to excite the magnetized sample in question. This opens the possibility to study the magnetic properties of different ions (here, Cu and Tb) element specifically, since the transition metal $L_{2,3}$ edges (2p → 3d transition) and rare earth $M_{4,5}$ edges (3d → 4f transition) are energetically separated. Employing well established sum rules allows the determination of the respective spin and orbital contributions to the overall magnetic moment. Since the Franck–Condon principle states that X-ray absorption is a very fast process with respect to vibrations, hence, XAS and XMCD spectra can be viewed as a superposition of all possible (vibrational) distorted positions of the probed element. The overall width of the bands obtained is dominated by core-hole lifetimes and effects like Coster–Kronig Auger decay, making it difficult to separate all broadening effects in the X-ray absorption spectra. However, since the measurements presented here have been performed at rather low temperatures down to 3 K, we can assume that dynamical (vibrational) effects are significantly reduced. Therefore, we employ XMCD to study the internal magnetic structure of this pair of macrocyclic, star shaped Cu_3Tb SMMs[29,30] as a very powerful technique to study heteronuclear molecule-based magnets because of its generally high sensitivity to the local electronic structure and, moreover, the force of element and shell selectivity of the Cu^{II} and Tb^{III} ions in our case. Furthermore, XMCD offers the unique capability to obtain element-selective spin and orbital moments separately in heteronuclear systems.[28,36–38]

Experimental and theoretical section

XMCD experiments were performed using a high field magnet system at the ID10 beamline for advanced dichroism (BLADE) at the lowest reachable temperature of 3 K and in external magnetic fields up to 13.5 T. The Cu_3Tb molecules were pasted on carbon tape before connecting the sample holder to the high field magnet system. The flux on I10 is about 10^{12} photons per second at 950 eV. In order to control potential radiation damage, we performed a number of scans at the Cu $L_{2,3}$ and Tb $M_{4,5}$ edges at several spots of the sample and reduced the time per scan to around one minute.

The propylene and butylene linked macrocyclic complexes, $Cu_3Tb(\mathbf{L^{Pr}})$ and $Cu_3Tb(\mathbf{L^{Bu}})$, were prepared as previously described, and the cif files for both are available from those papers.[29,30]

$Cu_3Tb(\mathbf{L^{Pr}})$ *i.e.* $[Cu^{II}_3Tb^{III}(\mathbf{L^{Pr}})(NO_3)_2(MeOH)(H_2O)_2](NO_3)\cdot H_2O$

Diffusion of diethyl ether vapour into the reaction solution yielded the crude product. This solid was re-dissolved in MeOH and the solution vapour diffused with diethyl ether to obtain the pure product as an olive brown powder. Found: C 33.28, H 3.36 N 10.00; calc. for $C_{34}H_{40}N_9O_{19}Cu_3Tb$ (1228.30 g mol^{-1}): C 33.25, H 3.28. N 10.26.

$Cu_3Tb(\mathbf{L^{Bu}})$ *i.e.* $[Cu^{II}_3Tb^{III}(\mathbf{L^{Bu}})(NO_3)_2(MeOH)(H_2O)](NO_3)\cdot H_2O$

Diffusion of diethyl ether vapour into the reaction solution yielded the crude product. This solid was re-dissolved in MeOH

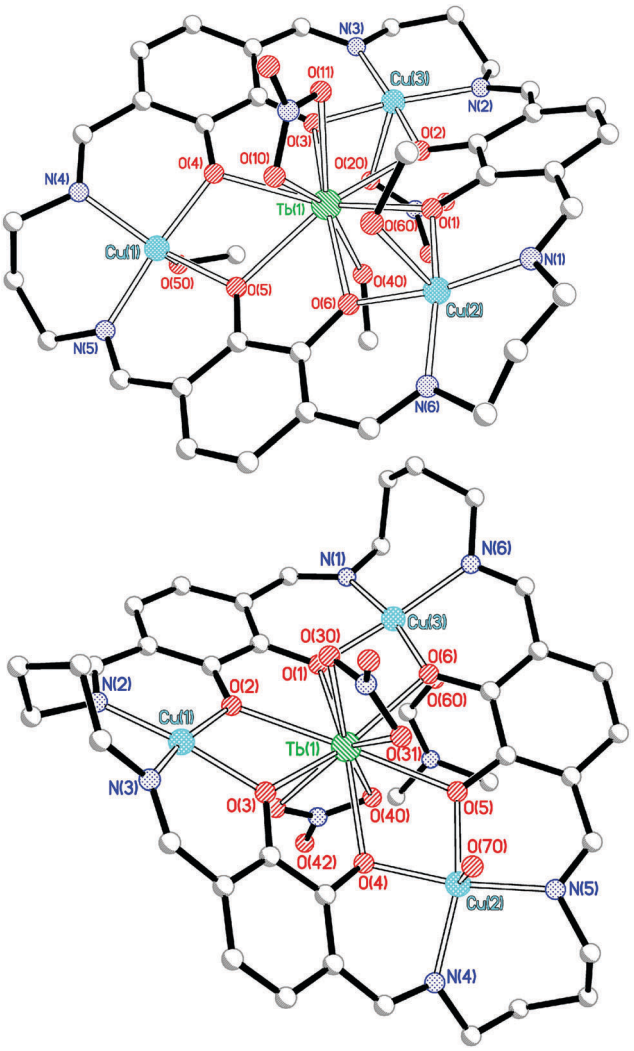

Fig. 2 Structures of the cations of the two tetrametallic 3d–4f macrocyclic complexes of interest in this work. Top: $[Cu^{II}_3Tb^{III}(\mathbf{L^{Pr}})(NO_3)_2(MeOH)_3](NO_3)$ (nickname: $Cu_3Tb(\mathbf{L^{Pr}})$). Bottom: $[Cu^{II}_3Tb^{III}(\mathbf{L^{Bu}})(NO_3)_2(DMF)(H_2O)](NO_3)\cdot DMF$ (nickname: $Cu_3Tb(\mathbf{L^{Bu}})$). Non-coordinated anions and solvent molecules have been omitted.

and the solution vapour diffused with diethyl ether to obtain the pure product as a brown powder. Found: C 35.51, H 3.79, N 10.19; calc. for $Cu_3TbC_{37}H_{44}N_9O_{18}$ (1252.37 g mol^{-1}): C 35.49, H 3.54, N 10.07.

For $Cu_3Tb(\mathbf{L^{Pr}})$, complementary XMCD measurements with a special emphasis on recording element specific magnetization curves were performed at the Surface and Interface Microscopy (SIM) beamline of the Swiss Light Source (SLS). We used the 7 T cryomagnetic TBT-XMCD endstation[39] at temperatures of 5 and 10 K. The samples were pasted on carbon tape before connecting the sample holder to the endstation. Using this setup, each single scan took around five minutes. The undulator based beamline delivers a photon flux in the order of 10^{12} photons per s at the Cu $L_{2,3}$ edges at a photon energy of around 950 eV. In order to control potential radiation damage effects, we tuned the beamline optics to reduce the flux of the incoming photons to around 1% of the maximum photon flux, and we measured several spots on each sample.

The XMCD spectra of the Cu and Tb ions were calculated by means of full multiplet simulations[40] using the multiX software.[41] The ligands are replaced by effective point charges at the atomic positions, which are extracted from the crystallographic information file (CIF) of the $Cu_3Tb(\mathbf{L^{Pr}})$ molecule for each of the three Cu sites and the Tb site separately. The whole molecule was used as the input for the crystal field calculation. The crystal field obtained from this calculation was not re-scaled for the simulations. This has the advantage that we do not have to deal with the crystal field strengths and symmetries as fitting parameters, since the crystal fields of the three Cu ions have different symmetries, leading to different ligand field strengths, and the Tb ligand field is also strongly anisotropic. Simulations were performed considering a temperature of $T = 5$ K and an external magnetic field of $B = 7$ T, with a number of holes $n_h = 1$ for Cu and $n_h = 6$ for Tb. The values of the spin–orbit coupling and coulomb interactions for Cu were reduced to 94% and 80%, and for Tb, to 97% and 60% of the atomic values, respectively. The reduction factors are tunable parameters and it is usual that electron–electron interactions need to be reduced to obtain a good fitting. The reduction of spin–orbit coupling is minor. Finally, we broadened the simulated spectra considering the lifetime broadening and spectrometer resolution of 0.4 eV for Cu and 0.5 eV for Tb.

Results and discussion

We want to shed light on the internal magnetic structure of macrocycles $Cu_3Tb(\mathbf{L^{Pr}})$ and $Cu_3Tb(\mathbf{L^{Bu}})$ (*cf.* Fig. 1). Fig. 3a and 4a present the polarization dependent X-ray absorption spectra across the Cu $L_{2,3}$ and Tb $M_{4,5}$ edges of $Cu_3Tb(\mathbf{L^{Pr}})$. The spectra were recorded at a temperature of 5 K and in an external magnetic field of 7 T. The XAS and XMCD spectra of $Cu_3Tb(\mathbf{L^{Bu}})$ and those recorded at 13.5 T and at different temperatures for both the molecules are somewhat less resolved but very similar in shape and not shown here. The Cu $L_{2,3}$ X-ray absorption spectrum (*cf.* Fig. 3a) comprises two prominent peaks at 934.2 eV (Cu L_3 edge), and 953.6 eV (L_2 edge). The corresponding XMCD is strongly negative ($\sim$42%) at the L_3 edge and has a positive sign at the L_2 edge. We applied the sum rules[36] to extract the spin (m_S) and orbital (m_L) contributions to the total magnetic moment (m_{tot}) for the spectra taken of both molecules at the different temperatures and external magnetic fields. The results are summarized in Table 1. Fig. 3b shows ligand field simulations of the Cu $L_{2,3}$ XAS and XMCD spectra with the parameters described in the Experimental and theoretical section. Cu^{II} ions have a $3d^9$ configuration and a $3d^{10}$ configuration in the excited state. Hence, 3d multipole interactions are not present and the spectra are dominated by crystal field effects, exchange field interactions and the 3d spin–orbit coupling. Since the samples are powders comprising nanocrystals in random orientation during the experiments we performed calculations in the [100], [010], and [001] directions (six point scheme) for all three Cu ions separately and averaged over all simulations. We find almost perfect agreement between the

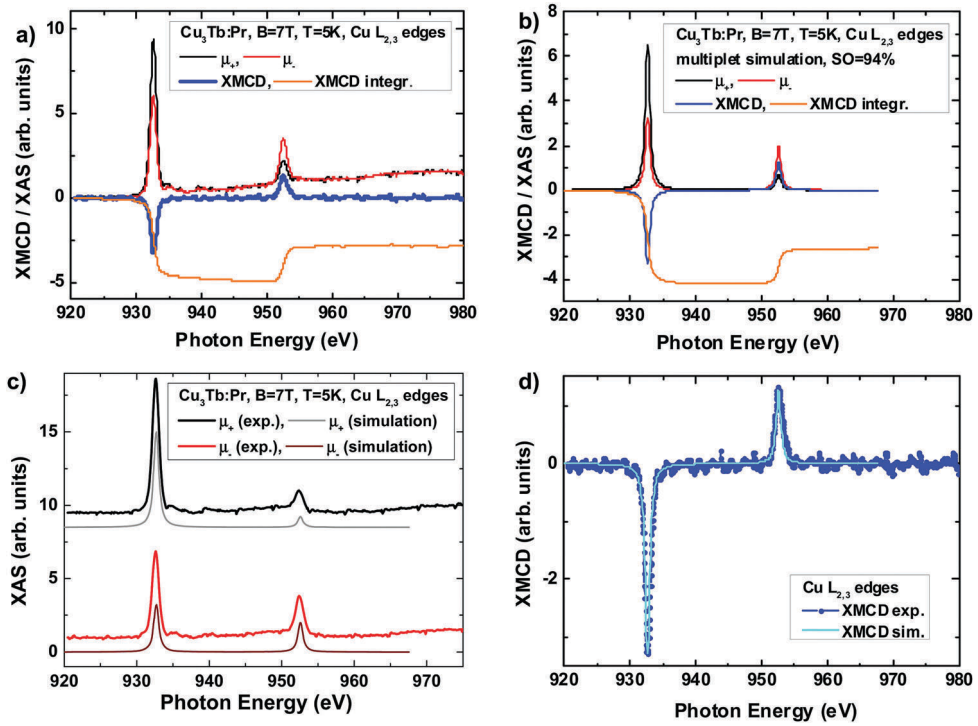

Fig. 3 (a) X-ray absorption spectra across the Cu $L_{2,3}$ edges of $Cu_3^{II}Tb^{III}(\mathbf{L}^{Pr})$ in an external magnetic field of $B = \pm 7$ T and at a temperature of $T = 5$ K, performed with left and right circular polarized photons leading to the overall dichroic spectra labelled μ_+ and μ_-. The corresponding XMCD signal and its integral are also shown. (b) Corresponding spectra from the ligand field simulations. (c) Comparison of the experimental and the simulated circularly polarized X-ray absorption spectra. (d) Comparison of the experimental and the simulated XMCD signal.

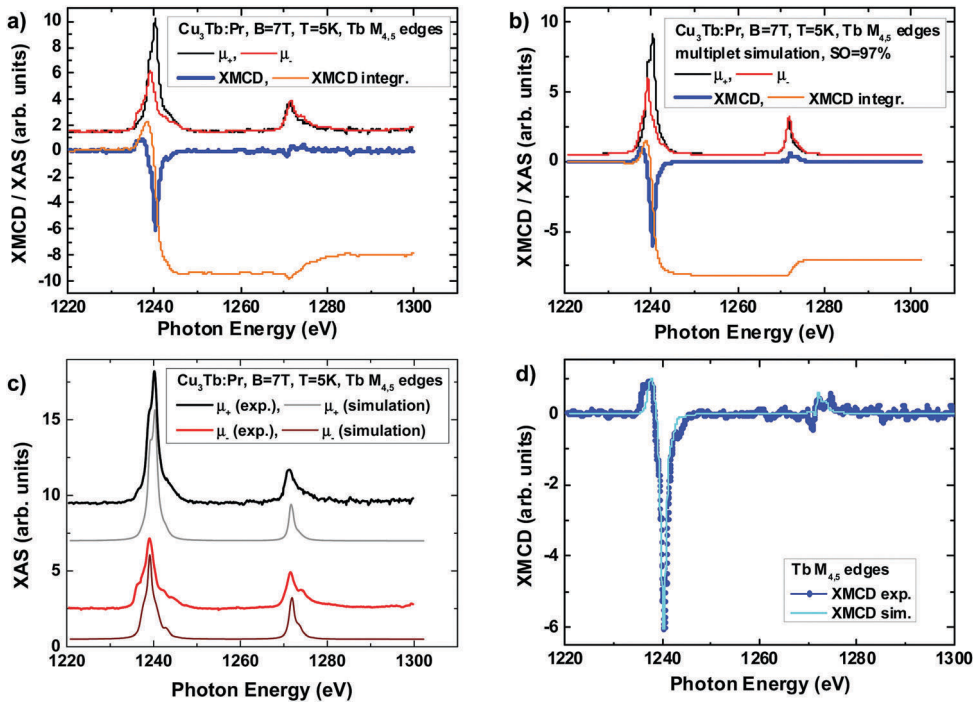

Fig. 4 (a) X-ray absorption spectra across the Tb $M_{4,5}$ edges of $Cu_3^{II}Tb^{III}(\mathbf{L}^{Pr})$ in an external magnetic field of $B = \pm 7$ T and at a temperature of $T = 5$ K, performed with left and right circular polarized photons leading to the overall dichroic spectra labelled μ_+ and μ_-. The corresponding XMCD signal and its integral are also shown. (b) Corresponding spectra from the ligand field simulations. (c) Comparison of the experimental and the simulated circularly polarized X-ray absorption spectra. (d) Comparison of the experimental and the simulated XMCD signal.

Table 1 Cu and Tb magnetic moments extracted from the XMCD experiments at different external magnetic fields and temperatures and from the multiplet simulations compared to the Hund's rule values

Molecule	B (T)	T (K)	Ion	m_L (μ_B per atom)	m_S (μ_B per atom)	m_{tot} (μ_B per atom)	m_{tot} (Hund) (μ_B per atom)	$\langle L_Z\rangle/\langle S_Z\rangle$	$\langle L_Z\rangle/\langle S_Z\rangle$ (Hund)
$Cu^{II}_3Tb^{III}(L^{Bu})$	13.5	3	Cu^{II}	0.09	0.62	0.71	3.0	0.29	4.0
$Cu^{II}_3Tb^{III}(L^{Bu})$	13.5	3	Tb^{III}	1.42	3.02	4.44	9.0	0.94	1.0
$Cu^{II}_3Tb^{III}(L^{Bu})$	7.0	3	Cu^{II}	0.08	0.42	0.50	3.0	0.38	4.0
$Cu^{II}_3Tb^{III}(L^{Bu})$	7.0	3	Tb^{III}	1.57	3.02	4.59	9.0	1.04	1.0
$Cu^{II}_3Tb^{III}(L^{Pr})$	13.5	3	Cu^{II}	0.05	0.50	0.55	3.0	0.20	4.0
$Cu^{II}_3Tb^{III}(L^{Pr})$	13.5	3	Tb^{III}	1.66	3.78	5.44	9.0	0.88	1.0
$Cu^{II}_3Tb^{III}(L^{Pr})$	7.0	3	Cu^{II}	0.08	0.42	0.50	3.0	0.38	4.0
$Cu^{II}_3Tb^{III}(L^{Pr})$	7.0	3	Tb^{III}	1.84	3.25	5.09	9.0	1.13	1.0
$Cu^{II}_3Tb^{III}(L^{Pr})$	**7.0**	**5**	**Cu^{II}**	**0.10**	**0.49**	**0.59**	**3.0**	**0.41**	**4.0**
$Cu^{II}_3Tb^{III}(L^{Pr})$	**7.0**	**5**	**Tb^{III}**	**1.25**	**3.09**	**4.34**	**9.0**	**0.81**	**1.0**
$Cu^{II}_3Tb^{III}(L^{Pr})$	7.0	10	Cu^{II}	0.03	0.37	0.40	3.0	0.16	4.0
$Cu^{II}_3Tb^{III}(L^{Pr})$	7.0	10	Tb^{III}	1.42	3.31	4.73	9.0	0.86	1.0
Cu^{2+} sim. $Cu_3Tb(L^{Pr})$	**7.0**	**5**	**Cu^{II}**	**0.22**	**0.92**	**1.14**	**3.0**	**0.48**	**4.0**
Tb^{3+} sim. $Cu_3Tb(L^{Pr})$	**7.0**	**5**	**Tb^{III}**	**1.57**	**3.34**	**4.91**	**9.0**	**0.94**	**1.0**

experimental and simulated spectra with respect to the spectral shape and the L_3/L_2 ratio in XAS and XMCD (*cf.* Fig. 3c and d). Analogous to the experimental spectra, we also applied the spin and orbital sum rules to the simulated spectra (*cf.* Table 1). For both molecules, we find significantly lower values for m_S in comparison with the simulations and rather low orbital contributions to the Cu^{II} magnetic moment, in agreement with the simulations. Hamamatsu *et al.* reported very similar values of the Cu^{II} spin and orbital magnetic moment in $Cu^{II}_2Tb^{III}$ clusters compared to those found here, on the other hand, the Cu^{II} ions in analogous $Cu^{II}_2Dy^{III}$ clusters have higher magnetic moments.[28] The low orbital moment is expected for 3d transition metal ions in crystal fields. The significantly lower spin moment compared to the simulation may be explained by a not completely ferromagnetic (parallel) alignment of the spins stemming from three different Cu^{II} sites. The simulations reflect the crystal field effect of each of the three Cu ions but not the 3d–3d and 3d–4f intramolecular interactions; in particular, the 3d–3d interactions may lead to a canted arrangement of the three Cu moments. Turning to the Tb $M_{4,5}$ spectra (*cf.* Fig. 4), the XAS and XMCD exhibit a shape typical for a Tb^{III} ion, with a strong negative XMCD signal ($\sim$74%) at the M_5 resonance. As for the Cu simulations, we apply the above described six point scheme to consider the random orientation of the molecules during experiment, and we obtain excellent agreement with the corresponding multiplet simulations (see Fig. 4c and d). The magnetic Tb^{III} moment is aligned parallel to those of the Cu^{II} ions, confirming the ferromagnetic coupling between Cu and Tb found by SQUID measurements.[29,31] Concerning the sum rules analysis, we considered $n_h = 6$ holes per 4f shell (Tb^{III} has eight 4f electrons). Furthermore, the value of the spin quadrupole coupling $\langle T_Z\rangle$ is important for lanthanides (*via* the LSJ-coupling).[42] For Tb^{3+}, $\langle T_Z\rangle/\langle S_Z\rangle = -0.11$. Thus, $\langle T_Z\rangle$ and $\langle S_Z\rangle$ have opposite signs and the value from the spin sum rule is significantly underestimated since $\langle S_{eff}\rangle = \langle S_Z\rangle + 3\langle T_Z\rangle$. Employing this correction to the experimental spectrum of $Cu^{II}_3Tb^{III}(L^{Pr})$ and the corresponding simulated results, we see that the obtained values for the orbital and spin magnetic moments are within a small deviation of 10% in line (*cf.* Table 1). The excellent agreement between experiment and theory verifies that the ligand field determines the easy axis of magnetization. The small differences might be associated with the weak 3d–4f interaction between the Tb and the Cu ions.

In the case of such an anisotropic Tb^{III} ion, one expects $m_S = 6.0\ \mu_B$ and $m_L = 3.0\ \mu_B$ per atom according to Hund's rules. Also, recent density functional theory (DFT) indicates a value close to $m_L = 3.0\ \mu_B$ for Tb^{III}.[31] The markedly reduced values can be explained as resulting from the combined effects of the strong uniaxial anisotropy of the Tb(III) site and the crystal field influences on the local geometries of the metal ions and thus central Tb(III).[29–31] We note that it has previously been shown that in the closely structurally related Zn_3Dy analogue, there is a strong magnetic axiality with the easy axis lying almost on the plane of the macrocyclic ring.[43] Since Dy(III) and Tb(III) both have oblate anisotropies, we can expect something similar here. Furthermore, very similar XMCD results concerning the

Tb orbital moment have been very recently reported for Cu_3Tb covalently grafted onto small nanoparticles.[44]

Due to the high anisotropy, and since the samples are powders, not all Tb moments will align with the external magnetic field, a behavior that has been recently also observed in a trinuclear Dy–Cr–Dy molecular cluster.[38] The obtained ratios between 1.1 and 0.8 for $\langle L_Z\rangle/\langle S_Z\rangle$ are in line with a value of 1.0 obtained following Hund's rules.

Next, we want to compare the results obtained for $Cu_3Tb(\mathbf{L^{Pr}})$ and $Cu_3Tb(\mathbf{L^{Bu}})$, which are summarized in Table 1. We obtain a spin moment of $m_S = 3.02\ \mu_B$ (3.78)/Tb atom and an orbital moment of $m_L = 1.42\ \mu_B$ (1.66)/Tb atom for $Cu_3Tb(\mathbf{L^{Bu}})$ ($Cu_3Tb(\mathbf{L^{Pr}})$). These values are close to those found for $Cu^{II}_2Tb^{III}$ clusters ($m_S = 3.9\ \mu_B$ and $m_L = 1.9\ \mu_B$ per Tb atom).[28] For the overall moment (three times m_{tot_Cu} plus m_{tot_Tb}), we obtain a magnetic moment of 6.09 (6.59) μ_B per molecule for $Cu_3Tb(\mathbf{L^{Bu}})$ ($Cu_3Tb(\mathbf{L^{Pr}})$) at $T = 3$ K and in an external magnetic field of 7 T, which is in almost perfect agreement with the results of a very recent XMCD investigation of immobilized $Cu_3Tb(\mathbf{L^{Bu}})$ molecules, which were grafted onto gold nanoparticles, wherein Feltham *et al.* report an overall magnetic moment of 6 μ_B per molecule.[44] The overall evaluation of magnetic moments exhibits around 0.5 μ_B per molecule higher moments of the $Cu_3Tb(\mathbf{L^{Pr}})$ molecule compared to that of the $Cu_3Tb(\mathbf{L^{Bu}})$ molecule under external magnetic fields of 13.5 T and 7 T at $T = 3$ K. This might indicate that the larger, butylene linked, macrocycle leads to stronger 3d–3d interactions between the Cu(II) ions, leading to an enhanced canting of Cu moments compared to that of the molecule prepared using the propylene linked macrocycle.

Fig. 5 shows the element specific magnetization curves, which were obtained at the dichroic maxima of the Cu L_3 and the Tb M_5 edges of $Cu^{II}_3Tb^{III}(\mathbf{L^{Pr}})$ at $T = 5$ K and $T = 10$ K, respectively. Circles represent the total (spin and orbital) moment of the Tb^{III} ions and squares represent the total Cu^{II} moments as derived from the corresponding sum rules. The Tb^{III} and Cu^{II} magnetization curves reflect the ferromagnetic behavior found at external magnetic fields of 13.5 T and 7 T over the whole range between 0 and 7 T. However, at lower temperatures (5 K), the

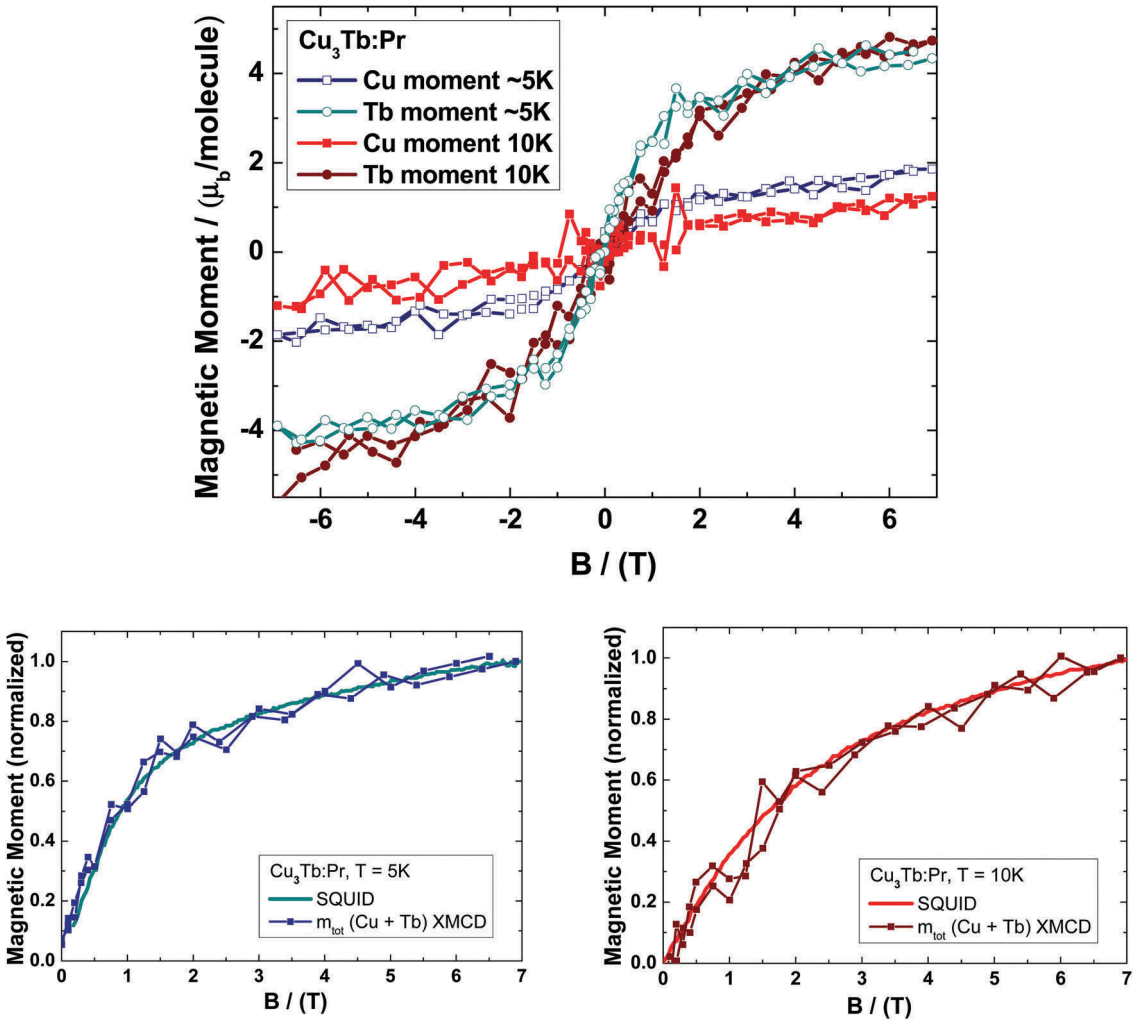

Fig. 5 Top panel: element specific magnetization curves of $Cu^{II}_3Tb^{III}(\mathbf{L^{Pr}})$ recorded at the Cu L_3 resonance (squares), representing the magnetization of the three Cu(II) sites, and the Tb M_5 resonance (circles) at $T = 5$ K (solid symbols) and $T = 10$ K (filled symbols). Bottom panel: comparison of normalized M(B)-curves of $Cu^{II}_3Tb^{III}(\mathbf{L^{Pr}})$ recorded by SQUID[29] and XMCD in the range from 0–7 Tesla at temperatures of 5 K (right) and 10 K (left).

Cu contribution to the overall moment of the molecule becomes higher compared to higher temperatures (10 K), whereas the Tb contribution remains the same within the experimental accuracy in this temperature range. This result reflects a low value of the Cu 3d–Tb 4f coupling in the $Cu_3Tb(\mathbf{L^{Pr}})$ molecule. The lower panel of Fig. 5 compares the (normalized) magnetization curves of the total magnetic moment per $Cu_3Tb(\mathbf{L^{Pr}})$ molecule recorded by XMCD and SQUID. Within the statistics of the measurement, the XMCD magnetization curves have the same shape and characteristics as those probed by SQUID, which is also another indication that the molecules remained intact during the XMCD experiments. Since the SQUID and XMCD magnetization curves are closed, we find no direct evidence for SMM behavior, which is nevertheless predicted due to the slow relaxation of the magnetization measured by ac susceptibility.[29,30] To further verify and study the SMM behavior of $Cu_3Tb(\mathbf{L^{Pr}})$ and $Cu_3Tb(\mathbf{L^{Bu}})$, low temperature magnetization and XMCD experiments in the (sub)-100 mK regime would be highly desirable.

Conclusions and outlook

We employed soft X-ray magnetic circular dichroism to study the Cu $L_{2,3}$ and Tb $M_{4,5}$ edges of 3d–4f SMMs $Cu_3Tb^{III}(\mathbf{L^{Bu}})$ and $Cu_3Tb(\mathbf{L^{Pr}})$ in external magnetic fields up to B = 13.5 T and at external temperatures between T = 3 K and T = 10 K. Sum rule analysis yields small but non-zero orbital moments for Cu^{II}, whereas an essentially orbital magnetic moment is present at the Tb^{III} site. The m_L/m_S ratios found for Tb are comparable for both molecules within the limits of the experimental technique, and the ratio corresponds to that expected from Hund's rules for a free Tb^{III} ion. The spin-quadrupole coupling $\langle T_Z \rangle$ has a significant influence on the spin moment of Tb^{III} (*via* the almost pure LSJ-coupling). We find excellent agreement between the experiment and the corresponding multiplet simulations using a point charge approximation for the crystal field. The moments of the Cu(II) ions may be canted due to 3d–3d intramolecular interactions, and the magnetic easy axis of the highly anisotropic Tb is determined by the ligand field. Element specific magnetization curves obtained for $Cu_3Tb(\mathbf{L^{Pr}})$ show ferromagnetic coupling between the Cu^{II} and Tb^{III} cations. Whereas the Cu^{II} contribution to the overall magnetic moment is strongly temperature dependent between T = 5 K and T = 10 K, the Tb^{III} contribution remains nearly unchanged, likely due to the high orbital contribution to the Tb magnetic moment in this temperature range, also implying a low value for the Cu 3d–Tb 4f coupling. We demonstrated that XMCD in the soft X-ray regime (*i.e.* transition metal $L_{2,3}$ and rare earth $M_{4,5}$ edges) is a powerful, element specific tool to study the magnetic properties of 3d–4f coupled SMMs such as the star shaped $Cu_3Tb(\mathbf{L^{Bu}})$ and $Cu_3Tb(\mathbf{L^{Pr}})$ investigated here. To obtain even deeper and more precise information on the SMM behavior, low temperature magnetization and XMCD investigations are desirable. Future experiments might also include studies on single crystals or molecules deposited on different (magnetic and non-magnetic) substrates. In this way, crystal field parameters of Cu and Tb ions may be determined with high precision, and coupling phenomena of the molecules with ferromagnetic substrates might be studied. Furthermore, we noted that in particular, the spin sum rule is under quite a bit of discussion, since it relies on detailed knowledge of the value spin-quadrupole coupling $\langle T_Z \rangle$ in the case of lanthanide ions, for example. Since there are many studies on novel 3d/4f systems going on, which will likely lead to a significant amount of 3d/4f XMCD studies looking at the contributions of the 3d as well as the 4f ions in a combined way, the use of sum rules might need some development of more straightforward ways concerning correction factors in the spin sum rule analysis, for instance.

Conflicts of interest

There are no conflicts to declare.

Acknowledgements

Part of this work has been performed at the Swiss Light Source, Paul Scherrer Institut, Villigen, Switzerland. We thank the Diamond Light Source for access to beamline I10 (SI11190) that contributed to the results presented here and are grateful to Alexey Dobrynin for excellent technical support. KK acknowledges financial support from the Walter und Sibylle Kalkhof-Rose-Stiftung (ADW Mainz). AKP thanks DFG *via* SFB/TRR 33 "3MET", the Helmholtz through the POF STN and the RSNZ for the provision of the Julius von Haast fellowship (to support multiple visits to SB). We are grateful to the University of Otago for supporting this research (HLCF and SB) and for the award of an Honorary Research Professorship (AKP).

References

1 M. Verdaguer, A. Bleuzen, C. Train, R. Garde, F. Fabrizi de Biani and C. Desplanches, *Philos. Trans. R. Soc., A*, 1999, **357**, 2959–2976.
2 M. N. Leuenberger and D. Loss, *Nature*, 2001, **410**, 789–793.
3 O. Kahn, *Molecular Magnetism*, VCH, New York, 1993.
4 H. Wende, M. Bernien, J. Luo, C. Sorg, N. Ponpandian, J. Kurde, J. Miguel, M. Piantek, X. Xu, P. Eckhold, W. Kuch, K. Baberschke, P. M. Panchmatia, B. Sanyal, P. M. Oppeneer and O. Eriksson, *Nat. Mater.*, 2007, **6**, 516–520.
5 F. Mögele, D. Fantauzzi, U. Wiedwald, P. Ziemann and B. Rieger, *Langmuir*, 2009, **25**, 13606–13613.
6 R. Sessoli, D. Gatteschi, A. Caneschi and M. A. Novak, *Nature*, 1993, **365**, 141–143.
7 R. W. Saalfrank, A. Scheurer, B. Bernt, F. W. Heinemann, A. V. Postnikov, V. Schünemann, A. X. Trautwein, M. S. Alam, H. Rupp and P. Müller, *Dalton Trans.*, 2006, 2865–2874.
8 H. U. Güdel and U. Hauser, *Inorg. Chem.*, 1980, **19**, 1325–1328.
9 S. Khanra, K. Kuepper, T. Weyhermüller, M. Prinz, M. Raekers, S. Voget, A. V. Postnikov, F. M. F. de Groot, S. J. George, M. Coldea, M. Neumann and P. Chaudhuri, *Inorg. Chem.*, 2008, **47**, 4605–4617.
10 V. Pavlishchuk, F. Birkelbach, T. Weyhermüller, K. Wieghardt and P. Chaudhuri, *Inorg. Chem.*, 2002, **41**, 4405–4416.

11 M. Prinz, K. Kuepper, C. Taubitz, M. Raekers, S. Khanra, B. Biswas, T. Weyhermüller, M. Uhlarz, J. Wosnitza, J. Schnack, A. V. Postnikov, C. Schröder, S. J. George, M. Neumann and P. Chaudhuri, *Inorg. Chem.*, 2010, **49**, 2093–2102.
12 K. Kuepper, D. M. Benoit, U. Wiedwald, F. Mögele, A. Meyering, M. Neumann, J. P. Kappler, L. Joly, S. Weidle, B. Rieger and P. Ziemann, *J. Phys. Chem. Lett.*, 2011, **2**, 1491.
13 K. Petukhov, M. S. Alam, H. Rupp, S. Strömsdörfer, P. Müller, A. Scheurer, R. W. Saalfrank, J. Kortus, A. Postnikov, M. Ruben, L. K. Thompson and J.-M. Lehn, *Coord. Chem. Rev.*, 2009, **253**, 2387–2398.
14 M. Mannini, F. Pineider, P. Sainctavit, C. Danieli, E. Otero, C. Sciancalepore, A. M. Talarico, M.-A. Arrio, A. Cornia, D. Gatteschi and R. Sessoli, *Nat. Mater.*, 2009, **8**, 194–197.
15 D. Gatteschi, R. Sessoli and A. Cornia, *Chem. Commun.*, 2000, 725–732.
16 C. J. Milios, R. Inglis, A. Vinslava, R. Bagai, W. Wernsdorfer, S. Parsons, S. P. Perlepes, G. Christou and E. K. Brechin, *J. Am. Chem. Soc.*, 2007, **129**, 12505.
17 R. Sessoli and A. K. Powell, *Coord. Chem. Rev.*, 2009, **253**, 2328.
18 M. Murrie, *Chem. Soc. Rev.*, 2010, **39**, 1986.
19 N. Ishikawa, *Polyhedron*, 2007, **26**, 2147.
20 G. E. Kostakis, I. J. Hewitt, A. M. Ako, V. Mereacre and A. K. Powell, *Philos. Trans. R. Soc. London, Ser. A*, 2010, **368**, 1509.
21 D. N. Woodruff, R. E. P. Winpenny and R. A. Layfield, *Chem. Rev.*, 2013, **113**, 5110.
22 C. Benelli and D. Gatteschi, *Chem. Rev.*, 2002, **102**, 2369.
23 M. Ferbinteanu, T. Kajiwara, K.-Y. Choi, H. Nojiri, A. Nakanoto, N. Kojima, F. Cimpoesu, Y. Fujimura, S. Takaishi and M. Yamashita, *J. Am. Chem. Soc.*, 2006, **128**, 9008.
24 M. Andruh, J.-P. Costes, P. Diaz and S. Gao, *Inorg. Chem.*, 2009, **48**, 3342.
25 V. Mereacre, A. Baniodeh, C. E. Anson and A. K. Powell, *J. Am. Chem. Soc.*, 2011, **133**, 15335.
26 M. Ibrahim, V. Mereacre, N. Leblanc, W. Wernsdorfer, C. E. Anson and A. K. Powell, *Angew. Chem., Int. Ed.*, 2015, **54**, 15574.
27 J. D. Rinehart and J. R. Long, *Chem. Sci.*, 2011, **2**, 2078.
28 T. Hamamatsu, K. Yabe, M. Towatari, S. Osa, N. Matsumoto, N. Re, A. Pochaba, J. Mrozinski, J. Gallani, A. Barla, P. Imperia, C. Paulsen and J.-P. Kappler, *Inorg. Chem.*, 2007, **46**, 4458.
29 H. L. C. Feltham, R. Clérac, A. K. Powell and S. Brooker, *Inorg. Chem.*, 2011, **50**, 4232.
30 H. L. C. Feltham, R. Clérac, L. Ungur, L. F. Chibotaru, A. K. Powell and S. Brooker, *Inorg. Chem.*, 2013, **52**, 3236–3240.
31 H. L. C. Feltham, R. Clérac, L. Ungur, V. Vieru, L. F. Chibotaru, A. K. Powell and S. Brooker, *Inorg. Chem.*, 2012, **51**, 10603–10612.
32 F. J. Kettles, V. A. Milway, F. Tuna, R. Valiente, L. H. Thomas, W. Wernsdorfer, S. T. Ochsenbein and M. Murrie, *Inorg. Chem.*, 2014, **53**, 8970–8978.
33 H. L. C. Feltham, S. Dhers, M. Rouzieres, R. Clérac, A. K. Powell and S. Brooker, *Inorg. Chem. Front.*, 2015, **2**, 982.
34 O. Waldmann, *Inorg. Chem.*, 2007, **46**, 10035–10037.
35 W. W. Lukens and M. D. Walter, *Inorg. Chem.*, 2010, **49**, 4458–4465.
36 C. T. Chen, Y. U. Idzerda, H.-J. Lin, N. V. Smith, G. Meigs, E. Chaban, G. H. Ho, E. Pellegrin and F. Sette, *Phys. Rev. Lett.*, 1995, **75**, 152–155.
37 T. Funk, A. Deb, S. J. George, H. X. Wang and S. P. Cramer, *Coord. Chem. Rev.*, 2005, **249**, 3.
38 J. Dreiser, K. S. Pedersen, C. Piamonteze, S. Rusponi, Z. Salman, M. E. Ali, M. Schau-Magnussen, C. A. Thuesen, S. Piligkos, H. Weihe, H. Mutka, O. Waldmann, P. Oppeneer, J. Bendix, F. Nolting and H. Brune, *Chem. Sci.*, 2012, **3**, 1024.
39 I. Letard, P. Sainctavit, C. Cartier dit Moulin, J.-P. Kappler, P. Ghigna, D. Gatteschi and B. Doddi, *J. Appl. Phys.*, 2007, **101**, 113920.
40 F. de Groot and A. Kotani, *Core Level Spectroscopy of Solids. Advances in Condensed Matter Science*, CRC Press, Boca Raton, 2008, vol. 6.
41 A. Uldry, F. Vernay and B. Delley, *Phys. Rev. B: Condens. Matter Mater. Phys.*, 2012, **85**, 125133.
42 P. Carra, B. T. Thole, M. Altarelli and X. D. Wang, *Phys. Rev. Lett.*, 1993, **70**, 694.
43 H. L. C. Feltham, Y. Lan, F. Klöwer, L. Ungur, L. F. Chibotaru, A. K. Powell and S. Brooker, *Chem. – Eur. J.*, 2011, **17**, 4362.
44 H. L. C. Feltham, C. Dumas, M. Mannini, E. Otero, P. Sainctavit, R. Sessoli, C. J. Meledandri and S. Brooker, *Chem. – Eur. J.*, 2017, **23**, 2517.